Computational Electrochemistry

A thesis submitted for the degree of

Doctor of Philosophy

in Physical and Theoretical Chemistry

Haotian Chen

Lady Margaret Hall

University of Oxford

Trinity Term 2022

Abstract

This thesis focuses on the study of electrochemical reaction and mass transport processes via numerical simulation, parameter estimation and deep learning enabled inferences. The significance of computation to understanding of electrochemistry will be shown and discussed.

Chapter 1 presents the fundamentals of electrochemistry, including concepts, theories and experimental practices to provide background information to this thesis. Chapter 2 provides the basics of simulation, including simulation of mass transport and models for interfacial reactions and boundary conditions. Testing and validation methods are also introduced.

Chapter 3 analyzes the Tafel slope of cyclic voltammetry recorded for a heterogeneous electrochemically reversible electron transfer process coupled with non-linear homogeneous chemical kinetics. Tafel plots are shown to be markedly non-linear with potential, indicating the essential need to be analysed via simulation rather than approximate analytical theory. A super-Nernstian Tafel slope is observed for EC_2 reaction. Chapter 4 models a non-unity stoichiometric reversible electrode reaction, using the oxidation of bromide with coupled chemical kinetics as an example.

Chapter 5 generalizes the simulations of the previous chapters with a focus on the effect of coupled preceding or following chemical reaction on Tafel analysis predicted with finite difference simulation. Four cases of coupled chemical reactions are elaborated.

Chapter 6 introduces the application of artificial intelligence (AI) in electrochemical studies, using neural networks to extract rate and equilibrium constants from voltammograms of dissociative CE reaction and predict voltammograms from these constants. AI provides an

excellent tool to map the relationship between experimental data and parameters of interest. The training data of neural networks is facilitated by numerical simulation, an optimal alternative to experimental data which is hard and expensive to collect and process. Chapter 7 introduces the "simulation, experiment and machine learning" framework for parameter estimation and is validated with the dissociation of acetic acid experiment: by training neural network with simulated steady state current to correlate with kinetic and thermodynamic constants of acetic acid dissociation, AI can accurately predict these constants based on experimental data. This framework provides a new tool for parameter estimation by combining simulation and AI for extracting data from experiments.

Chapter 8 introduces the state-of-art physics-informed neural network (PINN) for solving partial differential equations (PDEs). By imposing physical constraints in the form of PDEs on neural network, the PDEs can be solved without discretization. PINN is applied to solve diffusive mass transport problems in electrochemical reactions with boundary conditions enforcing interfacial reactions to predict voltammetry. PINNs are applied to a variety of 1D and 2D models, introducing a faster and/or easier way of simulation of voltammetry.

Chapter 9 elaborates on further exploration of PINN notably in hydrodynamic voltammetry. Using curriculum learning, PINN can solve the convective-diffusion problem of a single microband channel electrode and predict the mass transport limited current. PINN can also predict the collection-efficiency of double microband channel electrode in generator-detector formation. Furthermore, convective-diffusion coupled with chemical kinetics is also solved to predict the kinetically controlled mass transport limited current. The results are validated by experimental data and/or analytical expression where applicable.

Acknowledgements

My choice to study for a PhD, has the same motivation as JFK chose to go to the moon: not because it is easy, but because it is hard. It is the best way to measure my dedication and contribution to science, and the best situation to conquer the toughest challenge of my intellectuality and endurance. It is a journey I have *huge* gain in weight and suffer *huge* loss in hair. Fortunately, it is also a journey with guidance and companion.

When COVID-19 struck the world on early 2020, I became a spacecraft wandering in space. While astronauts called Houston whenever they had a problem, I sent emails to my supervisor and received very timely responses, sometimes less than a minute. Even segregated thousands of miles away, the transmission of knowledge was never interrupted: we derived equations, reviewed simulations, then drafted and edited papers together. We are never satisfied with the territory discovered, and we are always eager to explore technology formerly unheard of. Warm and sincere thanks to my supervisor, Prof. Richard Compton, for paving and leading my quest of science. Besides, this thesis is just a small landmark and we don't stop here!

I would also like to acknowledge Dr. Haonan Le, Dr. Minjun Yang and Dr. Enno Kätelhön for their supports towards computation and Maxim Shaw for his support of cloud computing. Huge thanks to Dr. Danlei Li for guiding me through my sole experiment performed here. To my other coauthors, Dr. Christopher Batchelor-McAuley, Dr. Ruiyang Miao, Joseph Elliot and Archana Kaliyaraj Selva Kumar, thank you for your contribution. Huge thanks to Grace, Yuanzhe, Yuanyuan, Yifei, Yuqi and other lab members to create such a lovely working atmosphere. Once again, thank you for your company.

I would like to thank Prof. Wei Xiong, Prof. Yitzhak Tor and Prof. Ming Tian for their recommendations so I can study here. I would like to mention other professors/teachers leading me here. Thank you for your support and hopefully I have met your expectations.

I would never forget my friends, both current and lost. Tears, laughter and memories with you are my most precious treasure. Thank you, so that I can be brave to face any life's obstacles.

I would like to thank my college, Lady Margaret Hall, for the exceptional meals and scholarship provided for my study.

Finally, my deepest gratitude to my parents and grandparents. Thank you for working so hard to support my study and I am proud to be a first-generation university student! Without their support, this thesis would not have been possible.

Contents

Glossary

Roman Symbols

Symbol	Meaning	Unit
a_j	Activity of species *j*	mol m^{-3}
A	Area	m^2
c_j	Concentration of species j	mol m^{-3}
$[j]_{bulk}$	Bulk concentration of species *j*	mol m^{-3}
C_d	Double layer capacitance	F m^{-2}
D_j	Diffusion coefficient of species *j*	m^2 s^{-1}
E	Potential at the working electrode	V
E^0	Standard electrode potential	V
E_f^0	Formal potential	V
$E_{1/2}$	Half wave potential	V
ΔE_{pp}	Peak-to-peak potential	V
F	Faraday Constant, ≈ 96485	C mol^{-1}
G	Gibbs energy	J mol^{-1}
$\Delta G_0^{\dagger}$	Standard Gibbs energy	J mol^{-1}
$\Delta G_{OX}^{\dagger}$	Gibbs energy of activation of oxidation	J mol^{-1}
$\Delta G_{red}^{\dagger}$	Gibbs energy of activation of reduction	J mol^{-1}
I	Current	A
I_p	Peak current	A
I_{ss}	Steady state current	A

J_j	Flux of species j	$\mathrm{mol\ m^{-2}\ s^{-1}}$
k_0	Standard electrochemical rate constant	$\mathrm{m\ s^{-1}}$
k_{ox}	Electrochemical rate constant for oxidation	$\mathrm{m\ s^{-1}}$
k_{red}	Electrochemical rate constant for reduction	$\mathrm{m\ s^{-1}}$
K_{eq}	Equilibrium constant	$\mathrm{m^3\ mol^{-1}}$
m	Mass	g
m_T	Mass transfer coefficient	$\mathrm{m\ s^{-1}}$
n	Number of electrons transferred	Dimensionless
N_j	Number of species j	Dimensionless
N_A	Avogadro's number $\approx 6.022 \times 10^{23}$	$\mathrm{mol^{-1}}$
Q	Charge	C
R	Universal gas constant ≈ 8.314	$\mathrm{J\ K^{-1}\ mol^{-1}}$
r_e	Electrode radius	m
T	Absolute temperature	K
t	Time	s
v	Potential scan rate	$\mathrm{V\ s^{-1}}$
x, y, z	Cartesian coordinates	Dimensionless
z_j	Ionic charge of species j	Dimensionless

Greek Symbols

Symbol	Meaning	Unit
α	Reductive transfer coefficient	Dimensionless
β	Oxidative transfer coefficient	Dimensionless

δ	Diffusion layer thickness	M
κ_0	A parameter quantifying the reversibility level of microdisc voltammetry, $\kappa_0 = \frac{r_e k_0}{D_A}$. Avoid confusion with k_0, the standard electrochemical rate constant.	Dimensionless
η	Overpotential ($E - E_f^0$)	V
γ	Activity coefficient	dimensionless
μ	Chemical potential	J mol^{-1}
μ_0	Standard chemical potential	J mol^{-1}
$\bar{\mu}$	Electrochemical potential	J mol^{-1}
ϕ	Electric potential	V
ϕ_m	Electric potential of the metallic electrode	V
ϕ_s	Electric potential of the solution	V

Dimensional and dimensionless parameters for simulations. Definition of dimensionless parameters is subject to problem setup and can be found in chapters below where applicable.

Parameter	Dimensional	Dimensionless
Concentration of species j	c_j	C_j
Diffusion coefficient of species j	D_j	d_j
Spatial coordinate, x-axis	x	X
Time	t	T
Potential	E	θ

Scan rate	ν	σ
Heterogenous rate constant	k_0	K_0
Flux	j	J

Chapter 1 Introduction

This chapter provides an overview of the theoretical foundations of electrochemistry and voltammetry more specifically. A discussion of electroanalytical techniques is preceded by theories of mass transport and the fundamentals of electrode kinetics. These will serve as the bedrock of the simulations discussed in Chapter 2. A good overview of voltammetry can be found in the literature[1-5].

1.1 Mass transport in electrochemistry

The mass transport of electroactive material from bulk solution to an electrode surface is of primary importance in electrochemistry studies. Mass transport combined with electrode kinetics and often coupled homogeneous chemical kinetics can determine the rate and magnitude of an electrochemical reaction at the electrode surface.

1.1.1 Types of mass transport

There are three primary modes of mass transport: diffusion, migration and convection. Diffusion is the movement of material across a concentration gradient, convection is movement of material either by mechanical forces or by density gradients of solution, and migration is the movement of charged material due to potential gradient[1, 2].

The most commonly encountered form in voltammetry is a diffusion only flux in the x-direction which can be expressed as:

$$j = -D_j \frac{\partial c_j}{\partial x} \qquad \textbf{(1.1)}$$

where D_j and C_j is the diffusion coefficient and concentration of the species j respectively. Migration is usually considered in weakly supported media and convection contributes

dominantly to hydrodynamic electrodes. The Nernst-Planck equation takes the three modes of mass transport into consideration:

$$j = -\left(D_j\left(\frac{\partial c_j}{\partial x}\right) + D_j\frac{z_j F}{RT}c_j\left(\frac{\partial \phi(x)}{\partial \mathrm{x}}\right) - v(x)c_j\right) \quad \textbf{(1.2)}$$

where z_j is the charge of species j. F, R, T are the Faraday Constant, the Gas Constant and the absolute temperature respectively. $\phi(x)$ is the potential at spatial point x and $v(x)$ is the solution velocity in the x direction.

Diffusion as a phenomenon has been readily observed when steeping a cup of tea, when molecules from the tea cross from the tea bag and diffuse throughout the cup of water, or when lighting a cigarette, the smoke spreads to all space of the room. To be more precise, diffusion refers to the processes where molecules move from high concentration to low concentration due to Brownian motion. Fick's First and Second Law of diffusion, describe the relationship between the rate of diffusion and factors affect diffusion, including diffusion layer thickness, concentration gradient and surface area. Details of simulation of diffusional mass transport is articulated in the next chapter.

Migration is the movement of charged material due to potential gradient, which can be formed as a result of the electrostatic interaction between an electrode surface and the ions in solution. When migration is not the mass transport of interest nor desirable, it is minimized by adding an excessive amount of inert electrolyte to spatially compress the interfacial potential drop and in addition decrease the resistance of the solution, reducing electric fields in the bulk of the solution. When high concentration of electrolyte (>0.1M) is present in solution such that the potential drop $(\phi_m - \phi_m)$ is compressed to a distance within 10-20Å, migration can usually be neglected[1].

Convection is caused by mechanical means like stirring, pumping, or shaking, leading to hydrodynamic flow or density gradients in solution. Rotating disc and channel electrodes are examples of hydrodynamic electrodes which introduce convection to the electrochemical system. Convection is usually minimized during diffusion only experiments by maintaining a stable temperature, minimizing vibration and other mechanical forces. In this thesis, convection is not considered unless simulating the channel electrode.

In summary, in the following diffusion is the primary mass transport of interest unless otherwise stated.

1.1.2 Fick's Laws

Fick's Laws serve as the basis of simulation of diffusion in this thesis. When observing the diffusion of a drop of ink into water, people may conclude that diffusion occurs from high to low concentrations (down the concentration gradient). At any point in x, the diffusive flux can be quantified by Fick's First Law:

$$j = -D_j \frac{\partial c_j}{\partial x} \tag{1.3}$$

where j is the flux (mol m^{-2} s^{-1}), corresponding to the number of moles passing through unit area in unit time, $\frac{\partial c_j}{\partial x}$ is the concentration gradient at point x and D_j is the diffusion coefficient for j. Usually, there is an inverse relationship between the size of the redox ions and the diffusion coefficient. Note that the negative sign implies that the flux is *down* the concentration gradient. Diffusion coefficients are strongly temperature dependent, and often following an Arrhenius type relationship:

$$D = D_\infty \exp\left(-\frac{E_a}{RT}\right) \tag{1.4}$$

where $E_a/kJ\ mol^{-1}$ is an activation energy for diffusion and D_∞ is the hypothetical value of D at infinite dilution. Thus, to ensure consistency and reproducibility of experiments, temperature should be carefully controlled using a thermostat or other devices.

Fick's Second Law answers the question how the concentration at point x varies with time. The temporal evolution of concentration in one dimension is:

$$\frac{\partial c_j}{\partial t} = D\frac{\partial^2 c_j}{\partial x^2} \tag{1.5}$$

and the diffusion in three dimensions are:

$$\frac{\partial c_j}{\partial t} = D\left(\frac{\partial^2 c_j}{\partial x^2} + \frac{\partial^2 c_j}{\partial y^2} + \frac{\partial^2 c_j}{\partial z^2}\right) = D\nabla^2 c_j \tag{1.6}$$

where ∇ is the Laplace operator.

While the First Law was derived by experimental phenomenon that molecules diffuse down the concentration gradient, the Fick's second law was derived to solve the temporal relationship of concentration at certain points. The Second Law was derived from the First Law following the principle of mass conservation. Based on the First Law, the change in the number of moles, δn, of the diffusing species overtime through a "slab" is:

$$\delta n = [J(x) - J(x + \delta x)]A\delta t \tag{1.7}$$

Follows Taylor expansion that:

$$J(x + \delta x) \approx J(x) + \delta x\left(\frac{\partial J}{\partial x}\right) \tag{1.8}$$

Accordingly,

$$\delta n \sim -\delta x\left(\frac{\partial J}{\partial x}\right)A \cdot \delta t \tag{1.9}$$

The concentration is changed as:

$$\delta c = \frac{\delta n}{A} \cdot \delta x \tag{1.10}$$

which gives the rate of change of concentration at point x, and the Second Law:

$$\frac{\delta c}{\delta t} \sim \frac{\partial c}{\partial t} = -\frac{\partial J}{\partial x} = D\frac{\partial^2 c}{\partial x^2} \tag{1.11}$$

The diffusion equation for the (hemi-)spherical electrode and cylinder electrode is:

$$\frac{\partial c_j}{\partial t} = \frac{\partial^2 c}{\partial r^2} + \frac{\xi}{r}\frac{\partial c_j}{\partial r} \tag{1.12}$$

where r is the radial coordinate and $\xi = 1$ for a cylindrical electrode and 2 for a (hemi-)spherical electrode. The diffusion equations for other electrochemical systems will be introduced where relevant.

1.1.3 Diffusion layer

Diffusion is the dominant mode of mass transport is a process of spontaneous movement down the concentration gradient to maximize entropy. When electrochemical reaction depletes the species at the surface of electrode, a concentration gradient is formed between the electrode and the bulk solution. Figure 1.1 illustrates a depletion zone near the surface of electrode known as “diffusion layer”.

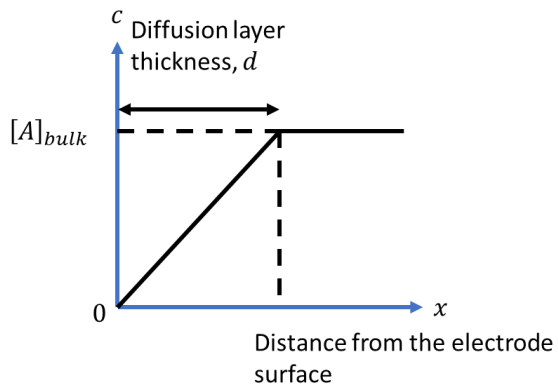

Figure 1.1. Nernst diffusion layer.

The diffusive model above dictates that the molecules diffuse further away from their original position as time passes. The Einstein-Von Smoluchowski equation relates, in one dimension, the root-mean-square displacement x of a molecule to diffusion coefficient and time:

$$\sqrt{\langle x^2 \rangle} = \sqrt{2Dt} \tag{1.13}$$

The physical basis of Fick's first law was given by Einstein and Van Smoluckowskii[6].The molecular basis of Fick's law relating to diffusion is illustrated in Figure 1.2 in one dimension: it highlights a "box" of width $2\delta x$ composed of two half boxes. Assuming that in each "half box", molecules are indifferent moving right or left, and a particle, on average, move δx in δt. Thus, the number of molecules traveling from the left half box to the right half box is $\frac{1}{2} c_1 A \delta x$ and the number of molecules traveling from the right half box to the left is $\frac{1}{2} c_2 A \delta x$. The net rate of mass transfer through a plane positioned at x is:

$$\text{Rate} = \frac{(c_1 - c_2) A \delta x}{2\delta t} \tag{1.14}$$

The concentration difference can also be expressed as:

$$c_1 - c_2 \sim -\delta x \left(\frac{\partial c}{\partial x}\right) \tag{1.15}$$

Substituting **(1.15)** into **(1.14)** gives:

$$J = -\frac{(\delta x)^2}{2\delta t}\frac{\partial c}{\partial t} \tag{1.16}$$

which is equivalent to Fick's First Law when:

$$D = \frac{(\delta x)^2}{2\delta t} \tag{1.17}$$

Therefore, the diffusion coefficient of a molecule in solution describes how far it travels in time. The root-mean-square displacement in time, t, in one dimension is thus **(1.13)**. When considering diffusion in three dimensions, the root mean square distance is:

$$\sqrt{\langle x^2 \rangle + \langle y^2 \rangle + \langle z^2 \rangle} = \sqrt{6Dt} \tag{1.18}$$

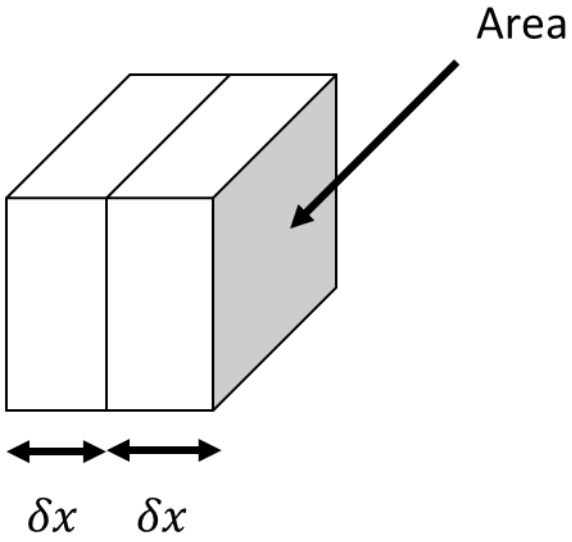

Figure 1.2. The molecular model for Fick's First Law. The slab on the left has a concentration of c_1 and the slab on the right side has a concentration of c_2.

1.2 Electrochemistry fundamentals

To understand the underlying fundamental physics underpinning the simulation of electrochemistry reactions, it is necessary to introduce the basics of experimental practices and the underlying theories.

1.2.1 The Nernst equation

The electrochemical reactions involve the charge transfer between molecules in solution phase and the solid electrode, as for example in the following simple electrochemical reaction:

$$A_{aq}^{Z_A} \pm e \rightleftarrows B_{aq}^{Z_B} \tag{1.19}$$

where Z_a and Z_b are the charge of the two species respectively. Hence, for the case of any electrochemical reaction, the position of equilibrium corresponds to a balance between chemical energies and electrical energies. The electrical energy may be different in different phase due to the different electrical potentials. To account for both the chemical and electrical energies, the electrochemical potentials, $\bar{\mu_j}$ are introduced:

$$\bar{\mu_j} = \mu_j + Z_j F \phi \tag{1.20}$$

where Z_j is the charge on molecule *j* and ϕ is the potential in the particular phase *j* is found. μ_j is the chemical potential:

$$\mu_j = \frac{\partial G_j}{\partial n_j} \tag{1.21}$$

which is the partial derivative of Gibbs energy (G_j) and its molar amount (N_j). For solution phase species j, the chemical potential relates to the activity of solute as:

$$\mu_j = \mu_j^0 + RT \ln \frac{a_j}{c^0}, a_j = \gamma_j c_j \quad \textbf{(1.22)}$$

where μ_j^0 is the standard chemical potential, a_j is the activity, and γ_j corresponds to the activity coefficient for species j. c^0 is the standard concentration equal to 1 Molar (1 mol L^{-1}).

When an equilibrium is reached, the change in Gibbs energy is zero, which leads to the balancing of the electrochemical potentials:

$$\overline{\mu_A} + \overline{\mu_e} = \overline{\mu_B} \quad \textbf{(1.23)}$$

which can be expanded into:

$$(\mu_A + Z_A F \phi_s) + (\mu_e - F\phi_m) = (\mu_B + Z_B F \phi_s) \quad \textbf{(1.24)}$$

where ϕ_s and ϕ_m are the electrical potential in solution phase and electrode respectively. Therefore, the interfacial potential difference is:

$$\phi_m - \phi_s = \frac{1}{F}(\mu_A^0 + \mu_e - \mu_B^0) + \frac{RT}{F} \ln \frac{a_A}{a_B} \quad \textbf{(1.25)}$$

Substituting $\mu_A^0 + \mu_e - \mu_B^0$ with $\Delta\mu^0$, the Nernst equation is expressed as:

$$\phi_m - \phi_s = \frac{\Delta\mu^0}{F} + \frac{RT}{F} \ln \frac{a_A}{a_B} \quad \textbf{(1.26)}$$

In addition, the measured potential difference between the working electrode and a reference electrode is:

$$E = (\phi_m - \phi_s) - (\phi_m^r - \phi_s^r) \quad \textbf{(1.27)}$$

thus:

$$E = \frac{\Delta\mu^0}{F} + \frac{RT}{F} \ln \left(\frac{\gamma_A}{\gamma_B}\right) - (\phi_m^r - \phi_s^r) + \frac{RT}{F} \ln \frac{c_A}{c_B} \quad \textbf{(1.28)}$$

The standard electrode potential E^0 is expressed as:

$$E^0 = \frac{\Delta\mu^0}{F} - (\phi_m^r - \phi_s^r) \tag{1.29}$$

The formal potential is introduced to allow for solution non-ideality:

$$E_f^0 = E^0 + \frac{RT}{F}\ln\frac{\gamma_A}{\gamma_B} \tag{1.30}$$

Therefore, the potential measurement becomes:

$$E = E_f^0 + \frac{RT}{F}\ln\left(\frac{c_A}{c_B}\right) \tag{1.31}$$

The formal potential misses the thermodynamic generality of the standard potential, and is only applicable to very specific conditions, but it enables the experimentalists to find the relationship between concentration and potential, and to proceed with practical voltammetric experiments.

1.2.2 The Butler-Volmer equation

The Nernst equation introduced in the last section characterises the equilibrium state in electrochemistry. Kinetics, on the other side, describes evolution of electrochemical reaction towards the steady state. In this section, the Butler-Volmer equation is introduced[7, 8], which serves as the theoretical basis for simulation of electrode kinetics discussed later.

We next consider the simple cathodic electrochemical reaction:

$$A_{aq}^{Z_A} + e \underset{k_a}{\overset{k_c}{\rightleftarrows}} B_{aq}^{Z_B} \tag{1.32}$$

at an electrode of area, A_{elec}, where k_c and k_a are heterogeneous electron transfer fate constant of the cathodic reaction (reduction of A^{Z_A} to B^{Z_B}) and anodic reaction (oxidation of B^{Z_B} to A^{Z_A}). At the electrode-solution interface, the electron transfer process between the electrode and the reactant A^{Z_A} is controlled by quantum tunnelling, only effective within $1 \sim 2$ nm of the electrode so the electron wavefunctions of the two parties can overlap. The rate of

tunnelling decreases significantly with distance. Thus, the effective concentration near the surface of electrode predominately affects the rate of electron transfer at the electrode. With the counter electrode, as a result of the electron transfer the electron flux, J, will lead to current through the electrode:

$$I = nFA_{elec}J \tag{1.33}$$

where J is the number of transferred electrons, which is 1 for **(1.32)**. The net heterogeneous reaction flux J is:

$$J = k_C[A^{Z_A}]_{x=0} - k_a[B^{Z_B}]_{x=0} \tag{1.34}$$

where $[A^{Z_A}]_{x=0}$ and $[B^{Z_B}]_{x=0}$ is the concentration at the surface of electrode.

For electrolysis reactions, early studies[9-11] found that the current is often related exponentially to overpotential η $\left(\eta = E - E_f^0\right)$ while equation **(1.33)** and **(1.34)** suggest that current is dominated by interfacial dynamics, indicating the relationship between electrode kinetics and the potential applied. Transition state theory [12, 13] was introduced as an general theory for electrode kinetics, stating that reactions proceed by passing through a transition state or activated complex as quantified by equation **(1.35)**.

Arrhenius proposed that the natural logarithm of most rate constants in solution phase is linear with respect to the reciprocal of the temperature. The Arrhenius equation is:

$$k = Ae^{\frac{-\Delta G^{\ddagger}}{RT}} \tag{1.35}$$

where $\Delta G^{\ddagger}$ is the standard Gibbs energy. The exponential term represents the probability of surmounting the energy barrier between the reactant and product whilst A is the pre-exponential factor, or "frequency" factor for the reaction. R and T are the Universal Gas Constant and absolute temperature respectively.

Figure 1.3 shows the reaction pathway of **(1.32)** in terms of energy along the reaction coordinate. The change in standard Gibbs energy (energy barrier) of the forward (cathodic) reaction to the transition state is $\Delta G_a^{\ddagger}$ and for the reverse reaction (anodic) reaction is $\Delta G_a^{\ddagger}$.

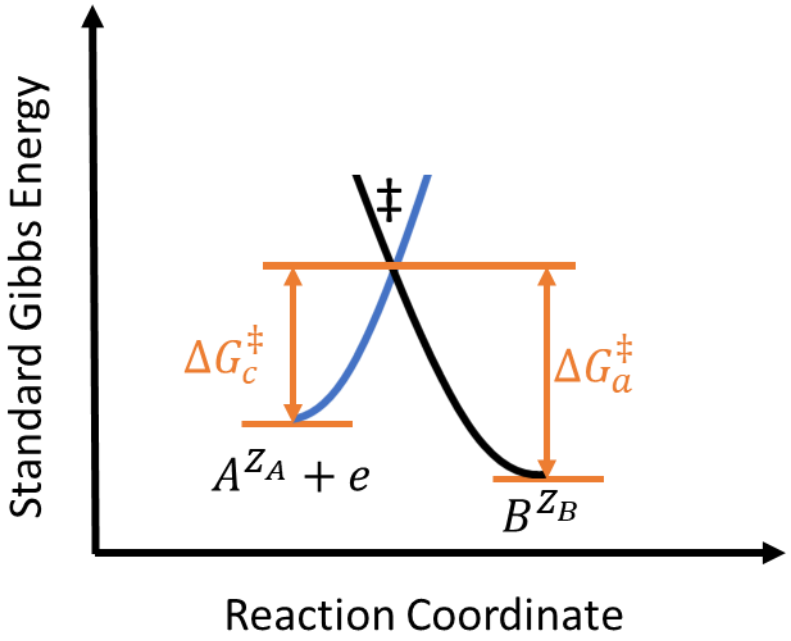

Figure 1.3. Standard Gibbs energy profiles of an electrochemical reaction. Blue line is the energy curve for the cathodic reaction and the black line is for the anodic reaction.

As electrode is actively involved in the reaction, the standard Gibbs energy of reactant is changes as different potentials, ϕ_M are applied to the electrode such that:

$$G^0 = c_1 - ZF(\phi_m - \phi_s) \qquad \textbf{(1.36)}$$

where c_1 is a constant. Changing the electrode potential from its formal potential E_f^0 to E, the energy level of electrode is changed by $F\Delta E = -F\left(E - E_f^0\right)$ and the energy profile of forward reaction shifts up or down by ΔE. Figure 1.4 shows the energy profile of the forward reaction shifted by a positive potential difference ΔE. Figure 1.4b show that the energy barrier of the reverse reaction drops by a fraction of the total energy change, and the fraction is denoted $1 -$

α, alternatively denoted as β. The dimensionless parameter α, called the transfer coefficient ranges between $0 < \alpha < 1$. Therefore the activation energy for the anodic reaction,

$$\Delta G_a^{\ddagger} = \Delta G_{0,a}^{\ddagger} - (1-\alpha)F\left(E - E_f^0\right) \tag{1.37}$$

Figure 1.4b also reveals that the positive overpotential increases the cathodic reaction energy barrier by $\alpha F\left(E - E_f^0\right)$ and therefore for the cathodic reaction activation energy:

$$\Delta G_c^{\ddagger} = \Delta G_{0,c}^{\ddagger} - \alpha F\left(E - E_f^0\right) \tag{1.38}$$

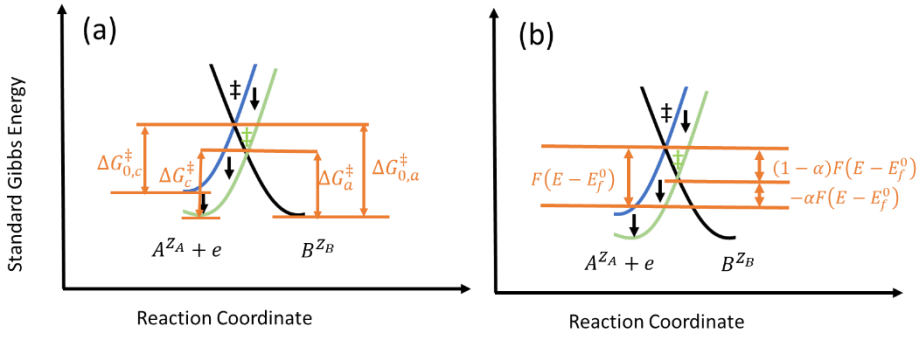

Figure 1.4. Effect of a positive overpotential on the working electrode on the activation energy. Green curve shows the shifted energy curve due to the positive overpotential.

The rate constants k_c and k_a in Arrhenius form are:

$$\begin{cases} k_c = A_c e^{-\Delta G_c^{\ddagger}} \\ k_a = A_a e^{-\Delta G_a^{\ddagger}} \end{cases} \tag{1.39}$$

At equilibrium when with zero net current at $E = E_f^0$ and equal surface concentration:

$$J = k_c[A^{Z_A}]_{x=0} - k_a[B^{Z_B}]_{x=0} = 0 \tag{1.40}$$

Thus, $k_a = k_c = k^0 = A_c e^{\frac{-\alpha F\left(E-E_f^0\right)}{RT}} = A_a e^{\frac{(1-\alpha)F\left(E-E_f^0\right)}{RT}}$ where k_0 is called standard electrochemical rate constant. The rate constants at other potential in terms of k_0 are:

$$k_c = k_0 e^{\frac{-\alpha F\left(E-E_f^0\right)}{RT}} \qquad \textbf{(1.41)}$$

$$k_a = k_0 e^{\frac{(1-\alpha) F\left(E-E_f^0\right)}{RT}}$$

The transfer coefficient α usually approximates 0.5 for a one electron process (but see Chapter 3 below):

$$\alpha \approx 0.5 \qquad \textbf{(1.42)}$$

At the typical *approximate* value of $\alpha = 0.5$, when electrode potential is changed by one volt, the rate constants changes by $e^{\frac{0.5F1V}{RT}} \approx 2.86 \times 10^8$, suggesting that a tiny change in overpotential can have significant impact on electrochemical reaction rates.

Substituting **(1.41)** into **(1.40)** gives the following flux-potential relationship and results in the famous Butler-Volmer equation[7, 8]:

$$J = k_0 e^{\frac{-\alpha F\left(E-E_f^0\right)}{RT}} [A^{Z_A}]_{x=0} - k_0 e^{\frac{(1-\alpha) F\left(E-E_f^0\right)}{RT}} [B^{Z_B}]_{x=0} \qquad \textbf{(1.43)}$$

Interestingly, for a reversible one-electron process, (k_0 is large), the Butler-Volmer equation reduces to Nernst equation. When k_0 is large, such that net flux, $J = 0$. Under these conditions:

$$k_0 e^{\frac{-\alpha F\left(E-E_f^0\right)}{RT}} [A^{Z_A}]_{x=0} = k_0 e^{\frac{(1-\alpha) F\left(E-E_f^0\right)}{RT}} [B^{Z_B}]_{x=0} \qquad \textbf{(1.44)}$$

Note that for one-electron transfer, $\alpha + \beta = 1$. Rearranging **(1.44)** leads to:

$$\frac{[B^{Z_B}]_{x=0}}{[A^{Z_A}]_{x=0}} = \exp\left[\frac{-F}{RT}\left(E - E_f^0\right)\right] \qquad \textbf{(1.45)}$$

which is the Nernst equation. Using the Butler-Volmer equation, the famous Tafel law[14] is derived in later section.

1.2.3 Marcus-Hush Theory

Although Butler-Volmer equation can parameterize and classify the kinetics for systems where the electroactive species diffuse to electrode, it was not very successful applying to the case of electroactive monolayers[15]. Furthermore, the Butler-Volmer equation has limited capability for understanding the physical-chemical properties underpinning electron transfer of systems. To fill the gap, microscopic kinetic models can be employed for example using the Marcus-Hush theory[16, 17]. This theory introduced the concept of reorganization energy, $\lambda\ (eV)$, corresponding to the energy required to distort the atomic configuration of the reactant molecule and its solvation shell to the product in its equilibrium configuration. Hence, the reorganization energy has a clear relationship with the property of the system and knowledge of potential energy curves can enable quantitative prediction of electron transfer rate constants. Marcus theory provides a rule-of-thumb of estimating electrochemical rate constant. For a simple reaction:

$$A \pm e \xrightarrow{k_0} B \qquad \textbf{(1.46)}$$

- If A and B are close in molecular geometry, for example, in respect of bond length and bond angles, then k_0 should be large to correspond to low activation barrier for reaction.
- If A and B are structurally dissimilar, a large activation barrier would lead to smaller k_0.

The Marcus-Hush theory can be related to the Butler-Volmer kinetics. The Marcus-Hush theory expression for the Gibbs energy of activation of an electrode process is:

$$\Delta G(\dagger) = \frac{\lambda}{4}\left(1 + \frac{\Delta G}{\lambda}\right)^2 \qquad \textbf{(1.47)}$$

where λ is the reorganization energy and ΔG is the Gibbs energy of reaction. For the electrode process:

$$\Delta \mathrm{G} = -\mathrm{FE} = \mathrm{G_p} - G_R \tag{1.48}$$

where G_P and G_R are the Gibbs energy of product and reactant respectively. The Arrhenius equation is:

$$k = KZ \exp\left(\frac{-\Delta G(\dagger)}{RT}\right) \tag{1.49}$$

Furthermore, when the electrochemical reaction was irreversible, under BV kinetics,

$$\alpha = \frac{RT}{F}\frac{\partial \ln|I_{red}|}{\partial E} = \frac{RT}{F}\frac{\partial \ln|k|}{\partial E} \tag{1.50}$$

And from **(1.47)**, the transfer coefficient can be expressed as:

$$\alpha = \frac{1}{2}\left(1 + \frac{\Delta G}{\lambda}\right) \tag{1.51}$$

From **(1.51)**, $\alpha \sim \frac{1}{2}$ when $\lambda \gg \Delta G$, which provide a satisfactory linkage between Marcus-Hush theory and Butler-Vomer kinetics.

In general, Marcus-Hush theory provides a physical insight into the factors affecting the electrode kinetics, and it enables predictions of electrochemical rate constant and energy of activation. It also provides suitable description of voltammetry of surface-bound systems[18, 19].

1.2.4 The Tafel Law

If a very negative overpotential is applied on the working electrode so that the cathodic reduction reaction is significantly faster than the anodic oxidation reaction, the expression for flux approximates to:

$$J_{red} = k_0 e^{\frac{-\alpha F\left(E-E_f^0\right)}{RT}}[A^{Z_A}]_{x=0} \quad \textbf{(1.52)}$$

Similarly, when the oxidation process dominates the reduction process, the flux is dependent solely on oxidation:

$$J_{ox} = -k_0 e^{\frac{(1-\alpha) F\left(E-E_f^0\right)}{RT}}[B^{Z_B}]_{x=0} \quad \textbf{(1.53)}$$

The natural logarithm of **(1.52)** and **(1.53)** gives:

$$\alpha = -\frac{RT}{F}\frac{\partial \ln|J_{red}|}{\partial E}$$
$$1-\alpha = \beta = \frac{RT}{F}\frac{\partial \ln|J_{ox}|}{\partial E} \quad \textbf{(1.54)}$$

Plots of $\ln|J_{red}|\ vs.E$ and $\ln|J_{ox}|\ vs.E$ are called Tafel plots, and the slope of which is related to the transfer coefficient α and β. Note that for Tafel analysis to generate accurate result, the concentration of analyte should be constant over the range of potential studied. Literature suggests that Tafel analysis generate more accurate results when analysing a small fraction of current before peak current in cyclic voltammetry so as to minimise concentration depletion near the electrode[20].

1.2.5 The electrochemical cell

The three-electrode electrochemical cell is the basic experimental setup for electrochemistry. It consists of the working electrode (WE), the reference electrode (RE) and the counter electrode (CE) as illustrated in Figure 1.5. The electrodes are submerged in electrolyte, which contains electro-inactive ions that increase the conductivity of the solution. The concentration of electrolyte is assumed to be ideally high so that migration does not influence the mass transport (see section 1.1.1) and compresses the double layer to distances compatible with interfacial electron transfer via tunnelling.

In a typical electrochemical experiment, the potential is controlled between the working electrode and the reference electrode and current is measured between working electrode and counter electrode. The working electrode is where the electrochemical reaction of interest happens and its potential is measured relative to the reference electrode. Important reference electrodes include the standard hydrogen electrode (SHE), the saturated calomel electrode (SCE) and the silver/silver chloride electrode. The potential determining equilibrium for these electrodes are discussed below.

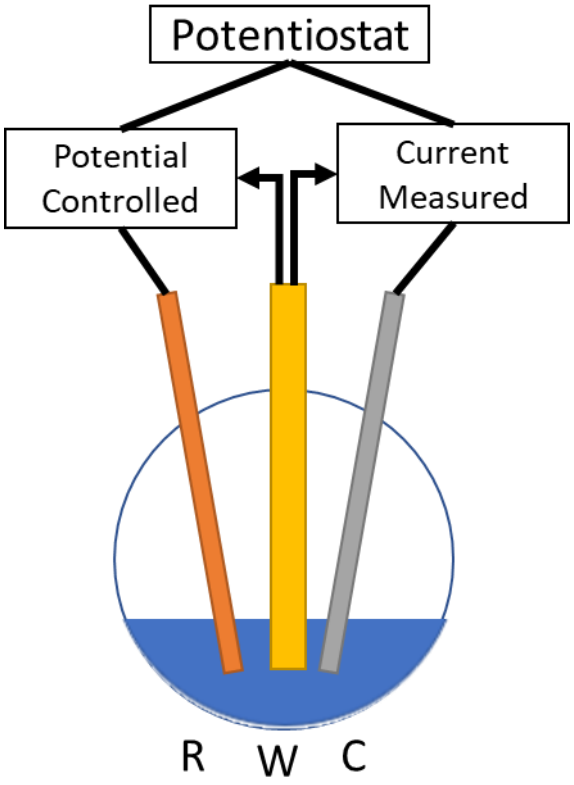

Figure 1.5. Illustration of a typical electrochemical cell. Left: reference electrode (R); Middle: working electrode (W); Right: counter electrode (C).

The potential determining equilibrium for the hydrogen electrode at equilibrium is:

$$H^+(aq) + e^- \rightleftarrows \frac{1}{2}H_2(g) \qquad \textbf{(1.55)}$$

The chemical potentials of H^+ and H_2 are:

$$\mu_{H^+} = \mu^0_{H^+} + RT \ln\left(\frac{[H^+]}{[\ ]^0}\right)$$
$$\mu_{H_2} = \mu^0_{H_2} + RT \ln\left(\frac{P_{H_2}}{P^0}\right) \quad \textbf{(1.56)}$$

The corresponding Nernst equation is:

$$\phi_m - \phi_s = \frac{\Delta\mu^0}{F} + \frac{RT}{F} \ln\left(\frac{\frac{[H^+]}{[\ ]^0}}{\left(\frac{P_{H_2}}{P_0}\right)^{1/2}}\right) \quad \textbf{(1.57)}$$

where $[\ ]^0$ and P_0 are the standard concentration (1 M) and pressure (1 bar) respectively.

For silver/silver chloride electrode, the potential determining equilibrium and Nernst equation are:

$$AgCl(s) + e^-(m) \rightleftarrows Ag(s) + Cl^-(aq) \quad \textbf{(1.58)}$$

The chemical equilibrium for Cl^- is:

$$\mu_{Cl^-} = \mu^0_{cl^-} + RT \ln\left(\frac{[Cl^-]}{[\ ]^0}\right) \quad \textbf{(1.59)}$$

The chemical potentials for $AgCl$ and Ag as solids are their standard chemical potentials:

$$\mu_{AgCl} = \mu^0_{AgCl}$$
$$\mu_{Ag} = \mu^0_{Ag} \quad \textbf{(1.60)}$$

The Nernst equation obtained for silver/silver chloride electrode is just:

$$\phi_m - \phi_s = \frac{\Delta\mu^0}{F} + \frac{RT}{F} \ln\left(\frac{[\ ]^0}{[Cl^-]}\right) \quad \textbf{(1.61)}$$

The potential determining equilibrium for theSCE is:

$$\frac{1}{2}Hg_2Cl_2(s) + e^-(m) \rightleftharpoons Hg(l) + Cl^-(aq) \quad \textbf{(1.62)}$$

Since the chemical potential of pure solids and liquids equates to their standard chemical potential as in the case of silver/silver chloride electrode in **(1.60)**:

$$\begin{aligned} \mu_{Hg_2Cl_2} &= \mu^0_{Hg_2Cl_2} \\ \mu_{Hg} &= \mu^0_{Hg} \end{aligned} \quad \textbf{(1.63)}$$

This leads to the Nernst equation for this electrode:

$$\phi_m - \phi_s = \frac{\Delta\mu^0}{F} - \frac{RT}{F}\ln\frac{[Cl^-]}{[\ ]^0} \quad \textbf{(1.64)}$$

which suggests that the interfacial potential difference for the SCE only depends on the concentration of chloride, hence it is essential to keep chloride solution in a SCE saturated at constant temperature to ensure consistency of the electrode potential.

Typical non-aqueous reference electrodes include the silver/silver nitrate electrode in tetrabutylammonium hexafluorophosphate (NBu_4PF6)electrolyte in CH_2Cl_2, acetonitrile or other organic solvents[21, 22]. The potential determining equilibrium for the silver/silver cation (Ag/Ag^+) electrode is:

$$Ag^+(sol) + e^-(m) \rightleftarrows Ag(s) \quad \textbf{(1.65)}$$

The $e^-(m)$ is electron transferred from the metal electrode to the silver cation in solution. A good reference electrode has a reversible reference redox pair with a known electrochemical equilibrium, and ideally is less affected by temperature or local chemical composition. The counter electrode is for the purpose of making a complete electrical circuit in the

electrochemical system and is made of conductive but inert material. Typical counter electrodes include platinum wire and graphite rod electrodes. Note that the electrical current flows through the working and counter electrode, not through the reference electrode.

The applied potential E between working and reference electrodes is given by:

$$E = (\phi_m - \phi_s) + IR - (\phi_m^r - \phi_s^r) \quad \textbf{(1.66)}$$

where ϕ is the chemical potential. ϕ_m and ϕ_e are the electrical potentials on the working electrode and the adjacent solution phase respectively. ϕ_m^r and ϕ_s^r are the corresponding electrical potentials for the reference electrode. The IR term indicates the passage of electrical charge between the two electrodes in the form of an electrical current, I. It is intentionally kept that there is no current passing through the working and reference electrode, so that the potential of reference electrode is fixed, and $IR = 0$, which ensures that the changes in E only reflect the change in $(\phi_m - \phi_s)$, which is the driving force of electrochemical reaction.

1.3 Electroanalytical tools

This section is concerned with electrochemical methods in which the working electrode is controlled by setting a potential which can be either held constant or varied with time. Then current can be measured as a function of time or potential. Two of the arguably most powerful techniques: cyclic voltammetry and chronoamperometry result from this idea.

1.3.1 Cyclic voltammetry

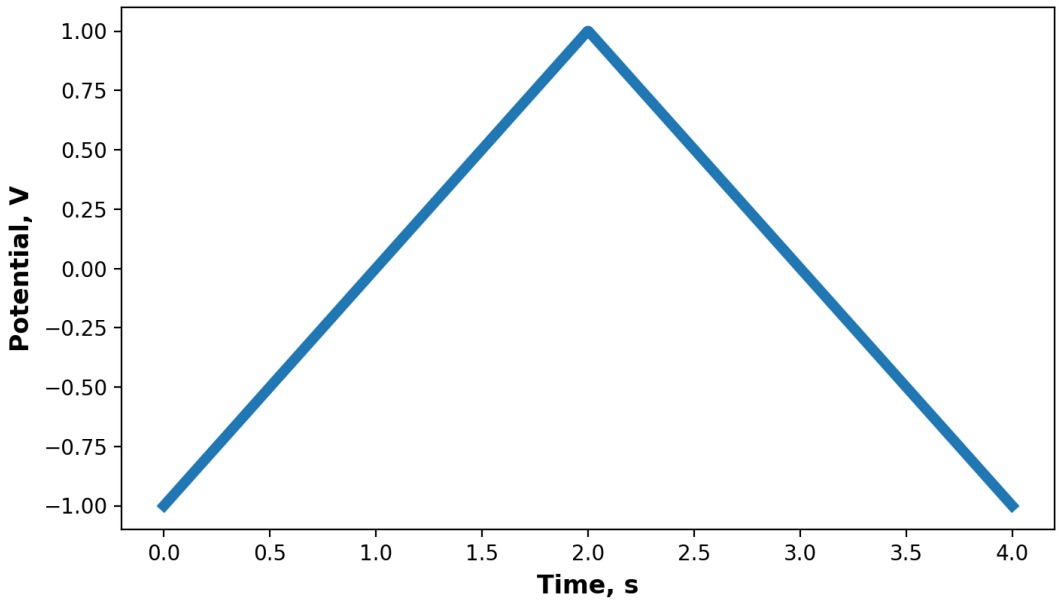

Figure 1.6. An example of triangular waveform applied to voltammetry It has a scan range of -1 V to 1 V and a scan rate of 1 V/s.

As arguably the most popular electrochemical methods, cyclic voltammetry is performed by apply a triangular waveform on the working electrode (relative to the reference electrode) as shown in Figure 1.6. The scan begins at a potential, E_i usually where no Faradaic current flows, then linearly swept to a value, E_v, at which a high overpotential typically fully drives the reaction of interest. The direction of scan is reversed at E_v and in the Figure is seen to stop at the starting potential, E_i. In practice, the linear sweep is a large number of digitally generated small steps and the plot of the resulting current against the potential applied on the working electrode is the resulting "voltammogram".

The shape of a voltammogram is an interplay between mass transport and electrode kinetics. Mass transport is determined by not only by the diffusion coefficients of the species in the reaction under study, but also the patterns of diffusion to the working electrode. Linear diffusion at a macro electrode and convergent diffusion at a microelectrode are two modes of

diffusion discussed in the simulations reported in this thesis. Figure 1.7 shows the linear diffusion to a macroelectrode and convergent diffusion to a microdisc and a hemispherical electrode. Macroelectrodes usually have a size in the millimeter or centimeter range, while microelectrodes lie at and below the micrometer range. The relative size of the electrode and diffusion layer thickness (size of the zone of reactant depletion around the electrode) dictates the mode of diffusion. For a macroelectrode with a radius significantly larger than diffusion layer thickness, diffusion towards the electrode surface is linear within typical experimental timescales, even with the expansion of diffusion layer to due passage of time.

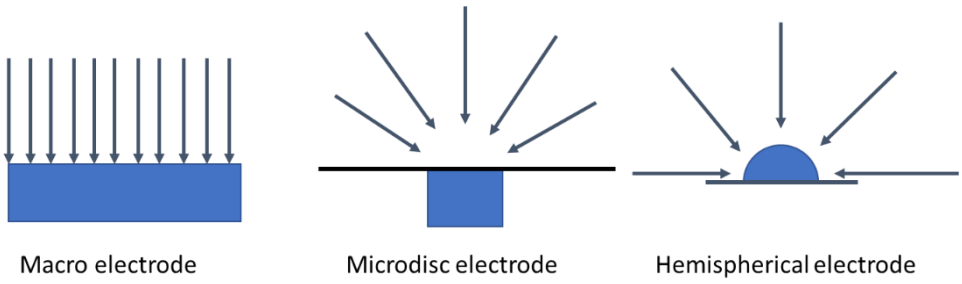

Figure 1.7. An illustration of diffusion to macro electrode, microdisc electrode and hemispherical electrode.

On the other hand, the smaller microdisc electrode has a radius significantly smaller than that of diffusion layer, so electroactive species "converge" to the electrode surface from all directions. The more efficient three-dimensional diffusive flux leads to higher rate of mass transport than at macroelectrodes, thus the measurement of faster electron transfer processes becomes possible at microelectrodes[23-25]. At the same time, the three-dimensional flux toward the microelectrode surface complicates the simulation and will be introduced in Chapter 2.

The effects of the reversibility of the voltammetry are next considered and shown in Figure 1.8. With decreasing standard electrochemical rate constant from purple to yellow curve, a significantly higher overpotential is required to drive the electrochemical reaction. In the

irreversible scan (yellow curve), a significant potential in excess of the minimum thermodynamically required is needed for reduction and oxidation. This is referred to as 'overpotential'. In contrast, in the reversible limit there is significant current flow at potentials around the formal potential of the couple.

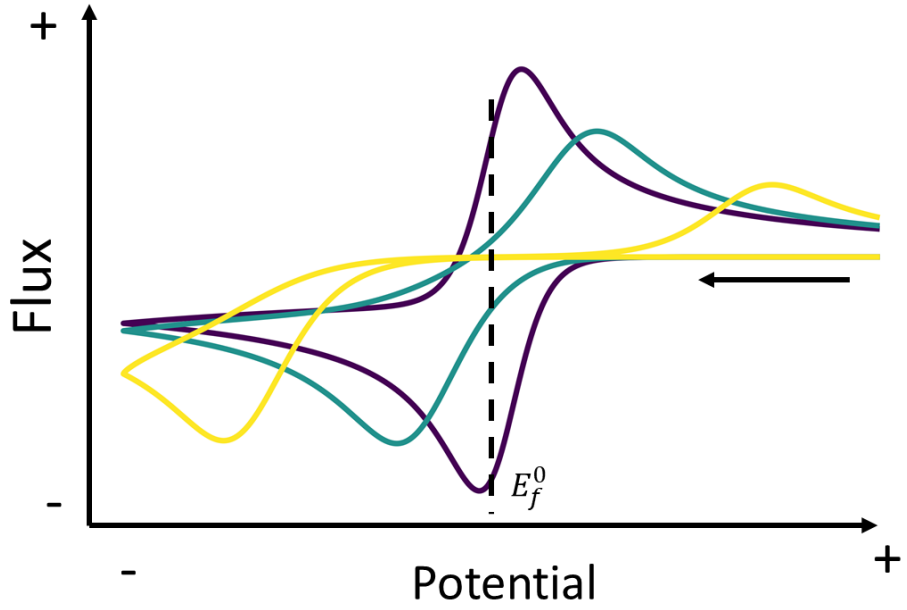

Figure 1.8. Reductive voltammogram at macroelectrode. From purple to yellow, the reversibility decreases as the standard electrochemical rate constant decreases. The three curve corresponds to three magnitude of irreversibility: purple – reversible; green – quasi-reversible, yellow – irreversible.

1.3.1.1 Voltammetry at a Macroelectrode

The electrochemical reversibility at a macroelectrode can be quantified by comparing the standard electrochemical rate constant, k_0 $(m\ s^{-1})$, with the mass transport coefficient, m_T $(m\ s^{-1})$. The mass transport coefficient is defined as:

$$m_T = \frac{D}{d} \tag{1.67}$$

where D is the diffusion coefficient and d is the diffusion layer thickness. As **(1.13)** suggests, $d = \sqrt{2Dt}$, and the experimental time t relates to the scan rate as:

$$t \sim \frac{RT}{F\nu} \tag{1.68}$$

Hence m_T can be expressed as:

$$m_T \sim \sqrt{\frac{DF\nu}{RT}} \tag{1.69}$$

Matsuda and Ayabe [26]has derived an indicator, Λ, to evaluate reversibility as:

$$\Lambda = \frac{k_0}{\sqrt{\frac{DF\nu}{RT}}} \tag{1.70}$$

The following ranges are suggested for three different classification of macroelectrode reversibility as:

Reversible:

$$\Lambda \geq 15, k_0 \geq 0.3\nu^{0.5}\ cm\ s^{-1}$$

Quasi-reversible:

$$15 > \Lambda > 10^{-3}, 0.3\nu^{0.5} > k_0 > 2 \times 10^{-5}\ \nu^{0.5}\ cm\ s^{-1}$$

Irreversible:

$$\Lambda \leq 10^{-3}, k_0 \leq 2 \times 10^{-5}\nu^{0.5}\ cm\ s^{-1}$$

where T, D and α are assumed to be 298 K, $1 \times 10^{-5}\ cm^2\ s^{-1}$ and 0.5 respectively.

In terms of experimental measurements, the peak-to-peak separation, the peak current and the voltammetric waveshape can give hints about the classification as reversible or irreversible for measured voltammogram.

The peak to peak separation, ΔE_{pp}, is the potential difference between the forward and reverse peaks, and takes the value of $\Delta E_{pp} = 57.4\ mV$ at 298K if the process is

electrochemically reversible. ΔE_{pp} is not affected by scan rate in the reversible limit whilst for non-reversible systems, $\Delta E_{pp} > 57.4\, mV$. The voltammetric wave is also characterized by E_{mid}, which is the mid-point potential between the forward and backward peak and $E_{mid} = \frac{E_{p,forward}+E_{p,reverse}}{2}$. For a reversible process,

$$E_{mid} = E_f^0 + \frac{RT}{2F}\ln\left(\frac{D_B}{D_A}\right) \quad \textbf{(1.71)}$$

For an irreversible process, assuming $\alpha = \beta = 0.5$,

$$E_{mid} = E_f^0 + \frac{RT}{F}\ln\left(\frac{D_B}{D_A}\right) \quad \textbf{(1.72)}$$

Assuming equal diffusion coefficient, the mid-point potential is also the formal potential regardless of reversibility.

The peak current in the forward scan of a reductive one electron voltammogram is described by the Randles-Ševčík equation[27, 28]. This equation is used to validate simulations reported later in the thesis in the limit of no coupled homogeneous chemistry:

$$\text{Reversible: } I_p = -0.446FA_{elec}[A]_{bulk}\sqrt{\frac{F\nu D}{RT}}$$
$$\text{Irreversible: } I_p = -0.496\sqrt{\alpha}FA_{elec}[A]_{bulk}\sqrt{\frac{F\nu D}{RT}} \quad \textbf{(1.73)}$$

The waveshape of voltammogram is another indicator of reversible vs. irreversible voltammogram. The waveshape is characterized by the difference of peak potential, E_p and half peak potential, $E_{1/2}$:

$$\text{Reversible: } \left|E_p - E_{1/2}\right| = 2.218\frac{RT}{F}$$

$$\text{Irreversible reduction: } \left|E_p - E_{1/2}\right| = 1.857\frac{RT}{\alpha F} \quad \textbf{(1.74)}$$

$$\text{Irreversible oxidation: } \left|E_p - E_{1/2}\right| = 1.857\frac{RT}{\beta F}$$

1.3.1.2 Voltammetry at microelectrodes

Microelectrodes are defined as electrodes with characteristic dimensions at a scale of micrometers. Microelectrodes are different from macroelectrode by having non-planar diffusion, reduced capacitance[29] (due to smaller surface areas) and smaller ohmic drop[30] (due to the smaller total current passed). Besides that, microelectrodes permit study in high resistance organic solvents[31-33] or even it is claimed in the gas phase[34, 35].

Steady state behavior is seen when cyclic voltammetry at a microelectrode is conducted at sufficiently low scan rates, as in Figure 1.9. The limiting current is defined as the current when a high overpotential drives the reaction heavily in the direction of the product so that the concentration of the electroactive species at the electrode surface falls to zero. When performing cyclic voltammetry at a microdisc electrode, a limiting current is seen at sufficiently low scan rates as the efficient convergent diffusion replenishes the material lost by electrolysis. The half wave potential. $E_{1/2}$ is the potential at half of the limiting current, which when compared to the formal potential (if known) indicates the degree of reversibility of the electrochemical reaction, as discussed below.

At sufficiently low scan rate, microdisc voltammetry generates steady state behavior, which can be analyzed, at the irreversible and quasi-irreversible limit, to give information of

electrode kinetics. Such analysis is possible when electrode size is sufficiently small such that the mass transport coefficient, m_T, is significantly larger than k_0:

$$m_T \sim \frac{D}{r_e} \gg k_0 \tag{1.75}$$

where the inequality is satisfied as r_e gets adequately small.

Aoki [34] has summarized, based on the work of Oldham and Zoski[36], the analytical expression of the voltammetric wave of a simple one-electron electrochemical reaction, where the diffusion coefficients are all equal:

$$\frac{I}{I_{lim}}(1 + \exp(\pm\zeta)) = \frac{\lambda}{\left\{\lambda + \frac{2\lambda + 12}{\lambda + 3\pi}\right\}} \tag{1.76}$$

$$\text{where } \lambda = \frac{k_0 r_e}{D}\left\{e^{-\alpha\zeta} + e^{\beta\zeta}\right\}, \zeta = \frac{F}{RT}\left(E - E_f^0\right)$$

and I_{ss} is the limiting current, α and β are the transfer coefficients. Note that when k_0 becomes large, $\frac{\lambda}{\left\{\lambda+\frac{2\lambda+12}{\lambda+3\pi}\right\}} \to 1$ and the waveshape can be simplified into:

$$\frac{I}{I_{lim}} = \frac{1}{1 + \exp(\pm\zeta)} \tag{1.77}$$

where + and − are for reduction and oxidation respectively and the equation is a sigmoid function.

The boundaries of the three kinetic regimes regarding the reversibility level of microdisc voltammetry are defined and quantified in a similar manner as for a macroelectrode above. A parameter κ_0 to quantify the transition is defined as:

$$\kappa_0 = \frac{r_e\, k_0}{D_A} \qquad \textbf{(1.78)}$$

where r_e is the radius of electrode. The following are the three kinetic regimes at a microelectrode:

Reversible:

$$\kappa_0 > 10$$

Quasi-reversible:

$$10 \geq \kappa_0 \geq 10^{-2\alpha}$$

Irreversible:

$$\kappa_0 \leq 10^{-2\alpha}$$

where α is the transfer coefficient.

Figure 1.9 illustrates typical steady state voltammograms for decreasing values of k_0 for a simple one electron reduction in which the potential is scanned from E_i to E_v. From the blue to the yellow curves, the voltammogram transforms from reversible to irreversible, evidenced by the shift of $E_{1/2}$ from coinciding with E_f^0 for the case of the reversible blue curve to the presence of significant negative overpotential for the yellow curve. The decreasing $E_{1/2}$ from blue to yellow curve can be explained by the decreasing electrochemical rate constant k_0: significant overpotential are required to drive the reaction when k_0 is small, as explained by the Butler-Volmer equation. Note that regardless of the electrochemical reversibility a steady-state current instead of a peak current is seen and attributed to the highly efficient convergent diffusion at the microdisc electrode. The diffusion to electrode is sufficient to compensate the depletion at the electrode surface, and a steady state is reached. Note that at very fast scan rate,

the diffusion may transit to linear diffusion because of the short timescale, and again generates a normal "duck" shaped voltammogram[37].

Quantitatively speaking, if the time to reach steady state ($\sim\frac{r_e^2}{D}$) is short compared with the time for sweeping the voltammogram ($\sim\frac{RT}{F\nu}$), then steady-state like behavior will be seen.

A parameter p is defined as $p=\sqrt{\frac{Fr_e^2\nu}{RTD}}$ such that when $p \ll 1$ corresponds a "steady-state" limit and when $p \gg 1$ corresponds to a "cyclic voltammetry" limit.

Quantification of the steady-state voltammogram at a micro-disc electrode gives the half-wave potential, $E_{1/2}$ relative to the formal potential:

$$\begin{aligned}\text{Reversible: } E_{1/2} &= E_f^0 + \frac{RT}{2F}\ln\left(\frac{D_B}{D_A}\right)\\ \text{Irreversible: } E_{1/2} &= E_f^0 + \frac{RT}{\alpha F}\ln\left(\frac{r_e k_0}{D_A}\right)\end{aligned} \quad \textbf{(1.79)}$$

where $E_{1/2}$ is defined as the potential where current is half of the steady state current. For a reversible process, $E_{1/2}=E_f^0$ if the diffusion coefficients of A and B are equal, while for an irreversible process, $E_{1/2}$ of the couple is dependent on electrochemical rate constants. The steady state current scales with $[A]_{bulk}$, the bulk concentration of species A. At a microdisc electrode, I_{ss} is:

$$I_{ss} = 4nFD[A]_{bulk}r_e \quad \textbf{(1.80)}$$

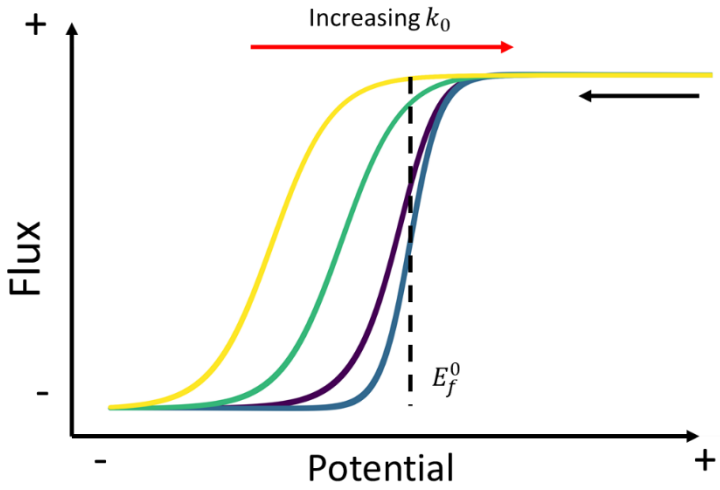

Figure 1.9. Reductive voltammetry at microdisc electrode. From blue to yellow, the voltammogram transits from reversible to irreversible. The black arrow indicates the start and initial direction of scan. The red arrow indicates the increasing k_0 from the yellow to the blue curve.

In this section, cyclic voltammetry has been introduced and the influence of the electrochemical reversibility and diffusion elucidated. We next consider chronoamperometry, another very important tool, as introduced in the next section.

1.3.2 Chronoamperometry

Chronoamperometry is another very popular electrochemical technique. Chronoamperometry measurements involve a potential sequence which starts at a potential E_1 where usually no electrochemical reaction happens, and at t_0, changes the potential instantaneously to E_2, where electrolysis of interest occurs. As shown in Figure 1.10, a large current flow immediately after the application of E_2, and the current decreases with time due to the continuous depletion of reactants near the surface of electrode. The diffusion mode towards the electrode determines the shape of chronoamperogram, and diffusion to macroelectrode and microdisc electrode is discussed sequentially.

For a macroelectrode where mass transport is dominant linear diffusion, the Cottrell equation[38] is used to describe the current response as a function of time at sufficient high overpotential (so the mass transport dominates the electrode kinetics):

$$I = \frac{nFA_{elec}\sqrt{D}[A]_{bulk}}{\sqrt{\pi t}} \tag{1.81}$$

where I is the net current, n is the number of electrons transferred and A_{elec} is the electrode area. According to the equation, I becomes zero when t is infinite, as the weakly efficient linear diffusion can no longer sustained a large transport of molecules to electrode surface when the diffusion layer is too thick since the concentration gradients become extremely low so that the flux, as given by Fick's First law is tiny.

For a microdisc electrode with convergent diffusion, the current decay can be estimated with Shoup and Szabo equation[39]:

$$I = 4nFD[A]_{bulk}r_e f(\tau)$$
$$f(\tau) = 0.7854 + 0.8862\tau^{-0.5} + 0.2146\exp(-0.7823\tau^{-0.5}) \tag{1.82}$$

where the dimensionless time, τ is defined as $\tau = \frac{4Dt}{r_e^2}$. This expression is not mathematically derived like Cottrell equation, but fitted from simulation results[39]. This expression is used extensively to validate simulation of microdisc electrode. The steady state current of microdisc electrode is:

$$I_{ss} = 4nFD[A]_{bulk}r_e \tag{1.83}$$

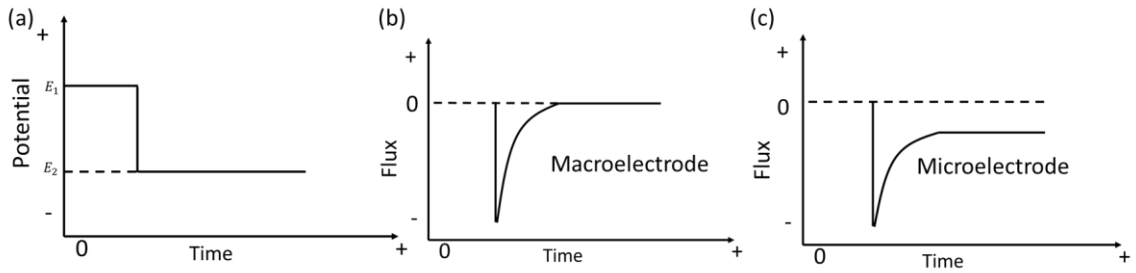

Figure 1.10. (a) The potential-time profile of a chronoamperometry. (b) a schematic plot of chronoamperogram ta a macroelectrode and (c) a microelectrode respectively.

1.3.3 Faradaic and Non-Faradaic Process

Both Faradaic and non-faradaic process can occur at the electrode surface to incur a current flow when overpotential is applied. The Faradaic process defines electron transfer across electrode-solution interface, leading to redox reaction of the electroactive species. The Faraday's law of electrolysis as $m = \frac{QM}{nF}$ where m and M are the mass (g) and molar mass (g/mol) of the electroactive species. Q is the total electric charge passed and F is the Faraday constant.

In experiment, however, currents can still be observed when on electroactive species is present in the solution. In a non-Faradaic process, no electron passes through the electrode-solution interface, but the build-up of charge local to the electrode alters the structure of the interface as electric potential changes. The charging process of the electrode-solution interface is similar to charging a capacitor, as no electrons are transferred. The accumulated charge at the electrode surface by imposed potential causes the redistribution of solvent molecules in the vicinity of electrode. As a result, a charging current, known as the capacitive current flows through the external circuit, which is defined by: $I = \frac{dQ}{dt} = C_d A \frac{dE}{dt} = C_d A_{elec} v$ where Q is the charge, C_d is the capacitance of double layer per unit area. The charged species at the electrode-solution interface is called electrical double layer, and its first model formulated by Helmholtz[38, 40] is shown in Figure 1.11.

The electrical double layer has several components. The inner layer, adjacent to the electrode, is called the compact layer, which contains the solvent molecules and other ions adsorbed on the electrode surface. The distance between the electrode surface and electrical centre of these molecules and ions is called Inner Helmholtz Plane (IHP). The solvated ion can

only interact with the electrode by electrostatic force and the distance from the electrical surface to the electrical centre of the closest solvated ions is known as Outer Helmholtz Plane (OHP). The distribution of non-specifically absorbed ions in the region between OHP and bulk solution is called diffuse layer.

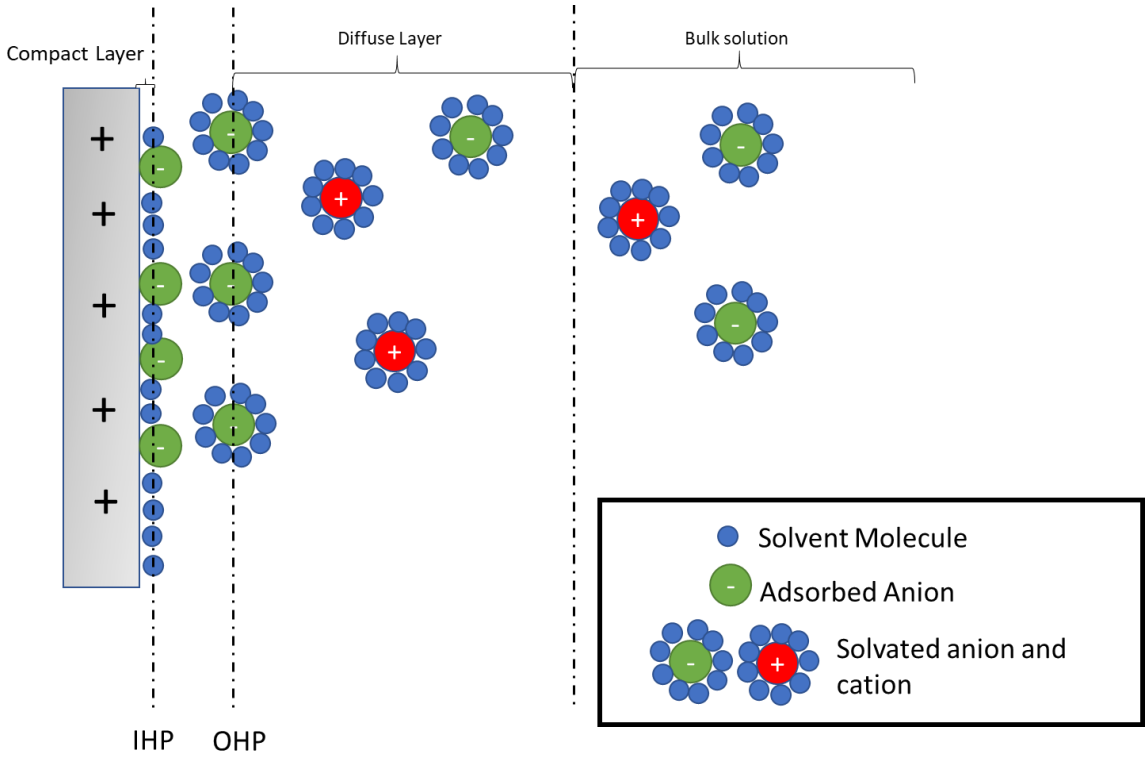

Figure 1.11. Structure of the Helmholtz double layer (HDL). The green red and blue spheres represent anions. Cations and solvent molecules, respectively.

The Helmholtz theory by no means is a perfect theory of electrical double layer by only considering Helmholtz layer capacitance. Other theories, like Gouy-Chapman theory[41,42]considering only diffuse later capacitance, and Stern model that combines the two theories[43]. Grahame introduces "effective dense layer capacitance" which is independent of surface inactive electrolyte concentration[44]. A more compressive review of development of electrical double layer theory can be found in literature[45].

The charging current of double layer is a major contributor of non-faradaic current[46]. As the potential of the electrode-solution interface changes, the nature of double-layer changes

and a charging current must flow to compensate the double layer. Depending on potential waveform, transient and continuous charging current exist. A transient charging current flows when potential changes by ΔE, as:

$$i_c(t) = \frac{\Delta E}{R_u} \exp\left(\frac{-t}{R_u C A_{elec}}\right) \quad \textbf{(1.84)}$$

where R_u represents the uncompensated resistance that exists between the working and reference electrodes. C is the average capacitance over the potential range E and $E + \Delta E$ and A_{elec} is the area of electrode.

Continuous charging current can be important if electrode area or the potential is changing with time.

$$i_c = C(E_{PZC} - E)\frac{dA}{dt} - CA\frac{dE}{dt} \quad \textbf{(1.85)}$$

where E_{PZC} is the potential of zero charge at which the electrode is completely uncharged. In experiment, one term of the equation above disappears if A or E is kept constant.

1.4 Coupled homogeneous kinetics

In the previous section, electrochemical reaction was introduced with the simplest $A(aq) + e^- \rightleftarrows B(aq)$ form. In this section, effect of chemical instability of B and the effect generating A via chemical reaction is studies. The electrochemical reactions with coupled chemical kinetics are described using the Testa and Reinmuth notation. The letter E denotes heterogenous electron transfer step while C denotes the homogenous chemical step. C_n, denotes nth order homogeneous chemical reaction. For example, C_2, denotes a second order homogenous chemical reaction.

1.4.1 EC reaction

When a product of an electrochemical reaction is unstable, the product can further react to form an electrochemically inactive product. Figure 1.12 is the oxidation of 4-aminophenol in acidic aqueous solution[47].

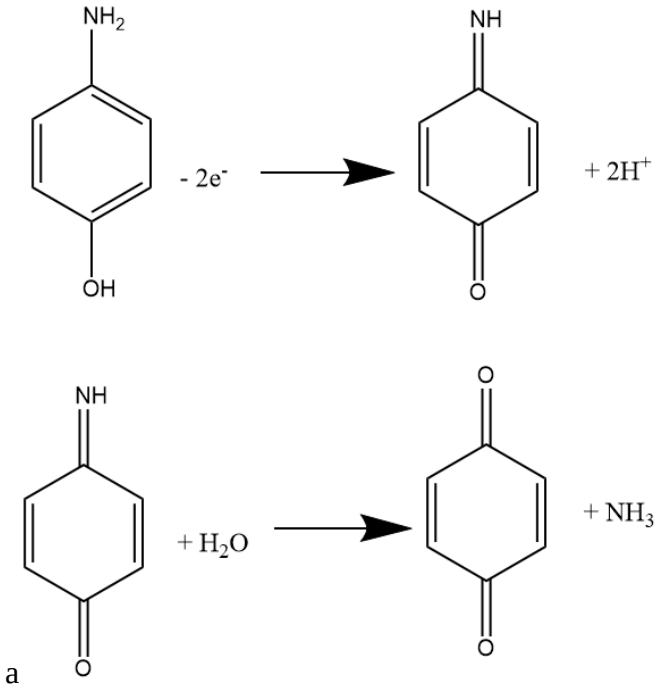

a

Figure 1.12. Oxidation of 4-aminophenol in acidic aqueous solution.

1.4.2 EC_2 reaction

A typical example of EC_2 reaction is dimerization of the product generated by electrochemical reaction. Figure 1.13 is an example of dimerization[48] where S-S is S_2CNMe_2.

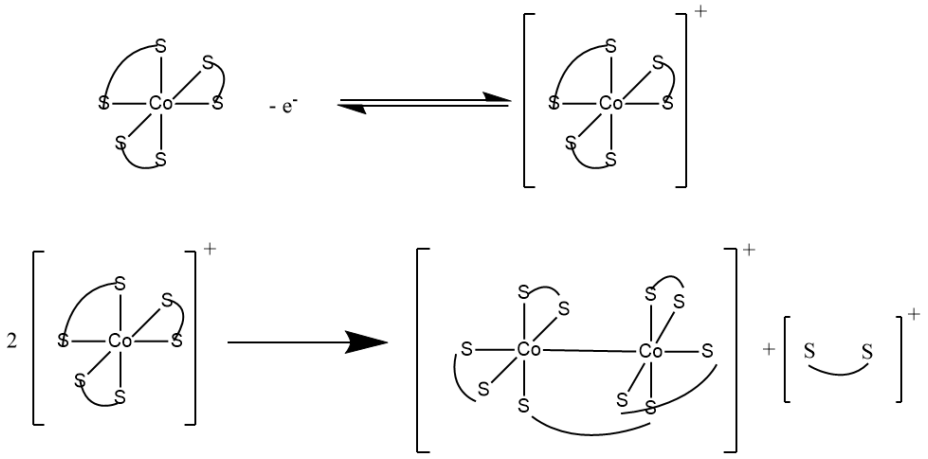

Figure 1.13. The electro-oxidation of tris(dithiocarbamato)cobalt(III) complexes.

1.4.3 ECE reaction

The ECE reaction, as the name suggests, is where the chemical step generates a product which is itself electrochemically active in the potential range studied. Figure 1.14 shows the reduction of 2-bromonitrobenezene in aprotic solvents[49].

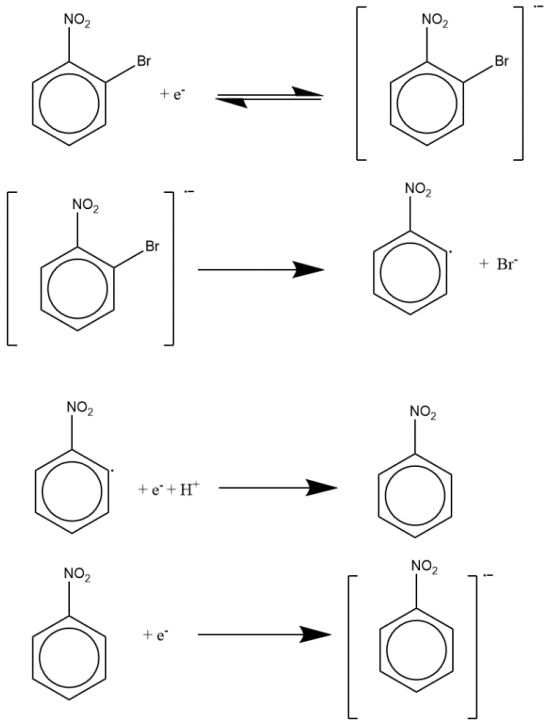

Figure 1.14. The electrochemical reduction of 2-bromonitrobenezene in aprotic solvents.

1.4.4 Dissociative CE reaction

The preceding dissociation reaction generates an electrochemically active species. Hydrogen evolution reaction in acetic acid is an example as shown in Figure 1.15.

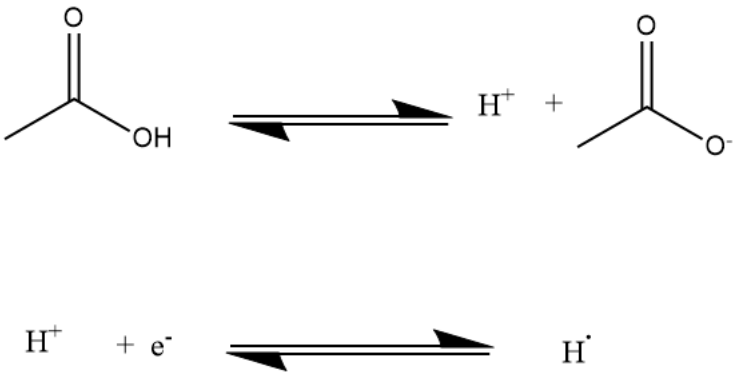

Figure 1.15. Hydrogen evolution reaction in acetic acid solution.

The introduction above serves as the experimental context and theoretical backbone for the simulations introduced in the next chapter.

References

1. R. G. Compton and C. E. Banks, *Understanding voltammetry*, World Scientific, London, 3rd edn., 2018.
2. A. J. Bard and L. R. Faulkner, *Electrochemical Methods: Fundamentals and Applications*, 2nd edn., 2001.
3. C. Batchelor-McAuley, E. Kätelhön, E. O. Barnes, R. G. Compton, E. Laborda and A. Molina, *ChemistryOpen*, 2015, **4**, 224-260.
4. P. T. Kissinger and W. R. Heineman, *J. Chem. Educ.*, 1983, **60**, 702.
5. G. A. Mabbott, *J. Chem. Educ.*, 1983, **60**, 697.
6. A. Einstein, *J Annalen der physik*, 1905, **17**, 549-560.
7. J. A. V. Butler, *Trans. Faraday Soc.*, 1924, **19**, 729-733.
8. T. Erdey-Grúz and M. Volmer, *Z. Phys. Chem.*, 1930, **150**, 203-213.
9. G. Inzelt, *J. Solid State Electrochem.*, 2011, **15**, 1373-1389.
10. J. Heyrovsky, *Lond. Edinb. Dubl. Phil. Mag.*, 1923, **45**, 303-315.
11. R. Audubert, *Revue de Métallurgie*, 1924, **21**, 567-584.
12. D. G. Truhlar, W. L. Hase and J. T. Hynes, *J. Phys. Chem.*, 1983, **87**, 2664-2682.
13. D. G. Truhlar, B. C. Garrett and S. J. Klippenstein, *J. Phys. Chem.*, 1996, **100**, 12771-12800.

14. J. Tafel, *Physik. Chem.*, 1905, **50**, 641-712.
15. C. E. D. Chidsey, *Science*, 1991, **251**, 919-922.
16. R. A. Marcus, *J. Chem. Phys.*, 1965, **43**, 679-701.
17. N. S. Hush, *J. Chem. Phys.*, 1958, **28**, 962-972.
18. M. C. Henstridge, E. Laborda and R. G. Compton, *J. Electroanal. Chem.*, 2012, **674**, 90-96.
19. M. C. Henstridge, E. Laborda, N. V. Rees and R. G. Compton, *Electrochim. Acta*, 2012, **84**, 12-20.
20. D. Li, C. Lin, C. Batchelor-McAuley, L. Chen and R. G. Compton, *J. Electroanal. Chem.*, 2018, **826**, 117-124.
21. B. Kratochvil, E. Lorah and C. Garber, *Anal. Chem.*, 1969, **41**, 1793-1796.
22. G. Inzelt, A. Lewenstam and F. Scholz, *Handbook of reference electrodes*, Springer, 2013.
23. C. Andrieux, D. Garreau, P. Hapiot, J. Pinson and J. Savéant, *J. Electroanal. Chem. Interfacial Electrochem.*, 1988, **243**, 321-335.
24. P. R. Birkin and S. Silva-Martinez, *Anal. Chem.*, 1997, **69**, 2055-2062.
25. A. Bond, T. Henderson, D. Mann, T. Mann, W. Thormann and C. Zoski, *Anal. Chem.*, 1988, **60**, 1878-1882.
26. H. Matsuda and Y. Ayabe, *Ber. Bunsen. Phys. Chem.*, 1955, **59**, 494-503.
27. A. Ševčik, *Collect. Czech. Chem. Commun.*, 1948, **13**, 349-377.
28. J. E. B. Randles, *Trans. Faraday Soc.*, 1948, **44**, 327-338.
29. R. J. Forster, *Chem. Soc. Rev.*, 1994, **23**, 289-297.
30. C. Amatore, A. Oleinick and I. Svir, *Anal. Chem.*, 2008, **80**, 7947-7956.
31. A. M. Bond, M. Fleischmann and J. Robinson, *J. Electroanal. Chem. Interfacial Electrochem.*, 1984, **168**, 299-312.
32. M. Hernandez-Olmos, L. Agüí, P. Yanez-Sedeno and J. Pingarron, *Electrochim. Acta*, 2000, **46**, 289-296.
33. L. Agüí, J. Lopez-Guzman, A. Gonzalez-Cortes, P. Yanez-Sedeno and J. Pingarron, *Anal. Chim. Acta*, 1999, **385**, 241-248.
34. K. Aoki, *Electroanalysis*, 1993, **5**, 627-639.
35. Z.-B. Zhou, Q.-H. Wu and C.-C. Liu, *Sensors Actuators B: Chem.*, 1994, **21**, 101-108.
36. K. B. Oldham and C. G. Zoski, *J. Electroanal. Chem. Interfacial Electrochem.*, 1991, **313**, 17-28.
37. N. Elgrishi, K. J. Rountree, B. D. McCarthy, E. S. Rountree, T. T. Eisenhart and J. L. Dempsey, *J. Chem. Educ.*, 2018, **95**, 197-206.
38. F. G. Cottrell, *Z. Phys. Chem.*, 1903, **42U**, 385-431.
39. D. Shoup and A. Szabo, *J. Electroanal. Chem. Interfacial Electrochem.*, 1982, **140**, 237-245.
40. H. Von Helmholtz, *Wied. Ann*, 1879, **7**, 337-382.
41. D. L. Chapman, *Lond. Edinb. Dubl. Phil. Mag.*, 1913, **25**, 475-481.
42. M. Gouy, *J. Phys. Theor. Appl.*, 1910, **9**, 457-468.
43. O. Stern, *Zeitschrift für Elektrochemie und angewandte physikalische Chemie*, 1924, **30**, 508-516.
44. D. C. Grahame, *Chem. Rev.*, 1947, **41**, 441-501.
45. B. B. Damaskin and O. A. Petrii, *J. Solid State Electrochem.*, 2011, **15**, 1317-1334.
46. C. G. Zoski, *J. Chem. Educ.*, 1986, **63**, 910.
47. J. B. Conant and M. F. Pratt, *J. Am. Chem. Soc.*, 1926, **48**, 3178-3192.
48. R. G. Compton, J. C. Eklund, L. Nei, A. M. Bond, R. Colton and Y. A. Mah, *J. Electroanal. Chem.*, 1995, **385**, 249-255.

49. R. G. Compton, R. G. Wellington, P. J. Dobson and P. A. Leigh, *J. Electroanal. Chem.*, 1994, **370**, 129-133.

Chapter 2 Electrochemical Simulation

This chapter introduces the simulation of electrochemical processes including cyclic voltammetry and chronoamperometry. All the research mentioned later in this thesis is based on simulation or validated by simulation. Thus, it is of paramount importance to understanding numerical simulation using the finite difference method as applied to voltammetry. A systematic review of simulation can be found in literature[1-9].

2.1 Modelling of electrochemical systems

For any scientific discipline, if a rigorous mathematical theory can define the experiment, then numerical simulation using the theory may provide data consistent with experiments to help scientists understand better. In addition to allowing parameter extraction, modelling can also help to understand experiments, by cross-validating simulation and experimental results to identify inconsistencies and imperfections in experiments. The goal of this thesis is not to treat simulation as a black-box as in (hopefully) fool-proof commercial software, but to understand and develop simulation from the very basics, and to develop easier simulation tools for the scientific community, for example, the physics-informed neural networks introduced in later chapters. Typical programming languages for simulation includes Fortran, C++, MATLAB, and Python. The simulations in this thesis were extensively written with Python, which offer more readability (closer to a natural language), versatility (easy access to matrix manipulation, data processing, plotting and machine learning) and reasonable efficiency with properly constructed code. With Python, there is no need to reinvent the wheels, and users can focus on the electrochemical models instead of the housekeeping work encountered in other languages with significantly steeper learning curves.

In the context of voltammetry, modelling and simulation usually starts with solving differential equations with the voltammetry imposing boundaries conditions and initial

conditions. The differential equations are usually second-order partial differential equations (Fick's Second Law) and may involve diffusion coupled with chemical kinetics or other forms of mass transport. With focuses on responses at different electrode geometries and electrochemical systems, simulations accelerated by expanding spatial or temporal grid can offer accurate solutions within a timeframe of minutes. This chapter introduces the basics of simulating an electrochemical reaction and tools for testing and validating the simulations.

2.1.1 The diffusion equation

Diffusion, as a key form of mass transport in all electrochemical experiments, was modelled using Fick's Second Law, a 2nd order partial differential equations (PDE) to predict the temporal evolution of concentrations in the reaction. For diffusion in the three dimensions, the diffusion equation is:

$$\frac{\partial c}{\partial t} = D\left(\frac{\partial^2 c}{\partial x^2} + \frac{\partial^2 c}{\partial y^2} + \frac{\partial^2 c}{\partial z^2}\right) \quad \textbf{(2.1)}$$

where D is the diffusion coefficient with a value usually around $10^{-9}\ m^2\ s^{-1}$ in liquids. Note that since D varies from one species to another, each species is described by its own version of diffusion equation. Table 2.2 shows diffusions coefficients of some inorganic ions in water. Chemical kinetics, if relevant, can also be incorporated into diffusion equations. For example, if the species is converted to another species with a first order rate constant k, the diffusion equation is modified as:

$$\frac{\partial c}{\partial t} = D\left(\frac{\partial^2 c}{\partial x^2} + \frac{\partial^2 c}{\partial y^2} + \frac{\partial^2 c}{\partial z^2}\right) - kc \quad \textbf{(2.2)}$$

Electrochemical modelling, in principle, solves equations like **(2.2)** subject to specific boundary conditions to determine the time evolution of the system.

Table 2.1. Diffusion coefficients of some hydrated inorganic cations and anion in water, at 298.15 K and infinite dilution[10].

Inorganic Cations		Inorganic anions	
Hydrated cation	$D(10^{-10}\ m^2\ s^{-1})$	Hydrated anion	$D(10^{-10}\ m^2\ s^{-1})$
$\mathbf{H_3O^+}$	93.11	$\mathbf{OH^-}$	52.7
$\mathbf{Ag^+}$	16.48	$\mathbf{H_2AsO_4^-}$	9.05
$\mathbf{Al^{3+}}$	5.41	$\mathbf{Br^-}$	20.8
$\mathbf{Ba^{2+}}$	8.47	$\mathbf{CO_3^{2-}}$	9.2
$\mathbf{Be^{2+}}$	5.99	$\mathbf{Cl^-}$	20.3
$\mathbf{Ca^{2+}}$	7.92	$\mathbf{ClO_4^-}$	17.92
$\mathbf{Cd^{2+}}$	7.19	$\mathbf{F^-}$	14.8
$\mathbf{Co^{2+}}$	7.32	$\mathbf{Fe(CN)_6^{3-}}$	8.96
$\mathbf{Cr^{3+}}$	5.95	$\mathbf{Fe(CN)_6^{4-}}$	7.35
$\mathbf{Cs^{3+}}$	20.56	$\mathbf{I^-}$	20.45
$\mathbf{Cu^{2+}}$	7.14	$\mathbf{IO_3^-}$	10.78
$\mathbf{Fe^{2+}}$	7.19	$\mathbf{MnO_4^-}$	16.32
$\mathbf{Fe^{3+}}$	6.04	$\mathbf{NO_3^-}$	19.02
$\mathbf{Hg^{2+}}$	8.47	$\mathbf{PO_4^{3-}}$	6.1
$\mathbf{Hg_2^{2+}}$	9.13	$\mathbf{HPO_4^{2-}}$	7.59
$\mathbf{K^+}$	19.57	$\mathbf{H_2PO_4^-}$	9.59
$\mathbf{La^+}$	6.19	$\mathbf{HS^-}$	17.3
$\mathbf{Li^+}$	10.29	$\mathbf{SCN^-}$	17.58

Solving three-dimensional system like **(2.1)**, is very time-consuming, and maybe impractical, though not impossible armed with sufficiently large resources, in numerical simulations. So, simplifications are necessary to reduce the problem to a magnitude that for example an average workstation can handle in a reasonable timeframe. For example, for diffusion to a macroelectrode, only diffusion perpendicular to the electrode surface is considered as there is negligible diffusion parallel to the surface, as shown in Figure 1.7. Hence, we only consider diffusion in one dimension as:

$$\frac{\partial c}{\partial t} = D\left(\frac{\partial^2 c}{\partial x^2}\right) \qquad \textbf{(2.3)}$$

To be considered a macroelectrode, the shape of the electrode is not important, provided the surface is flat and the electrode is large compared with diffusion layer thickness, $\delta \sim \sqrt{Dt}$. If

the electrode radius, for example, is 10 times larger than the estimated diffusion layer thickness, it can be considered a macroelectrode and simplified to one dimension.

For diffusion to a microelectrode, the problem can still be simplified due to symmetry and other approximations. When simplification is impossible, the high-dimension diffusion equation might be solvable using physics-informed neural network introduced in Chapter 8.

2.1.2 Boundary conditions

To solve the PDE describing mass transport, the solution (concentration profile for each species) must meet several conditions, which depends on the number of independent variable and the order of differential equations. Figure 2.1 illustrates the boundary conditions and simulation scheme for voltammetry at a macro electrode.

Fick's Second Law is first order in time $\left(\frac{\partial c}{\partial t}\right)$ so that only one temporal boundary condition is required for each species. The boundary condition is usually the initial concentrations in the reaction system. If at equilibrium, then the concentration of all species is uniform across the system such that for any species j:

$$c_j(x, t = 0) = c_j^*$$

where c_j^* is the initial concentration under equilibrium conditions.

To solve the second order spatial problem, two boundary conditions are needed for a one-dimensional simulation. The two spatial boundaries are, in voltammetry, for the surface of electrode and outer boundary of simulation respectively.

The surface boundary condition relates to transformation of species which involves surface concentrations/gradients of the corresponding species. If the species is electrochemically inert, a no flux boundary conditions applies. For electroactive species, their

transformation depends on the potential applied at the electrode. For a one-electron transfer process, $A(aq) + e \rightleftarrows B(aq)$,it can be expressed as a first order rate law:

$$D_A \left(\frac{\partial c_A}{\partial x}\right)_{x=0} = k_f c_A(x=0) - k_b c_B(x=0) \quad \textbf{(2.4)}$$

where k_f and $k_b, m\ s^{-1}$ are heterogenous rate constants. As discussed in 0, the value of k_f and k_b can be related to those predicted by electrode kinetics theory such as the Butler-Volmer or Marcus-Hush equations. If the electrochemical reaction is fast, both models would reach a Nernstian equilibrium at the surface of electrode as:

$$\frac{c_A(x=0)}{c_B(x=0)} = e^{\left(\frac{F}{RT}\left(E - E_f^0\right)\right)} \quad \textbf{(2.5)}$$

Regardless of electrode mechanics employed, the law of mass conservation dictates that, for a $A + e \rightarrow B$ reaction, the flux of A must be identical to that of B:

$$D_B \left(\frac{\partial c_B}{\partial x}\right)_{x=0} = \mp D_A \left(\frac{\partial c_A}{\partial x}\right) \quad \textbf{(2.6)}$$

where the upper sign is for reactants and products diffusing in the same phase (as in most electrochemistry reactions) and the lower sign is for diffusion in different phases like amalgamation processes and ion transfers.

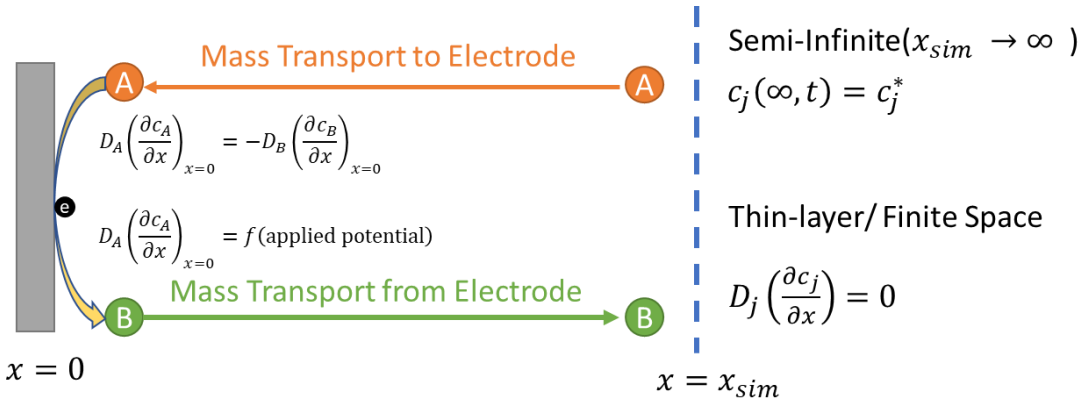

Figure 2.1. Schematic illustration of simulation boundary conditions for a one electron reduction of A (orange circle) to B (green circle). The small black dot represents the electron. $x = 0$ is the surface of electrode and $x = x_{sim}$ is the outer boundary of simulation.

The boundary conditions for the outer boundary can be defined in several ways. For an electrochemical reaction in a large system, it is not necessary to extend the simulation to a distance overly large in terms of voltammetry scale. Einstein's work on Brownian motion demonstrated that, as introduced in 0, the root-mean-square displacement of a particle in the x-dimension, $\sqrt{\langle x^2 \rangle}$, is equal to $\sqrt{2Dt}$. To ensure that change in concentration from the surface of electrode cannot propagate to the outer boundary, a typical value of outer boundary for simulation, x_{sim}, is set to:

$$x_{sim} = 6\sqrt{Dt_{sim}} \tag{2.7}$$

where t_{sim} is the time duration of the experiment/simulation. Since the reaction near the electrode cannot affect the outer boundary, the concentration of any species at outer boundary should equate with its bulk concentration as:

$$c_j(x = x_{sim}, t \geq 0) = c_j^* \tag{2.8}$$

Assuming $D = 10^{-9}\, m^2\, s^{-1}$ and $t_{sim} = 100\, s$, the calculated $x_{sim} \approx 1.89\, mm$, a very small distance considering the size of a typical electrochemical cell. Therefore, the distance from the container wall to the electrode surface, in practice, will usually exceed x_{sim}. The fixed concentration boundary condition at the outer boundary is an example of Dirichlet boundary condition.

When simulating for thin-layer electrochemistry when x_{sim} is the width of the layer, the reaction at the electrode surface can propagate to the outer boundary, a no-flux boundary condition can be applied:

$$D_j \left(\frac{\partial c_j}{\partial x} \right)_{x=x_{sim}} = 0 \qquad \textbf{(2.9)}$$

The no-flux boundary condition incorporates the first derivative of concentration and is an example of a Neumann boundary conditions.

2.1.3 Dimensionless parameters

The solution to Fick's Second Law mentioned above is dependent on parameters like the bulk concentration, c^*, the radius of electrode, ϵ and the diffusion coefficient, D. If simulations were conducted using dimensional units, for every set of parameters, new simulations would be mandatory. But by transforming the system to dimensionless form, we can run simulations independent of these parameters, so that it becomes unnecessary to run more simulations if these parameters change. Dimensionless parameters are also less error prone as it eliminates risks due to SI vs. non-SI units, and imperial vs. metric systems[11, 12]. In machine learning, using dimensionless parameters can help to avoid the diminishing/exploding gradient problem[13]. A table of conversion between some dimensional and dimensionless units

are shown in Table 2.2. Dimensional variables are transformed to the dimensionless form by multiples of some reference values with the same dimensionality. For example, the concentration of any species j is normalized against the bulk concentration of species A, namely c_A^* and distance is often normalized to the radius of electrode.

Table 2.2. Table of dimensionless parameters and variables

Parameter	Normalization
Concentration	$C_j = \frac{c_j}{c^*}$
Diffusion coefficient	$d_j = \frac{D_j}{D_A}$
Spatial coordinate	$X = \frac{x}{\epsilon}$
Time	$T = \frac{D_A t}{\epsilon^2}$
Potential	$\theta = \left(\frac{F}{RT}\right)\left(E - E_f^0\right)$
Scan rate	$\sigma = \left(\frac{\epsilon^2}{D_A}\right)\left(\frac{F}{RT}\right)\nu$
Heterogeneous rate constant	$K_0 = \frac{k_0\,\epsilon}{D_A}$
1st order homogeneous rate constant	$K = \frac{k\epsilon^2}{D_A}$
2nd order homogeneous rate constant	$K_{2nd} = \frac{k\,c_A^*\,\epsilon^2}{D_A}$
Current (uniformly accessible electrode)	$I = \left(\frac{FAc_A^* D_A}{\epsilon}\right) J_{0,A}$

The derivation of the dimensionless scan rate and flux may require more mathematical transformation using combinations of the quantities in table 2.1. The dimensionless scan rate, σ, is the derivative of the dimensionless potential against time:

$$\sigma = \frac{\partial \theta}{\partial T} \tag{2.10}$$

Then σ is related to ν using the chain rule:

$$\frac{\partial E}{\partial t} = \frac{\partial E}{\partial \theta}\frac{\partial \theta}{\partial t} = \frac{RT}{F}\frac{\partial \theta}{\partial T} \tag{2.11}$$

where R and T are the Gas Constant and absolute temperature respectively.

Then,

$$\frac{\partial \theta}{\partial t} = \frac{\partial \theta}{\partial T}\frac{\partial T}{\partial t} = \frac{D_A}{\epsilon^2}\frac{\partial \theta}{\partial T} \tag{2.12}$$

which leads to:

$$\frac{\partial E}{\partial t} = \frac{D_A}{\epsilon^2}\frac{RT}{F}\frac{\partial \theta}{\partial T} \tag{2.13}$$

Therefore:

$$\sigma = \frac{\epsilon^2}{D_A}\frac{F}{RT}\,\nu \tag{2.14}$$

Thus the expression for dimensionless flux is derived. For point X_1 in the system, the dimensionless flux at X_1 is defined as:

$$J_{X_1,j} = -d_j \left(\frac{\partial C_j}{\partial X}\right)_{X_1} \tag{2.15}$$

Then using chain rule to determine how dimensionless flux J relates to dimensional values j:

$$\frac{\partial c_j}{\partial x} = \frac{\partial c_j}{\partial X}\frac{\partial X}{\partial x} = \frac{1}{\epsilon}\frac{\partial c_j}{\partial X}$$
$$\frac{\partial c_j}{\partial X} = \frac{\partial c_j}{\partial C_j}\frac{\partial C_j}{\partial X} = c_A^*\frac{\partial C_j}{\partial X} \quad \textbf{(2.16)}$$

This leads to:

$$\frac{\partial c_j}{\partial x} = \frac{c_A^*}{\epsilon}\frac{\partial C_j}{\partial X}$$
$$j_j = -d_j\frac{c_A^* D_A}{\epsilon}\frac{\partial C}{\partial X} \quad \textbf{(2.17)}$$
$$j_j = \frac{c_A^* D_A}{\epsilon}J_j$$

Knowing that $I = FA\, j_{0,A}$ for a uniformly accessible electrode, we get:

$$I = \frac{FA\, c_A^*\, D_A}{\epsilon}\, J_{0,A}$$
$$J_{0,A} = -\left(\frac{\partial C_A}{\partial X}\right)_{X=0} \quad \textbf{(2.18)}$$

Furthermore, the dimensionless form of the linear diffusion equation in one dimension remains simply:

$$\frac{\partial C_j}{\partial T} = d_j\left(\frac{\partial^2 C_j}{\partial X^2}\right) \quad \textbf{(2.19)}$$

2.2 Solution of diffusion equations

Following the above brief introduction to the finite difference method and other tools to solve partial differential equation are introduced in this section.

2.2.1 The Finite Difference Method

The Finite difference (FD) method, along with the Finite Element (FE) method, are probably the most widely used methods to solve partial differential equations (PDE) numerically. The FD method discretise the spatial and time domains into a finite number of

intervals, and the solution at discrete points is approximated by finding algebraic equations containing the finite differences and values from nearby points. Compared with the FE method, the FD method is easier to implement and manipulate for the purpose of electrochemical simulation. Simulations in this thesis are performed using finite difference methods unless otherwise stated.

2.2.2 Spatial derivatives

The finite difference method represents a continuous function using a series of finite steps. For example, for simulation of voltammetry in 1D (usually for macroelectrode or microelectrode with some approximations), we want to solve the concentration profile, $C(X)$. Ignoring time for now, to approximate $C(X)$, the one-dimensional space under consideration is divided into n discrete points, $X_0, X_1, \dots, X_{n-1}$, and each pair of spatial points is separated by ΔX such that for any point i,

$$X_{i+1} - X_i = X_i - X_{i-1} = \Delta X$$
$$n = 1 + \frac{X_{sim} - X_0}{\Delta X} \quad \textbf{(2.20)}$$

where X_{sim} is the outer boundary of simulation and X_o is the electrode surface. For simulation of a macroelectrode, $X_0 = 0$. The notation of the spatial array is zero-indexed as in $X_0, \dots, X_{n-1}$ instead of one indexed $X_1, \dots, x_n$ to accommodate zero-indexed programming languages like C++ and Python. Figure 2.2 illustrates the spatial grid and its relationship with the concentration profile. The next step is to approximate the first derivative and second derivative using the discrete concentration profile.

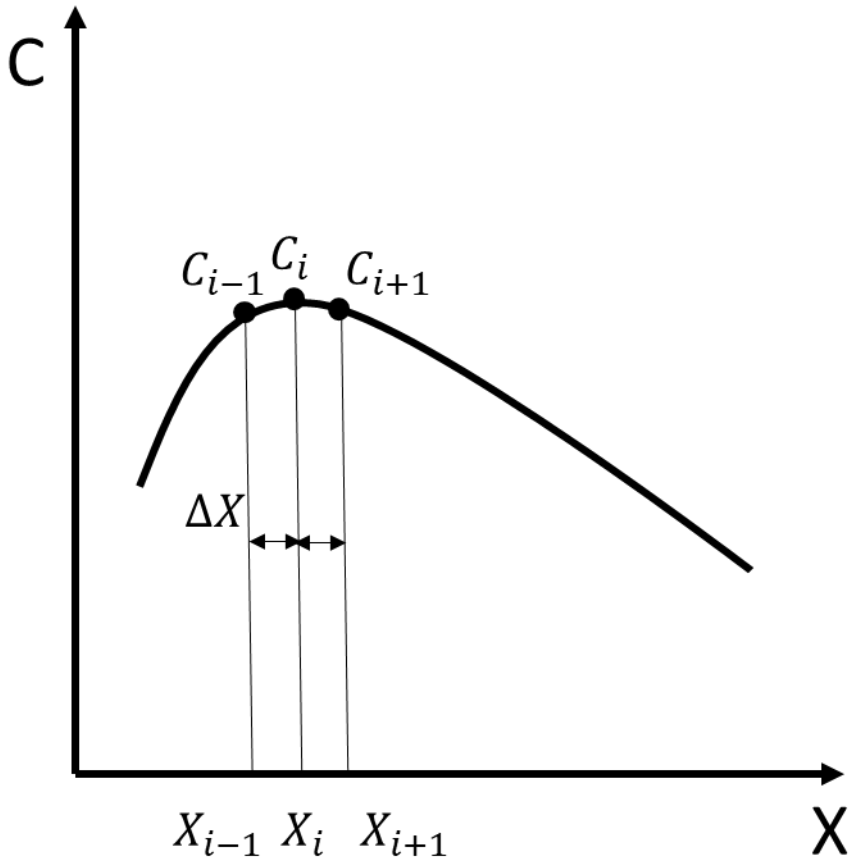

Figure 2.2. Discrete values of concentration in a discrete space with constant spacing, ΔX.

The first derivative of the concentration profile can be approximated using forward or backward difference approximations, or a central difference approximation. The forward and backward approximations of the first derivative are:

$$\text{Forward: } \left(\frac{dC}{dX}\right)_{X_i} \approx \frac{C_{i+1}-C_i}{\Delta X}$$
$$\text{Backward: } \left(\frac{dC}{dX}\right)_{X_i} \approx \frac{C_i-C_{i-1}}{\Delta X} \qquad \textbf{(2.21)}$$

The central approximation for the first derivative is:

$$\left(\frac{dC}{dX}\right)_{central} = \frac{1}{2}\left[\left(\frac{dC}{dX}\right)_{forward} + \left(\frac{dC}{dX}\right)_{backward}\right] \qquad \textbf{(2.22)}$$

$$\left(\frac{dC}{dX}\right)_{central} = \frac{C_{i+1} - C_{i-1}}{2\Delta X} + \Gamma_{central}$$

where $\Gamma_{central}$ is the truncation error for the central difference approximation, which is the error of both the forward and backward difference approximations as $\Gamma_{central} = \frac{\Gamma_{forward} - \Gamma_{backward}}{2}$. Using Taylor expansion, the truncation error:

$$\Gamma_{central} = -\frac{(\Delta X)^2}{6}\left(\frac{d^3c}{dX^3}\right)_{X_i} - \frac{(\Delta X)^4}{120}\left(\frac{d^5C}{dX^5}\right)_{X_i} + \cdots \quad \textbf{(2.23)}$$

Since in simulation, $0 < \Delta X \ll 1$, it is necessarily true that $\Delta X > (\Delta X)^2 > (\Delta X)^3$ so that the first term is the most significant term. Thus,

$$\Gamma_{central} \propto (\Delta X)^2 \quad \textbf{(2.24)}$$

while for forward or backward approximation (derivation not shown here):

$$\Gamma_{forward/backward} \propto \Delta X \quad \textbf{(2.25)}$$

By comparison of truncation errors, central differencing is more accurate as the error is proportional to $(\Delta X)^2$. Thus, first derivatives in this thesis are approximated as:

$$\left(\frac{\mathrm{dC}}{dX}\right)_{X_i} \approx \frac{C_{i+1} - C_{i-1}}{2\Delta X} \quad \textbf{(2.26)}$$

The second derivative is approximated by summing the forward and backward approximations:

$$C_{i+1} + C_{i-1} = 2C_i + (\Delta X)^2\left(\frac{d^2C}{dX^2}\right)_{X_i} + \frac{(\Delta X)^4}{12}\left(\frac{d^4C}{dX^4}\right)_{X_i} + \cdots \quad \textbf{(2.27)}$$

Rearranging gives:

$$\left(\frac{d^2C}{dX^2}\right)_{X_i} = \frac{C_{i-1} - 2C_i + C_{i+1}}{(\Delta X)^2} + \Gamma$$
$$\Gamma = -\frac{(\Delta X)^2}{12}\left(\frac{d^4C}{dX^4}\right)_{X_i} + \cdots \quad \textbf{(2.28)}$$

So the second derivative of concentration is approximated by:

$$\left(\frac{d^2C}{dX^2}\right)_{X_i} \approx \frac{C_{i-1} - 2C_i + C_{i+1}}{(\Delta X)^2} \quad \textbf{(2.29)}$$

with error $\Gamma \propto (\Delta X)^2$. Assuming ΔX is small, the approximations for the first and second derivative given above offer an optimal balance between accuracy and complexity. These approximations are implemented in simulations to solve diffusion equations.

2.2.3 Time evolution and the time derivative

For simulation of one-dimensional diffusion systems, the state of system depends on two things: the spatial boundary condition and the state in the previous time moment. The spatial dependence has been considered in the last section, and the next step is to approximate the first order derivative of concentration against time. As introduced for the spatial grid, a time grid is also necessary to keep track of the time function. With a constant interval, ΔT between two time steps, the total number of timesteps, m, is:

$$m = \frac{T_{sim} - T_0}{\Delta T} \quad \textbf{(2.30)}$$

where T_0 and T_{sim} are the start and finishing time respectively.

To solve $\frac{dC}{dT}$, it is only possible to use the backward difference approximation as we have no information at any timestep beyond the current one. Denoting the current time step,

when the concentration is unknown, as T^k and the last time step, when the concentration is known, as T^{k-1}, the approximation is:

$$\frac{\partial C_i}{\partial T} \approx \frac{C_i^k - C_i^{k-1}}{\Delta T} \tag{2.31}$$

The discretized version of Fick's second law is:

$$\frac{C_i^k - C_i^{k-1}}{\Delta T} = \frac{C_{i-1} - 2C_i + C_{i+1}}{(\Delta \mathrm{X})^2} \tag{2.32}$$

Now we have a choice for the time step on the right side of the above equation: we can choose either the last time step, T^{k-1} or the current time step, T^k. This leads to different approaches that are called explicit and implicit methods respectively.

The explicit form of solution to diffusion equation consists of:

$$\frac{C_i^k - C_i^{k-1}}{\Delta T} = \frac{C_{i-1}^{k-1} - 2C_i^{k-1} + C_{i+1}^{k-1}}{(\Delta \mathrm{X})^2} \tag{2.33}$$

which can be arranged into:

$$\begin{aligned} C_i^k &= C_i^{k-1} + \lambda\left(C_{i-1}^{k-1} - 2C_i^{k-1} + C_{i+1}^{k-1}\right) \\ \lambda &= \frac{\Delta T}{(\Delta X)^2} \end{aligned} \tag{2.34}$$

The equation above are easy to solve as the only unknown is C_k^i. Simulation using explicit method consists of iterating from T_0 (when all concentrations are their bulk concentrations) till T_{sim}.

Unfortunately, the numerical stability of this method is only guaranteed stable if[14, 15]:

$$\lambda < 0.5 \tag{2.35}$$

The explicit method is ineffective, as to maintain accuracy, ΔT must decrease with decreasing ΔX. Thus, the explicit method is not used for simulation in this thesis.

The backward implicit method, however, solves the equation as:

$$\frac{C_i^k - C_i^{k-1}}{\Delta T} = \frac{C_{i-1}^k - 2C_i^k + C_{i+1}^k}{(\Delta \mathrm{X})^2} \tag{2.36}$$

And rearranges into the more useful form as:

$$C_i^{k-1} = C_i^k - \lambda\left(C_{i-1}^k - 2C_i^k + C_{i+1}^k\right) \tag{2.37}$$

which has a single known variable C_i^{k-1}. Thus, at any timestep, k, the complete set of equations must be solved simultaneously:

$$\begin{gathered} \ldots \\ -\lambda C_{43}^k + (1+2\lambda)C_{44}^k - \lambda C_{45}^k = C_{44}^{k-1} \\ -\lambda C_{44}^k + (1+2\lambda)C_{45}^k - \lambda C_{46}^k = C_{45}^{k-1} \\ -\lambda C_{45}^k + (1+2\lambda)C_{46}^k - \lambda C_{47}^k = C_{46}^{k-1} \\ \ldots \end{gathered} \tag{2.38}$$

with the boundary conditions:

$$\begin{gathered} C_0^k = f(\theta) \\ C_{n-1} = 1 \end{gathered} \tag{2.39}$$

where $f(\theta)$ reflects the electrode kinetics controlling the surface condition, which is dependent on the potential applied. For each timestep, we have n unknown variables and n non-degenerate equations, which can solve simultaneously. Although the implicit scheme is more complicated than the explicit scheme, it is unconditionally stable[15, 16],making it more efficient for simulation of voltammetry.

2.2.4 The Thomas algorithm[15]

The rearranged diffusion equation in implicit form can be written as:

$$\alpha_i C_{i-1}^k + \beta_i C_i^k + \gamma_i C_{i+1}^k = \delta_i^k \tag{2.40}$$

and the coefficients, α, β, γ and δ are defined as:

$$\begin{gathered} i = 0, \quad \alpha_0 = 0, \quad \beta_0 = 1, \quad \gamma_0 = 0, \quad \delta_0^{(k)} = f(\theta) \\ i = [1, n-2], \quad \alpha_i = -\lambda, \quad \beta_i = 1 + 2\lambda, \quad \gamma_i = -\lambda, \delta_i^k = C_i^{k-1} \\ i = n-1, \quad \alpha_{n-1} = 0, \quad \beta_{n-1} = 1, \gamma_{n-1} = 0, \quad \delta_{n-1} = 1 \end{gathered} \tag{2.41}$$

The equation above can be written as a matrix multiplication of:

$$Ax = b \tag{2.42}$$

which in full is:

$$\begin{pmatrix} 1 & 0 & 0 & 0 & 0 & 0 & \dots \\ \alpha & \beta & \gamma & 0 & 0 & 0 & \dots \\ 0 & \alpha & \beta & \gamma & 0 & 0 & \dots \\ \dots & \dots & \dots. & \dots & \dots & \dots & \dots. \\ \dots & 0 & 0 & 0 & \alpha & \beta & \gamma \\ \dots & 0 & 0 & 0 & 0 & 0 & 1 \end{pmatrix} \begin{pmatrix} C_0^k \\ C_1^k \\ C_2^k \\ \dots \\ C_{n-1}^k \\ C_{n-1} \end{pmatrix} = \begin{pmatrix} f(\theta) \\ C_1^{k-1} \\ C_2^{k-1} \\ \dots \\ C_{n-1}^{k-1} \\ 1 \end{pmatrix} \tag{2.43}$$

where A is a tridiagonal matrix and b is a single column and x is the single column to be solved. Solving large using Gaussian elimination[17] are very computational expensive, but fortunately, the Thomas algorithm[18] offers an easier approach to solve tridiagonal matrices. Using LU factorization, the above matrix can be decomposed into two matrices, L and U so that $LUx = b$:

$$A = \begin{pmatrix} \beta_0' & 0 & 0 & 0 & 0 & \dots \\ \alpha_1 & \beta_1{}' & 0 & 0 & 0 & \dots \\ \dots & \dots & \dots & \dots & \dots & \dots \\ \dots & 0 & 0 & \alpha_{n-2} & \beta_{n-2}{}' & 0 \\ \dots & 0 & 0 & 0 & \alpha_{n-1} & \beta_{n-1}{}' \end{pmatrix} \begin{pmatrix} 1 & \gamma_0{}' & 0 & 0 & 0 & \dots \\ 0 & 1 & \gamma_1{}' & 0 & 0 & \dots \\ \dots & \dots & \dots & \dots & \dots & \dots \\ \dots & 0 & 0 & 0 & 1 & \gamma_{n-2}{}' \\ \dots & 0 & 0 & 0 & 0 & 1 \end{pmatrix} \quad \textbf{(2.44)}$$

where $\beta_i{}'$ and $\gamma_i{}'$ are modified coefficients. Pre-multiplying both sides of $LUx = b$ with L^{-1}, gives:

$$Ux = L^{-1}b \quad \textbf{(2.45)}$$

Let $d = L^{-1}b$, the equation above can be rewritten as:

$$\begin{pmatrix} 1 & \gamma_0{}' & 0 & 0 & 0 & \dots \\ 0 & 1 & \gamma_1{}' & 0 & 0 & \dots \\ \dots & \dots & \dots & \dots & \dots & \dots \\ \dots & 0 & 0 & 0 & 1 & \gamma_{n-2}{}' \\ \dots & 0 & 0 & 0 & 0 & 1 \end{pmatrix} \begin{pmatrix} C_0^k \\ C_1^k \\ \dots \\ C_{n-1}^k \\ C_{n-1} \end{pmatrix} = \begin{pmatrix} \delta_0' \\ \delta_1{}' \\ \dots \\ \delta_{n-2}' \\ \delta_{n-1}' \end{pmatrix} \quad \textbf{(2.46)}$$

where δ_i' is a modified coefficient. To complete the first step, the modified $\gamma_i{}'$ and δ_i' are calculated as:

$$\gamma_i' = \begin{cases} \dfrac{\gamma_i}{\beta_i}, & i = 1 \\ \dfrac{\gamma_i}{\beta_i - \gamma_{i-1}'\alpha_i}, & i = [1, n-1] \end{cases}$$

$$\delta_i' = \begin{cases} \dfrac{\delta_i}{\beta_i}, & i = 0 \\ \dfrac{\delta_i^k - \delta_{i-1}'^{,k}\alpha_i}{\beta_i - \gamma_{i-1}'\alpha_i}, & i = [1, n-1] \end{cases} \quad \textbf{(2.47)}$$

Lastly, the target concentration vector can be solved by back substitution by multiplying $UX = L^{-1}b$ by U^{-1} and the concentration is calculated as:

$$C_i^k = \begin{cases} \delta_{n-1}', & i = n-1 \\ \delta_i'^k - \gamma_i' C_{i+1}^k, & i = [n-2, n-3, \dots, 0] \end{cases} \quad \textbf{(2.48)}$$

The Thomas algorithm offers easy matrix solution in the context voltammetry due to its relative simplicity and efficient implementation. Implementing it in computer programs from scratch, however, is still challenging for beginners. As mentioned in 2.1, modern high-level programming languages offers one-line solution for matrix operations. For example, using MATLAB or Python, x matrix can be solved directly by a single command:

$$\begin{gathered}\text{MATLAB: x = linsolve(A,B)} \\ \text{Python: import numpy as np; x = np.linalg.solve(A,B)}\end{gathered} \quad \textbf{(2.49)}$$

Nevertheless, these out of box methods are not as effective as the Thomas method when solving a tridiagonal matrix in the context of simulation of voltammetry: these methods will treat the tridiagonal matrix (a sparse matrix) as a dense matrix, leading to redundant computations. In addition, introduction of the Thomas method can serve as a mathematical background to the simulation and help to understand implementation in other languages like C++ in Chapter 3. Introduction of the algorithm also unveils the "gear and spring" behind a simulation software, instead of treating it like a black box, as highlighted in section 2.1.

2.3 Simulation of electrochemical processes

Using the discretized diffusion equations, common electrochemistry experiments like cyclic voltammetry and chronoamperometry can be simulated. This section introduces the procedure of simulation and adds some caveats.

2.3.1 1D simulations

A simulation of cyclic voltammetry is performed by sequentially solving for the tridiagonal matrix from the initial time step to the last time step while updating the applied potential, θ, at each time step. Five parameters are specified before simulation: three experimental parameters: the initial potential, θ_i, the vertex potential, θ_v and the scan rate, σ; two parameters controlling the separation of the discretized points in space and time, which

affects the truncation error: ΔX and ΔT. From the experimental parameter, the dimensionless time and space for the simulation, is:

$$T_{sim} = \frac{2|\theta_v - \theta_i|}{\sigma}$$
$$X_{sim} = 6\sqrt{T_{sim}} \quad \textbf{(2.50)}$$

where the factor two reflects the forward and reverse scans of a cyclic voltammetry experiment. The total number of time steps is:

$$m = \frac{T_{sim}}{\Delta T} \quad \textbf{(2.51)}$$

where ΔT is specified by the potential increment, $\Delta\theta$, so that m does not vary with scan rate, as:

$$\Delta T = \frac{\Delta\theta}{\sigma} \quad \textbf{(2.52)}$$

In typical simulations, $\Delta X = 10^{-5}$ and $\Delta\theta = 10^{-2}$ are good starting parameters.

At each time step k, the flux can be estimated by a two-point approximation or a three-point approximation:

$$\text{Two} - \text{point approximation: } J^k = -\left(\frac{C_1^k - C_0^k}{\Delta X}\right)$$
$$\text{Three} - \text{point approximation: } J^k = -\left(\frac{-C_2^k + 4C_1^k - 3C_0^k}{2\Delta X}\right) \quad \textbf{(2.53)}$$

With knowledge of electrode area, A_{elec} and assuming a uniformly accessible electrode, the dimensionless flux can be converted to current:

$$I = \left(\frac{FA_{elec}c_A^* D_A}{\epsilon}\right) J_{X=0,A} \tag{2.54}$$

where ϵ is the radius of electrode, c_A^* is the bulk concentration of species A and $J_{X=0,A}$ is the dimensionless flux of species A.

2.3.2 The expanding spatial grid

In an electrochemical reaction, the concentration gradient is steep near the surface of electrode and becomes flatter further away from the electrode. Therefore, the spatial interval between nodes near the electrode should be small to minimize the error of finite difference approximation, and the nodes further away from electrode should be large to save memory and time. An expanding grid is constructed for this purpose:

$$h_i = X_{i+1} - X_i = h\omega_X^i \tag{2.55}$$

where $i = [0, n-1]$, h_i is the distance between the node X_{i+1} and X_i and ω_X^i is the expanding factor. The discretized diffusion equation for expanding grid is:

$$\frac{C_i^k - C_i^{k-1}}{\Delta T} = \frac{\frac{C_{i+1}^k - C_i^k}{\Delta X_+} - \frac{C_i^k - C_{i-1}^k}{\Delta X_-}}{\frac{1}{2}[\Delta X_+ + \Delta X_-]} \tag{2.56}$$

The modified coefficient of Thomas method mentioned in 2.2.4 is:

$$\begin{aligned} \alpha_i &= -\frac{2\Delta T}{\Delta X_-^2 + \Delta X_+ \Delta X_-} \\ \beta_i &= \frac{2\Delta T}{\Delta X_+^2 + \Delta X_+ \Delta X_-} + \frac{2\Delta T}{\Delta X_-^2 + \Delta X_+ \Delta X_-} + 1 \\ \gamma_i &= -\frac{2\Delta T}{\Delta X_+^2 + \Delta X_+ \Delta X_-} \end{aligned} \tag{2.57}$$

Numerical simulations introduced in later chapters use expanding grids to save time and maintain accuracy. Figure 2.3 compares a uniform grid ($\Delta X = 0.01$) and an expanding grid ($h = 0.01, \omega = 1.1$) for X ranging from 0 to 1. The uniform grid has 101 nodes while the expanding grid has only 51, showing that the expanding grid can save computer memory and accelerate computation. An expanding grid factor between 1.01 and 1.05 is usually applied.

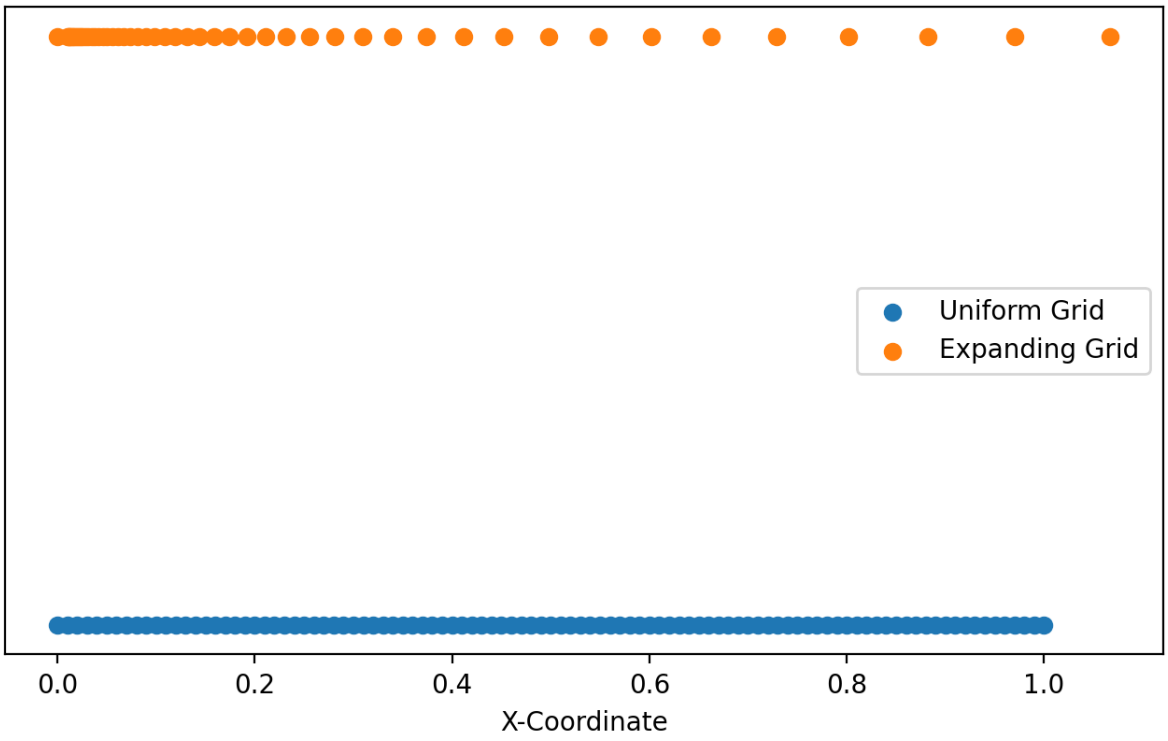

Figure 2.3. A comparison of an expanding grid with a uniform grid for X ranging from 0 to 1. Blue: uniform grid with $\Delta X = 0.01$ with a total of 101 nodes. Orange: Expanding grid with h $= 0.01$ and $\omega = 1.1$, with a total of 51 nodes.

2.3.3 Random walk method

The random walk is another popular method, in the context of electrochemistry, to study the electrochemical behaviour of a small number of molecules[19-21], adsorption effects[22], noise modelling[23], nanoparticles[24, 25], single molecular detection[26], simulation[27, 28], electrochemical correlation spectroscopy[29] and others. Simulating voltammetry using random walks, can reveal

the stochastic current response at very low analyte concentration and/or the associated current response (often femtoampere level).

The random walk method focuses on individual analyte entities rather than macroscopic ensembles. Each analyte particle moves stochastically and interacts as an individual entity with its environment. The simulation process involves simulating a large number of individual molecules, followed by sampling features of interest to gain insight of the entire system. When simulating for voltammetry, consider a molecule which has equal probability (50%) moving ΔX forward or backward:

$$x \xrightarrow{p=50\%} x + \Delta \mathrm{x}$$
$$x \xrightarrow{p=50\%} x - \Delta X \qquad \textbf{(2.58)}$$

An analyte reaches a position $\mathrm{x} < 0$ suggest that it has reached the electrode, it is then "bounced" back:

$$\text{if } \mathrm{x} < 0, \text{then } \mathrm{x} = -\mathrm{x} \qquad \textbf{(2.59)}$$

Consider a simple $A + e \rightleftarrows B$ process and assume the couple obeys Nernst equation that $c_{A,x=0} = c_{B,x=0} e^{\theta}$, the probability of an analyte molecule at the electrode in oxidation state of A is:

$$p_A = \frac{1}{1 + \exp -\theta} \qquad \textbf{(2.60)}$$

Similarly, the probability of being at state B is:

$$p_B = \frac{1}{1 + \exp \theta} = 1 - p_A \qquad \textbf{(2.61)}$$

When a molecule reaches the electrode surface, its oxidation state is randomized using p_A and p_B to mimic a Nernstian equilibrium. The current can be estimated when an oxidation state is changed, the reaction contributes $\pm\Delta I$ to total current:

$$\Delta I = \pm\frac{e_0}{\Delta T} \tag{2.62}$$

where e_0 is the charge on the electrode and ΔT is the discrete time interval. Figure 2.4 illustrates a voltammogram predictedby random walk method from simulating 454058 molecules for a $10^{-4}\ M$ solution and the number of molecules simulated is proportional to the concentration of interest, suggesting that random walk method will be very expensive when simulating for high concentrations. In essence, the random walk method complements finite difference simulation and is best used when the concentration of redox species < 10^{-5} M if computing power is limited.

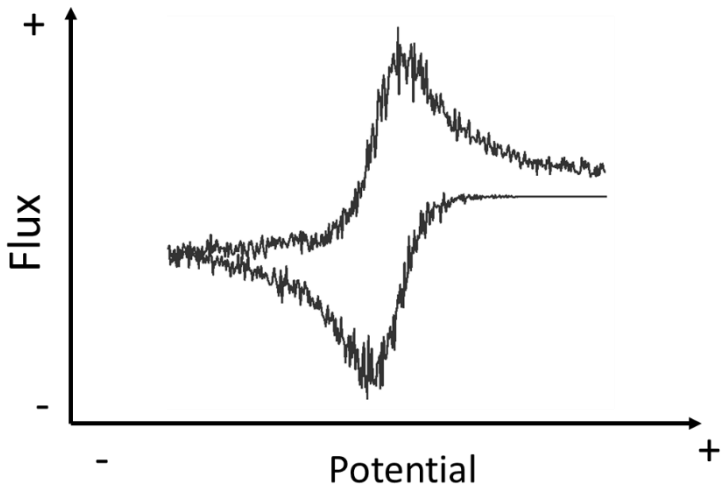

Figure 2.4. A voltammogram predicted by random walk method from simulating 454058 molecules for a $10^{-4}\ M$ solution.

2.3.4 Validation and convergence studies

After simulations, it is very important, indeed essential, to validate the results. Two forms of analysis are most common in practice: self-convergence testing which estimates truncation errors and specific test, which uses analytical solutions and reference values[30-32].

Self-convergence tests analyze the effect of ΔX and $\Delta\theta$ on the consistency of simulation results by observing characteristic features of voltammogram like $E_{1/2}$, E_p and J_p. Another example of the test is to check the mass conservation. For example, for a generic electron transfer with the following stoichiometry:

$$s_A A + ne^- \rightleftarrows s_B B \qquad \textbf{(2.63)}$$

which has to fulfill the following:

$$\frac{n_A}{s_A} + \frac{n_B}{s_B} = \frac{n_A^*}{s_A} + \frac{n_B^*}{s_B} \qquad \textbf{(2.64)}$$

where n_A and n_B are the total number of moles of species A and B and n_A^* and n_B^* are the initial total number of moles of A and B.

The second type of test is the specific tests, using well-established analytical expression and values to validate the results of simulation usually in certain limits such as realized by putting homogeneous rate constants to zero or making electrochemical rate constant very high or low to confer full electrochemical reversibility or irreversibility on a redox couple. For example, the analytical expression for the chronoamperogram and the concentration profiles of A and B of a chronoamperometry at a macroelectrode for the simple process $A + e \rightleftarrows B$, in dimensionless units are:

$$|J(T)| = \frac{1}{\sqrt{\pi T}}$$

$$C_A(X,T) = \text{erf}\left(\frac{X}{2\sqrt{T}}\right) \qquad \textbf{(2.65)}$$

$$C_B(X,T) = \frac{c_B^*}{c_A^*} + \frac{1}{\sqrt{d_B}}\left(1 - \text{erf}\left(\frac{X}{2\sqrt{T}}\right)\right)$$

where $\text{erf}(x)$ is the error function. Reversible cyclic voltammograms can be checked by characteristic values for quantities such as peak flux, J_p, peak potential, θ_p, half peak potential, $\theta_{1/2}$ and peak to peak separation,$\Delta\theta_p$:

$$\left|J_p\right| = 0.4463\sqrt{\sigma}$$

$$\theta_p = \theta_{1/2} \mp 1.109$$

$$\theta_{1/2} = 0.5 \ln dB \qquad \textbf{(2.66)}$$

$$\left|\Delta\theta_p\right| \approx 2.3$$

where the upper sign of $\mp$ applies to a reduction and the lower one applies to an oxidation process.

The expressions and values listed above offer a short overview of validation tool employed for simulation. More expression and values will be introduced in later chapters when relevant.

The next chapter uses the knowledge and tools summarised in the first two chapters to analyse the effect of coupled chemistry on Tafel analysis.

References

1. R. G. Compton, E. Laborda, E. Kaetelhoen and K. R. Ward, *Understanding voltammetry: simulation of electrode processes*, World Scientific London, 2nd edn., 2020.
2. J. H. Brown, *J. Chem. Educ.*, 2015, **92**, 1490-1496.
3. D. K. Gosser, *Cyclic voltammetry: simulation and analysis of reaction mechanisms*, VCH New York, 1993.

4. T. Nann and J. Heinze, *Electrochem. Commun.*, 1999, **1**, 289-294.
5. D. J. Gavaghan and A. M. Bond, *J. Electroanal. Chem.*, 2000, **480**, 133-149.
6. A. M. Bond, N. W. Duffy, S.-X. Guo, J. Zhang and D. Elton, *Anal. Chem.*, 2005, **77**, 186 A-195 A.
7. S. J. Messersmith, *J. Chem. Educ.*, 2014, **91**, 1498-1500.
8. L. K. Bieniasz, *Modelling electroanalytical experiments by the integral equation method*, Springer, 2015.
9. G. F. Kennedy, A. M. Bond and A. N. Simonov, *Curr. Opin. Electrochem.*, 2017, **1**, 140-147.
10. J. Buffle, Z. Zhang and K. Startchev, *Environ. Sci. Technol.*, 2007, **41**, 7609-7620.
11. R. Lee Hotz, *Los Angles Times*, 1999.
12. *CBC Archives*, 2018.
13. R. Leiteritz and D. Pflüger, *arXiv preprint arXiv:2112.05620*, 2021.
14. K. W. Morton and D. F. Mayers, *Numerical solution of partial differential equations: an introduction*, Cambridge university press, 2005.
15. G. D. Smith, G. D. Smith and G. D. S. Smith, *Numerical solution of partial differential equations: finite difference methods*, Oxford university press, 1985.
16. N. J. Higham, *Accuracy and stability of numerical algorithms*, SIAM, 2002.
17. N. J. Higham, *Wiley Interdisciplinary Reviews: Computational Statistics*, 2011, **3**, 230-238.
18. W. H. Press, S. A. Teukolsky, W. T. Vetterling and B. P. Flannery, *Numerical recipes 3rd edition: The art of scientific computing*, Cambridge university press, 2007.
19. S. Liang and X. Dong, *J. Solid State Electrochem.*, 2008, **12**, 701-706.
20. I. J. Cutress, E. J. Dickinson and R. G. Compton, *J. Electroanal. Chem.*, 2011, **655**, 1-8.
21. C. Amatore, F. Grün and E. Maisonhaute, *Angew. Chem.*, 2003, **115**, 5094-5097.
22. A. J. Samin, *AIP Advances*, 2016, **6**, 055101.
23. P. S. Singh, H.-S. M. Chan, S. Kang and S. G. Lemay, *J. Am. Chem. Soc.*, 2011, **133**, 18289-18295.
24. S. J. Kwon, H. Zhou, F.-R. F. Fan, V. Vorobyev, B. Zhang and A. J. Bard, *Phys. Chem. Chem. Phys.*, 2011, **13**, 5394-5402.
25. E. Kätelhön and R. G. Compton, *Chem. Sci.*, 2014, **5**, 4592-4598.
26. P. S. Singh, E. Kätelhön, K. Mathwig, B. Wolfrum and S. G. Lemay, *ACS nano*, 2012, **6**, 9662-9671.
27. E. Kätelhön, K. J. Krause, P. S. Singh, S. G. Lemay and B. Wolfrum, *J. Am. Chem. Soc.*, 2013, **135**, 8874-8881.
28. E. Kätelhön, K. J. Krause, K. Mathwig, S. G. Lemay and B. Wolfrum, *ACS nano*, 2014, **8**, 4924-4930.
29. M. A. Zevenbergen, P. S. Singh, E. D. Goluch, B. L. Wolfrum and S. G. Lemay, *Anal. Chem.*, 2009, **81**, 8203-8212.
30. E. Kätelhön and R. G. Compton, *Analyst*, 2015, **140**, 2592-2598.
31. E. Kätelhön and R. G. Compton, *Analyst*, 2015, **140**, 3290-3290.
32. E. Kätelhön and R. G. Compton, *Analyst*, 2016, **141**, 1154-1154.

Chapter 3 Super-Nernstian Tafel slopes: An Origin in coupled homogeneous kinetics

This chapter analyzes the influence of a second order homogeneous chemical reaction (EC_2) coupled to a reversible electron transfer as indicated by Tafel slopes which characterize the apparent degree of reversibility of the electrochemical reaction. The work has been published in the Journal of Electroanalytical Chemistry[1].

Simulations are reported relating to the predicted Tafel slopes of voltammograms recorded for a heterogeneous electrochemically reversible electron transfer process coupled to non-linear homogeneous chemical kinetics. Tafel plots are shown to be markedly non-linear with potential, indicating the essential need to be analysed via simulation. In the case of the EC_2 reaction, for a simple one-electron reversible electron transfer, the following second order kinetics lead to Tafel slopes with apparent transfer coefficients notably above unity, and so gain an *apparent* super-Nernstian response.

3.1 Introduction

A key component in the analysis of any current-voltage data embracing a Faradaic process is that of Tafel analysis, originating in the early 20th century work of Julius Tafel who, in the course of his work on electro-organic reactions, noted that plots of the logarithm of the Faradaic current, *I*, as a function of potential, *E*, were often linear at potentials near the onset of the reaction [2, 3]. Most recently IUPAC[4 5] have defined, in the case of an electro-reduction, the cathodic Tafel transfer coefficient α to be:

$$\alpha = -\frac{RT}{F}\frac{d\ln(I)}{dE} \qquad \textbf{(3.1)}$$

with the corresponding definition for an anodic process, an electro-oxidation, as:

$$\beta = \frac{RT}{F}\frac{d\ln(I)}{dE} \qquad \textbf{(3.2)}$$

where R is the Gas Constant, T is the temperature and F is the Faraday Constant. Note that these definitions relate exclusively to the *experimentally* measured quantities *I* and *E*. Earlier definitions involving the 'number of electrons transferred, n', and leading to expressions containing the term '$n\alpha$', are eschewed, not least since *n* may be unknown, difficult or impossible to measure, and in any case likely to be a function, for $n > 1$, of the voltammetric timescale on which it is measured, so that different values of *n* can be, and often are, seen at microelectrodes and at macroelectrodes.

In implementing equation **(3.1)** and **(3.2)** in respect of modern voltammetry - typically either cyclic voltammetry or steady-state voltammetry derived from a hydrodynamic or micro-electrode - it is necessary, in order that the Tafel slope or transfer coefficient reflects the heterogeneous electron transfer event, that the part of the voltammogram analysed is essentially free of mass transport limitations. The practical implication of this leads to the recommendation that no more than 30% of the maximum current of an electrochemical irreversible process be subject to Tafel analysis, a limit which has been recently recommended via numerical simulations.

In the case of a simple one electron transfer involving two solution phase species,

$$A + e^{-} \rightleftarrows B \qquad \textbf{(3.3)}$$

the Tafel slope reflects the transfer coefficient within the Butler-Volmer formulation of electrode kinetics where, for an electron transfer which is slow compared with the prevailing mass transport,

$$I \propto \exp\left(-\frac{\alpha FE}{RT}\right) \qquad \textbf{(3.4)}$$

and $0 < \alpha < 1$; whilst for a multi-electron process,

$$A + ne^- \rightleftarrows B \tag{3.5}$$

and if the reaction proceeds via a series of separate, non-concerted electron transfers and chemical steps,

$$I \propto \exp\left(-\frac{(n' + \alpha_{RDS})FE}{RT}\right) \tag{3.6}$$

where n' is the number of electrons transferred before the rate determining step and $\alpha_{RDS}$is the transfer coefficient of the rate determining electron transfer step. In the latter case the measured Tafel slope indicates the value of $n' + \alpha_{RDS}$. Both **(3.4)** and **(3.6)** predict an exactly linear Tafel plot of $\ln(I)$ versus E, in the absence of any depletion of the electroactive species.

In the Marcus-Hush theory of a simple one-electron transfer, in contrast, the transfer coefficient is not constant but is a function of applied potential giving rise to Tafel plots with a weak curvature, controlled by magnitude of the reorganization energy, λ, which has both inner and outer sphere contributions,

$$\alpha = \frac{1}{2} + \frac{F\left(E - E_f^0\right)}{2\lambda} \tag{3.7}$$

where $E^0_{f,A/B}$ is the formal potential of the *A*/*B* redox couple. Such curvature has been observed experimentally[6-11]. **(3.7)** shows that $\alpha \approx 0.5$ at small overpotentials, which results from the Marcus-Hush theory in its simplest, symmetric form and assuming the curvature of the Gibbs energy parabola of the reactant *A* and product *B* to be the same[12]. In its asymmetric form the theory gives rise to values deviating from $\alpha \approx 0.5$ by an extent reflecting the difference in vibrational force constants in the *A* and *B* species[13] as is, for example, thought to explain the low value of α seen for the reduction of di-oxygen to superoxide [14].

In the case of fast (compared to prevailing mass transport), so-called reversible electrode kinetics, Tafel analysis shows for a simple, one-electron, reaction an "apparent" transfer coefficient of unity, where "apparent" cautions against relating this to Butler-Volmer or Marcus-Hush theories. In particular, Albery[15] shows that for reversible steady-state voltammetry in which a limiting current I_{lim} is observed, for example at a rotating macro disc electrode or at a micro electrode, then for a reduction:

$$\ln\left[\frac{1}{I}+\frac{1}{I_{lim}}\right] = +\frac{EF}{RT} + \text{constant} \qquad \textbf{(3.8)}$$

In this situation the Tafel analysis with $\alpha = 1$ simply shows the electron transfer is fast compared with mass transport. The process can be characterised as "Nernstian".

In this chapter the Tafel analysis of electron-transfer reactions is further explored, notably in the electrochemically reversible limit, and, in particular, the effect of a homogeneous chemical reaction following an electron transfer is explored. First we confirm that there is a marked effect on the Tafel slope such that, as previously inferred[16, 17], fast follow-up kinetics leads to irreversibility, since the rapid loss of B prevents Nernstian equilibrium being established, and hence the Tafel analysis reflects the electron-transfer kinetics of A alone. Second, and notably, we show that in the case of relatively slow second-order chemical reaction, the effect of the following chemical reaction is to increase the Tafel slope so that apparent transfer coefficients in excess of unity can be observed. This provides one explanation for the observation of "super-Nernstian" Tafel slopes even for the case of a rigorous one-electron process.

In order to identify "super-Nernstian" regimes, we focus on the EC_2 reaction,

$$\begin{aligned} A + e^- &\rightleftarrows B \\ B + B &\xrightarrow{k_2} Y \end{aligned} \qquad \textbf{(3.9)}$$

where k_2 is the second order rate constant for EC_2 reaction. The next section develops the theory for EC_2 reaction.

3.2 Theory

This study primarily focuses on the electrochemically reversible, or quasi-reversible, heterogeneous, one-electron reduction of species *A* to *B*, followed by a homogeneous chemical step under diffusion-only mass transport. Planar geometry is considered.

The electrode kinetics are described using the Butler-Volmer theory of electrode kinetics, which states that, for a mechanism $A + e^- \rightleftharpoons B$:

$$j = k_0 \exp\left[\frac{-\alpha F\left(E - E_f^0\right)}{RT}\right] c_A(0,t) - k_0 \exp\left[\frac{(1-\alpha) F\left(E - E_f^0\right)}{RT}\right] c_B(0,t) \qquad \textbf{(3.10)}$$

where j is the flux of the reductant on the electrode surface, $c_A(0,t)$ and $c_B(0,t)$ are the concentrations of species *A* and *B* at the electrode surface at time t respectively, and k_0 is the standard electrochemical rate constant.

The EC_2 reaction was simulated on a planar macroelectrode. By assuming that the scale of the electrode is significantly larger than the distance the species are able to diffuse over during the timescale of the simulation, the model is simplified to a one-dimensional system where only diffusion perpendicular to the surface of the electrode needs to be considered. In combination with Fick's Second Law of diffusion, the diffusion equation of this model can be expressed as:

$$\frac{\partial c_j}{\partial t} = D_j \frac{\partial^2 c_j}{\partial x^2} \qquad \textbf{(3.11)}$$

where j is the species under study and D_j is the diffusion coefficient. For simplicity, during simulation, the diffusion coefficients of all species are set to be equal.

The rate of change in concentration with time in the solution phase can be expressed with Fick's Second Law of diffusion with appropriate terms accounting for the second-order homogeneous chemical reactions. See **(3.9)**, when two *B* molecules react and form *Y*, the process is irreversible and controlled by the second order rate constant, k_2,

$$\begin{cases} \dfrac{\partial c_A}{\partial t} = D_A \dfrac{\partial^2 c_A}{\partial x^2} \\ \dfrac{\partial c_B}{\partial t} = D_B \dfrac{\partial^2 c_B}{\partial x^2} - k_2 c_B^2 \\ \dfrac{\partial c_Y}{\partial t} = D_Y \dfrac{\partial^2 c_Y}{\partial x^2} + \dfrac{1}{2}\, k_2\, c_B^2 \end{cases} \qquad \textbf{(3.12)}$$

To solve these differential equations, boundary conditions at the start of the simulation and at both spatial boundaries (the electrode surface and outer boundary) must be defined (see also Figure 3.1). The initial concentration of *A* in bulk solution is set to c_A^* with no *B* or *Y* present in the system.

$$\begin{matrix} t = 0,\ x \geq 0 \\ t > 0, x = x_{sim} \end{matrix} \begin{cases} c_A = c_A^* \\ c_B = 0 \\ c_Y = 0 \end{cases} and\ c_A^* \geq 0 \qquad \textbf{(3.13)}$$

where x approaches x_{sim}, on outer spatial boundary, the concentration of each species equals its initial bulk concentration. This boundary needs to be sufficiently far from the electrode that changes in concentration at its surface have no effect in the simulation on the concentration at the outer boundary. The size of the Nernst diffusion layer, δ, depends on time as $\delta \propto Dt$. It is understood from Einstein's work on Brownian motion[18] that in one dimension for a particle: $\sqrt{\langle x^2 \rangle} = \sqrt{2Dt_{sim}}$, which can be used to approximate the distance from the electrode at which one might expect concentration perturbations to persist. The distance of the outer boundary from the electrode, x_{sim}, in the simulations, is selected to be greater than this[19]:

$$x_{sim} = 6\sqrt{Dt_{sim}} \qquad \textbf{(3.14)}$$

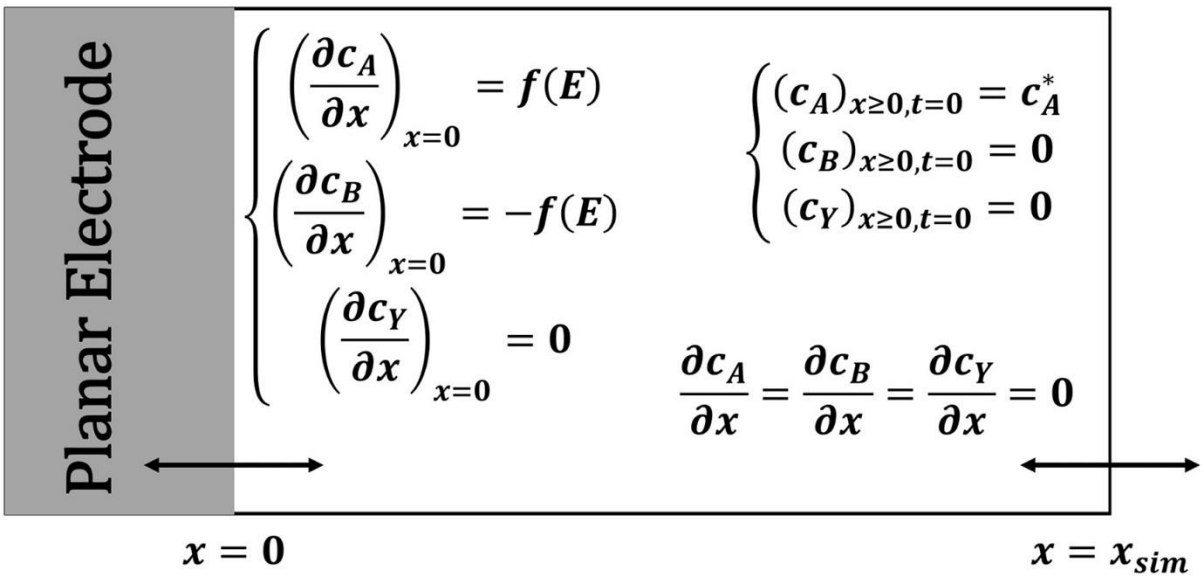

Figure 3.1. The boundary conditions used for the planar EC_2 model. c_i is the concentration of the species *j* at a certain space point, c_A^* is the initially homogeneous concentration of the analyte *A*, *x* is the perpendicular distance from the electrode, x_{sim} is the boundary of the simulated space in the x-axis and $f(E)$ is a function of the potential according to Butler-Volmer kinetics.

The boundary conditions at the surface of the electrode reflect the electroactivity of the species in the potential range of study:

$$\begin{cases} \mathrm{D}_A \left(\frac{\partial c_A(x,t)}{\partial x}\right)_{x=0} = k_0 e^{-\frac{\alpha F\left(E-E_f^0\right)}{RT}} c_A(0,t) - k_0 e^{\frac{(1-\alpha)F\left(E-E_f^0\right)}{RT}} c_B(0,t) \\ D_B \left(\frac{\partial c_B(x,t)}{\partial x}\right)_{x=0} = -D_A \left(\frac{\partial c_A(x,t)}{\partial x}\right)_{x=0} \\ \left(\frac{\partial c_Y(x,t)}{\partial x}\right)_{x=0} = 0 \end{cases} \quad \textbf{(3.15)}$$

where *A* and *B* are electro-active and follow Butler-Volmer kinetics, whilst *Y* is electro-inactive and has zero flux at the electrode.

3.3 Dimensionless parameters

The dimensionless parameters mentioned in this chapter were introduced in 2.1.3. Note that the second order chemical reaction rate constant is defined as:

$$K_2 = \frac{k_2 c_A^* \epsilon^2}{D_A}$$

3.4 Results and discussion

In this section, the simulated results with the corresponding analysis and discussion for the two models are presented. The simulated cyclic voltammograms of EC_2 reaction model are shown first to generate "super-Nernstian" Tafel slopes.

Two sets of simulations were performed for the EC_2 reaction model for slow (irreversible) and fast (reversible) electrode kinetics of the electrochemical reaction by setting K_0 to 10^{-3} and 10^{-8}, respectively, at a fixed dimensionless scan rate σ = 38943, which corresponds to the dimensional scan rate $\nu = 1V/s$ for the dimensional parameters of $\epsilon = 1mm$, $c_A^* = 1\ mM$, $D_A = 10^{-5}\ cm^2 s^{-1}$ and $\alpha = 0.5$. Irreversible and reversible Randles-Ševčík equations[20, 21] were used to validate the simulation model and compare with the peak currents of the simulated voltammograms:

$$\begin{cases} \left|I_{p,I}\right| = 0.496\sqrt{\alpha} F A c_A^* \sqrt{\dfrac{FD\nu}{RT}} \\ \left|I_{p,R}\right| = 0.446 F A c_A^* \sqrt{\dfrac{FD\nu}{RT}} \end{cases} \quad \textbf{(3.16)}$$

where $I_{p,I}$ is the predicted peak current for irreversible Randles-Ševčík equation, $I_{p,R}$ is the predicted peak current for the reversible Randles-Ševčík equation, and A is the electrode area. By varying the chemical reaction kinetics K_2 for both slow and fast electrode kinetics, a marked dependence of the simulated cyclic voltammograms on K_2 is seen and presented in Figure 3.2.

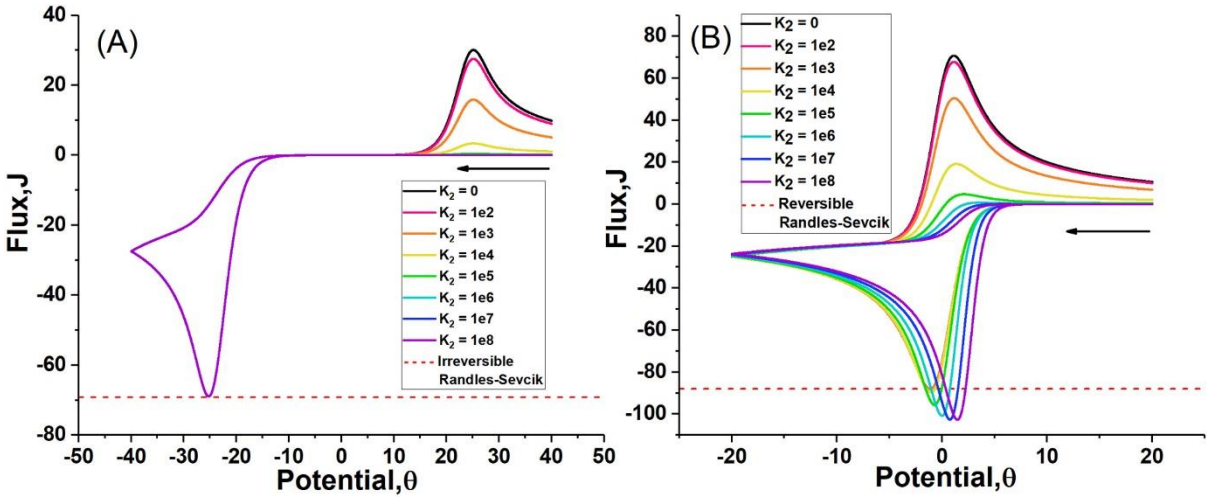

Figure 3.2. Cyclic Voltammograms of the slow (A) and fast (B) electrochemical kinetics K_0 for different values of chemical kinetics K_2 in the EC_2 reaction model. The red dashed lines in figures represent the values of peak flux predicted by the irreversible (A) and reversible (B) Randles-Ševčík equations. The solid lines represent the cyclic voltammograms for different K_2. The black arrows indicate the start and initial direction of the potential sweep.

As shown in Figure 3.2 (A), the forward peak is almost unaffected as the K_2 value increases, so the apparent transfer coefficient stays at a similar level. See Figure 3.3 (A), $\alpha \approx 0.5$, for slow regimes of electrode kinetics K_0 since the electron transfer is 'blind' to the following kinetics. However, the back peak of the voltammogram decreases when K_2 increases for the slow electrode kinetics reflecting the loss of B via homogeneous chemistry.

In Figure 3.2 (B), for the reversible case, by increasing K_2, not only does the back peak of the voltammogram decrease, the forward peak flux increases as the forward peak position moves towards more positive potentials. See Figure 3.3 (B), the value of α also changes: in the range of K_2 simulated in Figure 3.2(B), the forward scan peak becomes "sharper" as K_2 increases, and α increases from unity at $K_2 = 0$ to a maximum of 1.4 at $K_2 = 10^8$.

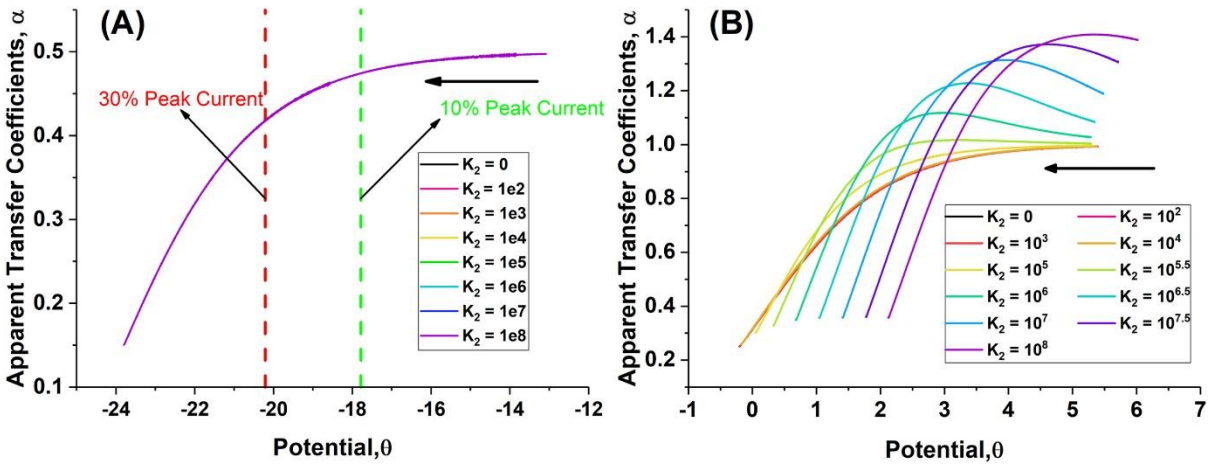

Figure 3.3. (A) shows the apparent transfer coefficients as a function of potential extracted from EC_2 reactions with slow electrode kinetics at $K_0 = 10^{-3}$ as shown in Figure 3.2 (A). 0.1% to 99% of peak current is analysed and plotted. The positions of 10% to 30% peak current are plotted with vertical lines on this figure. (B) is the apparent transfer coefficients extracted from EC_2 reactions with fast electrode kinetics at $K_0 = 10^8$ as shown in Figure 3.2 (B) with the follow up chemical reaction rate constants from 0 to 10^8. Note that more values of K_2 than shown in Figure 3.3 are considered for better visualization. The range of the apparent transfer coefficients to be analysed is from 0.1% to 99% of the peak current. The black arrows indicate the start and initial direction of the potential sweep.

The decrease in the back peak fluxes for both the fast electrode kinetics and the slow reflects the fact that larger K_2 increases the chemical irreversibility of the electrochemical reaction as the increasing K_2 results in a decreased amount of species *B* in the system after the forward scan. Whilst, the forward scan of the electrochemical reaction of an irreversible process is independent of the further reaction of species *B*, in contrast, the changes in forward peak shape in Figure 3.2(B) as K_2 increases can be explained by the fact that, as the K_2 increases, the concentration of *B* is reduced by the homogeneous chemical reaction, which drives the reaction from *A* towards *B* and leads to a less negative starting potential of the forward peak and larger magnitude of the peak flux.

To further investigate the changes in the apparent transfer coefficients α of the voltammograms for slow ($K_0 = 10^{-3}$) and fast electrode kinetics ($K_0 = 10^8$), the values

of α are extracted as shown in Figure 3.3 (A) and (B), by calculating the derivative of the natural log of flux, $\ln J$ with respect to potential, θ, using:

$$\alpha = \lim_{\Delta\theta=0} \frac{\ln J_{(\theta+\Delta\theta)} - \ln J_{\theta}}{\Delta\theta} \qquad \textbf{(3.17)}$$

In Figure 3.3 (A), the apparent transfer coefficients for the irreversible process stays at around 0.5 at less reductive potentials and decreases to around 0.15 near the peak of the forward scan due to change of concentration at the electrode surface and mass transport. The apparent transfer coefficient curves for different K_2 overlap with each other, indicating that the follow up homogeneous chemical reaction does not significantly affect the behaviour of forward scan peaks, and thus leaves the transfer coefficients unaffected. But this behaviour is very different for the reversible process, as discussed below.

In Figure 3.3 (B), the apparent transfer coefficients increase once K_2 reaches around 10^5 and "super-Nernstian" behaviour appears when $K_2 > 10^{5.5}$. The increasing apparent transfer coefficients are consistent with the a "sharper" forward scan peak at higher K_2 as shown in Figure 3.2 (B). The curves in Figure 3.3 (B) show two patterns. At low K_2, when the rate of follow up chemical reaction is slow compared with electrode kinetics, apparent transfer coefficients curves are not significantly affected, and the curve behaves like a simple one-electron reduction, as the apparent transfer coefficients curve steadily decreases from around unity at the onset of reduction to lower values at 0.3. However, when K_2 increases, the apparent transfer coefficients increase first at higher potential, and then drops as the potential shifts to more reductive values. As explained above, the fast removal of reduced B from A by homogeneous chemical reaction requires less reductive potential for the start of reduction and thus the super-Nernstian curves are at higher potential when K_2 is large.

To better appreciate the super-Nernstian behaviour in a voltammogram, the portion of the voltammogram with an apparent transfer coefficient greater than unity is labelled with a solid line as shown in Figure 3.4 Four cyclic voltammograms are shown: a reference of $K_2 = 0$ and three voltammograms with fast chemical kinetics of $K_2 = 10^6, 10^7, 10^8$. It can be seen that super-Nernstian responses can be seen at potentials typically used for Tafel analysis and that they are maximal for intermediate values of K_2 between very fast and relatively slow. Note that K_2 depends on c_A^*that the studied experimental ranges of K_2 can be adjusted accordingly.

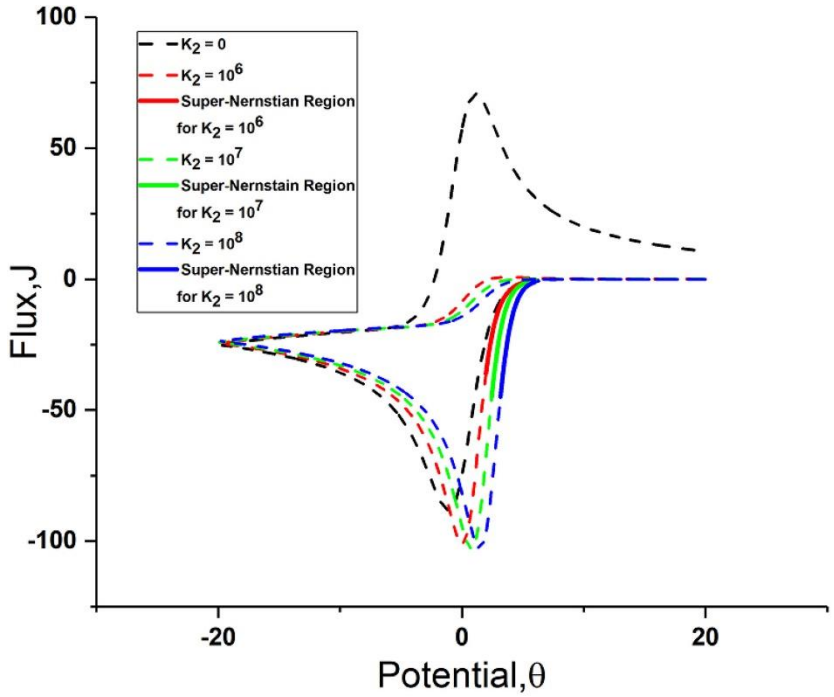

Figure 3.4. Among the four voltammograms (dash lines) selected from Figure 3.2(B), the regions of the voltammograms where super-Nernstian behaviours exist are highlighted with solid lines.

The cathodic peak potential can also provide insights into the voltammograms as shown in Figure 3.5 for the fully reversible limit. When K_2 is smaller than 10^5, the peak potential stays around −1.12. But when K_2 reaches around 10^5, the forward scan potential starts to increase.

Beyond this point exists a linear relationship between $\log_{10}K_2$ and forward scan peak potential, θ_{peak}. The linear relationship can be expressed as $\theta_{peak} = 0.736\log(K_2) - 4.402$ and the R^2 value is 0.999, indicating a strong linear correlation between $\log_{10} K_2$ and peak potential θ_{peak}. With this equation, the forward scan peak position at high K_2 can be easily inferred.

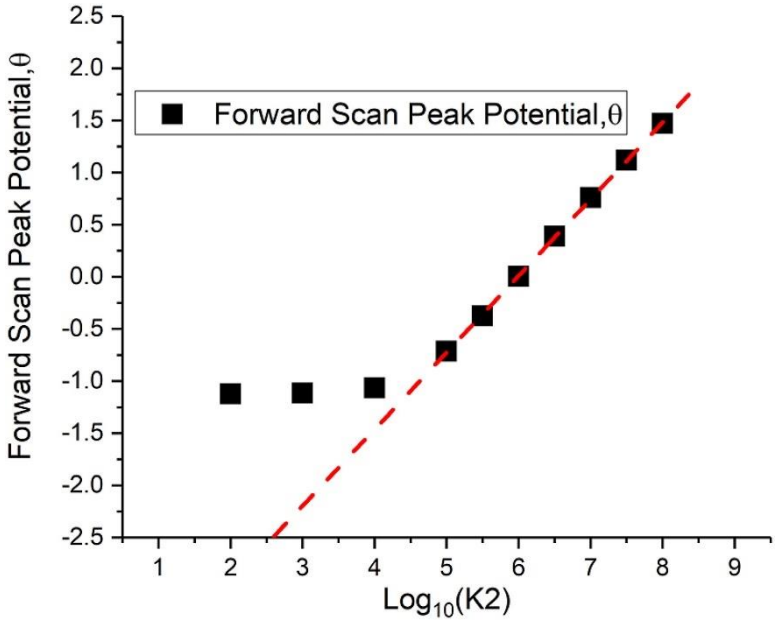

Figure 3.5. At $K_0 = 10^8$, σ = 38943, the forward scan peak potential at different K_2 is plotted. When $K_2$is greater than 10^5, there is a strong linear relationship between $\log_{10} K_2$and θ. When $K_2 = 0$, the peak potential is constant at −1.12.

The increase in value of α from $K_2 = 10^5$ can be attributed to the same fact that the reduction in the concentration of *B* drives the electrode reaction to generate more *B*. The second-order following kinetics means that the loss is increasingly promoted at more negative potentials as the kinetic term becomes relatively more important relative to transport.

Note that simulations were also carried out for a simple EC process ($A + e^- \leftrightharpoons B, B \rightarrow C$), that is with first order following kinetics. No such super-Nernstian behaviors were seen. Rather as the following rate constant increases, when the electrode kinetics are fast, the apparent Tafel slope changes monotonically from unity to $\alpha = \frac{1}{2}$, the value

set in the simulation. This reflects the linearity of the system so that changing concentration influences both diffusion and chemical reaction proportionally.

3.4.1 Dimensional mapping

The apparent transfer coefficient is dependent on various parameters including some of the key dimensional parameters: scan rate, k_0, and k_2. In order to establish a simulation model that can be used to predict the value of α under the various influences of these parameters in a EC_2 system, the values of apparent α are extracted for voltammograms of various σ and K_2 for three different electrode kinetics ($K_0 = 10^4, 10^2, 10^0$ which correspond to $k_0 = 10^0, 10^{-2}, 10^{-4}\ cm/s$) at ($\epsilon = 1mm, c_A^* = 1mM, D_A = 10^{-5}\ cm^2\ s^{-1},\ \alpha = 0.5$) shown in Figure 3.6. The range of K_2 in these simulations is from K_2 = 1.0 to $K_2 = 10^{10}$, and corresponds to $k_2 = 1.0\ M^{-1}\ s^{-1}$ to $k_2 = 10^{10}\ M^{-1}s^{-1}$. The range of dimensionless scan rate σ is from σ = 3.8943 to $\sigma = 3.8943 \times 10^6$, and corresponds to practical experimental scan rates of 10^{-4} *V/s* to 10^2 *V/s* with the other dimensional parameters mentioned above. The apparent transfer coefficients are calculated based on the common experimental approach by finding the linear fitting of the natural logarithm of 10% to 30% of peak flux with potential and the fitted slope is taken as the apparent transfer coefficients. For better illustration, the plots are presented in dimensional parameters as the scan rate and k_2 are chosen to relate to experiments.

As presented in Figure 3.7, the value of α decreases as the scan rate increases for all three k_0 if k_2 is kept constant. The value of α increases as k_2 increases before it reaches a maximum roughly 1.3 for smaller scan rates (up to $10^{-2}\ V/s$in (A) and $10^{-3}\ V/s$ in (B)). However, for larger scan rates (from 10^{-2} *V/s* to 10^2 *V/s* in (A), from 10^{-3} *V/s* to 10^2 *V/s* in

(B), and all scan rates in (C)), the value increases as k_2 increases before reaching a maximum and subsequently decreasing.

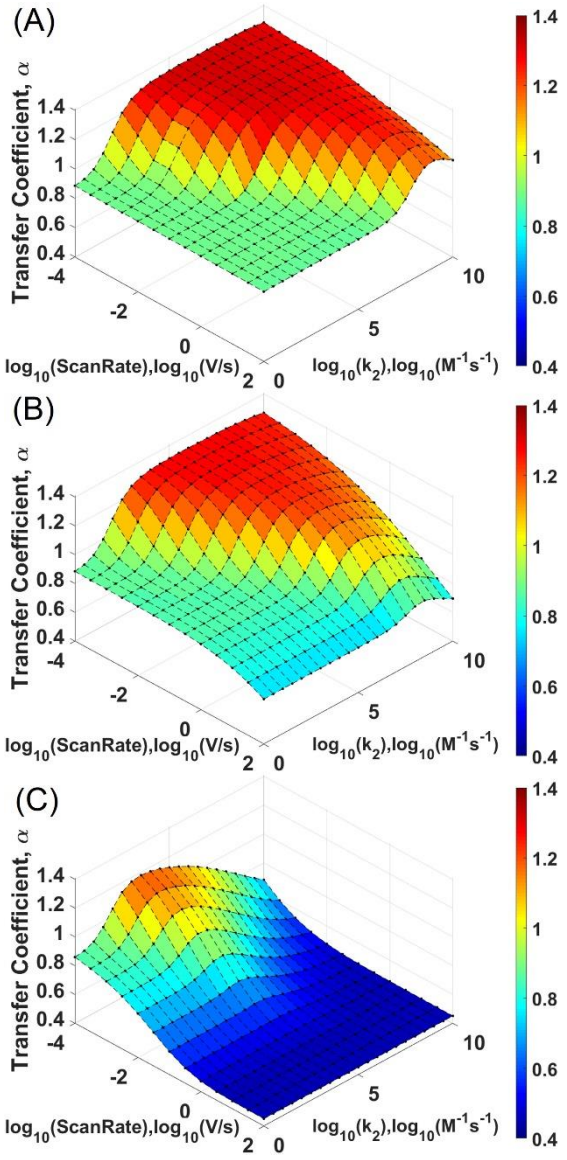

Figure 3.6. Apparent transfer coefficients α obtained from cyclic voltammograms for various scan rate σ and the homogeneous chemical kinetics k_2 at $k_0 = 10^0$ (A), 10^{-2} (B), $10^{-4}\ cm\ s^{-1}$(C) with corresponding dimensional parameter at ($\epsilon = 1\ mm, c_A^* = 1mM, D_A = 10^{-5}\ cm^2 s^{-1}, and\ \alpha = 0.5$). The homogeneous chemical kinetics dimension, k_2, is from 1 to $10^{10}\ M^{-1}s^{-1}$, corresponding to dimensionless K_2 from 1 to 10^{10}.The dimensional scan rate is from 10^{-4} to $10^2\ V/s$, corresponding to dimensionless scan rate σ from 3.8943 to 3.8943×10^6.

3.4.2 Guidance for experimentalists

In this EC_2 model, the dimensionless homogeneous chemical kinetic parameter K_2 is dependent not only on its intrinsic dimensional rate constant k_2, but also on the concentration of species *A*. Therefore, altering c_A^* can assist experimentalists to observe a "super-Nernstian" α for a system with a known k_2. As shown in Figure 3.7, the values of α are shown for a selection of k_2 (10^1, 10^3, 10^6, $10^9\ M^{-1}\ s^{-1}$) for three different k_0 (10^0, 10^{-2}, $10^{-4}\ cm/s$) at different scan rates.

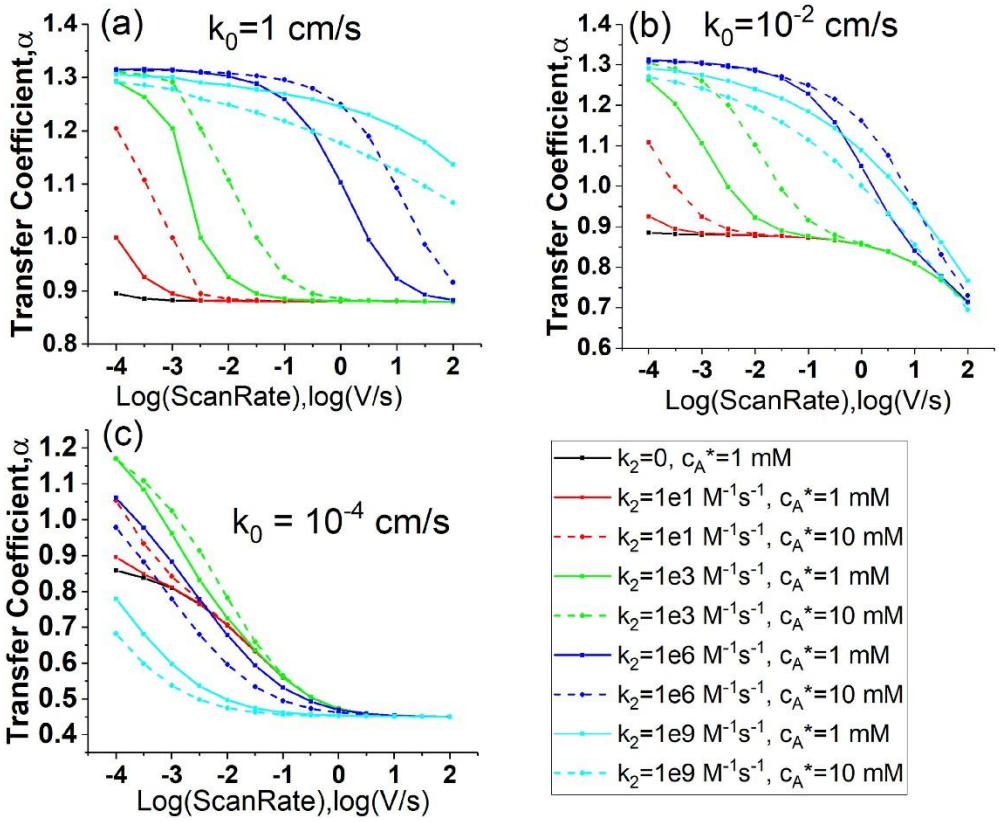

Figure 3.7. Apparent transfer coefficients α obtained from cyclic voltammograms for various scan rate σ and the homogeneous chemical kinetics k_2 for $c_A^* = 1\ mM$, $10\ mM$ (dashed lines) at $k_0 = 10^0(A)$, $10^{-2}(B)$, $10^{-4}\ cm/s(C)$.

For all the curves with $c_A^* = 1\ mM$ in Figure 3.7 (solid lines), as k_2 increases, the α values for all scan rates and k_0 increase until a maximum occurs ($k_2 = 10^1\ M^{-1}\ s^{-1}$ for (A) and (B), $k_2 = 10^1\ M^{-1}s^{-1}$ for (C)). Then the α decreases except for simulations at extremely high scan rates ($k_2 = 10^9\ M^{-1}s^{-1}$ for (A) and (B)). Additionally, the α values for

higher scan rates decreases as k_0 decreases. As for simulations with $c_A^* = 10\ mM$ in Figure 3.7 (dashed lines), for those with larger k_2 than the maximum discussed above ($k_2 = 10^1 M^{-1}s^{-1}$ for (A) and (B), $k_2 = 10^1\ M^{-1}s^{-1}$ for (C)), their values of α decrease compared to their counterparts at $c_A^* = 1\ mM$ except high scan rates of $k_0 = 10^{-4}\ cm/s$. Otherwise, the values of α for the other situations increases as concentration increase except for high scan rates for all three k_0. Overall, in practice, one can observe a higher value of α, even "super-Nernstian" α, by simply adjusting the concentration of the starting material *A*.

3.5 Conclusions

Tafel analysis is a routine and insightful component of voltammetric analysis. Whilst the interpretation in the limit of full electrochemical irreversibility is relatively simple, the simulations reported in this chapter reveal marked complexity for faster electron transfer when coupled with non-linear chemical kinetics as evidenced for EC_2 and reaction, most notably the super-Nernstian behaviour anticipated by the title of the chapter and also the contrasting behaviour of the titration reaction for macro and micro electrodes where simple mathematically analytical approaches to data analysis lose their value. Rather we again[22] conclude that the full simulation of experimental voltammograms is essential for even qualitative insight, as well as, of course, extraction of quantitative data.

Next chapter extends the simulation and analysis of coupled chemistry to real experiments: oxidation of bromide ion and formation of tribromide ion.

Reference

1. H. Chen, J. R. Elliott, H. Le, M. Yang and R. G. Compton, *J. Electroanal. Chem.*, 2020, **869**, 114185.
2. J. Tafel, *Physik. Chem.*, 1905, **50**, 641-712.
3. G. T. Burstein, *Corros. Sci.*, 2005, **47**, 2858-2870.

4. R. Guidelli, R. G. Compton, J. M. Feliu, E. Gileadi, J. Lipkowski, W. Schmickler and S. Trasatti, *Pure Appl. Chem.*, 2014, **86**, 259-262.
5. R. Guidelli, R. G. Compton, J. M. Feliu, E. Gileadi, J. Lipkowski, W. Schmickler and S. Trasatti, *Pure Appl. Chem.*, 2014, **86**, 245-258.
6. M. C. Henstridge, E. Laborda, N. V. Rees and R. G. Compton, *Electrochim. Acta*, 2012, **84**, 12-20.
7. J. M. Saveant and D. Tessier, *J. Phys. Chem.*, 1978, **82**, 1723-1727.
8. S. Fletcher and T. S. Varley, *Phys. Chem. Chem. Phys.*, 2011, **13**, 5359-5364.
9. C. E. D. Chidsey, *Science*, 1991, **251**, 919-922.
10. H. O. Finklea and D. D. Hanshew, *J. Am. Chem. Soc.*, 1992, **114**, 3173-3181.
11. L. Tender, M. T. Carter and R. W. Murray, *Anal. Chem.*, 1994, **66**, 3173-3181.
12. R. A. Marcus, *J. Chem. Phys.*, 1965, **43**, 679-701.
13. N. S. Hush, *J. Chem. Phys.*, 1958, **28**, 962-972.
14. E. E. Tanner, E. O. Barnes, C. B. Tickell, P. Goodrich, C. Hardacre and R. G. Compton, *J. Phys. Chem. C*, 2015, **119**, 7360-7370.
15. W. J. Albery, *Philosophical Transactions of the Royal Society of London. Series A, Mathematical and Physical Sciences*, 1981, **302**, 221-235.
16. R. P. Bacil, L. Chen, S. H. Serrano and R. G. Compton, *Phys. Chem. Chem. Phys.*, 2020, **22**, 607-614.
17. E. R. Lowe, C. E. Banks and R. G. Compton, *Anal. Bioanal. Chem.*, 2005, **383**, 523-531.
18. A. Einstein, *J Annalen der physik*, 1905, **17**, 549-560.
19. I. B. Svir, A. I. Oleinick and R. G. Compton, *Russ. J. Electrochem.*, 2003, **39**, 160-164.
20. J. E. Randles, *Trans. Faraday Soc.*, 1948, **44**, 327-338.
21. A. Ševčik, *Collect. Czech. Chem. Commun.*, 1948, **13**, 349-377.
22. D. Li, C. Batchelor-McAuley and R. G. Compton, *Applied Materials Today*, 2020, **18**, 100404.

Chapter 4 Non-unity stoichiometric reversible electrode reactions. The effect of coupled kinetics and the oxidation of bromide

This chapter builds on the insights of the previous chapter and elaborates on the simulation of bromide oxidation in aqueous solution, and the implications on the voltammetry of follow-up coupled chemical reaction. This chapter has been published in the Journal of Electroanalytical Chemistry[1]. The work is a combination of simulation and experiments. The experiments were performed by Archana Kaliyaraj Selva Kumar.

We explore via simulation, the cyclic voltammetry of the following mechanism involving a reversible electrode process coupled with a follow up reaction in which the product (B) of the electrode reaction reacts chemically with the reactant, A, to form a species C:

$$2A - 2e^- \rightleftarrows B$$
$$B + A \underset{k_b}{\overset{k_f}{\rightleftarrows}} C$$

Such a mechanism is shown, under certain critical combinations of rate constant and reactant concentration to give rise to two voltammetric peaks despite the assumption of a single redox couple (A/B). This results from the formation of C during the first peak whilst the second peak, seen at more oxidizing potentials, reflects the dissociation of C releasing A. A mechanism of the type investigated may hold during the oxidation of bromide (Br^-, A) in solution to form bromine(Br_2, B) and tribromide (Br_3^-,C). Simulations are used to explore the conditions for which two peaks are expected in the bromide oxidation system in aqueous solution and for which the two following limiting cases operate

$$3Br^- - 2e^- \rightleftarrows Br_3^-$$

and

$$2Br^- - 2e^- \rightleftarrows Br_2$$

We report experimental data for the bromide oxidation in aqueous solution. These are interpreted via simulations using independent literature values for the rate and equilibrium constants for tribromide formation.

4.1 Introduction

Cyclic voltammetry at macro-electrodes is the technique at the heart of modern electrochemistry yielding qualitative important information such as electrode reaction mechanisms and pathways together with quantitative data such as equilibrium, rate and adsorption constants, and diffusion coefficients. The characterisation of electrochemically reversible voltammograms in terms of peak currents and their voltage scan rate dependence and peak to peak separations are well established for the simple one-electron process

$$A - e^- \rightleftarrows B \qquad \textbf{(4.1)}$$

where the Randles-Ševčík equation describes the peak currents, I_p,[2, 3]

$$I_p = 0.446FA[A]_{bulk}\sqrt{\frac{FD\nu}{RT}} \qquad \textbf{(4.2)}$$

where F, R and T are the Faraday constant, Gas constant and absolute temperature respectively. A is the area of electrode, $[A]_{bulk}$ is the bulk concentration of reductant, D is the diffusion coefficient of the reductant, and ν is the scan rate. **(4.2)** allows the inference of the diffusion coefficient of A, or, alternatively, if this is already known, can allow the inference of the overall stoichiometry as that given by **(4.1)**.

Whilst **(4.2)** is very widely used to interpret voltammetry, it is very important to recognise that it applies exclusively to electrode reactions of a unity stoichiometry. Thus, for the general reaction,

$$aA - ne^- \rightleftarrows bB \qquad \textbf{(4.3)}$$

(4.3) is applicable for the case $a = b$. However, it is not valid for the frequent case of a **not** equal to b. as has recently been clarified both elegantly and definitively by Molina and colleagues [4]. Specifically, Molina et al highlight the fact that the peak currents in the case of electrode reactions of non-unity stoichiometry deviate markedly from the predictions of **(4.2)** with implications for the inference of electrode reaction mechanisms as well as for the reliability of quantitative inferences, for example of diffusion coefficients, if the equation is mis-applied.

One particularly important electrode reaction of non-unity stoichiometry is that of the oxidation of bromide ions

$$2Br^- - 2e^- \rightleftarrows Br_2 \qquad \textbf{(4.4)}$$

which is of importance in batteries, specifically redox flow batteries and electrochemical capacitors [5-10]. The reaction is complicated because of the following chemical reaction in which the bromine product combines reversibly with the bromide reactant to form the tribromide ion,

$$Br_2 + Br^- \rightleftarrows Br_3^- \qquad \textbf{(4.5)}$$

so that in the presence of a large excess of bromide the electrode process tends to the following limiting overall reaction

$$3Br^- - 2e^- \rightleftarrows Br_3^- \qquad \textbf{(4.6)}$$

The reaction is well studied in both aqueous and non-aqueous media (including acetic acid, acetonitrile, nitrobenzene and some room temperature ionic liquids [11-14]). In the case of aqueous

media the equilibrium constant is reported as $17\ M^{-1}$ at $25\ ℃$ [15] whilst the forward rate constant for reaction **(4.5)** is reported as $1.5 \times 10^9\ M^{-1}s^{-1}$.[16]

The purpose of this chapter is to explore the consequence of the follow up solution phase chemistry on the predicted voltammetry of the bromide oxidation system using both simulation and experiment. It concludes that with very special combinations of rate constants and voltage scan rates, two voltammetric peaks are discernible despite the occurrence of the sole electron transfer process given in **(4.4)**. However, comparison between simulations based on literature rate constants and equilibrium constants for **(4.5)** shows that the experimental voltammetry at a platinum electrode cannot be interpreted solely in terms of a mechanism based exclusively on the solution phase chemistry of the bromine/bromide/tribromide system.

4.2 Theory

We consider the electrochemically reversible, heterogeneous, one-electron oxidation of species A to B, followed by a homogeneous chemical reaction of A with B, as described in the introduction, with diffusion-only mass transport at a planar macro-electrode. We assume the presence of excess supporting electrolyte to suppress migration [17] and voltammetry on a sufficiently short timescale to avoid natural convection effects [18, 19] . The reaction scheme is:

$$\begin{gathered} 2A\ -\ 2e^- \rightleftarrows B \\ B + A \underset{k_b}{\overset{k_f}{\rightleftarrows}} C \end{gathered} \qquad \textbf{(4.7)}$$

The electrode kinetics are assumed to be described by the Butler Volmer theory of electrode kinetics [20, 21], and for the mechanism $2A - 2e^- \rightleftarrows B$,

$$j = k_0 \exp\left[\frac{\beta F}{RT}\left(E - E_f^0\right)\right]\left(\frac{c_A(0,t)}{[A]^0}\right)^2 - k_0 \exp\left[-\frac{\alpha F}{RT}\left(E - E_f^0\right)\right]\left(\frac{c_B(0,t)}{[A]^0}\right) \qquad \textbf{(4.8)}$$

where j is the net flux of the oxidant on the surface of the electrode, k_0 is the standard electrochemical rate constant, $c_A(0,t)$ and $c_B(0,t)$ are the concentrations of species A and B

on the surface of electrode at time t. Note that $[A]^0$ is a standard concentration, conventionally given the value of 1M , but as will become apparent below, for the purposes of the simulation reported it is more convenient to define the standard state as the bulk concentration of species A namely c_A^*. The quantities F, R, and T are the Faraday Constant, the Gas Constant and the absolute temperature respectively. α and β are the transfer coefficients, where usually, but not always, for a two-electron transfer process, $\alpha + \beta = 2$ at potentials close to equilibrium. In the following simulation the electrochemical rate constant, k_0, is made artificially high to ensure the process is Nernstian in character and hence independent of the values of α and β subject to their summing to 2.

Note that when the net flux is zero **(4.8)** reduces to the Nernst equation in which the standard concentration $[\quad]^0$ is defined to be 1 M, and the Nernst Equation can be written as

$$E = E_f^0(A/B) + \frac{RT}{F}\ln\left(\frac{\left(\frac{[B]}{[\quad]^0}\right)^{\frac{1}{2}}}{\frac{[A]}{[\quad]^0}}\right) \qquad \textbf{(4.9)}$$

However, if during simulation, the standard concentration is the bulk concentration of bromide, $[A]^0$, it is helpful to define a new formal potential and a new factor q is introduced as:

$$q = \frac{[A]^0}{[\quad]^0} \qquad \textbf{(4.10)}$$

So, the new formal potential, $E_f^{0\prime\prime}$, related to standard state $[A]^0$ is:

$$E = E_f^{0\prime\prime}\left(\frac{A}{B}\right) + \frac{RT}{F}\ln\left(\frac{\left(\frac{[B]}{[A]^0}\right)^{\frac{1}{2}}}{\frac{[A]}{[A]^0}}\right) \qquad \textbf{(4.11)}$$

$$= E_f^{0''}\ (A/B) + \frac{RT}{F}\ln\left(\frac{\left(\frac{[B]}{q[\ \ ]^0}\right)^{\frac{1}{2}}}{\frac{[A]}{q[\ \ ]^0}}\right)$$

$$= E_f^{0''}\ (A/B) + \frac{RT}{F}\ln\left(\frac{\left(\frac{[B]}{[\ \ ]^0}\right)^{\frac{1}{2}}}{\frac{[A]}{[\ \ ]^0}}\right) + \frac{RT}{F}\ln\left(q^{\frac{1}{2}}\right)$$

And,

$$E_f^0(A/B) = E_f^{0''}\ (A/B) + \frac{RT}{F}\ln\left(q^{\frac{1}{2}}\right) \qquad \textbf{(4.12)}$$

Hence the new formal potential of A/B couple becomes:

$$E^{0''}_f(A/B) = E_f^0(A/B) - \frac{RT}{F}\ln\left(q^{\frac{1}{2}}\right) \qquad \textbf{(4.13)}$$

4.3 Reaction model

The heterogeneous electrochemical reaction followed by homogeneous chemical reaction is simulated on a planar macroelectrode. The scale of the electrode is assumed to be significantly larger than the distance the species can diffuse during the timescale of simulation, hence the model is simplified to a one-dimensional system, and only diffusion perpendicular to the electrode surface is taken into consideration. Using Fick's second law of diffusion [22, 23], the diffusion equation can be expressed as:

$$\frac{\partial c_j}{\partial t} = D_j \frac{\partial^2 c_j}{\partial x^2} \qquad \textbf{(4.14)}$$

where j is the species under study, and D_j is the diffusion coefficient.

The variation in concentration of species in the solution phase can be simulated by considering Fick's second law of diffusion with second order homogeneous chemical reaction, when one A molecule and one B molecule react to form C reversibly. The process of the forward reaction, A and B forming C, is controlled by the rate constant k_f and the backward reaction is controlled by rate constant k_b.

$$\begin{cases} \frac{\partial c_A}{\partial t} = D_A \frac{\partial^2 c_A}{\partial x^2} - k_f c_A c_B + k_b c_C \\ \frac{\partial c_B}{\partial t} = D_B \frac{\partial^2 c_B}{\partial x^2} - k_f c_A c_B + k_b c_C \\ \frac{\partial c_C}{\partial t} = D_A \frac{\partial^2 c_C}{\partial x^2} + k_f c_A c_B - k_b c_C \end{cases} \quad \textbf{(4.15)}$$

To solve the differential equations, both temporal and spatial boundary conditions need to be specified. At the beginning of simulation, the bulk concentration of species A is set to c_A^*, with no B or C present in the system.

$$\begin{matrix} t = 0, x \geq 0 \\ t > 0, x = x_{sim} \end{matrix} \begin{cases} c_A = c_A^* \\ c_B = 0 \; and \; c_A^* \geq 0 \\ c_Y = 0 \end{cases} \quad \textbf{(4.16)}$$

where x_{sim} is the outer boundary for simulation, distant enough from the electrode that the concentration of each species equal to its bulk concentration. Thus, the boundary of simulation needs to be sufficiently far from the electrode that the reaction on the surface of the electrode would not affect the condition on the outer boundary. From Einstein's work on Brownian motion [24], in a one-dimensional system for a particle, $\sqrt{\langle x^2 \rangle} = \sqrt{2Dt_{sim}}$, which can be used to approximate the distance from the electrode that is unperturbed from the reaction on the electrode surface. So, the distance of outer boundary for simulation is chosen to be greater or equal to this:

$$x_{sim} = 6\sqrt{Dt_{sim}} \quad \textbf{(4.17)}$$

The boundary conditions at the surface of the electrode reflects the electrochemical activity of the species in the potential range of study [25] :

$$\begin{cases} D_A\left(\frac{\partial c_A}{\partial x}\right)_{x=0} = k_0 \exp\left[\frac{\beta F}{RT}\left(E - E_f^0\right)\right]\left(\frac{c_A(0,t)}{[A]^0}\right)^2 - k_0 \exp\left[-\frac{\alpha F}{RT}\left(E - E_f^0\right)\right]\left(\frac{c_B(0,t)}{[A]^0}\right) \\ D_B\left(\frac{\partial c_B}{\partial_x}\right)_{x=0} = -\frac{1}{2} D_A\left(\frac{\partial c_A}{\partial x}\right)_{x=0} \\ D_C\left(\frac{\partial c_C}{\partial x}\right)_{x=0} = 0 \end{cases} \quad \textbf{(4.18)}$$

where A and B are electro-active species and follow Butler-Volmer kinetics, whilst C is electrochemical inactive at the potential range under study, and thus has zero-flux at the electrode surface.

The dimensionless diffusion equation can be written as:

$$\begin{cases} \frac{\partial C_A}{\partial T} = d_A \frac{\partial^2 C_A}{\partial X^2} - K_f C_A C_B + K_b C_C \\ \frac{\partial C_B}{\partial T} = d_B \frac{\partial^2 C_B}{\partial X^2} - K_f C_A C_B + K_b C_C \\ \frac{\partial C_C}{\partial T} = d_A \frac{\partial^2 C_C}{\partial X^2} + K_f C_A C_B - K_b C_C \end{cases} \quad \textbf{(4.19)}$$

The boundary condition at the start of the simulation and at the surface of the electrode can be written in dimensionless form as:

$$\begin{matrix} T = 0, X \geq 0 \\ T > 0, X = X_{sim} \end{matrix} \begin{cases} C_A = 1 \\ C_B = 0 \\ C_Y = 0 \end{cases} \quad \textbf{(4.20)}$$

$$\begin{cases} \left(\frac{\partial C_A}{\partial X}\right)_{X=0} = K_0 \exp(\beta\theta)\ \left(C_A(0,T)\right)^2 - k_0 \exp(-\alpha\theta)\, C_B(0,T) \\ d_B\left(\frac{\partial C_B}{\partial X}\right)_{X=0} = -\frac{1}{2}\left(\frac{\partial C_A}{\partial X}\right)_{X=0} \\ d_C\left(\frac{\partial C_C}{\partial X}\right)_{X=0} = 0 \end{cases} \quad \textbf{(4.21)}$$

4.4 Simulation methods

Simulation was performed using home written C++ programs with *std::thread* for parallel computing running on an Intel Core i7 CPU. The differential equations were solved using the Newton-Raphson method [18] with at most eight iterations required for convergence. Graphs were plotted with Origin Pro 2019 and Python Matplotlib. Convergence studies were performed to and evaluated using various checks involving the magnitude of the peak currents and potentials and checking mass conservation[26-28]. The value of peak current and peak to peak separation matched with the values predicted by Molina's work [4].

4.5 Theoretical results

First simulations were made of a simple fully reversible $2A - 2e^- \rightleftarrows B$ process without any follow-up chemical reaction to permit comparison with the published work of Molina [3]. In particular, the simulation results were in quantitative agreement with Molina's work. Molina predicted that for such a process, the peak flux J in dimensionless form should be $J = 0.4995\sqrt{\sigma}$ and the peak to peak separation should be $42mV$ at 298 K, and in dimensionless form $\theta_{pp} = 1.6$. Figure 4.1 shows our simulation of a cyclic voltammogram at $\sigma = 1198$, corresponding to dimensional scan rate at 100 mV/s with dimensional parameters of $(\epsilon = 0.8mm, c_A^* = 5mM, c_B^* = 0mM, c_C^* = 0M,\ D_A = D_B = D_C = 2.08 \times 10^{-9}\ m^2/s)$. This set of dimensional parameters is used in the "Theoretical Results" section and the "Guidance to Experimentalists "section unless otherwise stated. The dimensionless peak flux was found to be 17.30, very close to Molina's prediction of 17.29[4] using the equation $J = 0.4995\sqrt{\sigma}$. Similarly, the dimensionless peak to peak separation, θ_{pp}, of the simulation voltammogram is 1.63, corresponding to 41.85 mV in dimensional form, also in excellent agreement with Molina. A similar level of accuracy was obtained for different dimensionless

scan rate in the range $\sigma = 0.1198$ to $\sigma = 119800$, corresponding to dimensional scan rate from $10^{-5}\ V/s$ to $10V/s$.

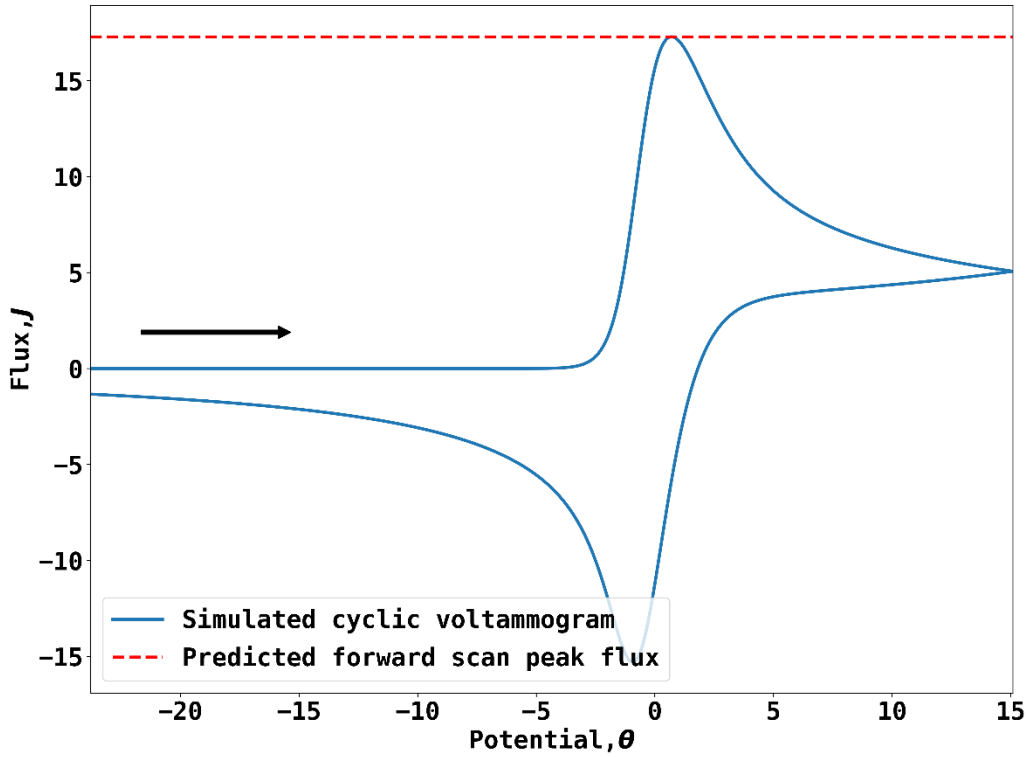

Figure 4.1. Cyclic voltammogram of a fast(reversible) electrochemical reaction at $\sigma = 1198$ of stoichiometry of 2:1, corresponding to $100mV/s$. The dashed red line is the predicted forward scan peak flux from Molina[4]. The forward scan peak flux is 17.30 and peak to peak separation,θ_{pp} is 1.63. The black arrow indicates the start and initial direction of potential sweep.

Next, we performed simulations on the two-electron oxidation process followed by homogeneous chemical reaction: $\begin{matrix} 2A\ -\ 2e^- \rightleftarrows B \\ B + A \rightleftarrows_{k_b}^{k_f} C \end{matrix}$.

Simulations were carried out on a range of parameters considering both reversible and irreversible electron transfer kinetics and varying degrees of the chemical reversibility of the chemical reaction. First, we consider reversible electron transfer.

With the follow up chemical reaction, a second peak can be observed in the voltammogram under certain conditions even though only a single electron transfer event is

modeled! To observe the second peak, some important conditions should be satisfied, as is next discussed.

First, the second peak can only be seen if $k_f > 0$ and $k_b > 0$. In contrast if the chemical reaction is fully irreversible, i.e., $k_f > 0$ and $k_b = 0$, the second peak cannot be observed. A simulation of a typical electrochemically reversible cyclic voltammetry at scan rate of $\sigma = 1198$, or 100 mV/s and a forward reaction rate constant, $K_f = 1.53 \times 10^9$, corresponding to $k_f = 10^9\ M^{-1}s^{-1}$ develops this hypothesis. As shown in Figure 4.2, for a reverse reaction rate constant, $K_b = 3.08 \times 10^7$, corresponding to dimensional form, $k_b = 10^5\ s^{-1}$ and if the chemical reaction is reversible, the second peak can be observed. But when $K_b = 0$, or $k_b = 0\ s^{-1}$, the second peak no longer appears. This behavior suggests that the presence of the second peak can only be seen when the chemical reaction is reversible, and is related to the backward chemical reaction, the decomposition of C to form A and B.

Since we ascribe the second peak to the dissociation of C formed during the oxidation of A to B on the voltammetric timescale, next simulations were made to explore more fully the conditions under which a second peak was visible.

Although the chemical reaction is required to be reversible to see the second peak, the electrochemical reaction can be either reversible (as above) or irreversible. For example, simulations were made when $K_0 = 0.1$, small enough to ensure irreversibility, with the dimensionless chemical reaction rate constants are $K_f = 1.53 \times 10^9$ and $K_b = 3.08 \times 10^7$ respectively, corresponding to $k_f = 10^9\ M^{-1}s^{-1}$ and $k_b = 10^5\ s^{-1}$. In Figure 4.3, the resulting voltammograms shows that for irreversible electrode kinetics, the second peak can still be observed at around $\theta = 14$.

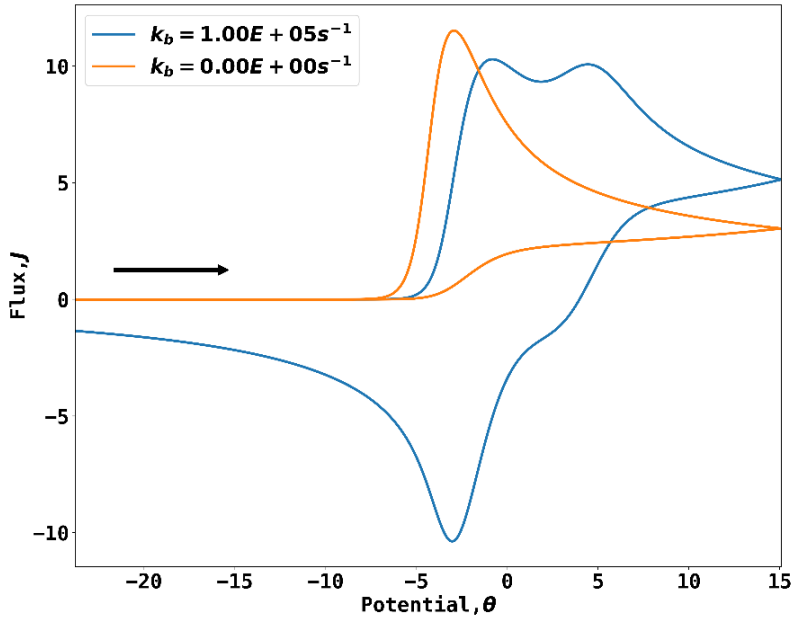

Figure 4.2. Simulated voltammetry showing that when $k_f = 10^9\ M^{-1}s^{-1}$ and $k_b = 10^5\ s^{-1}$, the second peak can observe (blue line). But when $k_f = 10^9\ M^{-1}\ s^{-1}$ and $k_b = 0$, the second peak cannot be observed (orange line). The dimensionless electrochemical rate constant is set to be $K_0 = 10^9$ in both cases. The black arrow indicates the start and initial direction of potential sweep.

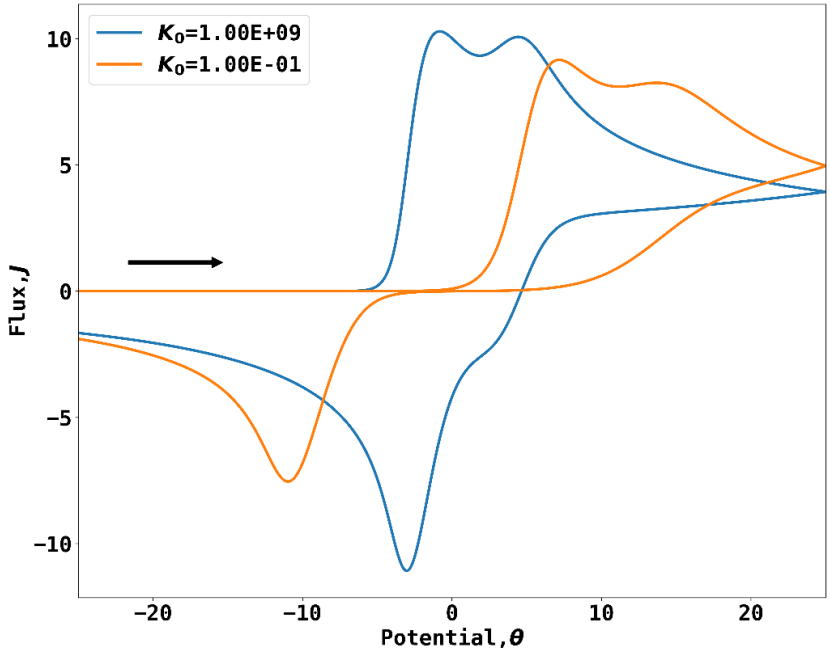

Figure 4.3. Simulated voltammetry showing that when $k_f = 10^9\ M^{-1}s^{-1}$ and $k_b = 10^5\ s^{-1}$, the electrochemical rate constant is varied from $K_0 = 10^9$ to $K_0 = 10^{-1}$ a second peaks can be observed in both cyclic voltammograms with fully reversible electrode kinetics($K_0 = 10^9$) and fully irreversible electrode kinetics($K_0 = 10^{-1}$).

Second, simulations were conducted to see the influence of the bulk concentration of A on the appearance or otherwise of the second peak. Simulations were performed at different c_A^* from $10^{-6}\ M$ to $10\ M$ at a scan rate $\sigma = 1198$, or $\nu = 0.1V/s$. The chemical rate constant modelled was $K_f = 1.53 \times 10^9$, corresponding to $k_f = 10^9\ M^{-1}s^{-1}$ and $K_{eq} = 500$,or $k_{eq} = 1e^5 M^{-1}$. As shown in Figure 4.4, the second peak appears at lower bulk concentration between $c_A^* = 0.1M$ to $c_A^* = 10^{-3}\ M$ around $\theta = 9$ and disappears as c_A^* increases to 1M and above or decreases to $10^{-4}M$ and below. From the simulations above we can conclude that the presence of the second peak also depends on the bulk concentration of species, and usually appears when the bulk concentration of A is neither too low nor too high. Lower concentrations of A facilitates the dissociation of C, but when the concentration drops below a threshold of around $10^{-4}\ M$, the amount of C generated during forward scan is too small to generate a second peak.

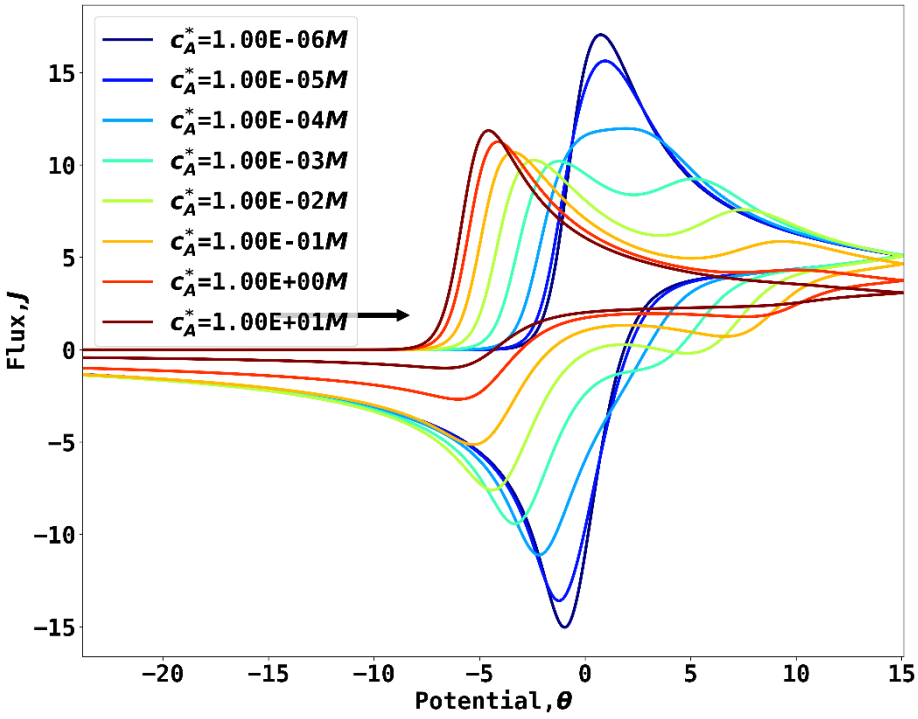

Figure 4.4. Simulations performed at different c_A^* from $10^{-6}\ M$ to 10M when k_{eq} is $10^5\ M^{-1}$. From the figure can be observed that the second peak appears at $\theta = 9$ when $c_A^* = 0.1\ M$ and disappears at higher bulk concentration. The black arrow indicates the start and initial direction of potential sweep.

Third, simulations were made to show that the peak can first appear and then disappear as the scan rate is changed. The scan rates analyzed were from $\sigma = 0.12$ to $\sigma = 1.2 \times 10^7$, corresponding to dimensional scan rate of $10^{-5}\ V/s$ to $10^3\ V/s$. A Standard electrochemical rate constant,K_0 is set to 10^9, or in dimensional form $k_0 = 1.3 \times 10^4\ mol\ m^{-2}\ s^{-1}$, large enough to ensure reversibility, and the chemical reaction rate constant $K_f = 1.53 \times 10^9$, or $k_f = 1 \times 10^9 M^{-1}s^{-1}$,and $K_{eq} = 500$, or $k_{eq} = 10^5 M^{-1}$ in dimensional form. As shown in Figure 4.5, by varying scan rate from very small to large, the second peak can first be seen at lower scan rate from $\sigma = 0.12$ to $\sigma = 1.2 \times 10^7$ at dimensionless potential around $\theta = 5$, but disappear when $\theta = 1.2 \times 10^6$ and higher. Note that the flux is normalized by dividing with the square root of scan rate.

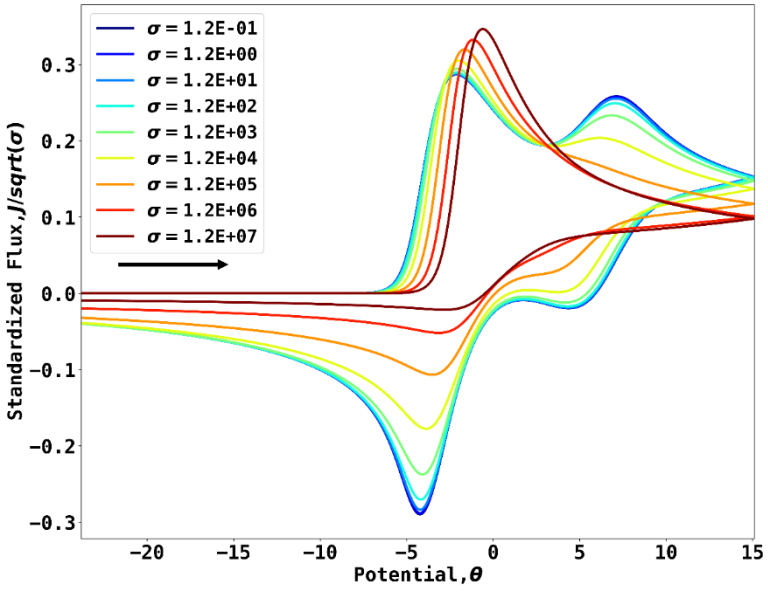

Figure 4.5. Simulated voltammetry showing that when $k_f = 10^9 M^{-1}s^{-1}$ and $k_{eq} = 10^5 M^{-1}$, second peak appears at low scan rate, but disappears when the scan rate increases to $\sigma = 1.2 \times 10^7$.The flux is normalized to the square root of scan rate. The black arrow indicates the start and initial direction of potential sweep.

Fourth simulations showed that the forward rate constant must be larger than a threshold value in order to see the second peak. During simulation, the forward reaction rate constants,

k_f, were varied from $10M^{-1}s^{-1}$ to $10^9M^{-1}s^{-1}$ while the equilibrium rate constant was set to $10^5\ M^{-1}$. As shown in Figure 4.6, at the range of study, forward scan peak height decreases and the forward scan peak shifts to a more reductive potential as k_f increases.

From k_f=$10^7\ M^{-1}s^{-1}$ and higher rate constants one can observe the second peak during forward scan at around $\theta = 5$. When k_f is increased, a second peak in the reverse scan can also be visualized. In conclusion; specifically, the second peak can be observed when the forward reaction rate constant is large enough than $10^7M^{-1}s^{-1}$.

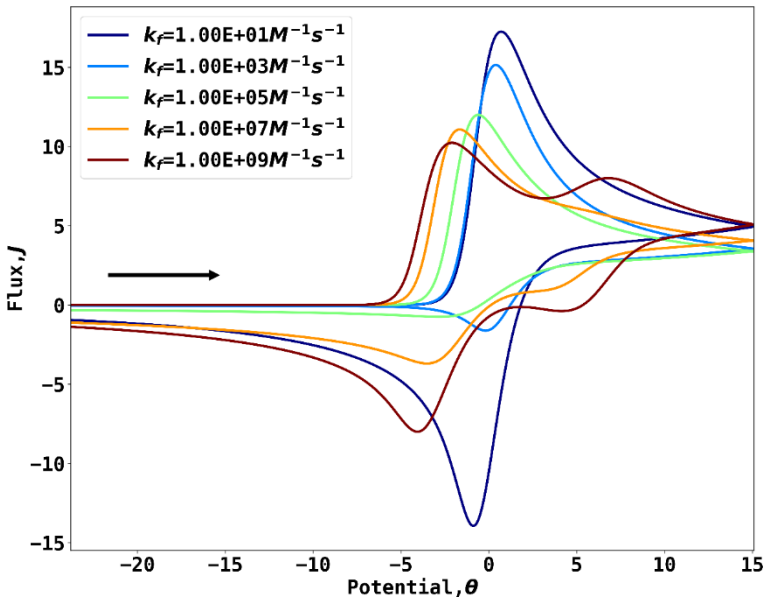

Figure 4.6. Voltammetry corresponding to Forward reaction rate constant k_f is simulated from $10M^{-1}s^{-1}$ to $10^9M^{-1}s^{-1}$ with the equilibrium constant k_f kept constant at 10^5M^{-1}. The black arrow indicates the start and initial direction of potential sweep.

4.5.1 Guidance to experimentalists

For fixed values of the forward and reverse rate constants of the following chemical reaction, it is possible to observe the second peak during experiment by altering ν,the scan rate and c_A^*, the bulk concentration of species A. A series of simulations were performed to by varying ν from $10^{-5}\ V/s$ to $10^3\ V/s$ and c_A^* from $10^{-6}\ M$ to $10^{2.5}\ M$ to show their joint

influence on the presence of the second peak and its peak height. The second peak was identified by locating the local maximum after the first peak, where the slope of the cyclic voltammogram equals zero. The simulations were performed with the following rate constants: $k_f = 1 \times 10^9 M^{-1}s^{-1}$,and $k_{eq} = 1 \times 10^3 M^{-1}$ in dimensional form Figure 4.7 shows the joint influence on the presence of second peak and its height is illustrated. The x axis and y axis represent the bulk concentration of species A and scan rate respectively. The third dimension, $J_{p,s}$ represents the peak height of the second peak in dimensionless standardized form. The peak height is standardized as $J_{p,s} = \frac{J_p}{\sqrt{\sigma}}$. If $J_{p,s}$ is 0, then no second peak can be found in the range of scanning. Figure 4.7 shows that the second peak tends to appear at lower scan rate as predicted above. But the influence of concentration at the second peak is more complicated. When the bulk concentration of species A is higher than $10^{-1.5}M$, the second peak is more visible at lower concentration and can reach a maximum of $J_{p,s} \approx 0.3$. But when concentration is below the threshold of $10^{-2}M$, the second peak can no longer be present. This can be explained by noting that at small c_A^*, not enough C species can be decomposed to form the second peak. In general, a second peak is most visible at low scan rate, and the bulk concentration of A is around 0.1 M.

4.5.2 Simulation of the bromine/bromide/tribromide system using literature kinetic data

According to the literature[29], the electrochemical oxidation of bromide to bromine can coincide with the reversible chemical reaction of bromine and bromide to form tribromide. The mechanism is shown:

$$\begin{aligned} 2Br^- - 2e^- &\rightleftarrows Br_2 \\ Br^- + Br_2 &\rightleftharpoons_{k_b}^{k_f} Br_3^- \end{aligned} \tag{22}$$

which fits the reaction model shown in **(4.7)**. Accordingly, simulations of the bromine/bromide/tribromide system in aqueous solution were made using literature rate and equilibrium constants.

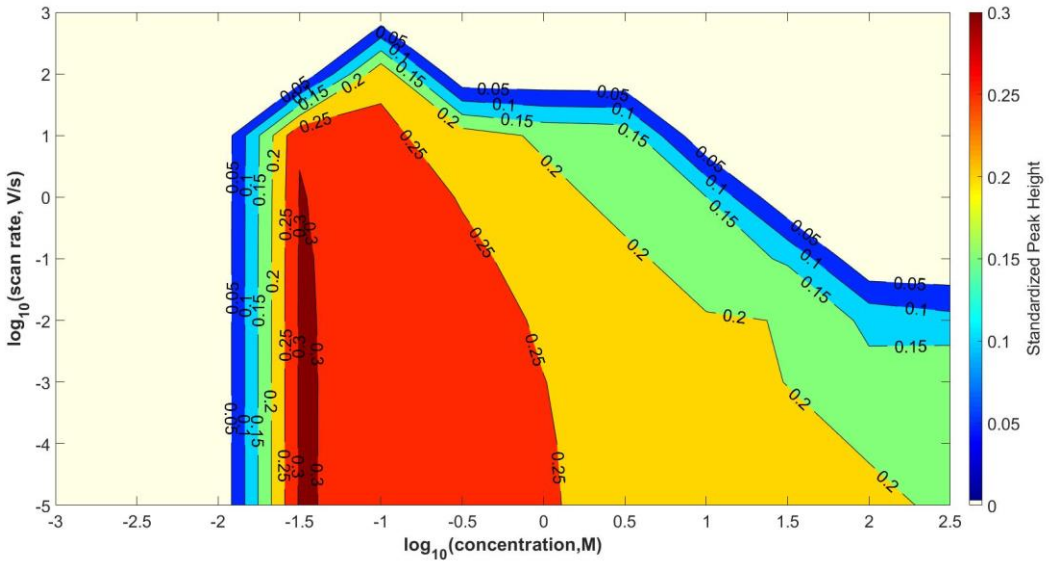

Figure 4.7. Two-dimensional plotting of the collective influence of bulk concentration of species A, c_A^* and scan rate on the presence and height of second peak. c_A^* is varied from $10^{-3}\ M$ to $10^{2.5}\ M$ with the scan rate varied from $10^{-5}\ V/s$ to $10^{3}\ V/s$. The contour plot shows the standardized peak height, and value of 0 means no second peak is observed. The area where the second peak is not present is in white color.

The forward reaction rate constants k_f and reverse reaction rate constant k_b in aqueous solution are reported to be $1.5 \times 10^9\ M^{-1}s^{-1}$ and $5 \times 10^7\ s^{-1}$ at 25 ℃ respectively as measured using the Temperature-Jump 2D IR spectroscopy technique[16]. These data are consistent with an independent measurement of the equilibrium constant of $17\ M^{-1}$ [16]. The measured diffusion coefficients of bromide and tribromide are reported with considerable precision and to be $2.08 \times 10^{-9}\ m^2/s$ and $1.145 \times 10^{-9}\ m^2/s$ respectively at 25℃ [30, 31].

The diffusion coefficient of bromide was confirmed by experiments shown later in this chapter. The diffusion coefficient of bromine is reported to be $1.18 \times 10^{-9}\ m^2/s$ at 25 ℃ [32].

The various dimensional parameters translate into dimensionless equivalents such as $K_f = 2.31 \times 10^9$ and $K_b = 1.54 \times 10^{10}$ with the dimensional parameters $(\epsilon = 0.8mm, c^*_{Br^-} = 5mM, c^*_{Br_2} = 0mM, c^*_{Br_3^-} = 0mM,\ D_{Br^-} = 2.08 \times 10^{-9}\, m^2/s,\ D_{Br_2} = 1.18 \times 10^{-9}\, m^2/s, D_{Br_3^-} = 1.145 \times 10^{-9} m^2/s)$. This set of dimensional parameters are used for simulation of bromine/bromide/tribromide system unless otherwise stated. At $\sigma = 1198$, corresponding to $0.1\, V/s$, the result of simulation is shown at Figure 4.8. No second peak can be observed in the voltammogram consistent with minimal generation of tribromide. The voltammogram shows that the forward scan peak flux is only very slightly lower (ca 2%) than Molina's prediction (red dashed line) for the bromide to bromine oxidation discounting the follow up chemical reaction. The slightly decreased peak flux can be attributed to a very small amount of competing chemical reaction of forming tribromide from bromine and bromide. The well-known Randles-Ševčík equation [2, 3] for the process $A - e \rightleftarrows B$ predicts a peak flux (green dashed line), almost 10 % lower than the simulation peak flux, suggesting that if the ordinary Randles-Ševčík equation derived for unity stoichiometry reaction used to analyse experimental data then this may lead to significant errors in inferred parameters such as concentrations or diffusion coefficients. This is explored experimentally by co-author Archana below.

We next predict the response of cyclic voltammetry at different bulk concentration of bromide. When $\sigma = 1198$, corresponding to dimensional scan rate of $100\, mV/s$, $c^*_{Br^-}$ is varied from $10^{-5}\, M$ to $10\, M$ and the results are shown in Figure 4.9. When $c^*_{Br^-}$ is smaller than $0.1M$, the voltammograms show a single peak corresponding to a simple two electron oxidation shown in Figure 4.1, indicating that the cyclic voltammetry is under the control of the electrochemical reaction.

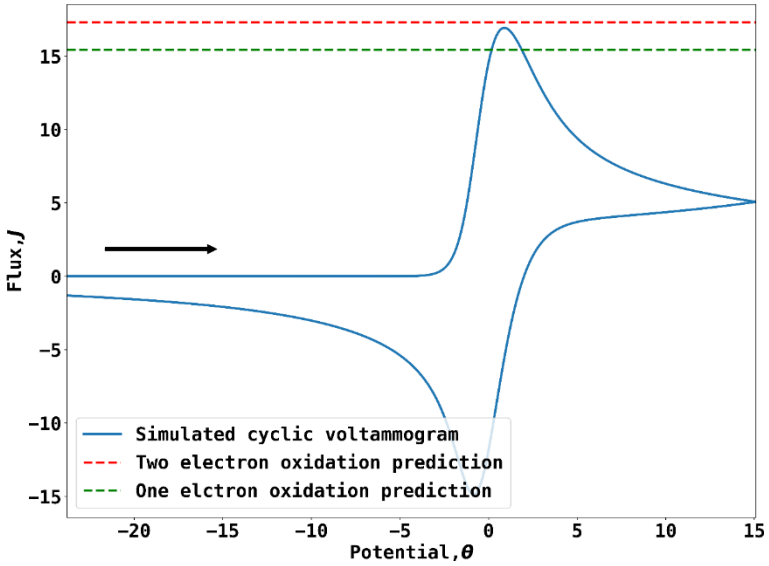

Figure 4.8. Simulation of a cyclic voltammogram at a dimensionless scan rate of $\sigma = 1198$, corresponding to a dimensional scan rate of 100 mV/s using the literature rate constants $k_f = 1.5 \times 10^9\ M^{-1}s^{-1}$ and $k_b = 5 \times 10^7\ s^{-1}$. The blue line is the simulated cyclic voltammogram, the red dashed line is the predicted flux from Molina considering no follow up chemical reactions[4] and the green dashed line represents the predicted peak flux from ordinary one-electron oxidation Randles-Ševčík equation[2, 3]. The black arrow indicates the start and initial direction of potential sweep.

As shown in Figure 4.9, increasing the bulk concentration of bromide above 0.1 M facilitates the competing chemical reaction of forming tribromide with bromine and bromide, and thus decreasing the peak flux of the first peak. The second peak appears as tribromide decomposes to bromine and bromide, and bromide is then oxidized. Hence, based on the voltammograms shown in Figure 4.9, at higher bulk concentration of bromide, usually higher than 1 M, one can observe the first peak with a reduced height and the presence of the second peak.

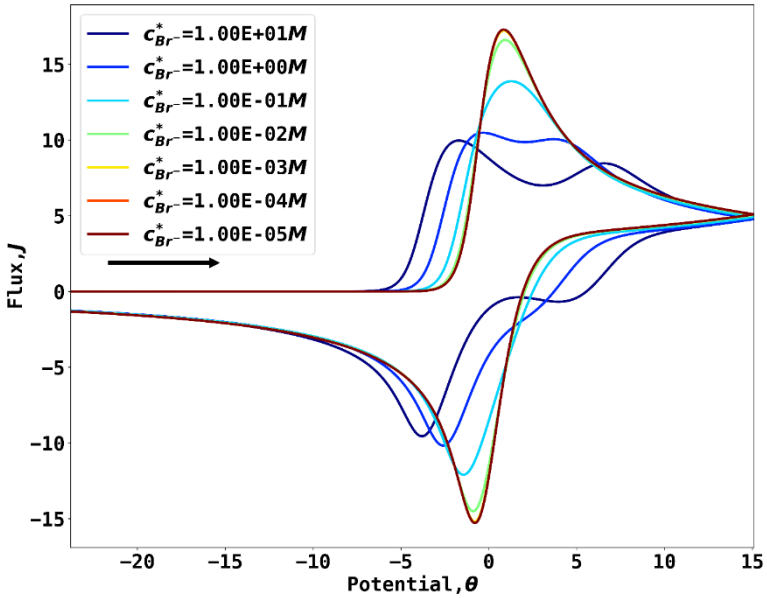

Figure 4.9. Voltammetry showing the effects of varying the bulk concentration of bromide from $10^{-5}\ M$ to $10\ M$ at scan rate of $100\ mV/s$. Second peak can be observed when $c^*_{Br^-}$ is larger than 1 M. The black arrow indicates the start and initial direction of potential sweep.

To observe the effect of altering the scan rate on the bromine/bromide/tribromide system, at two different bulk concentration of bromide ($5\ mM$ and $1\ M$), the scan rate is varied from $\sigma = 0.012$ to $\sigma = 1.2 \times 10^5$, corresponding to dimensional scan rate $10^{-6}\ V/s$ to $10\ V/s$. The chemical reaction rate constants k_f and k_b are the literature values mentioned above. In Figure 4.10 and Figure 4.11, when $c^*_{Br^-} = 5\ mM$ and $1\ M$ respectively, varying scan rate has no visible effect on the shape of the standardized voltammogram. Note that the dimensionless flux J, is standardized by dividing the flux with square root of dimensionless scan rate.

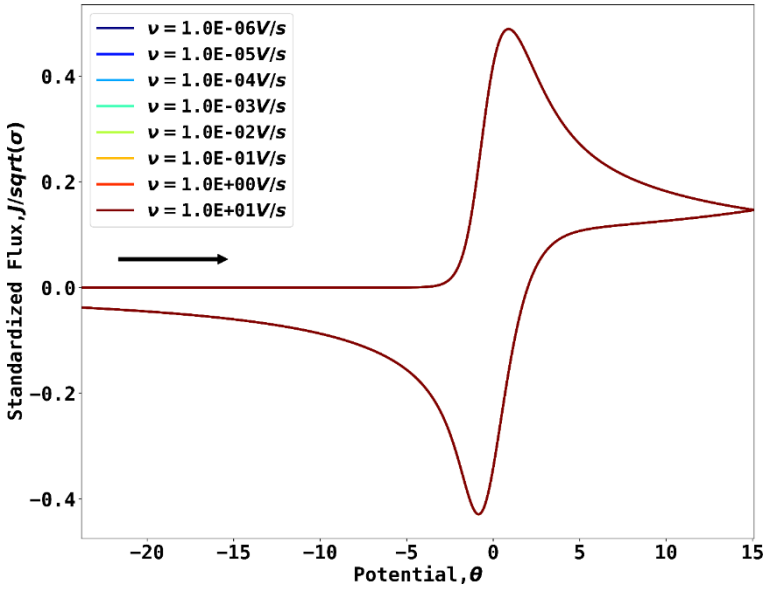

Figure 4.10. Voltammograms simulated to show the effect of varying the scan rate from $10^{-6}\ V/s$ to $10\ V/s$. When the bulk concentration of bromide is $5\ mM$, altering scan rate has no effect on the shape of standardized voltammogram: the second peak cannot be observed. Note that the flux is standardized against the square root of dimensionless scan rate. The black arrow indicates the start and initial direction of potential sweep.

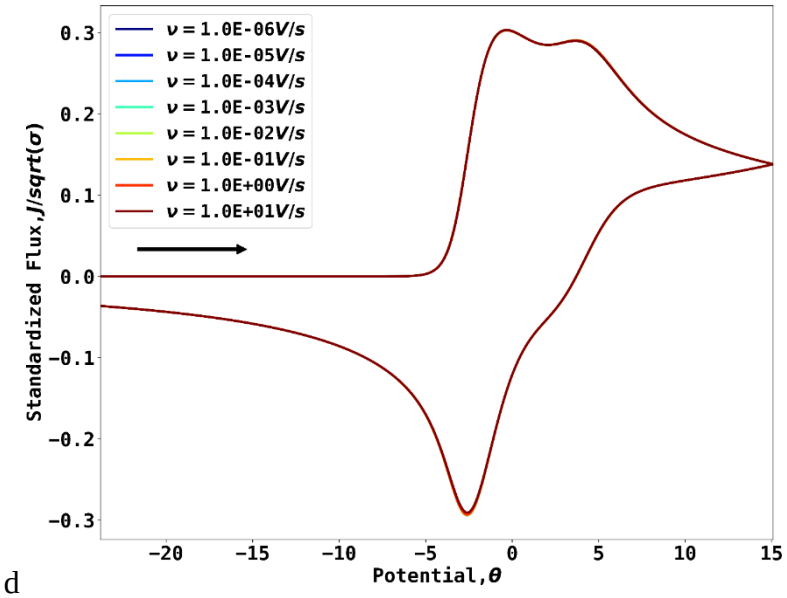

d

Figure 4.11. Voltammetry showing that varying the scan rate from $10^{-6}\ V/s$ to $10\ V/s$ when the bulk concentration of bromide is 1 M has no effect on the shape of standardized voltammogram. The second peak can be observed in this plot. The black arrow indicates the start and initial direction of potential sweep.

4.6 Experimental Results and Discussion

In the above, the voltammetry of the bromide oxidation in aqueous solution was predicted under conditions where the electron transfer was reversible and the follow up chemical reaction between bromide anions and bromine molecules leading to the formation of tribromide ions was characterised by the known equilibrium and rate constants for the reaction. In this section, we compare the predictions with experiment.

The experiment of bromide oxidation was performed by Ms. Archana K S Kumar and summarized here. First the diffusion coefficient of bromide in 0.1 $M\ HNO_3$ was determined to be $2.1 \times 10^{-9}\ m^2\ s^{-1}$ using steady-state voltammetry at a Pt microelectrode, which compares very well with the literature value of $2.08 \times 10^{-9}\ m^2\ s^{-1}$.

Then cyclic voltammetry of bromide was conducted in two potential windows: the first window was from 0.5 V to 1.05 V relative to SCE (Figure 4.12b) and the second wider window was from 0.5V to 1.3V relative to SCE (Figure 4.12a). Voltammetry of 5.0 mM of NaBr in 0.1 M HNO_3 conducted in the first potential window showed a peak potential of 0.95 V, attributed to the reaction:

$$2Br^- - 2e^- \rightleftarrows Br_2 \qquad \textbf{(4.22)}$$

The peak current at five different scan rates (0.02 V/s, 0.05 V/s, 0.1 V/s, 0.2 V/s, 0.4 V/s) was regressed with the square root of scan rates shown in the inset of Figure 4.12a, and the slope found to be $1.23 \times 10^{-4} \frac{A}{\sqrt{V/S}}$ after a tiny (<2%) baseline correction, which compares with a slope of $1.19 \times 10^{-4} \frac{A}{\sqrt{V/S}}$ predicted based on the simulations for the bromine/bromide/tribromide system. Note that in contrast the expected slope, on the basis of the Randles-Ševčík equation for a simple one electron oxidation, $A - e^- \rightleftarrows B$, is

$1.08 \times 10^{-4} \frac{A}{\sqrt{V/S}}$ whilst that for on the basis of Molina's equation [4] for $2A - 2e^- \rightleftarrows B$ (but without any following chemical reaction is $1.21 \times 10^{-4} \frac{A}{\sqrt{V/S}}$).

Interestingly when the voltammetry was extended to a wider potential window, a second wave with a peak potential of ca 1.2 V appeared. In the light of the simulations reported above and the concentrations and scan rates used it was clearly concluded that the origins of this second wave do **not** lie in the dissociation of tribromide ions exclusively in the solution phase on the voltammetric timescale. At present the origins of the second feature are unclear but are likely to reside in the neglect of adsorbed species in the above model [33].

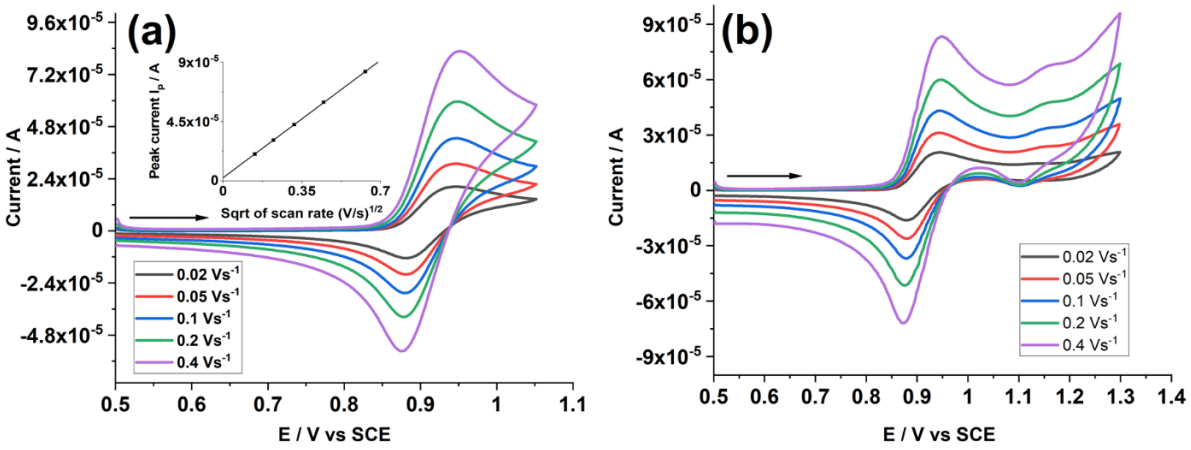

Figure 4.12. Cyclic voltammograms of 5 mM NaBr in 0.1 mM HNO_3 at Pt macro electrode of r = 0.75 mm as a function of scan rates. a) voltage scan range from 0.5 V to 1.05 V, inset; plot of oxidative peak current (I_p) vs square root of scan rate, b) voltage scan range from 0.5 V to 1.3 V. The black arrow indicates the start and initial direction of potential sweep. Plotted by Archana Kaliyaraj Selva Kumar.

4.7 Conclusions

The reaction $2A - 2e^- \rightleftarrows B$, of non-unity stoichiometry has been simulated under conditions of cyclic voltammetry at a macro-electrode. The effect of a follow up chemical reaction of the form $A + B \rightleftarrows C$ was specifically considered and shown, under certain critical

conditions of concentration and scan rate, to give rise to two voltammetric peaks where the second results from the dissociation of C. The modelling was later applied to the bromide oxidation system at platinum electrodes in aqueous solution with good quantitative agreement in respect of the first voltammetric wave, which is consistent with an electrochemically reversible oxidation forming molecular bromine, Br_2, with negligible tribromide formation. However, the model, which is based exclusively on solution phase species, does not correctly predict the appearance of the second wave as seen voltammetrically. This reflects the over-simplified nature of the model used and its neglect of the role of the adsorbed species. In the latter context we note the previous work of Conway and colleagues on the surface chemistry of bromine formation on platinum electrodes from bromide with the bromide ion strongly adsorbed on the surface [34].

Generically the interplay between simulations and experiments for the case of the oxidation of bromide has allowed clear mechanistic inferences (solution phase reaction vs. adsorbed reaction) to be drawn. When simulation and experiment are combined, the synergy created is enormous: simulations can produce new knowledge as experiments do, test the theory distilled from experiments, and communicate the results with a clear insight into complex systems.

Whilst this chapter has considered specifically the oxidation of bromide and its associated chemical reaction, the next chapter summarizes the influence of both preceding and follow-up coupled chemical reaction on the shapes and apparent transfer coefficients of voltammogram.

References

1. H. Chen, A. K. S. Kumar, H. Le and R. G. Compton, *J. Electroanal. Chem.*, 2020, **876**, 114730.
2. A. Ševčik, *Collect. Czech. Chem. Commun.*, 1948, **13**, 349-377.
3. J. E. B. Randles, *Trans. Faraday Soc.*, 1948, **44**, 327-338.
4. J. M. Gomez-Gil, E. Laborda and A. Molina, *Anal. Chem.*, 2020, **92**, 3728-3734.
5. K. Cathro, K. Cedzynska, D. Constable and P. Hoobin, *J. Power Sources*, 1986, **18**, 349-370.
6. D. J. Eustace, *J. Electrochem. Soc.*, 1980, **127**, 528.
7. S. J. Yoo, B. Evanko, X. Wang, M. Romelczyk, A. Taylor, X. Ji, S. W. Boettcher and G. D. Stucky, *J. Am. Chem. Soc.*, 2017, **139**, 9985-9993.
8. Q. Li, M. Haque, V. Kuzmenko, N. Ramani, P. Lundgren, A. D. Smith and P. Enoksson, *J. Power Sources*, 2017, **348**, 219-228.
9. K. S. Archana, R. pandiyan Naresh, H. Enale, V. Rajendran, A. V. Mohan, A. Bhaskar, P. Ragupathy and D. Dixon, *J. Energy Storage*, 2020, **29**, 101462.
10. F. Yu, L. Pang, X. Wang, E. R. Waclawik, F. Wang, K. K. Ostrikov and H. Wang, *Energy Storage Materials*, 2019, **19**, 56-61.
11. O. W. Kolling, *Transactions of the Kansas Academy of Science (1903-)*, 1970, **73**, 452-459.
12. G. D. Allen, M. C. Buzzeo, C. Villagrán, C. Hardacre and R. G. Compton, *J. Electroanal. Chem.*, 2005, **575**, 311-320.
13. R. Caminiti, M. Carbone, G. Mancini and C. Sadun, *J. Mater. Chem.*, 1997, **7**, 1331-1337.
14. T. Iwasita and M. C. Giordano, *Electrochim. Acta*, 1969, **14**, 1045-1059.
15. R. O. Griffith, A. McKeown and A. G. Winn, *Trans. Faraday Soc.*, 1932, **28**, 101-107.
16. M. F. Ruasse, J. Aubard, B. Galland and A. Adenier, *J. Phys. Chem.*, 1986, **90**, 4382-4388.
17. R. G. Compton and C. E. Banks, *Understanding voltammetry*, World Scientific, London, 3rd edn., 2018.
18. R. G. Compton, E. Laborda, E. Kaetelhoen and K. R. Ward, *Understanding voltammetry: simulation of electrode processes*, World Scientific London, 2nd edn., 2020.
19. J. K. Novev and R. G. Compton, *Curr. Opin. Electrochem.*, 2018, **7**, 118-129.
20. J. A. V. Butler, *Trans. Faraday Soc.*, 1924, **19**, 729-733.
21. T. Erdey-Grúz and M. Volmer, *Z. Phys. Chem.*, 1930, **150**, 203-213.
22. A. Fick, *Ann. Phys.*, 1855, **170**, 59-86.
23. A. Fick, *Lond. Edinb. Dubl. Phil. Mag.*, 1855, **10**, 30-39.
24. A. Einstein, *J Annalen der physik*, 1905, **17**, 549-560.
25. I. B. Svir, A. I. Oleinick and R. G. Compton, *Russ. J. Electrochem.*, 2003, **39**, 160-164.
26. E. Kätelhön and R. G. Compton, *Analyst*, 2015, **140**, 2592-2598.
27. E. Kätelhön and R. G. Compton, *Analyst*, 2016, **141**, 1154-1154.
28. E. Kätelhön and R. G. Compton, *Analyst*, 2015, **140**, 3290-3290.
29. P. Adanuvor, R. E. White and S. Lorimer, *J. Electrochem. Soc.*, 1987, **134**, 1450.
30. R. E. White and S. Lorimer, *J. Electrochem. Soc.*, 1983, **130**, 1096.
31. W. M. Haynes, *CRC handbook of chemistry and physics*, CRC press, 2014.
32. E. L. Cussler and E. L. Cussler, *Diffusion: mass transfer in fluid systems*, Cambridge university press, 2009.
33. J. Xu, N. S. Georgescu and D. A. Scherson, *J. Electrochem. Soc.*, 2014, **161**, H392.

34. B. E. Conway, Y. Phillips and S. Y. Qian, *J. Chem. Soc., Faraday Trans.*, 1995, **91**, 283-293.

Chapter 5 Tafel slopes and Coupled Chemical Reactions

This chapter develops the ideas of the previous chapter and analyzes more generally the influence of coupled chemical reaction on the Tafel slopes associated with electrochemically reversible reactions. The work has been published in the *Journal of Electroanalytical Chemistry*[1].

A general scheme for an electrochemically reversible one-electron electrode reaction containing both preceding and following coupled chemical kinetics is analysed in the light of simulation in the context of linear sweep voltammetry at a macro-electrode. In particular, we explore the influence of the coupled chemistry on the observed Tafel slope at potentials where it is influenced minimally by mass transport effects. In the absence of coupled chemistry, an apparent transfer coefficient of unity is observed, as expected for a simple electrochemically reversible one-electron process. However, the presence of a preceding chemical reaction serves to lower the apparent transfer coefficient markedly below unity; the coupled kinetics create the illusion of electrochemical irreversibility. In contrast, a following chemical reaction can give an apparent transfer coefficient in excess of unity creating a 'super-Nernstian' response. Thus, a full range of Tafel slopes, both below and above unity, characterize an intrinsically reversible reaction in the presence of coupled kinetics.

5.1 Introduction

The IUPAC definitions [2, 3] of the transfer coefficients, α and β, relating to the analysis of experimental current (I) – voltage (E) data are, in the case of electro-reductions and electro oxidations given respectively by:

$$\alpha = -\frac{RT}{F}\frac{d\ln I}{dE} \; and \; \beta = \frac{RT}{F}\frac{d\ln I}{dE} \qquad \textbf{(5.1)}$$

where T, R and F are temperature, the Gas Constant and the Faraday Constant respectively. As such the definition relates the two experimentally measurable quantities, I and E, and is independent of any presumed theoretical model of the electron transfer event. In this way the values inferred are entirely experimental and this feature contrasts with some earlier definitions, for example, [4] involving the overall number of electrons transferred, n, which pre-suppose the knowledge or inference of this quantity which may not be known or measurable, and inherently depends on the voltammetric timescale studied.

For a general multi-step fully electrochemically reduction process within the widely adopted Butler-Volmer formalism [5]:

$$A + ne \rightleftarrows B \qquad \textbf{(5.2)}$$

the Tafel slope,

$$\frac{d \ln I}{dE} = -\frac{RT}{F}\,(n' + \alpha_{RDS}) \qquad \textbf{(5.3)}$$

where n' is the number of electrons transferred prior to the rate determining step which has the transfer coefficient α_{RDS} presumed to be potential independent [6]. The implication of **(5.1)** and **(5.2)** is that the current rises exponentially with the applied potential. However, of course, concentration depletion of A at the electrode surface leads to a weaker than the expected exponential relationship and an apparent potential dependence of the transfer coefficient on potential if no correction is made for mass transport effects. For this reason, it has been recommended that analysis of the current-voltage curves of irreversible processes is confined to no more than ca 30% of the peak or limiting current [7]. Alternatively, for a uniformly accessible electrode, such as a rotating disc electrode, a mass transport correction can be applied to an irreversible process in the following form:

$$\ln\left[\frac{1}{I}-\frac{1}{I_{LIM}}\right]=-(n'+\alpha_{RDS})\frac{FE}{RT}+constant \qquad \textbf{(5.4)}$$

where I_{LIM} is the transport-limited current and from which it is seen that a plot of $\ln\left[\frac{1}{I}-\frac{1}{I_{LIM}}\right]\ vs\ E$ generates a value of $n'+\alpha_{RDS}$. The corresponding plot applied to an electrochemically reversible one electron process system gives a slope of $\left(\frac{F}{RT}\right)$ and an *apparent* transfer coefficient of unity [8].

Simple Butler-Volmer (BV) theory assumes that the transfer coefficients are potential-independent and for n=1, sum to unity as $\alpha+\beta=1$, [5, 9] so effective mass transport correction is essential if experimental data is to be successfully analysed from the Butler-Volmer perspective [10]**.** Note that the sum of the two transfer coefficients to unity is a consequence of the Principle of Microscopic Reversibility [11] and so strictly only holds at a specific potential. In the case of quasi-reversible voltammograms where the reductive and oxidative peaks may occur at significantly different potential, there is no strict requirement that $\alpha+\beta=1$ since the two transfer coefficients are measured at different potentials.

The Marcus-Hush (MH) theory [12-14] of simple one-electron transfer suggests by geometrical consideration of the activation energy expected from the intersecting parabolic Gibbs energy curves of the reactants, $A+e$, and the product B, that the transfer coefficient is weakly dependent on the electrode potential. In the so-called symmetrical form of MH theory where the reactant and product Gibbs energy curves are presumed to have an identical curvature, then:

$$\alpha(E)=\frac{1}{2}\left(1+\frac{\Delta G}{\lambda}\right)=\frac{1}{2}+\frac{F\left(E-E_f^0\right)}{2\lambda} \qquad \textbf{(5.5)}$$

where λ is the reorganization energy and ΔG is the Gibbs energy. In the limit of a large reorganization energy, λ, the transfer coefficient tends to 0.5. In the asymmetric form [15] of MH

theory, the assumption of equal curvature is relaxed reflecting a greater approximation to reality and deviations from $\alpha = 0.5,$ reflect in part the difference in force constants relating to vibrations within the solvated A and B species. A notable example is the one electron reduction:

$$O_2 + e^- \rightleftarrows O_2^- \qquad \textbf{(5.6)}$$

which in various non-aqueous solvents shows reductive transfer coefficients markedly less than 0.5 and are attributed the weaker vibration within the superoxide anion as compared to di-oxygen [16] reflecting, in turn, the change in bond strength.

Experimentally curved Tafel plots (of $\ln I \ vs \ E$), or, equivalently, a potential dependence of the transfer coefficient is generally thought to indicate a breakdown of BV theory and to be evidence per se of the veracity of MH theory. Without disputing the benefits and insights of MH theory, the purpose of the present chapter is to explore via simulation an alternative origin of curved Tafel plots. In particular we build on our recent insight[17] that homogeneous chemical kinetics coupled to a reversible (Nernstian) electron transfer can produce 'super-Nernstian' Tafel slopes as inferred from linear sweep voltammograms. Specifically, whist **(5.1)** applies to a fully electrochemically reversible simple one electron process in the absence of any coupled kinetics predicts a Tafel slope consistent with an apparent transfer coefficient of unity, in the presence of second order following kinetics (an $E_{rev}C_2$ process) curved Tafel plots are simulated. Hence potential dependent transfer coefficients are inferred which could, dependent on conditions, be markedly greater than unity. Accordingly, we seek to generalize and now consider both preceding and following chemical reactions in a general scheme:

$$\begin{cases} X \rightleftarrows A \ or \ \boldsymbol{X} \rightleftarrows A + C \\ A + e \rightleftarrows B \\ B \rightleftarrows C \ or \ 2B \rightleftarrows C \end{cases} \qquad \textbf{(5.7)}$$

in which the electron transfer is constrained to be fully electrochemically reversible ('Nernstian') in character. As such any curvature of the Tafel plots as revealed by a deviation of the inferred transfer coefficient from unity is *necessarily* due to the presence of the coupled kinetics providing the analysis is made in the absence of significant mass transport effects and hence has no implications for the BV versus MH theory comparison. However, an important inference is that curved Tafel plots in themselves do not necessarily invalidate BV theory unless there are reasons to definitively preclude any coupled kinetics. Specifically, in the following we demonstrate that whilst following homogeneous chemical kinetics can cause seemingly super-Nernstian behaviour (apparent transfer coefficient > unity), preceding chemical kinetics can cause a fully reversible process to show sub-Nernstian responses (apparent transfer coefficient < unity) even in those portions of the IE curve where mass transport effects can be rigorously ruled out by means of simulation. In particular the curved Tafel plots for the CE processes, which despite the defined reversible character of the electron transfer, show values of the apparent transfer coefficient tending to 0.5, might without further investigation be attributed to an irreversible process showing Marcusian behaviour. Such a preceding chemical reaction might realistically arise from dehydration/hydration steps or chemical dissociation prior to electron transfer.

5.2 Theory

This study focuses primarily on the electrochemically reversible, one-electron reduction of species A to B, with preceding/following chemical reactions. A macro-electrode with a planar geometry is considered. By assuming the scale of the electrode is significantly larger than the distance the species can diffuse during the timescale of the simulation, the model can be simplified to one-dimension (x) and so only needs to consider diffusion perpendicular

to the surface of electrode. The system is assumed to be free of natural convection or migration, and thus diffusion is considered as the exclusive means of mass transport. Using Fick's Second Law of diffusion, the diffusion equation can be expressed as:

$$\frac{\partial c_j}{\partial t} = D_j \nabla^2 c_j = D_j \frac{\partial^2 c_j}{\partial x^2} \tag{5.8}$$

Though the electrochemical reaction can be preceded or followed with homogeneous chemical reaction, the electrochemical reaction can be described in the same manner for all the reaction schemes mentioned in this chapter. The electrode kinetics are, by hypothesis, described with the Butler-Volmer theory of electrode kinetics:

$$j_{BV} = k_0 \exp\left[\frac{-\alpha F\left(E - E_f^0\right)}{RT}\right] c_A(0,t) - k_0 \exp\left[\frac{(1-\alpha) F\left(E - E_f^0\right)}{RT}\right] c_B(0,t) \tag{5.9}$$

and j_{BV} is the net flux of the reductant on the electrode surface using Butler-Volmer kinetics. k_0 is the standard electrochemical rate constant, α and β are the transfer coefficients, with $c_A(0,t)$ and $c_B(0,t)$ as the concentration of species A and B (see **(5.7)**) at the surface of electrode at any time t. E_f^0 is the formal potential and E is the potential to be varied during linear sweep voltammetry. For a typical reduction-oxidation voltammetry, the potential E at time t during a cyclic voltammetry is:

$$\begin{cases} 0 < t < t_{switch}, E = E_i - \nu t \\ t = t_{switch}, E = E_v \\ t_{switch} < t \leq 2t_{switch}, E = E_V + \nu(t - t_{switch}) \end{cases} \tag{5.10}$$

where E_i is the starting potential of forward scan, t_{switch} is time to start the reverse scan at potential E_V and ν is the scan rate. In the following, when considering electrochemically 'reversible' processes, extremely large values of k_0 ($> 100\ cm/s$) are employed to ensure full reversibility as evidence by the insensitivity of the results to the choice of transfer coefficients.

We now consider various sub-cases of the general scheme **(5.7)** which will show the full range of Tafel behaviour possible for a reversible $A + e \rightleftarrows B$, which in this chapter, includes the CE reaction, the dissociative CE reaction, the EC reaction and the EC_2 reaction. The 'dissociative CE reaction' has a preceding chemical reaction which is dissociative forming two species from one, as $X \rightleftarrows A + C$, prior to A being reduced. The C and E notation is due to Testa and Reinmuth[18, 19] where 'C' and 'E' stand for chemical and electrochemical reactions respectively. If C is placed before E, it means the product of the chemical reaction later reacts electrochemically and vice versa. The subscript of C standards for the order of the chemical reaction so that EC_2 denotes a second order chemical reaction following an electron transfer.

To solve the differential equations for the diffusion of the different species requires specifying the temporal and spatial boundary conditions. The bulk concentration of species varies from cases to cases, but outer spatial boundary of simulation, x_{sim}, is invariably made distant enough from the electrode (located as $x = 0$) that the concentrations at the outer boundary are unperturbed by the electrochemical reaction and chemical reaction during the time scale of simulation. Deriving from Einstein's work [20] on Brownian motion for the root mean squared distance diffused by a particle in time t is $\sqrt{2Dt}$ and can be used to determine the distance unperturbed by the interfacial electrochemical reaction. Accordingly, if t_{sim} is the time duration of scanning the voltammetric peak of interest. In this work, the distance of outer spatial boundary is chosen [21] to be:

$$x_{sim} = 6\sqrt{Dt_{sim}} \qquad \textbf{(5.11)}$$

The spatial boundary condition at $x = 0$ is given by **(5.9)** and **(5.10)** as discussed above. The following subsections describe the boundary conditions and diffusion equations to be solved for each sub-case.

5.2.1 CE reaction

The CE reaction scheme defines a one-electron reduction reaction which is preceded by a simple first order chemical reaction as:

$$\begin{cases} \boldsymbol{X} \underset{k_b}{\overset{k_f}{\rightleftarrows}} A \\ A + e \rightleftarrows B \end{cases} \tag{5.12}$$

The diffusion equations with first order chemical reaction are:

$$\begin{cases} \dfrac{\partial c_{\boldsymbol{X}}}{\partial t} = D_{\boldsymbol{X}} \dfrac{\partial^2 c_{\boldsymbol{X}}}{\partial x^2} - k_f c_{\boldsymbol{X}} + k_b c_A \\ \dfrac{\partial c_A}{\partial t} = D_A \dfrac{\partial^2 c_A}{\partial x^2} + k_f c_{\boldsymbol{X}} - k_b c_A \\ \dfrac{\partial c_B}{\partial t} = D_B \dfrac{\partial^2 c_B}{\partial x^2} \end{cases} \tag{5.13}$$

The boundary conditions for the bulk concentrations are:

$$\begin{matrix} t = 0, x \geq 0 \\ t > 0, x = x_{sim} \end{matrix} \begin{cases} c_{\boldsymbol{X}} = c_{\boldsymbol{X}}^* \\ c_A = c_{\boldsymbol{X}}^* \dfrac{k_f}{k_b} \\ c_B = 0 \end{cases} \tag{5.14}$$

Note the pre-equilibrium of X and A is assumed prior the start of the voltammetric sweep.

The boundary conditions at the surface of electrode are:

$$\begin{cases} D_{\boldsymbol{X}} \left(\dfrac{\partial c_{\boldsymbol{X}}(x,t)}{\partial x} \right)_{x=0} = 0 \\ D_A \left(\dfrac{\partial c_A}{\partial x} \right)_{x=0} = j_{BV} \\ D_B \left(\dfrac{\partial c_B}{\partial x} \right)_{x=0} = -j_{BV} \end{cases} \tag{5.15}$$

5.2.2 Dissociative CE reaction

The dissociative CE scheme defines a one-electron reduction preceded by dissociative chemical reaction:

$$\begin{cases} \boldsymbol{X} \rightleftarrows_{k_b}^{k_f} A + C \\ A + e \ \rightleftarrows B \end{cases} \tag{5.16}$$

The diffusion equations with second order chemical reactions are:

$$\begin{cases} \dfrac{\partial c_{\boldsymbol{X}}}{\partial t} = D_{\boldsymbol{X}} \dfrac{\partial^2 c_{\boldsymbol{X}}}{\partial x^2} - k_f c_{\boldsymbol{X}} + k_b c_A c_C \\ \dfrac{\partial c_A}{\partial t} = D_A \dfrac{\partial^2 c_A}{\partial x^2} + k_f c_{\boldsymbol{X}} - k_b c_A c_C \\ \dfrac{\partial c_B}{\partial t} = D_B \dfrac{\partial^2 c_B}{\partial x^2} \\ \dfrac{\partial c_C}{\partial t} = D_C \dfrac{\partial^2 c_C}{\partial x^2} + k_f c_{\boldsymbol{X}} - k_b c_A c_C \end{cases} \tag{5.17}$$

Note the pre-equilibrium of $\boldsymbol{X}$, A and C is assumed prior the start of the voltammetric sweep.

The boundary conditions for the bulk concentrations are:

$$\begin{matrix} t = 0, x \geq 0 \\ t > 0, x = x_{sim} \end{matrix} \begin{cases} c_{\boldsymbol{X}} = c_{\boldsymbol{X}}^* \\ c_A = \sqrt{c_{\boldsymbol{X}}^* \dfrac{k_f}{k_b}} \\ c_B = 0 \\ c_C = \sqrt{c_{\boldsymbol{B}}^* \dfrac{k_f}{k_b}} \end{cases} \tag{5.18}$$

The boundary conditions at the surface of electrode are:

$$\begin{cases} D_X\left(\frac{\partial c_X}{\partial x}\right) = 0 \\ D_A\left(\frac{\partial c_A}{\partial x}\right) = j_{BV} \\ D_B\left(\frac{\partial c_B}{\partial x}\right) = -j_{BV} \\ D_C\left(\frac{\partial c_C}{\partial x}\right) = 0 \end{cases} \quad \textbf{(5.19)}$$

5.2.3 EC reaction

The EC reaction scheme defines a one-electron reduction reaction followed by a first order chemical reaction:

$$\begin{cases} A + e^- \rightleftarrows B \\ B \overset{k_f}{\underset{k_b}{\rightleftarrows}} C \end{cases} \quad \textbf{(5.20)}$$

The diffusion equations with first order follow-up chemical reaction can be described as:

$$\begin{cases} \frac{\partial c_A}{\partial t} = D_A \frac{\partial^2 c_A}{\partial x^2} \\ \frac{\partial c_B}{\partial t} = D_B \frac{\partial^2 c_B}{\partial x^2} - k_f c_B + k_b c_c \\ \frac{\partial c_C}{\partial t} = D_C \frac{\partial^2 c_C}{\partial x^2} + k_f c_B - k_b c_C \end{cases} \quad \textbf{(5.21)}$$

The boundary conditions for the bulk concentrations are:

$$\begin{matrix} t = 0, x \geq 0 \\ t > 0, x = x_{sim} \end{matrix} \begin{cases} c_A = c_A^* \\ c_B = 0 \\ c_C = 0 \end{cases} \quad \textbf{(5.22)}$$

The boundary conditions at the surface of electrode are:

$$\begin{cases} D_A\left(\frac{\partial c_A}{\partial x}\right)_{x=0} = j_{BV} \\ D_B\left(\frac{\partial c_B}{\partial x}\right)_{x=0} = -j_{BV} \\ D_C\left(\frac{\partial c_C}{\partial x}\right)_{x=0} = 0 \end{cases} \quad \textbf{(5.23)}$$

5.2.4 EC_2 reaction

The EC_2 reaction comprises a one-electron reduction reaction followed by second order chemical reaction:

$$\begin{cases} A + e \rightleftarrows B \\ 2B \overset{k_f}{\underset{k_b}{\rightleftarrows}} C \end{cases} \quad \textbf{(5.24)}$$

The corresponding diffusion equations with second order follow-up chemical reaction are:

$$\begin{cases} \frac{\partial c_A}{\partial t} = D_A \frac{\partial^2 c_A}{\partial x^2} \\ \frac{\partial c_B}{\partial t} = D_B \frac{\partial^2 c_B}{\partial x^2} - k_f c_B^2 + 2k_b c_C \\ \frac{\partial c_C}{\partial t} = D_C \frac{\partial^2 c_C}{\partial x^2} + \frac{1}{2} k_f c_B^2 - k_b c_C \end{cases} \quad \textbf{(5.25)}$$

The boundary conditions for the bulk concentrations are:

$$\begin{matrix} t = 0, x \geq 0 \\ t > 0, x = x_{sim} \end{matrix} \begin{cases} c_A = c_A^* \\ c_B = 0 \\ c_C = 0 \end{cases} \quad \textbf{(5.26)}$$

The boundary conditions at the surface of electrode are:

$$\begin{cases} D_A\left(\frac{\partial c_A}{\partial x}\right)_{x=0} = j_{BV} \\ D_B\left(\frac{\partial C_B}{\partial x}\right)_{x=0} = -j_{BV} \\ D_C\left(\frac{\partial c_C}{\partial x}\right)_{x=0} = 0 \end{cases} \quad \textbf{(5.27)}$$

5.2.5 Dimensionless parameters

Dimensionless parameters are used for simulation for the advantages of generality and simplicity. In other words, if certain dimensional parameters change, there is no need to re-run the simulation but all that is required is to just convert the dimensionless voltammogram generated from simulation to dimensional form with the new dimensional parameters. Definition of dimensionless parameters can be found in Chapter 2. The definition of 1st and 2nd order rate constants are illustrated in Table 5.1.

Table 5.1 List of definitions of dimensionless parameters for planar electrode simulations. c_j is the concentration of any species j and c_{ref} is the concentration of the reference species. c^*_{ref} and D_{ref} are the bulk concentration and diffusion coefficients of reference species ref. ϵ is the radius of planar electrode, assumed to be the flat surface of a circular disc.

Dimensionless Parameter	Definition
Homogeneous chemical Rate Constant, First Order	$K_{1st} = \frac{k_{1st}\epsilon^2}{D_{ref}}$
Homogeneous chemical Rate Constant, Second Order	$K_{2nd} = \frac{k_{2nd}c^*_{ref}\epsilon^2}{D_{ref}}$

5.3 Simulation Methods

The simulations are performed using self-written C++ programs with *std::thread* for parallel computing. The non-linear diffusion equations are solved using finite difference

method by discretizing the diffusion equations into an expanding space grid [22] and backward implicit method [6] as stated in Chapter 2. The resulting multi-diagonal sparse matrix is then solved using the root-finding Newton-Raphson algorithm for at least 8 iterations until the average error is smaller than 10^{-8}. The resulting voltammograms and Tafel plots are plotted using Python Matplotlib and Origin Pro.

5.4 Results and Discussion

To investigate the effect of preceding or following chemical reaction on the voltammetric Tafel slope in the four models mentioned above, numerical simulations of cyclic voltammetry are performed and are reported below. The study focuses primarily on reversible electrode kinetics, for the reasons clarified above, so the electrochemical rate constant is set fast enough to ensure reversibility. In the following simulations, K_0 is set to 10^9, corresponding to $k_0 > 100\ m/s$ for a circular disk electrode of area $1\ cm^2$, and diffusion coefficients of $10^{-9}\ m^2/s$, corresponding to typical experimental conditions for aqueous macro-electrode voltammetry, and the resulting voltammograms are insensitive to the value of k_0. During simulations, the diffusion coefficients of all species are fixed at $10^{-9}\ m^2/s$ and the concentration of reference species at $1\ mM$ for generality. The flux is shown in standardized form by dividing dimensionless flux, J, with the square root of dimensionless scan rate, $\sqrt{\sigma}$ so that voltammograms are more readily comparable at different scan rates. To investigate the apparent transfer coefficient at different potentials on the voltammogram, the values of α are calculated using the following expression:

$$\alpha = \lim_{\Delta\theta \to 0} \frac{\ln J_{(\theta+\Delta\theta)-} \ln J_\theta}{\Delta\theta} \qquad \textbf{(5.28)}$$

In Tafel plots, the range of transfer coefficient to be analysed is from 5% to 30% of the forward peak current so as to mostly, but not fully, exclude the effects of mass transfer [7]. The

voltammograms and Tafel plots of the four models are also compared with the voltammogram and Tafel plot of a simple one-electron reduction in each case. When plotting the Tafel slopes, the starting potential, corresponding to 5% of the peak current, of the Tafel plots are adjusted to $\theta = 0$ to make Tafel plots, usually had different range of potential, to be comparable. The Tafel plots for a simple E process in each case allow the inference of the chemical kinetics, often significant, to be clearly demarked from that of the residual effects of mass transport/concentration depletion.

5.4.1 CE reaction: Voltammograms and Tafel Slopes

When CE processes are studied by experimental scientists, it is usual that, as presumed below, the preceding chemical reaction, $X \rightleftarrows_{k_b}^{k_f} A$ favours the reactant $\boldsymbol{X}$. Otherwise if the preceding chemical reaction largely favours the product A, the situation can be simplified to a one-electron reduction problem with no need to consider the preceding chemical reaction. During simulations, the forward and reverse chemical reaction rate constants are set to $k_f = 10^4\ s^{-1}$ and $k_b = 10^9\ s^{-1}$ respectively so that $k_{eq} = 10^{-5}$. The concentration of reference species, X is set to $1\ mM$. Figure 5.1 shows the voltammograms simulated at different scan rate from $1\ mV/s$ to $10^5\ mV/s$.

Figure 5.1 shows that the effect of preceding chemical reaction is to introduce over-potential into the voltammetry and the voltammogram shifts to more negative potentials as compared to a simple reversible electrode electron transfer. Also, the peak current, scaled with square root of scan rate, decreases and the peak becomes less well defined and a tendency to a limiting current, rather than a peak, develops. This is expected as the process shifts to being under full kinetic control where the limiting current reflects the rate of dissociation of X.

Figure 5.2 shows Tafel plots from 5% to 30% of peak current, which shows that faster scan rates lead to lower Tafel plots. Also shown is the response of a simple E process where the deviation from unity reflects solely the consequences of reactant depletion at the electrode surface. Thus, even restricting the range of the voltammograms analysed to the 5% to 30% range does not fully exclude mass transport effects. At slower scan rates, the Tafel plots for the CE voltammetry approximates the Tafel plots of the one-electron reduction, but in all cases the effect of the preceding chemical reaction is to decrease the Tafel slope below the ideal value close to unity expected for a simple electron transfer thus giving the illusion of an electrochemically irreversible electron transfer.

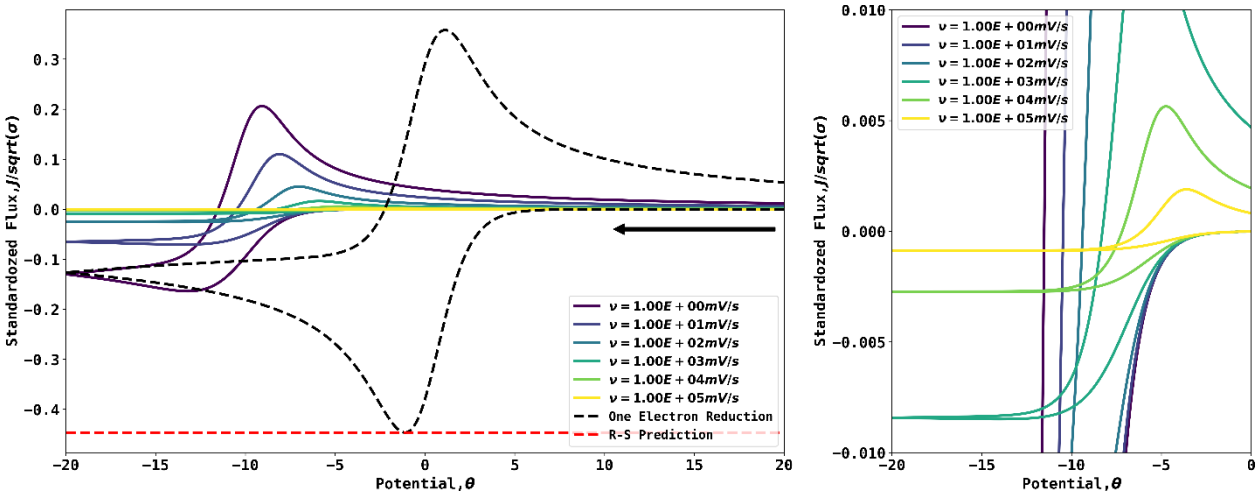

Figure 5.1. Left: voltammograms of CE reaction at scan rates from 1 mV/s to 10^5 mV/s. The voltammogram in black-dashed line is the one-electron reduction reference voltammogram. The red-dashed line is the peak flux predicted Randles-Ševčík equation for one-electron reduction. The Y-axis represents the standardized flux by dividing dimensionless flux, J with square root of scan rate, $\sqrt{\sigma}$. The black arrow indicates the start potential and initial direction of voltammetry. Right: Zoom-in view of the voltammogram on the left at high scan rate. Note that the standardized forward scan flux is larger than -0.01 when scan rate is above 10^3 mV/s.

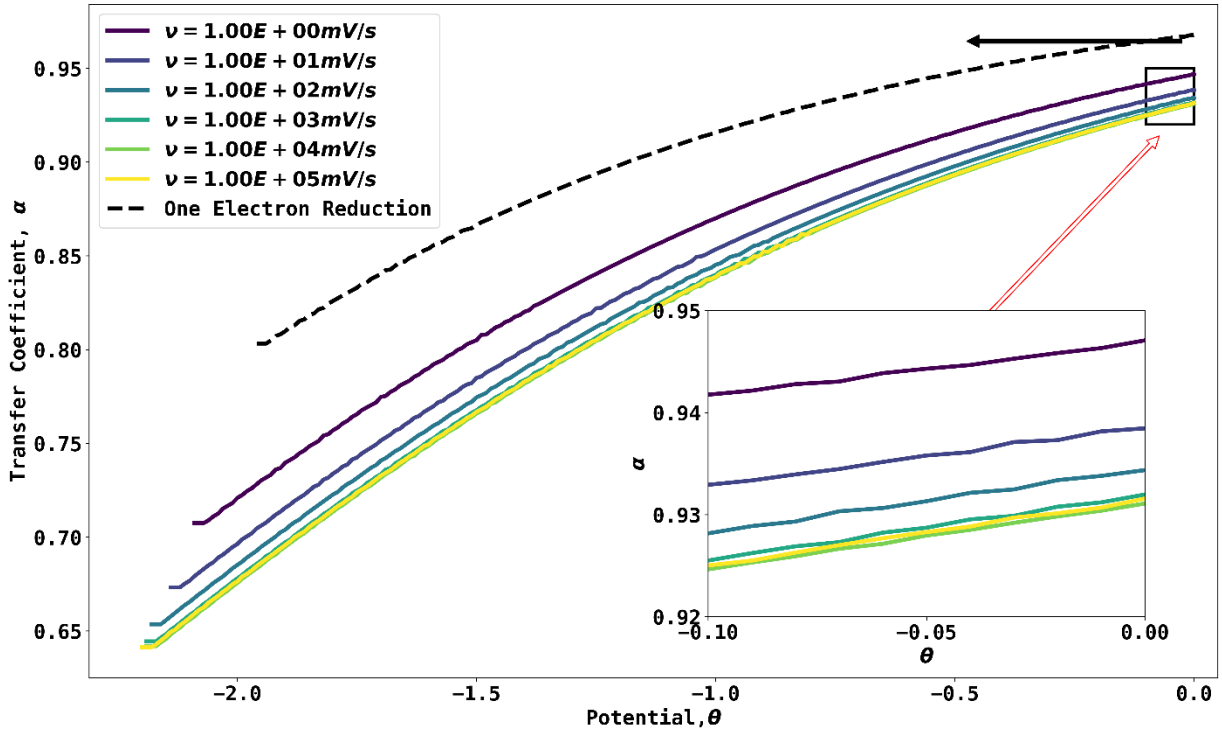

Figure 5.2. Tafel slopes deduced from CE reaction voltammograms at scan rates from 1 mv/s to 10^5 mV/s. The black-dashed curve is the Tafel plot of a simple one-electron reduction for reference. The starting potentials, corresponding to 5% peak flux, are adjusted to $\theta = 0$ to make Tafel plots, usually having different range of potentials, to be comparable. The inlet is zoom-in view of the Tafel plot from $\theta = -0.1$ to $\theta = 0$. The black arrow indicates the direction of voltammetric scan.

5.4.2 Dissociative CE Reaction: Voltammograms and Tafel slopes

As in the case of the simple CE reaction, the dissociative CE reaction is only meaningful when the preceding chemical reaction favours the reactant. During simulations, the forward and reverse chemical reaction rate constants are set to $k_f = 10^4\ s^{-1}$, with two different k_b, $10^9\ M^{-1}s^{-1}$ and $10^{12}\ M^{-1}s^{-1}$ so the equilibrium constants are $k_{eq} = 10^{-5}\ M$ and $k_{eq} = 10^{-8}\ M$. The concentration of reference species X is 1 mM.

Figure 5.3 shows voltammograms of the dissociative CE reaction model at scan rate from 1 mV/s to $10^5\ mV/s$ for the case of $k_{eq} = 10^{-5}\ M$, and qualitatively show similar features to the (non-dissociative) CE process, as above, notably a shift of the voltammetric

wave to greater overpotential and to kinetically rather than diffusion controlled currents at faster scan rates. Figure 5.4 shows similar behaviour for the case of $k_{eq} = 10^{-8}M$ where a further increase in the overpotential is observed consistent with the increased thermodynamic barrier caused by the preceding chemical reaction. The scaled currents are also reduced for the same reason and the voltammetry shows a greater tendency to kinetic control.

The Tafel plots for the voltammograms of a dissociative CE reaction are shown in Figure 5.5 , for the case where $k_{eq} = 10^{-5}\ M$ and Figure 5.6 for $k_{eq} = 10^{-8}\ M$. It is observed that the transfer coefficients are significantly below that of a simple one-electron reduction without the complication of any homogeneous coupled kinetics. In the case of the smaller k_{eq} value the transfer coefficients drop very markedly, even below the value around 0.5 expected for many fully electrochemically irreversible reactions. Figure 5.5 and Figure 5.6 also suggests that the effect of increasing scan rates is to lead to transfer coefficients closer to unity. This is the opposite effect to that seen for the non-dissociative CE reaction. This is attributed to be the fact that in the dissociative case slower scan rates lead to the greater build-up of the electro-inactive species C (see **(5.24)**) during the voltammetric scan which in turn increases the kinetic barrier and giving a greater apparent irreversibility to the voltammetry.

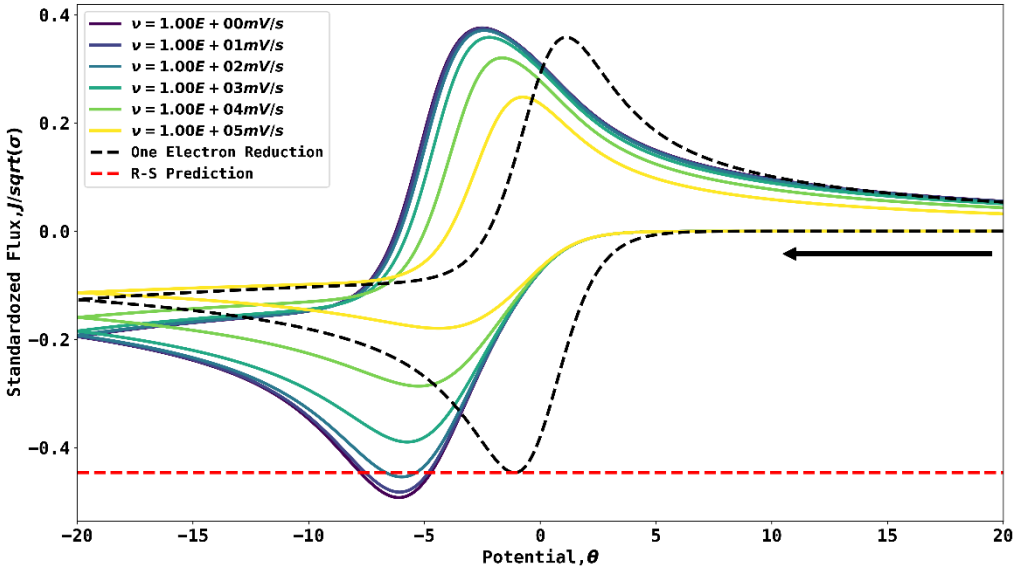

Figure 5.3. Voltammograms of the dissociative CE reaction at scan rates from $1\ mV/s$ to $10^5\ mV/s$ when $k_{eq} = 10^{-5}\ M$. The voltammogram in black line is the one-electron reduction reference voltammogram. The red-dotted line is the peak flux predicted Randles-Ševčík equation for one-electron reduction. The Y-axis represents the standardized flux by dividing dimensionless flux, J with square root of scan rate, $\sqrt{\sigma}$.

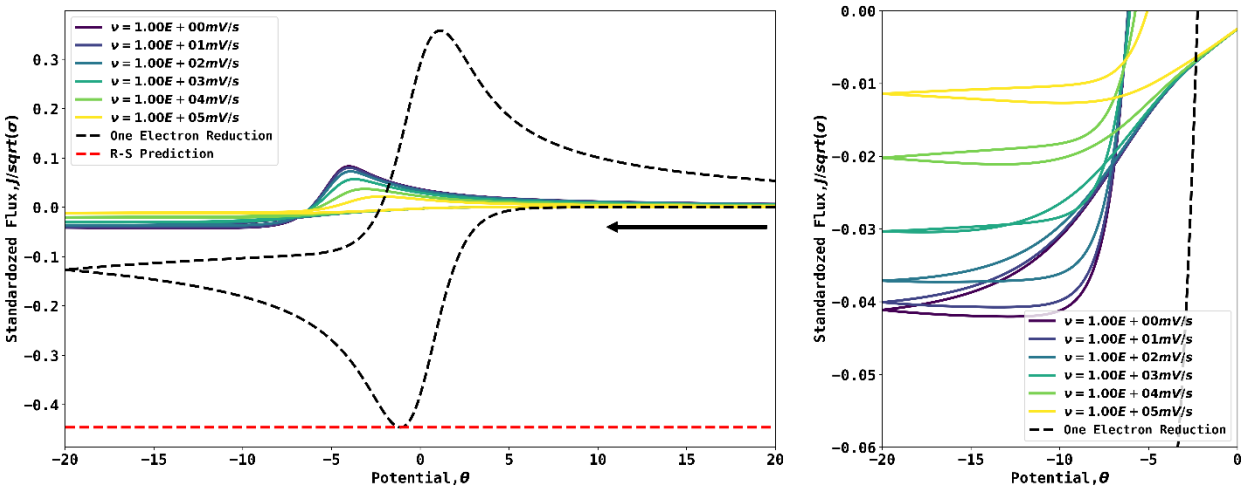

Figure 5.4. Left: the voltammograms simulated for a dissociative CE reaction at scan rates from $1\ mV/s$ to $10^5\ mV/s$ when $k_{eq} = 10^{-8}\ M$. The voltammogram in black line is the one-electron reduction reference voltammogram. The red-dotted line is the peak flux predicted Randles-Ševčík equation for one-electron reduction. The Y-axis represents the standardized flux by dividing dimensionless flux, J with square root of scan rate, $\sqrt{\sigma}$. The black arrow indicates the start and initial direction of voltammetric scan. Right: the zoom-in view of the voltammogram on the left at high scan rate. Note that the standardized forward scan flux is greater than -0.05 when scan rate is above $1\ mV/s$.

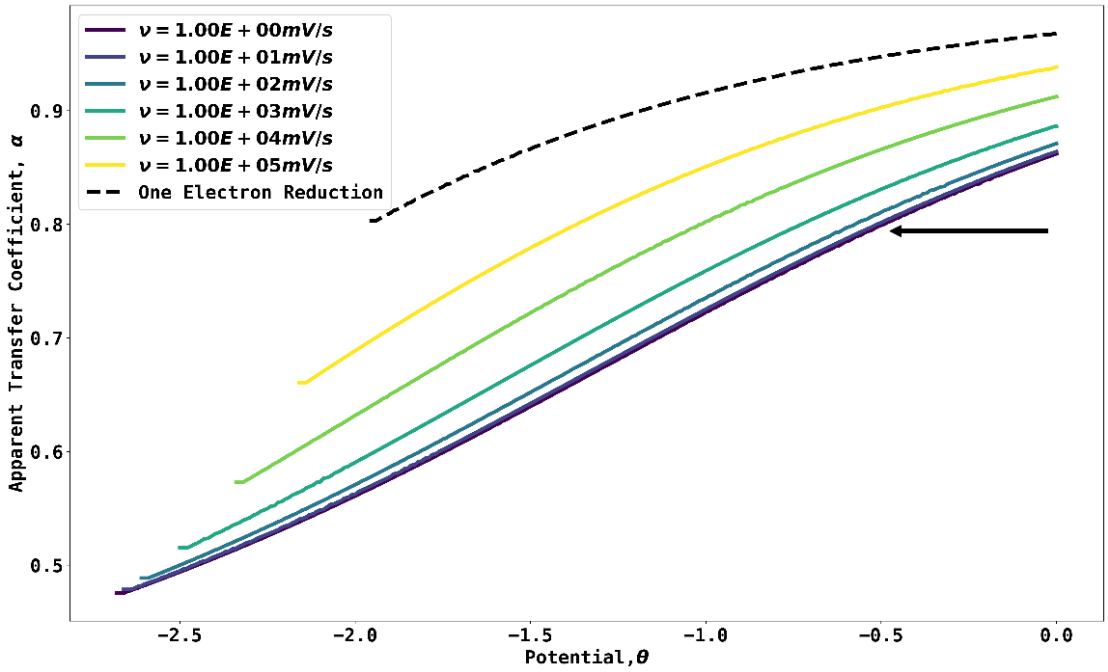

Figure 5.5. Tafel slopes for a dissociative CE reaction at scan rates from 1 mV/s to 10^5 mV/s when $k_{eq} = 10^{-5}\ M$. The black-dashed curve was the Tafel plot of a simple one-electron reduction for reference. The starting potentials, corresponding to 5% peak flux, are adjusted to $\theta = 0$ to make Tafel plots, usually having different range of potentials, to be comparable. The black arrow indicates the initial direction of voltammetric scan.

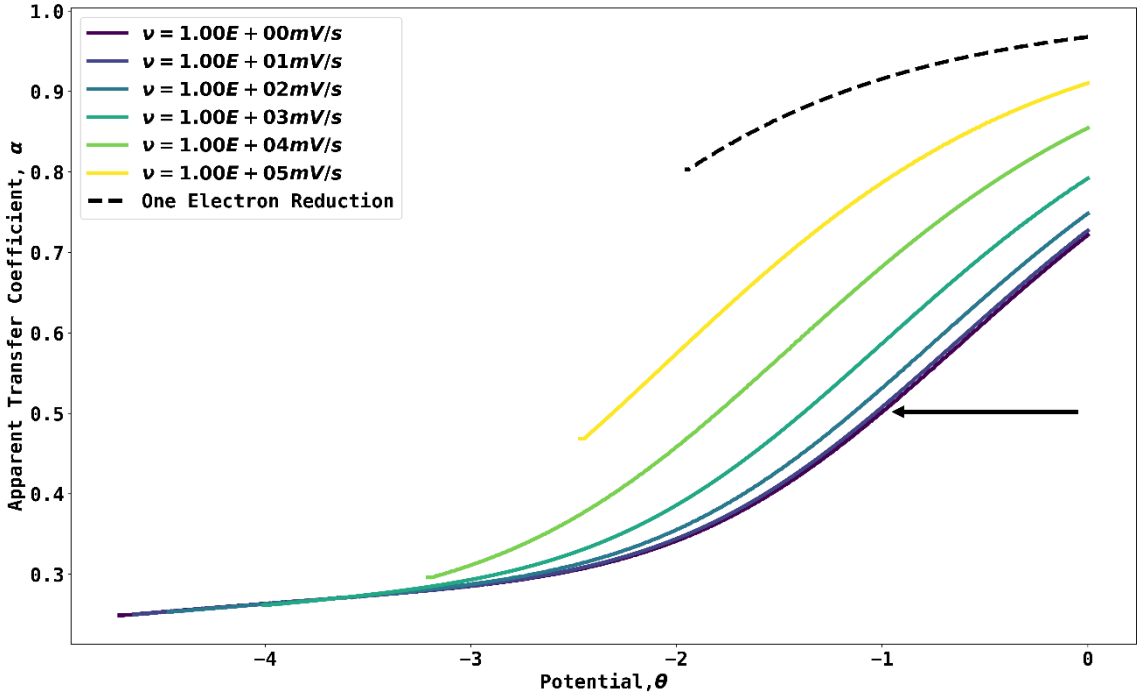

Figure 5.6. Tafel slopes deduced from voltammograms for a dissociative CE reaction model at scan rate from 1 mV/s to 10^5 mV/s when $k_{eq} = 10^{-8}\ M$. The black-dashed curve is the Tafel plot of a simple one-electron reduction for reference. The starting potentials, corresponding to

5% peak flux, are adjusted to $\theta = 0$ to make Tafel plots, usually having different range of potentials, to be comparable. The black arrow indicates the initial direction of voltammetric scan.

5.4.3 EC reaction: Voltammograms and Tafel plots

Simulation are made for EC processes in which the reaction of B to form C favours the product C. During simulation, the forward reaction and reverse reaction rate constant are set to $k_f = 10^9\ s^{-1}$ and $10^3\ s^{-1}$ with $k_b = 1\ s^{-1}$ and $10^{-6}\ s^{-1}$, so that obtaining a fixed $k_{eq} = 10^9$. The bulk concentration of reference species A is set to be 1 mM.

The simulated voltammograms are shown in Figure 5.7 at scan rates from 1 mV/s to $10^5\ mV/s$. The effect of the following reaction is to shift the reductive wave to less negative potentials and for an increase loss of the back peak as the rate of the following chemical reaction increases. In addition, the forward scan peak flux is slightly but clearly higher than simple one-electron reduction references. The reverse scan peaks almost disappear at slow scan rates because almost all B reduced from A is converted to C, leaving little B to be oxidized during reverse scan. Tafel plots are shown in Figure 5.8 , and the transfer coefficients of EC reaction are also above the Tafel plot of simple one-electron reduction, suggesting that a following chemical reaction increases the transfer coefficients. Figure 5.9 and Figure 5.10 shows analogous plots to those in Figure 5.7 and Figure 5.8 except that $k_f = 10^{-3}\ s^{-1}$ and with k_{eq} unchanged. The slower forward rate constant reduces the impact of the following kinetics on the voltammetry and on the deviation of the transfer coefficient from the response of the simple E process. Moreover, as the scan rate increases, providing a shorter time window for the follow up chemistry, the response transitions smoothly into that of an essentially unperturbed E process. That said, in both Figure 5.9 and Figure 5.10 the influence of the

following chemistry is to increase the transfer coefficient over and above that expected for a simple E process.

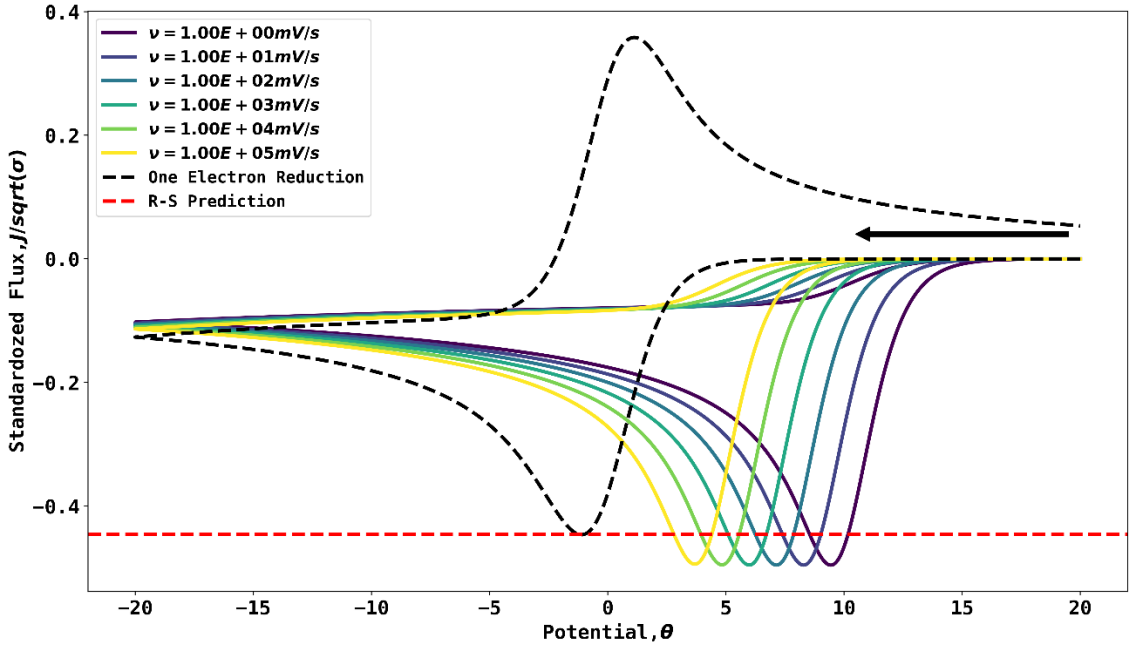

Figure 5.7. Voltammograms simulated for a EC reaction at scan rates from $1\,mV/s$ to $10^5\,mV/s$. The voltammogram in black-dashed line is the one-electron reduction reference voltammogram. The red-dashed line is the peak flux predicted Randles-Ševčík equation for one-electron reduction. The Y-axis represents the standardized flux by dividing dimensionless flux, J with square root of scan rate, $\sqrt{\sigma}$. The black arrow indicates the start and initial direction of voltammetric scan.

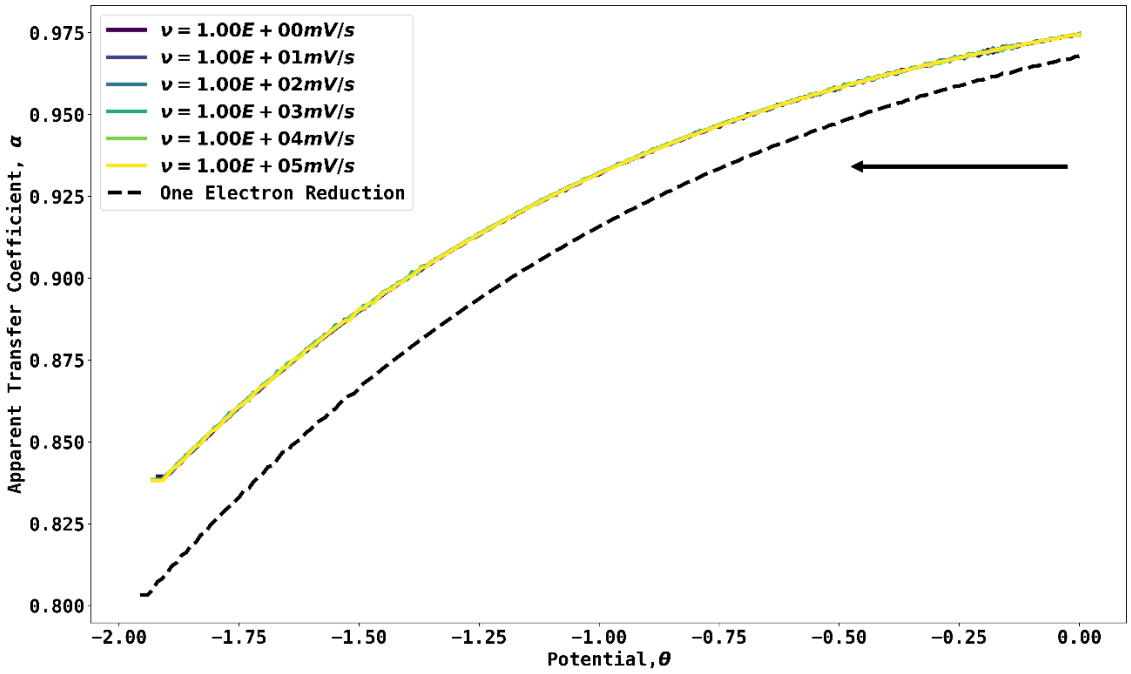

Figure 5.8. Tafel slopes inferred for an EC reaction at scan rates from $1\,mV/s$ to 10^5 mV/s. The black curve is the Tafel plot of a simple one-electron reduction for reference. The starting potentials, corresponding to 5% peak flux, are adjusted to $\theta = 0$ to make Tafel plots, usually having different range of potentials, to be comparable. The black arrow indicates the start and initial direction of voltammetric scan.

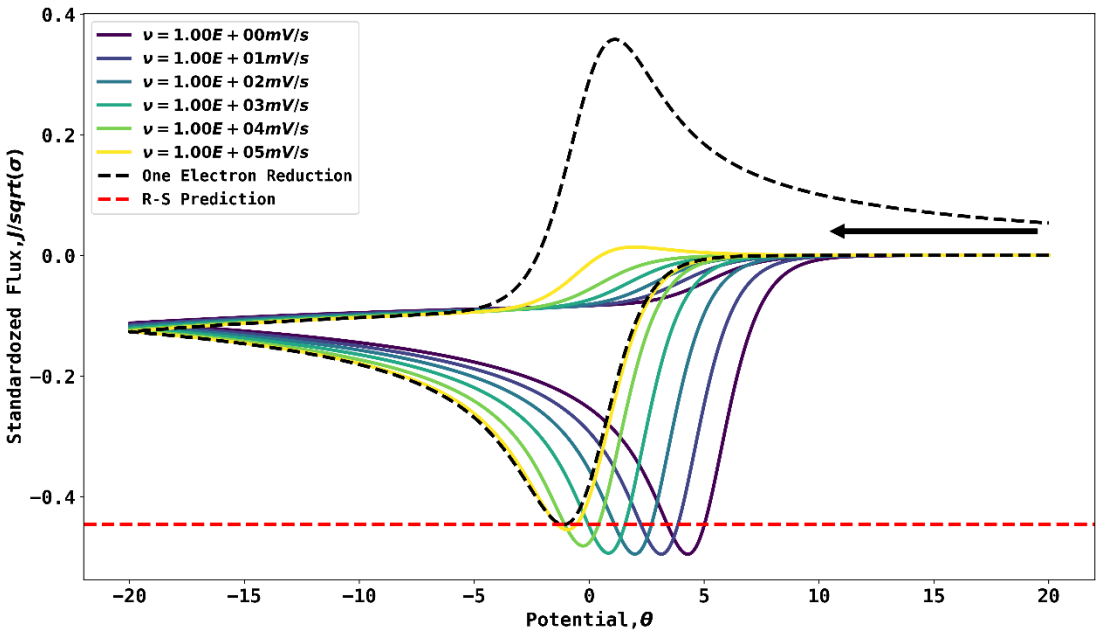

Figure 5.9. Voltammograms simulated for an EC reaction from scan rates of $1\,mV/s$ to $10^5\,mV/s$. The voltammogram in black-dashed line is the one-electron reduction reference voltammogram. The red-dashed line is the peak flux predicted Randles-Ševčík equation for one-electron reduction. The Y-axis represents the standardized flux by dividing dimensionless

flux, J with square root of scan rate, $\sqrt{\sigma}$. The black arrow indicates the start and initial direction of voltammetric scan.

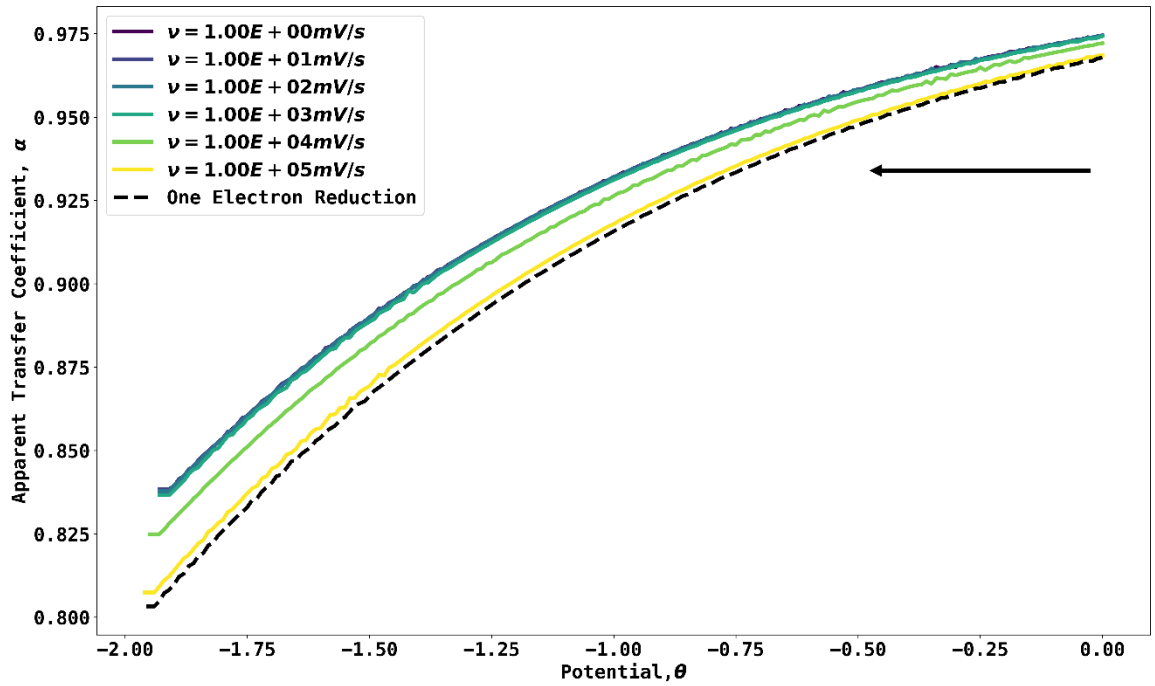

Figure 5.10. Tafel slopes inferred from the simulated voltammetry of an EC reaction at scan rates from 1 mV/s to 10^5 mV/s. The black curve is the Tafel plot of a simple one-electron reduction for reference. The starting potentials, corresponding to 5% peak flux, are adjusted to $\theta = 0$ to make Tafel plots, usually having different range of potentials, to be comparable. The black arrow indicates the start and initial direction of voltammetric scan.

5.4.4 EC_2 reaction: Voltammograms and Tafel slope

Next simulations for an EC_2 reaction are considered. The forward reaction rate constant and reverse reaction rate constant are set to $k_f = 10^9 M^{-1}s^{-1}$ and $10^3\ M^{-1}s^{-1}$,with $k_b = 1\ s^{-1}$ and $10^{-6}\ s^{-1}$, so keeping a fixed $k_{eq} = 10^9\ M^{-1}$.

The resulting simulated voltammograms are shown in Figure 5.11, showing that the forward scan peak flux of EC_2 reactions is higher than that of simple one-electron reduction. Higher scan rates shift the peaks to more negative potentials. When $\nu = 1\ mV/s$, at 5% of peak current, the transfer coefficient reaches the maximum value of around 1.5. The Tafel plots are shown in Figure 5.12 , showing that the Tafel plots of EC_2 reaction are higher in magnitude

than seen for a one-electron reduction (shown in Figure 5.12). Across the entire range of analysis, the observed transfer coefficients are above unity despite the simulation constraining the electron transfer to be fully electrochemically reversible (Nernstian) in character. For a fixed scan rate, a higher scan rate leads to lower values of the transfer coefficient indicating a smaller influence of the follow up chemistry as a consequence of he lowered time window. Figure 5.13 and Figure 5.14 show analogous plots to this in Figure 5.11 and Figure 5.12 but for a reduced following rate constant of $k_f = 10^3\ M^{-1}s^{-1}$, and keeping k_{eq} fixed at $10^9\ M^{-1}$. The effect is to lower the super-Nernstian character and for fast scan rates the voltammetry is relatively unperturbed compared to the simple E reaction to which the potential dependence of the transfer coefficient returns for suitably large scan rate.

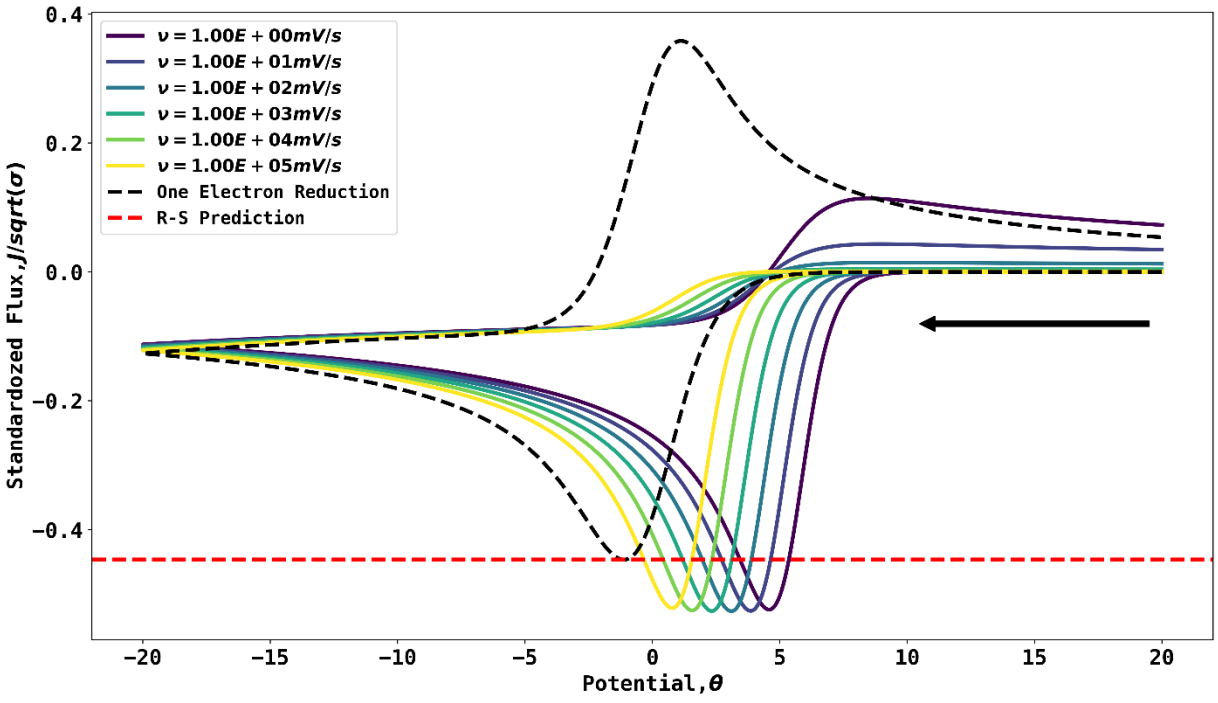

Figure 5.11. Voltammograms simulated for an EC_2 reaction for scan rates from $1\ mV/s$ to $10^5\ mV/s$ when $k_f = 10^9\ M^{-1}s^{-1}$. The voltammogram in black line is the one-electron reduction reference voltammogram. The red-dashed line is the peak flux predicted Randles-Ševčík equation for one-electron reduction. The peak flux of EC_2 model significantly exceeds Randles-Ševčík prediction and higher scan rate shifts the forward scan peak to more reductive potential. The Y-axis represents the standardized flux by dividing dimensionless flux, J with square root of scan rate, $\sqrt{\sigma}$.

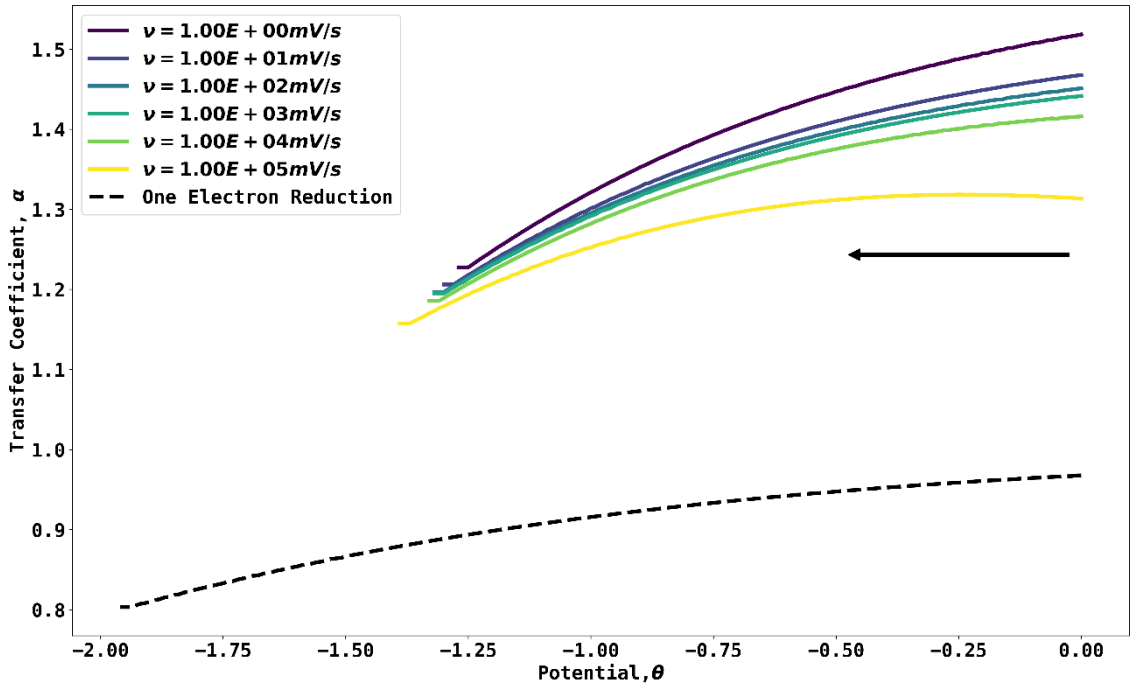

Figure 5.12. Tafel slopes inferred from the simulated voltammograms of an EC_2 reaction model at scan rates from $1\ mV/s$ to 10^5 mV/s when $k_f = 10^9\ M^{-1}s^{-1}$. The black curve is the Tafel plot of a simple one-electron reduction for reference. The starting potentials, corresponding to 5% peak flux, are adjusted to $\theta = 0$ to make Tafel plots, usually having different range of potentials, to be comparable.

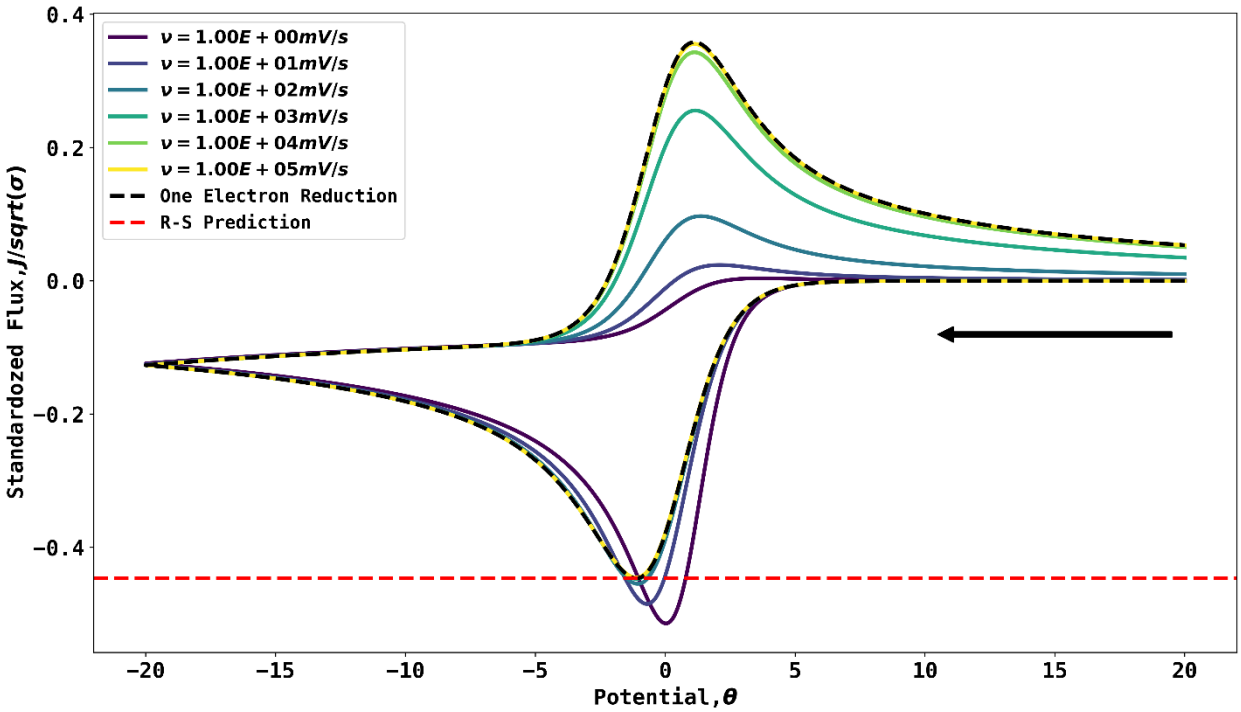

Figure 5.13. Voltammograms simulated for an EC_2 reaction at scan rates from $1\ mV/s$ to $10^5\ mV/s$ when $k_f = 10^3\ M^{-1}s^{-1}$. The voltammogram in black line is the one-electron

reduction reference voltammogram. The red-dashed line is the peak flux predicted Randles-Ševčík equation for one-electron reduction. The peak flux of EC_2 model significantly exceeds Randles-Ševčík prediction and higher scan rate shifts the forward scan peak to more reductive potential. The Y-axis represents the standardized flux by dividing dimensionless flux, J with square root of scan rate, $\sqrt{\sigma}$.

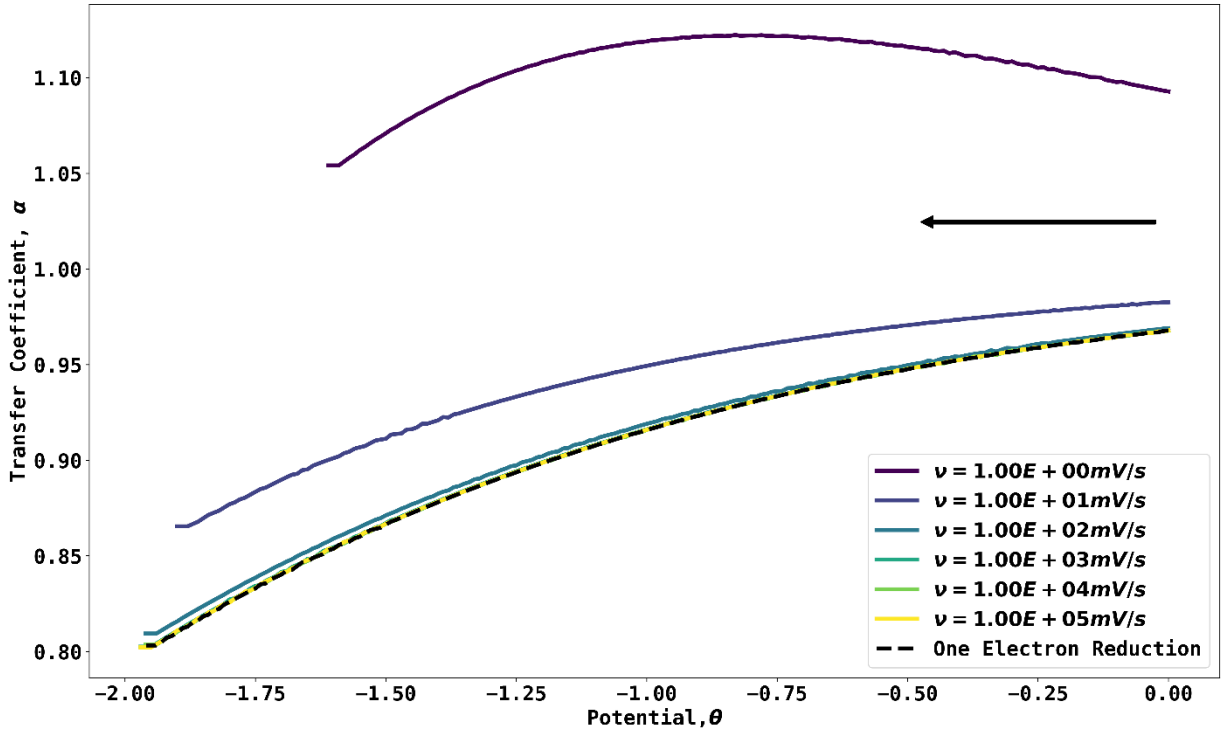

Figure 5.14. Tafel slopes inferred from the voltammetry simulated for an EC_2 reaction model at scan rates from 1 mV/s to 10^5 mV/s and $k_f = 10^3\ M^{-1}s^{-1}$. The black curve is the Tafel plot of a simple one-electron reduction for reference. The starting potentials, corresponding to 5% peak flux, are adjusted to $\theta = 0$ to make Tafel plots, usually having different range of potentials, to be comparable.

5.5 Tafel plots for irreversible electrode processes with coupled homogeneous kinetics

All the simulations presented above focus exclusively on electron transfers constrained to be electrochemically reversible in character. A few further simulations were conducted for electrochemically irreversible processes. The simulations show, as expected, that when electrode processes are irreversible, the electrode reaction is by definition slow compared with diffusion, and the overall electrochemical reaction is more under the control of the electron transfer dynamics and less susceptible to perturbation by the coupled kinetics. Thus, the

influences identified above for the following and preceding kinetics are seen to be greatly reduced in comparison with the corresponding electrochemically reversible cases and hence the transfer coefficients in all examples studied were close to the value assumed for the electron transfer step.

5.6 Conclusions

We have simulated the various sub-cases of the general kinetic scheme defined by **(5.6)**. The effect of preceding chemical reaction is to diminish the transfer coefficient expected for an electrochemically reversible process leading to apparent but illusory sub-Nernstian behaviour. In contrast a following reaction deceptively promotes the effective degree of reversibility and hence the observed transfer coefficients so giving a super-Nernstian response. The desirable need to identify independently the absence of coupled kinetics when selecting 'model' systems particularly for the evaluation of fundamental theories of electron transfer as well as in the general mechanistic analysis of electrode reaction is caveated.

This chapter used numerical simulation to analyse the influence of coupled chemical reaction on Tafel slopes. In text chapter we expand the applicability of simulation in voltammetry: using simulation to generate data for the training and testing of a neural network, we can train the neural network to both predict voltammograms from rate constants or to extract kinetic or thermodynamic constants from experimental voltammograms.

Reference

1. H. Chen and R. G. Compton, *J. Electroanal. Chem.*, 2021, **880**, 114942.
2. R. Guidelli, R. G. Compton, J. M. Feliu, E. Gileadi, J. Lipkowski, W. Schmickler and S. Trasatti, *Pure Appl. Chem.*, 2014, **86**, 259-262.
3. R. Guidelli, R. G. Compton, J. M. Feliu, E. Gileadi, J. Lipkowski, W. Schmickler and S. Trasatti, *Pure Appl. Chem.*, 2014, **86**, 245-258.
4. A. J. Bard and L. R. Faulkner, *Electrochemical Methods: Fundamentals and Applications*, 1st edn., 1980.
5. J. A. V. Butler, *Trans. Faraday Soc.*, 1924, **19**, 729-733.

6. R. G. Compton and C. E. Banks, *Understanding voltammetry*, World Scientific, London, 3rd edn., 2018.
7. D. Li, C. Lin, C. Batchelor-McAuley, L. Chen and R. G. Compton, *J. Electroanal. Chem.*, 2018, **826**, 117-124.
8. W. J. Albery, *Electrode kinetics*, Oxford University Press, 1975.
9. T. Erdey-Grúz and M. Volmer, *Z. Phys. Chem.*, 1930, **150**, 203-213.
10. C. Batchelor-McAuley, D. Li and R. G. Compton, *ChemElectroChem*, 2020, **7**, 3844-3851.
11. R. C. Tolman, *The principles of statistical mechanics*, Courier Corporation, 1979.
12. R. A. Marcus, *J. Chem. Phys.*, 1956, **24**, 966-978.
13. R. A. Marcus, *J. Chem. Phys.*, 1957, **26**, 867-871.
14. N. S. Hush, *J. Chem. Phys.*, 1958, **28**, 962-972.
15. M. C. Henstridge, E. Laborda, N. V. Rees and R. G. Compton, *Electrochim. Acta*, 2012, **84**, 12-20.
16. E. E. L. Tanner, E. O. Barnes, C. B. Tickell, P. Goodrich, C. Hardacre and R. G. Compton, *J. Phys. Chem. C*, 2015, **119**, 7360-7370.
17. H. Chen, J. R. Elliott, H. Le, M. Yang and R. G. Compton, *J. Electroanal. Chem.*, 2020, 114185.
18. A. Testa and W. Reinmuth, *Anal. Chem.*, 1961, **33**, 1320-1324.
19. V. G. Mairanovsky, *J. Electroanal. Chem. Interfacial Electrochem.*, 1979, **97**, 103-105.
20. A. Einstein, *J Annalen der physik*, 1905, **17**, 549-560.
21. I. B. Svir, A. I. Oleinick and R. G. Compton, *Russ. J. Electrochem.*, 2003, **39**, 160-164.
22. D. Gavaghan, *J. Electroanal. Chem.*, 1998, **456**, 1-12.

Chapter 6 Artificial Intelligence in Electrode Reaction Mechanism Studies

Machines, when trained to think like humans or mimic their actions, generate we call Artificial Intelligence (AI). While we can train AI to play Go[1], to fold proteins[2] etc, in this chapter we ask if we can train AI to learn electrochemistry to help electrochemists? The work was published at *Analytical Chemistry*[3].

In this chapter Artificial Intelligence is used to learn the key voltammetric characteristics of the dissociative CE mechanism via training from multiple simulations using bespoke code. This allows first the prediction of voltammograms without the need for further simulation given knowledge of the relevant experimental parameters (rate and equilibrium constants, electrode geometry and diffusion coefficients). Second it is applied to analyse noisy experimental voltammetry to characterize the mechanistic type and to successfully extract the key kinetic and thermodynamic parameters.

6.1 Introduction

The use of voltammetric methods to investigate electrode reaction mechanisms typically requires the analysis of experimental current – voltage curves ('voltammograms') measured under diffusion only conditions as a function of voltage scan rate in the case of macro electrodes or electrode size in the case of steady-state measurement at microelectrodes[4-6]. Evidence of mechanism and/or extraction of kinetic parameters requires the simulation of the voltammetry either via the creation of bespoke code or, for limiting cases the use of commercial software of which KISSA[7] and the DIGISIM pioneered by Rudolph[8] are particularly noteworthy or, alternatively, working surfaces such as appear in some textbooks [9]. Working

surfaces display how key observables such as peak or limiting currents and half-wave or peak potentials depend on various dimensionless parameters which reflect the controlling chemical and electrochemical processes, notably rate and equilibrium constants together with diffusion coefficients, the electrode geometry and the timescale of experiment (voltage scan rate, electrode size). Variation of these parameters allows mechanistic fingerprinting and rate constant extraction by tracking the variation of the observables across the working surface and comparing theoretical prediction with observation frequently via graphical means. The working curve approach is efficient in that if elaborate simulations are needed to characterise the mechanism, they need only be carried out once; the results are permanently captured in the form of the working surface.

In practice the use of working surfaces presents difficulties since they need to be simulated and recorded at high resolution to accurately allow interpolation. Thus, challenges appear in respect of their storage where a simple plot offers insufficient detail. Accordingly, in this chapter we explore the use of AI in learning from accurate simulations how the expected observables (current, peak potentials, etc.) and, simultaneously and more generally, the expected voltammetry is dependent on the various controlling parameters. On this basis we further explore the use of AI to analyse voltammetry in the light of the suggested mechanism. To this purpose we consider the dissociative CE mechanism such as may apply to the oxidation of hydrazine in acid solution [10-12] and the reduction of ethanoic acid [13, 14]:

$$\begin{cases} X \underset{k_b}{\overset{k_f}{\rightleftarrows}} A + C, K_{eq} = \dfrac{k_f}{k_b} \\ A + e \ \rightleftarrows B \end{cases} \qquad \textbf{(6.1)}$$

where the A/B redox couple is assumed to be electrochemically reversible and the voltammetry is conducted near steady-state at a (hemi)-spherical electrode to allow exploration of the transition from micro electrode to macro-electrode behaviour as the radius of electrode, r_e, is

increased. We first establish the relevant working surfaces, which have not been published previously to the author's knowledge, and second demonstrate demonstrated the use of AI in "storing" the simulation results via a trained neural network to allow the prediction of the voltammetry expected for defined parameters notably k_f and K_{eq} in Eq. 1 above as well as allowing the easy on-demand generation of the relevant working surfaces for limiting currents and halfwave potentials. Last the analysis of synthetic but noisy experimental data via AI is examined to show how AI might facilitate the analysis of experimental data.

6.2 Theory

We consider the electrochemically reversible, one-electron reduction of species A to B with preceding chemical reaction (CE process) at a (hemi-)spherical electrode of radius $\boldsymbol{r_e}$. It is further assumed that the preceding chemical step is dissociative forming the electrochemically inactive species $\boldsymbol{C}$ as well as active A.

A (hemi-)spherical micro-electrode was considered since, as well as being a useful and practical electrode geometry, notably through the use of mercury drop electrodes[15, 16] or spherical gold electrode by melting the tip of a gold wire[17]. It is often used as an approximation for a circular microdisc electrode since the assumption of spherical symmetry reduces the diffusion problem from two dimensions to one dimension [18]. The system is assumed to be free of natural convection caused by density gradients [19, 20], or any migration due to potential gradients. Using Fick's second law of diffusion [21, 22], the diffusion equation for species $j = (A, B, C \text{ or } X)$ can be expressed as:

$$\begin{cases} \dfrac{\partial[X]}{\partial t} = D_X \dfrac{\partial^2[X]}{\partial r^2} + \dfrac{2}{r}\dfrac{\partial[X]}{\partial r} - k_f[X] + k_b[A][C] \\ \dfrac{\partial[A]}{\partial t} = D_A \dfrac{\partial^2[A]}{\partial r^2} + \dfrac{2}{r}\dfrac{\partial[A]}{\partial r} + k_f[X] - k_b[A][C] \\ \dfrac{\partial[B]}{\partial t} = D_B \dfrac{\partial^2[B]}{\partial r^2} + \dfrac{2}{r}\dfrac{\partial[B]}{\partial r} \\ \dfrac{\partial[C]}{\partial t} = D_C \dfrac{\partial^2[C]}{\partial r^2} + \dfrac{2}{r}\dfrac{\partial[X]}{\partial r} + k_f[X] - k_b[A][C] \end{cases} \quad \textbf{(6.2)}$$

Note that pre-equilibrium of X, A and C is assumed prior the start of the experiment/simulation. The total concentration of X used to create the solution before any dissociation is $c_{X,total} = c_X^* + \frac{c_A^* + c_C^*}{2}$, where c_X^*, c_A^*, c_C^* are the bulk concentration of species X, A and C after establishment of chemical equilibrium from dissociation of X. The equilibrium constant for the dissociation is: $K_{eq} = \frac{k_f}{k_b}$.

The electrochemical reaction on the surface of electrode is assumed to obey Butler-Volmer kinetics as [23, 24]:

$$\begin{aligned} j_{BV} = \mathrm{k}_0 \exp\left[\frac{-\alpha F\left(E - E_f^0\right)}{RT}\right] c_A(r_e, t) \\ -k_0 \exp\left[\frac{(1-\alpha) F\left(E - E_f^0\right)}{RT}\right] c_B(r_e, t) \end{aligned} \quad \textbf{(6.3)}$$

where j_{BV} is the net flux of reductant on the electrode surface using Butler-Volmer kinetics and k_0 is the standard electrochemical rate constant. α is the transfer coefficient, and $c_A(r_e, t)$ and $c_B(r_e, t)$ are the concentration of species A and B at the surface of electrode at any time t. E_f^0 is the formal potential of the A/B redox couple, and E is the potential as varied during linear sweep voltammetry. For the latter, the potential E at time t during a cyclic voltammetry is:

$$\begin{cases} 0 < t < t_{switch}, E = E_i - \nu t \\ t = t_{switch}, E = E_v \\ t_{switch} < t \leq 2t_{switch}, E = E_V + \nu(t - t_{switch}) \end{cases} \quad \textbf{(6.4)}$$

where E_i is the starting potential of forward scan, t_{switch} is the start time of the reverse scan of potential E_V and ν is the scan rate.

All the results considered later are assumed to be electrochemically 'reversible' processes, and artificially large values of the standard electrochemical rate constant, k_0 ($> 100\ cm/s$) were employed to ensure reversibility.

For the inner boundary at the electrode surface ($r = r_e$),

$$\begin{cases} D_X \left(\frac{\partial [X]}{\partial r}\right)_{r=r_e} = 0 \\ D_A \left(\frac{\partial [A]}{\partial r}\right)_{r=r_e} = j_{BV} \\ D_B \left(\frac{\partial [B]}{\partial r}\right)_{r=r_e} = -j_{BV} \\ D_C \left(\frac{\partial [C]}{\partial r}\right)_{r=r_e} = 0 \end{cases} \quad \textbf{(6.5)}$$

The outer spatial boundary of the simulation, r_{sim}, is located distant enough from the surface of electrode ($r = r_e$,where r_e is the radius of electrode) for the bulk concentrations to prevail. From Einstein's work on Brownian motion, the root mean squared distance diffused in time t is $\sqrt{2Dt}$ and can be used to estimate the distance away from the electrode at which the concentrations are unperturbed from bulk[25]. Letting t_{sim} be the time duration of voltammetric scan, the distance of outer spatial boundary is chosen to be:

$$r_{sim} = r_e + 6\sqrt{Dt_{sim}} \quad \textbf{(6.6)}$$

where the value of 6 allows for a cautious over-estimate.

The boundary conditions for the bulk concentration are:

$$t = 0, r \geq r_e \quad t > 0, r = r_{sim} \begin{cases} c_X^* = c_{X,total} - \dfrac{-1 + \sqrt{1 + 4\dfrac{c_{X,total}}{K_{eq}}}}{\dfrac{2}{K_{eq}}} \\ c_A^* = \dfrac{-1 + \sqrt{1 + 4\dfrac{c_{X,total}}{K_{eq}}}}{\dfrac{2}{k_{eq}}} \\ c_B^* = 0 \\ c_C^* = \dfrac{-1 + \sqrt{1 + 4\dfrac{c_{X,total}}{K_{eq}}}}{\dfrac{2}{K_{eq}}} \end{cases} \quad \textbf{(6.7)}$$

where $c_{X,total}$ is the concentration of species X initially added to the solution before chemical equilibration forming A and C which are assumed absent in the initial solution. It follows that $c_{X,total} = c_A^* + c_C^*$ in the absence of electrolysis.

Dimensionless Parameters. Dimensionless parameters were used in all simulations to ensure generality and to avoid the need to repeat the simulation for different parameters [19]. Table 6.1 lists the pertinent parameters for the transformation between dimensional and non-dimensional forms. We have developed a graphical user interface (GUI) for user-friendly conversion of dimensional voltammograms to their dimensionless form and the inverse process. The formal potential of the A/B couple, diffusion coefficients of all four species and the radius of electrode are the input parameters for the conversion.

Table 6.1
List of definitions of dimensionless parameters for (hemi-)spherical electrode simulations.

Dimensionless Parameter	Definition
Standard Electrochemical Rate Constant	$K_0 = \dfrac{k_0 r_e}{D_X}$

Homogeneous chemical Rate Constant, Forward Reaction	$K_f = \frac{k_f r_e^2}{D_X}$
Homogeneous chemical Rate Constant, Reverse Reaction	$K_b = \frac{k_b c_{X,total} r_e^2}{D_X}$
Homogenous chemical reaction equilibrium constant	$\mathrm{K}_{eq} = \frac{K_f}{K_b} = \frac{K_{eq}}{c_{X,Total}}$
c_j is the concentration of any species j and r_e is the radius of electrode. The bulk concentration of X, $c_{X,Total}$ before chemical equilibrium and its diffusion coefficients D_X is used for the conversion between dimensions.	

6.2.1 Dimensionless Form of the equations.

Using Table 5.1, the Butler-Volmer (BV) equation in dimensionless form becomes:

$$J_{BV} = K_0 \exp[-\alpha\theta] C_A(1,T) - K_0 \exp[(1-\alpha)\theta] C_B(1,T) \quad \textbf{(6.8)}$$

The dimensionless diffusion equations are:

$$\begin{cases} \dfrac{\partial C_X}{\partial T} = d_X \dfrac{\partial^2 C_X}{\partial R^2} + \dfrac{2}{R}\dfrac{\partial C_X}{\partial R} - K_f C_X + K_b C_A C_C \\ \dfrac{\partial C_A}{\partial T} = d_A \dfrac{\partial^2 C_A}{\partial R^2} + \dfrac{2}{R}\dfrac{\partial C_A}{\partial R} + K_f C_X - K_b C_A C_C \\ \dfrac{\partial C_B}{\partial T} = d_B \dfrac{\partial^2 C_B}{\partial R^2} + \dfrac{2}{R}\dfrac{\partial C_B}{\partial R} \\ \dfrac{\partial C_C}{\partial T} = d_C \dfrac{\partial^2 C_C}{\partial R^2} + \dfrac{2}{R}\dfrac{\partial C_C}{\partial R} + K_f C_X - K_b C_A C_C \end{cases} \quad \textbf{(6.9)}$$

The dimensionless boundary conditions for the surface of electrode are:

$$\begin{cases} d_X \left(\frac{\partial C_X}{\partial R}\right)_{\boldsymbol{R}=1} = 0 \\ d_A \left(\frac{\partial c_A}{\partial R}\right)_{R=1} = J_{BV} \\ d_B \left(\frac{\partial c_B}{\partial R}\right)_{\boldsymbol{R}=1} = -J_{BV} \\ d_C \left(\frac{\partial c_C}{\partial R}\right)_{\boldsymbol{R}=1} = 0 \end{cases} \quad \textbf{(6.10)}$$

where $R = 1$ represents the surface of electrode.

The dimensionless boundary conditions for the bulk concentration are:

$$\begin{matrix} T = 0, R \geq 1 \\ T > 0, R = R_{sim} \end{matrix} \begin{cases} C_X = \frac{c_X^*}{c_{X,total}} \\ C_A = \frac{c_A^*}{c_{X,total}} \\ C_B = 0 \\ C_C = \frac{c_C^*}{c_{X,total}} \end{cases} \quad \textbf{(6.11)}$$

6.3 Simulation and machine learning methods

The simulation programs were written in two programming languages: C++ and Python for the user's preference. **std::thread** and **multiprocessing** were used for parallel computing and the programs were run using Intel i7 CPU and GTX 1060 GPU. The non-linear diffusion equations were solved using the finite difference method by discretising the diffusion equations using an expanding grid and solved with the backward implicit method [4, 19]. The resulting multi-diagonal sparse matrix was then solved using the root-finding Newton-Raphson algorithm for at most 10 iterations and the next iteration would be skipped if the error was smaller than 10^{-12} [19]. The resulting voltammograms were plotted using Python Matplotlib.

Machine learning of simulated voltammograms was performed using TensorFlow [26] with a multiheaded deep neural network (DNN). For demonstrating the extraction of kinetic/mechanistic data from experimental voltammetry normally distributed noise was added

to the simulated voltammograms to emulate experimental noise from devices. A learning rate scheduler was utilized to decrease the learning rate by 0.01% in each iteration after 2000 iterations to avoid overfitting. The machine learning program was also benchmarked with simple linear regression, Random Forest [27], and XGBoost [28].The voltammogram dimension conversion tool was written with PyQt5. Its source code is public and available on (https://github.com/nmerovingian/Dimension-Conversion-Tool), which can be packaged into executables to run on major platforms. The simulation and machine learning programs and weights of neural networks are available at https://github.com/nmerovingian/dissociativeCE-Simulation-MachineLearning.

6.3.1 Training with neural networks.

Voltammograms generated by the simulation program were analysed to extract the current and potential values corresponding to 1%,2%,3%…99% and 100% of the peak currents measured on the forward and reverse scans of the voltammogram, comprising of 400 data points in total as shown in Figure 6.1. This approach complements with that of viewing the voltammogram as a picture using a convolutional network [29] and makes our neural networks compatible with any potential window of scan and both steady state and normal peak shaped voltammograms. The two hundred data points would sufficiently reproduce the voltammogram and economises on the memory of devices and time for training without significantly compromising accuracy. To train the neural networks, the training voltammograms were generated via simulation, assuming $c_{X,Total} = 1\ mM$; The diffusion coefficients of all species were assumed to be $10^{-9}\ m^2 s^{-1}$ and the range of voltammetric scan is from $\theta = -20$ to $\theta = 20$, corresponding to scan range of $-0.51V$ to 0.51V relative to the formal potential of the A/B couple. The radius of electrode was assumed to be $1\ \mu m$. Note that the choice of $1\ \mu m$ electrode was arbitrary since the relevant parameters needed for training (such as peak currents

and half-wave potentials) are readily deduced from the working surfaces, which are completely general by virtue of their being formulated in terms of dimensionless parameters. Thus, the relevant parameters for electrodes of arbitrary size are generated as a function of k_f and K_{eq}. These dimensional values were converted into dimensionless form for simulation ensuring generality. Since the input and output of the AI model are dimensionless, users must convert dimensional voltammograms into their dimensionless form using the formula given above and/or the GUI mentioned in section *Dimensionless Parameters*. Because the rate and equilibrium constants varied in orders of magnitude, they were converted to $\log_{10}$ scale for training to handle exploding/diminishing gradient problem. Note that users should run independent simulations for training and testing if intending to simulate voltammogram with unequal diffusion coefficients.

Three neural networks were developed.

First, Method A can use a single given voltammogram to predict chemical reaction rate constants k_f and K_{eq} by learning the features on the training voltammograms shown in Figure 6.1. A schematic figure of the structure of this model is shown in Figure 6.2 which captures the process predicting K_f and K_{eq} from the features extracted from Figure 6.1. When training and testing with experimental voltammograms, the voltammograms were converted to dimensionless form using the methods mentioned above.

Second, Method B predicts voltammograms given prior knowledge of the chemical reaction rate constant K_f,the equilibrium constant K_{eq} and the formal potential of the A/B couple. The voltammogram predicted is in dimensionless form but is readily converted to dimensional form using the methods mentioned above.

Third, Method C predicts the dimensionless shift in half peak potential from the formal potential and the peak flux given dimensionless chemical reaction rate constant K_f, K_{eq} and dimensionless scan rate σ with prior knowledge of formal potential. The predicted dimensionless half peak potential and peak flux can be converted to dimensional form with Table 6.1.

All the three methods used different but similar neural networks as shown in Figure 6.2. The neural network depicted in Figure 6.2 for Method A, for example, composed of one input layer (green), five hidden layers (purple) and one output layer (orange). We may treat each layer as a simple function:

$$\begin{matrix} T = 0, R \geq 1 \\ T > 0, R = R_{sim} \end{matrix} \begin{cases} C_X = \dfrac{c_X^*}{c_{X,total}} \\ C_A = \dfrac{c_A^*}{c_{X,total}} \\ C_B = 0 \\ C_C = \dfrac{c_C^*}{c_{X,total}} \end{cases} \quad \textbf{(6.12)}$$

where h represents the output, X represents the matrix of input features, W represents the weight matrix containing all the connection weights and b represents the bias vector [30]. ϕ is called activation function, which is the Rectified Linear Unit (ReLU) function in this model.

$$ReLU: \phi(X) = \max(0, X) \quad \textbf{(6.13)}$$

In the first layer of the neural network, the input layer accepts features from voltammograms as its X matrix, and output $h_{w,b}$ would be the input matrix of next layer and so on. Finally, output layer accepts output from the fifth hidden layer, and gives the outputs(targets) of interest, for example, K_f and K_{eq} of method A. The weight matrix and bias vector are generated with random numbers at the start of training, and along progression (iterations) of the training, the optimizer of the model [31], minimises the loss function, the mean absolute error of prediction in

this case, by tweaking the weight matrix and bias vector of the model to learn both linear and non-linear correlations between the voltammogram and its rate constants. After hundreds of iterations, the weights and biases of the model are more optimized, and the errors of prediction become smaller and smaller. At that stage, we postulate that the AI has learned the implicit correlation between voltammogram and rate constants.

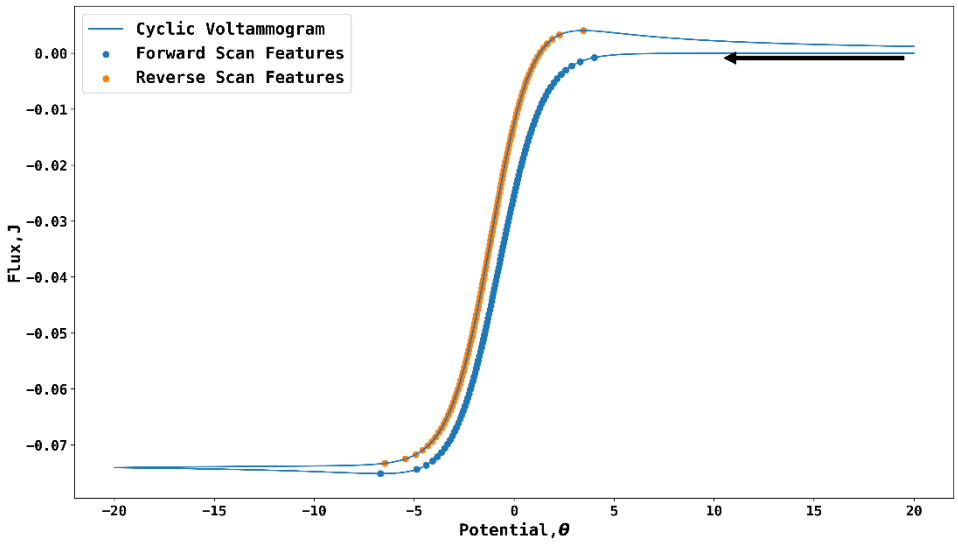

Figure 6.1. Schematic representation of extracting features from a voltammogram. Every 100 data points are extracted for forward scan and reverse scan at 1%, 2%, 3% … and 100% of peak current respectively.

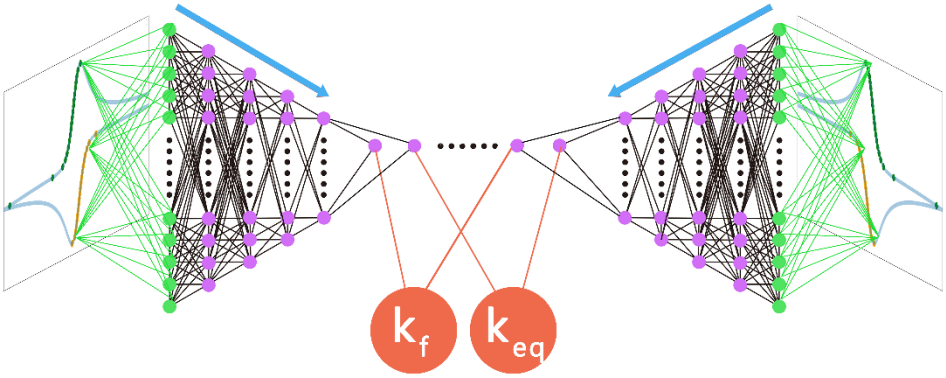

Figure 6.2. The structure of the neural network (Method A) predicting K_f and K_{eq} from features extracted from Figure 6.1. It consisted of two identical fully connected neural networks each with five hidden layers. Identical input was passed through each neural network, then the output of each network is then merged to predict k_f and K_{eq} of the voltammogram. This model took 2,000 iterations to obtain satisfactory result and 10,000 iterations were applied for optimal effect. The blue arrows indicate the direction of forward propagation.

The structure of the workflow of the three methods is captured in Figure 6.3. First, with a wide range of (dimensionless) scan rate σ, K_f and K_{eq} values, thousands of voltammograms were simulated (workflow shown in green). Then, the half peak potentials and peak fluxes were extracted from the voltammograms to be used sequentially in Method C later. Simulation parameters, voltammograms, half peak potentials and peak fluxes were then passed to the training steps of each method, with each method requiring different input and output data. In the training step, Method A (yellow workflow) used the voltammograms as training features, and the simulation parameters as training targets. Method B (blue workflow) used simulation parameters as training features, and voltammograms as training targets whilst Method C (purple workflow) used simulation parameters as training features, and half peak potentials and peak fluxes as its training targets. Then the trained neural networks were tested with features and targets from independent datasets to ensure sufficient accuracy. Finally, if the testing results were satisfactory by objectively judging the absolute or absolute percentage error of

prediction, the trained network models were ready for the prediction step where the models could use experimental data converted to dimensionless form for predictions of voltammograms and their related parameters as above.

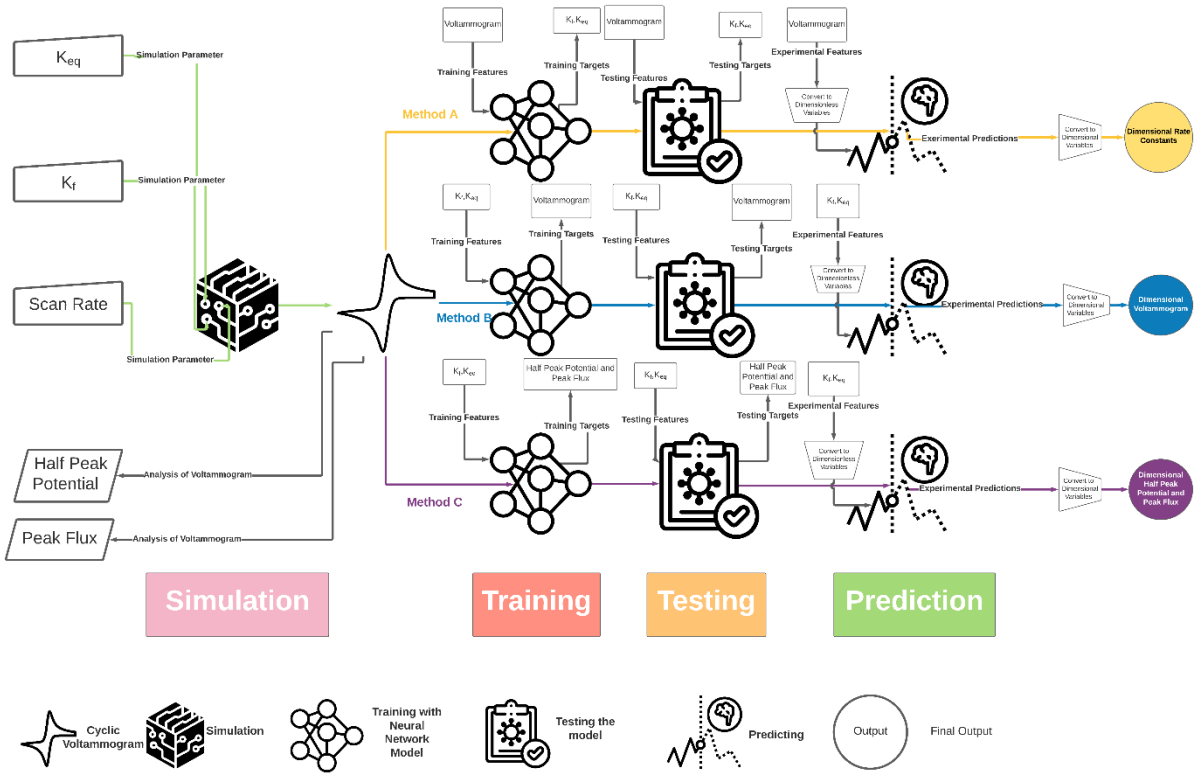

Figure 6.3. The workflow described in this chapter. From left to right, the figure describes the simulation, training, testing and prediction processes for Method A (yellow), Method B (blue) and Method C (purple). This flowchart has been designed using resources from Flaticon.com

6.4 Results and discussion

The data required by the three machine learning models was generated by simulation. We simulated voltammograms for different forward reaction rate constants, k_f, equilibrium constants K_{eq} and scan rates. Forty-one forward reaction rate constants from $10^{-2}\ s^{-1}$ to $10^{6}\ s^{-1}$ and 31 equilibrium constants from $10^{-3}\ M$ to $10^{-8}\ M$ in combination with 10 scan rates from $1\ mV/s$ to $10^{6}\ V/s$ were simulated. Note that voltammetry at $1\ mV/s$ is near the steady state limit which showed a slight current maximum (as expected due to residual traces

of linear diffusion) so that a peak current can be defined and hence "half peak potentials" can be correspondingly reported which very closely approximates the half wave potential under full steady state conditions. The range of simulations in dimensionless form was $10^{-5} \leq K_f \leq 10^3$, $10^{-5} \leq \mathrm{K}_{eq} \leq 1$ and $3.89 \times 10^{-5} \leq \sigma \leq 3.89 \times 10^4$. So, a total of 12710 voltammograms were generated for training to cover a wide range of parameters across the working surfaces and the generated voltammograms varied from steady state to normal peak-shaped voltammograms. Note that some combinations of k_f and K_{eq} would give k_b values outside of a reasonable physical magnitude, so simulations with $k_b > 10^9\ M^{-1}s^{-1}$ corresponding to diffusional control of the $A + C$ reaction in solution were not included for testing and are not shown on the working surfaces. Figure 6.4 shows the working surface of dimensionless steady state peak flux and half peak potential, respectively as a function of K_f and K_{eq} for a dimensionless scan rate of 3.89×10^{-5}; The peak flux presented is the peak flux of forward scan, and half peak potential is the potential of forward scan where the flux is half of peak flux. Figure 6.4a showed that smaller K_f and K_{eq} values would result in steady state flux close to zero, which was as expected since smaller K_{eq} value would generate smaller C_A^*, the bulk concentration of species A on the start of voltammetric scan. A smaller K_f value indicated a slow preceding chemical reaction to generate species A for the electrochemical reaction. Figure 6.4b shows the corresponding working surface of the shift in dimensionless half wave potential from the formal potential of the A/B couple again for the dimensionless scan rate of 3.89×10^{-5}. It is evident that higher K_f and K_{eq} values would move dimensionless half peak potential closer to zero, suggesting that the dissociative CE reaction was more apparently electrochemically reversible at such values. Lower K_f and K_{eq} values, on the contrary, would shift the half peak potential to more negative values, corresponding to higher overpotential.

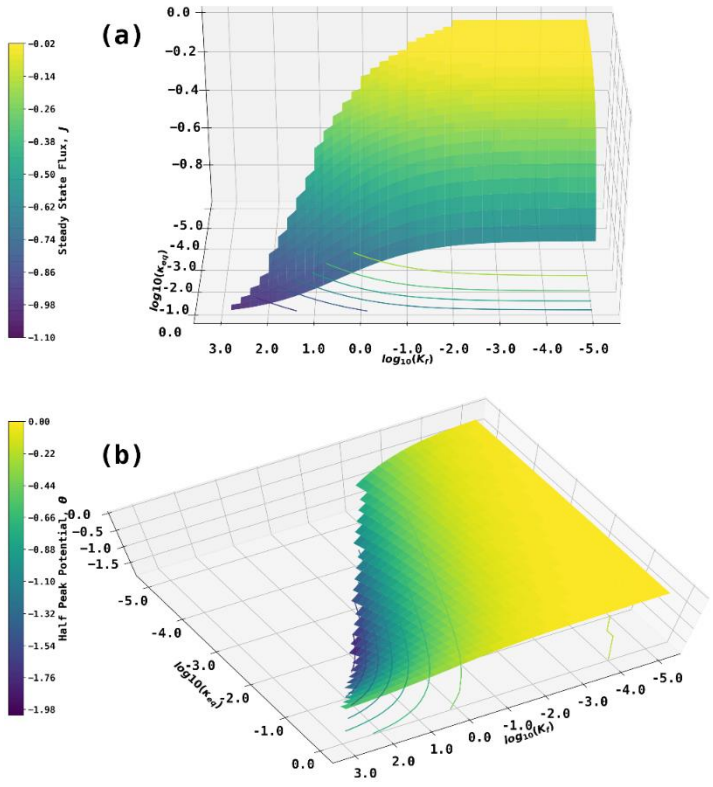

Figure 6.4. (a) The working surface of dimensionless peak flux at different combinations of K_f and K_{eq} values; (b) The working surface of dimensionless half peak potential at different combinations of K_f and K_{eq} values. The dimensionless scan rate for the working surfaces is 3.89×10^{-5}; X and Y axis are shown in log_{10} scale.

6.4.1 Method A: predicting rate and equilibrium constants from voltammograms

Simulated voltammograms were used for the training of Method A to predict rate constants from measured (or, as demonstrated in this chapter, simulated) voltammetry. Figure 6.5 shows the results of predicting K_{eq} from voltammograms generated with different combinations of K_f and K_{eq}. The X and Y axes represent the K_f and K_{eq} values of the voltammograms used for training plotted logarithmically, and the surface shown as the Z-axis represents the predicted K_{eq} values. To test the accuracy of the program, an independent set of

voltammograms were used for testing, and the predicted results are shown as scatter points in the space. Red scatter points represent predicted rate constants above the real values, and blue scatter points represent predicted rate constants below the real values. The sizes of scatter points are directly proportional to the absolute scale of the error magnitudes. The following equations describe calculation of the percentage error and its presentation as a scatter point on the 3D plot:

$$\epsilon = \frac{K_{prediction} - K_{real}}{K_{real}} \times 100\%, \quad \begin{cases} \epsilon > 0\%, red, size \propto |\epsilon| \\ \epsilon < 0\%, blue, size \propto |\epsilon| \end{cases} \tag{6.14}$$

Figure 6.6 similarly presents data regarding predicting K_f. From Figure 6.5 and Figure 6.6, 100% and 92.15% of the predicted rate constants, K_{eq} and K_f, respectively, were within 10% in absolute error, in the absence of any noise added to the voltammogram used for training and testing. The relatively small error suggested that Method A might reliably predict rate constants from the voltammograms. The distribution of errors, suggested by Figure 6.5b and Figure 6.6b, showed that the distributions of errors were centered around 0%, and the AI tends to underestimate the rate constants since the mode of distribution was below 0%. The scatter points in Figure 6.5b showed that the method tended to underestimate K_{eq} when input K_{eq} values were small and similarly, Figure 6.5b showed that the method tended to underestimate K_f when input K_f values were large. Although the method performed well as most predictions from the testing voltammograms were within 10% error, it should be still used with caution when suspecting the input K_{eq} is small and input K_f is large.

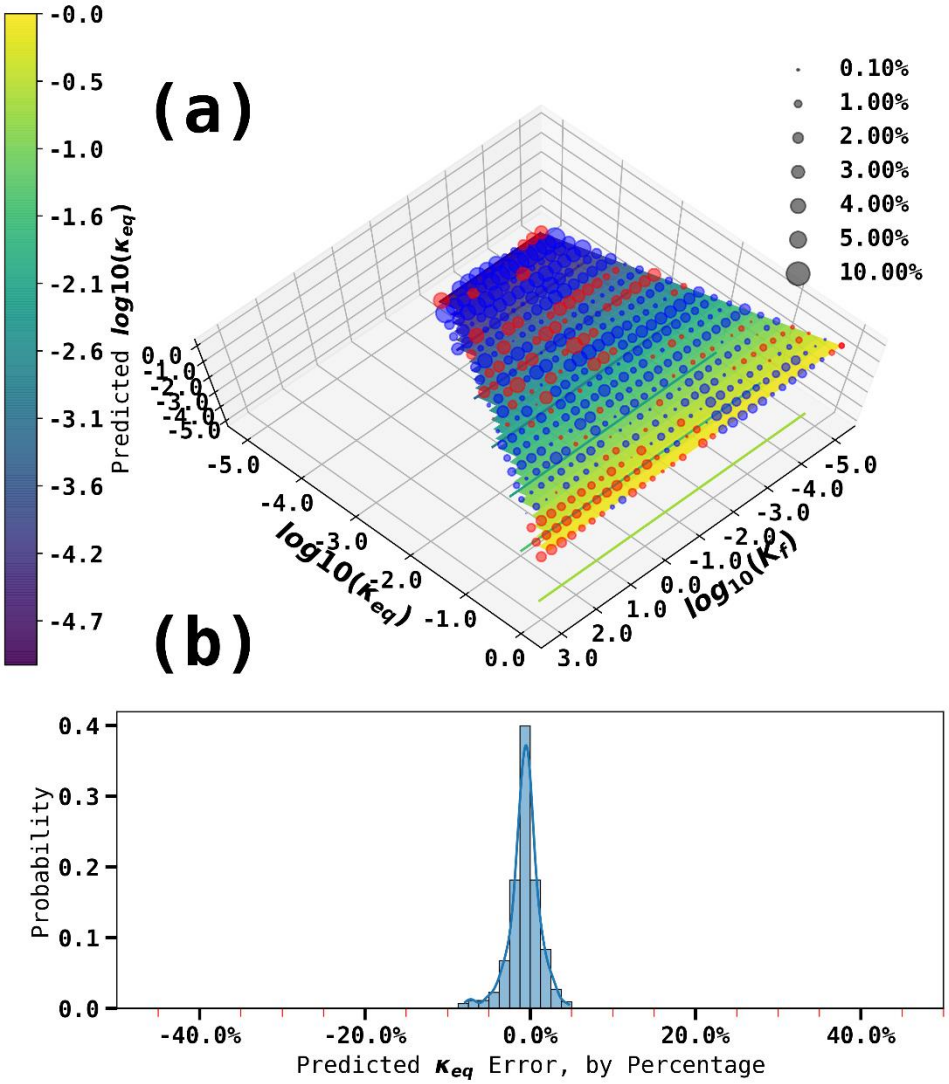

Figure 6.5. (a) Predicted K_{eq} as a function of the values of K_{eq} and K_f used for simulation with a scan rate of $\sigma = 3.89 \times 10^{-5}$. The surface represents the 'true' K_{eq}. The scatter points represent K_{eq} predicted from independent testing voltammograms. The sizes of the scatter points are proportional to the errors' magnitude. Only testing data points within 10% absolute percentage error are shown. (b) The distribution of errors for testing voltammograms with kernel density estimation.

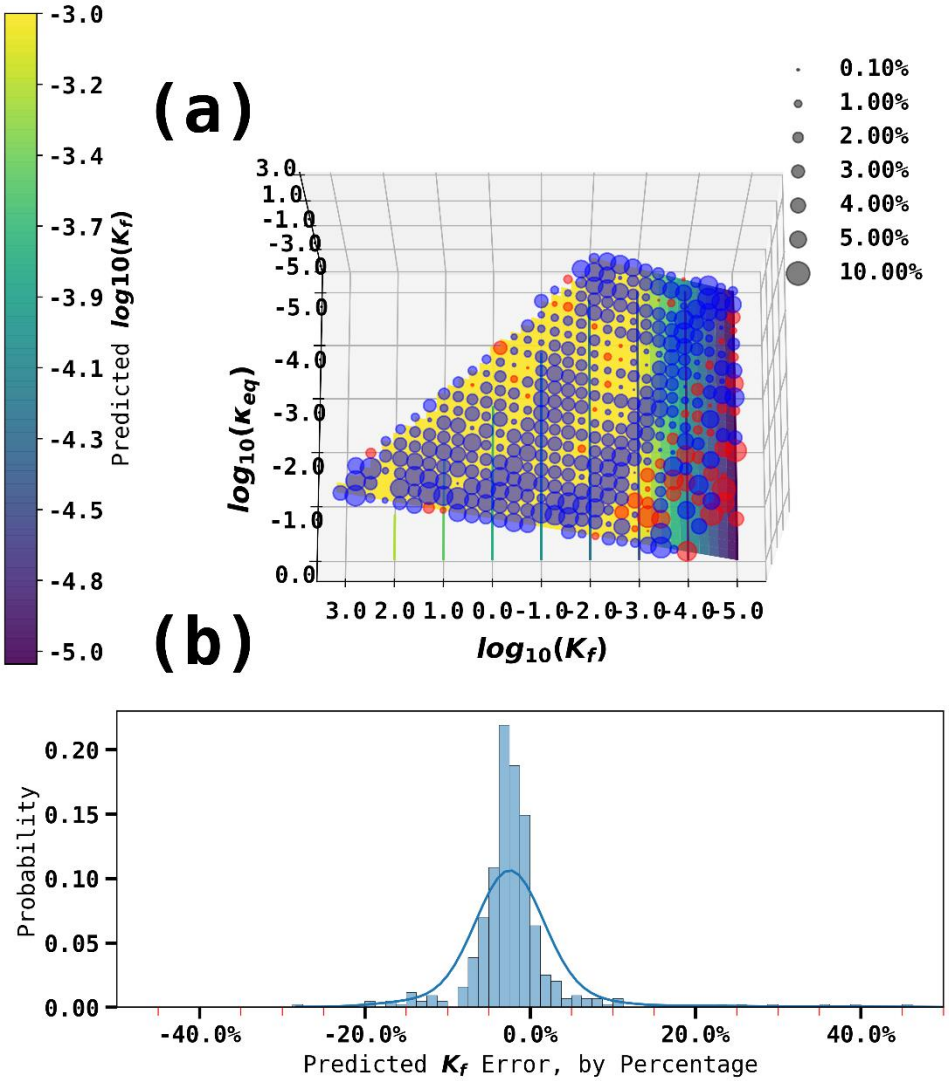

Figure 6.6. (a) predicted K_f as a function of the values of K_{eq} and K_f used for simulation with a scan rate of $\sigma = 3.89 \times 10^{-5}$. The surface represents the 'true' K_f. The scatter points represent K_f predicted from independent testing voltammograms. The sizes of the scatter points are proportional to the errors' magnitude. Only testing data points within 10% absolute percentage error are shown. (b) The distribution of errors for testing voltammograms with kernel density estimation.

All experimental data are subject to instrumental (and other) noise. We therefore evaluated the performance of all models, including Model A, when training after an appropriate noise level was added to the simulated voltammograms as illustrated in Figure 6.7 corresponding to small values of K_f and K_{eq} on the working surface: $K_{eq} = 10^{-5}$, $K_f = 10^{-5}$ and a scan rate of 3.89×10^{-5}. In Figure 6.7, normally distributed noise levels of different

magnitude from $10^{-4}J_{max}$ to $10^{-7}J_{max}$, are shown added to the original voltammogram, where J_{max} is the dimensionless current of the voltammetry of a simple $A + e \rightleftarrows B$ reaction at the same scan rate. For the results discussed below, a noise level of $10^{-4}\,J_{max}$ was used. The Gaussian noise was added to the flux of voltammogram as:

$$J_{with\ noise} = J + x \times 10^{-4}J_{max}, x{\sim}\varphi(x) \qquad \textbf{(6.15)}$$

and $\varphi(x)$ is the standard normal distribution function where $\varphi(x) = \frac{e^{-\frac{x^2}{2}}}{\sqrt{2\pi}}$ and x is the random number normally distributed with the standard normal distribution $\varphi(x)$.

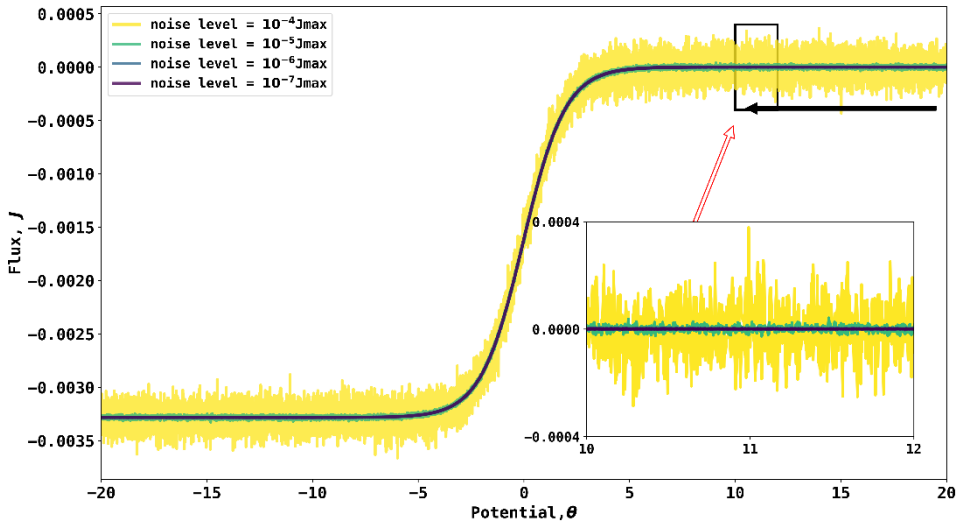

Figure 6.7. Simulated voltammogram at $\sigma = 3.89 \times 10^{-5}$, $K_{eq} = 10^{-5}$ and $K_f = 10^{-5}$ with different noise levels. The black arrow indicates the initial direction of voltammetric scan.

To test the performance of Method A with noisy voltammetry, noise of the magnitude $10^{-4}\,J_{max}$ was first added to the independent training and testing voltammograms. Then the resulting voltammograms were smoothened using a Savitzky-Golay filter [32] and then used for training and testing of the prediction of rate constants with Method A. Shown in Figure 6.8 and Figure 6.9, when predicting K_{eq} and k_f from testing voltammetry with noise level $10^{-4}J_{max}$ added, 93.50% and 80.27% of predictions were within 10% error. Figure 6.8b and Figure 6.9b

suggest that the errors centred around 0%, skewed slightly to the right, suggesting that the method tended to overestimate the rate constants.

Other levels of noises, $10^{-3}J_{max}$ and $10^{-5}\,J_{max}$ were also added to the training and testing voltammograms and their accuracy of predictions was also measured. When the noise level was $10^{-3}\,J_{max}$, 61.9% and 52.0% of predictions for K_{eq} and K_f respectively, were within 10% error; when noise level was $10^{-5}Jmax$, 97.78% and 89.46% of predictions were within 10% error. It was concluded that noise levels of up to $10^{-4}J_{max}$ allowed a realistic analysis of the data. Besides white noise, the neural network may be further tweaked by the user to handle influence of double-layer capacitance, convection and migration effects.

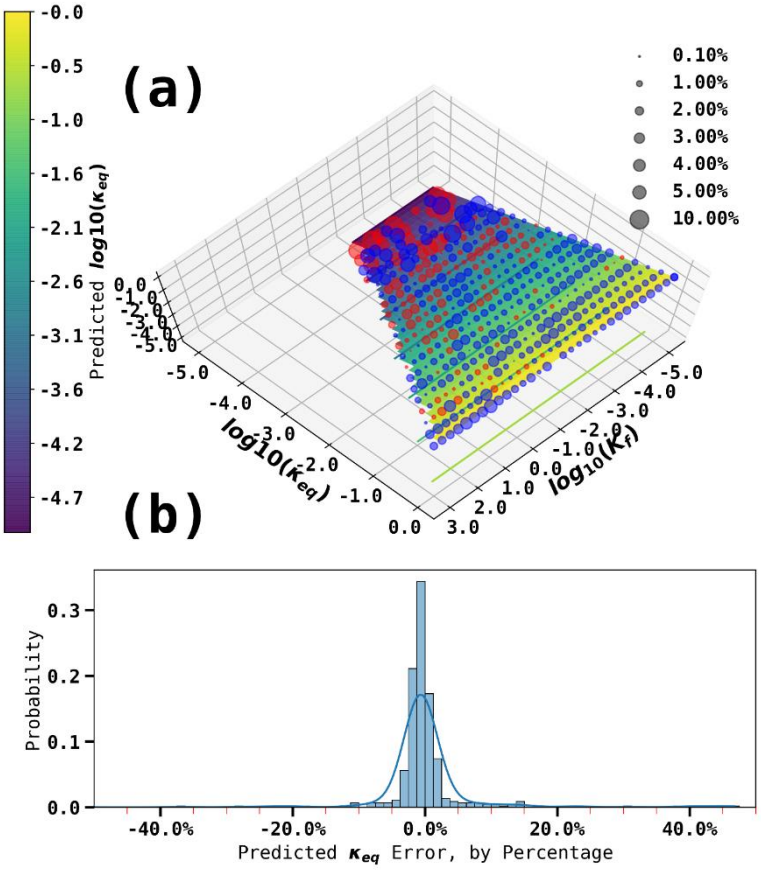

Figure 6.8. (a) predicted K_{eq} as a function of the values of K_{eq} and K_f used for simulation with a scan rate of $\sigma = 3.89 \times 10^{-5}$. The surface represents the 'true' K_{eq}. The scatter points represent K_{eq} predicted from independent testing voltammograms with noise level $10^{-4}J_{max}$. The sizes of the scatter points are proportional to the errors' magnitude. Only testing data points

within 10% absolute percentage error are shown. (b) The distribution of errors for testing voltammograms with kernel density estimation.

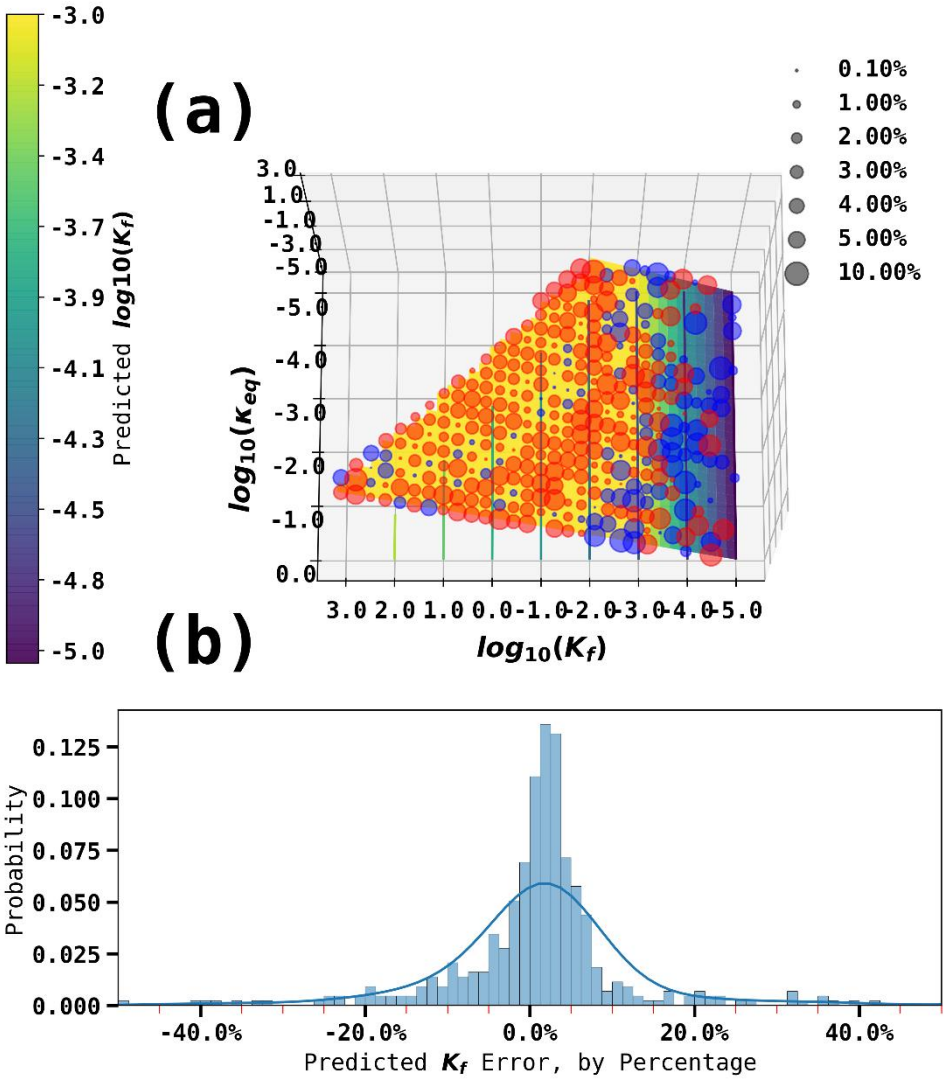

Figure 6.9. (a) predicted K_f as a function of the values of K_{eq} and K_f used for simulation with a scan rate of $\sigma = 3.89 \times 10^{-5}$. The surface represents the 'true' K_f. The scatter points represent K_f predicted from independent testing voltammograms with noise level $10^{-4} J_{max}$. The sizes of the scatter points are proportional to the errors' magnitude. Only testing data points within 10% absolute percentage error are shown. (b) The distribution of errors for testing voltammograms with kernel density estimation.

6.4.2 Method B: predicting voltammograms from known parameters

The functionality of method B is the reverse of method A: it predicts a voltammogram given the dimensionless parameters σ, K_f and K_{eq}. Using the same 12710 simulation

voltammograms mentioned above as the training dataset, the features used in the AI model were the 3 parameters and the targets were predicting the 200 potentials and 200 fluxes defining the voltammogram, from 1%, 2%, 3%…, 100% of the peak currents on the forward and reverse scans as discussed above. So, the targets contained 400 data points: the first 200 data points contained potentials and currents for the forward scan, and the other 200 data points contained potentials and currents for the reverse scan. The neural network model was trained using the same training dataset mentioned above for 500 iterations and then tested with independent datasets.

Typical results are shown in Figure 6.10, generated for the three dimensionless variables: $\sigma = 3.89 \times 10^{-5}, K_f = 7.36 \times 10^{-4}$ and $\mathrm{K_{eq}} = 1.78 \times 10^{-2}$ (corresponding for example to the dimensional values: $\nu = 1\ mV/\ s$, $k_f = 7.36 \times 10^{-1}\ s^{-1}$ and $K_{eq} = 1.78 \times 10^{-5}\ M$ when $r_e = 10^{-6}\ m$, $D_{all\ species} = 10^{-9}\ m^2/s$ and $c_{X,Total} = 1\ mM$). The neural network evidently sufficiently reproduces the characteristic features of the true voltammogram by visually inspecting Figure 6.10. To quantitatively assess the accuracy of the method, the errors of predicting forward scan potentials, forward scan fluxes, reverse scan potentials and reverse scan fluxes for all the testing datasets are shown in Figure 6.11, which suggests that method B tended to slightly overestimate fluxes and potentials, however more than 99% of predictions of dimensionless potentials had absolute errors within $\epsilon_\theta = 0.10$, corresponding to the dimensional potential of 2.6 mV (298K); more than 99% of predictions of dimensionless flux had absolute errors within $\epsilon_J = 0.01$, corresponding to a dimensional current of 6 nA, where ϵ_θ and ϵ_J are the difference between predicted potential and flux from "true" potential and flux, respectively. The relatively small errors of predicting characteristic potentials and fluxes of the voltammograms suggest that Method B can be usefully applied to predict voltammograms given suitable input parameters. Method B also has comparative advantage in

contrast with 2 hours on average to simulate a voltammogram, as predicting a voltammogram on average took only 0.015 second using Method B.

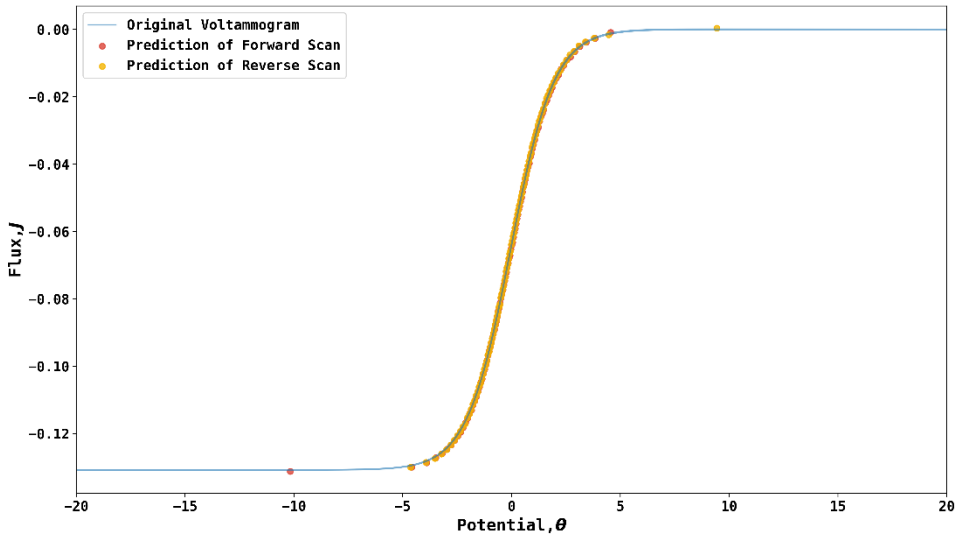

Figure 6.10. Using $\sigma = 3.89 \times 10^{-5}, K_f = 7.36 \times 10^{-4}$ and $K_{eq} = 1.78 \times 10^{-2}$ as input parameters, the neural network described in Method B predicted characteristics features of the steady state voltammogram. The features are plotted along with original voltammogram.

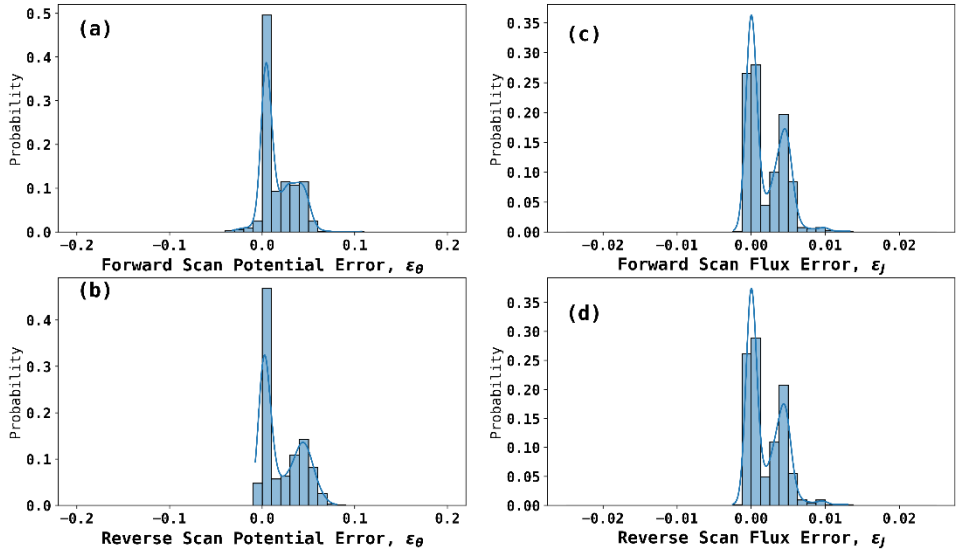

Figure 6.11. Errors of predicting voltammograms using dimensionless parameters including scan rate σ, K_f and K_{eq}. (a) Error distribution for prediction of forward scan potentials. (b) Error distribution for prediction of reverse scan potentials. (c) Error distribution for prediction of forward scan fluxes. (d) Error distribution for prediction of reverse scan fluxes. Kernel density estimations are included with the histogram

6.4.3 Method C: predicting the half peak potential and peak flux from rate and equilibrium constants

Method C is designed to be useful for experimental scientists to allow them to directly estimate half peak potentials and peak fluxes of steady state voltammogram by using various dimensional parameters including scan rate ν, forward reaction rate constant, k_f, equilibrium constant, K_{eq}, radius of electrode, r_e, diffusion coefficients and bulk concentration of all species to automatically calculate the three dimensionless parameters: σ, K_f and K_{eq}. The three dimensionless parameters are then used as inputs for the method and the outputs are peak flux and half peak potential. On the working surface, the peak flux presented is the peak flux of forward scan, and half peak potential is the potential of forward scan where the flux is half of peak flux. The neural network of this method was first trained with the three dimensionless parameters of training voltammograms mentioned above to predict peak flux and half peak potential extracted from the training voltammograms. It was then tested with an independent dataset to evaluate the accuracy of this method.

Typical results are shown in Figure 6.12, in which the working surface shows the half peak potential at different combination of K_{eq} and K_f values for a dimensionless scan rate of $\sigma = 3.89 \times 10^{-5}$. The scatter points show the predicted peak flux values using independent testing datasets; sizes and colours correspond to magnitude and direction of errors respectively: red and blue scatter points represent overestimations and underestimations of 'true' values and their sizes directly proportional to the magnitude of errors. The error of predicting half peak potential, ϵ_θ, is simply the difference between predicted half peak potential via AI and the 'true' half peak potential determined by simulation. As shown in Figure 6.12b, 97.09% of ϵ_θ were found within $\epsilon_\theta = 0.01$, corresponding to a dimensional potential of 0.3 mV (298K). Figure 6.13 shows the corresponding data similarly presented regarding the steady state flux prediction

again for $\sigma = 3.89 \times 10^{-5}$ and where ϵ_J is now the difference between predicted dimensionless peak flux and 'true' peak flux from simulation. As shown in Figure 6.13b, 100% of the absolute errors predicting dimensionless peak flux are within $\epsilon_J = 0.01$, corresponding to a dimensional current of 6 nA. The relatively small errors of predicting half peak potential and peak flux suggest that Method C can be usefully applied to predict the working surfaces of half peak potential and peak flux given suitable input parameters.

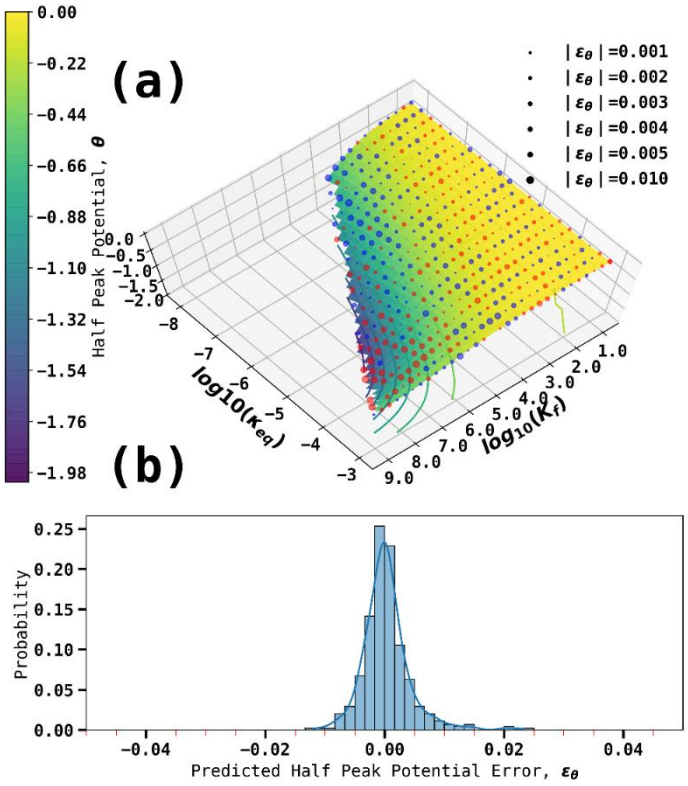

Figure 6.12. (a) The predicted half peak potential as a function of K_{eq} and K_f at $\sigma = 3.89 \times 10^{-5}$. The working surface shows the half peak potential predicted from simulation. The scatter points represent half peak potential predicted via AI and the sizes and colours of the scatter points are proportional to magnitude and direction of error, ϵ_θ as discussed in text. Only testing data points within $\epsilon_\theta = 0.01$ are shown. (b) The distribution of ϵ_θ.

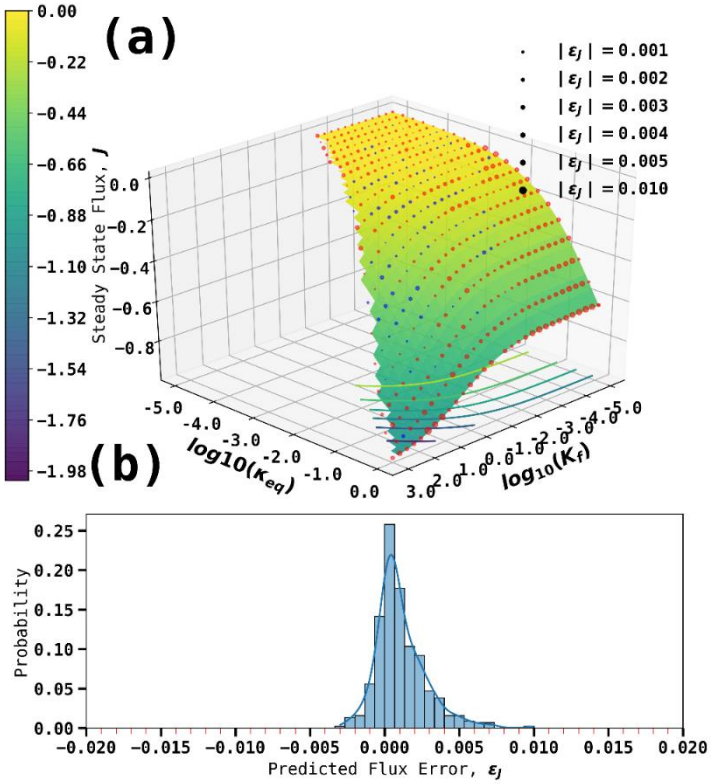

Figure 6.13. (a) the predicted peak flux as a function of K_{eq} and K_f at $\sigma = 3.89 \times 10^{-5}$. The working surface shows the peak flux predicted from simulation. The scatter points represent peak flux predicted via AI and the sizes and colours of the scatter points are proportional to magnitude and direction of error, ϵ_J as discussed in text. All testing data points are shown. (b) The distribution of ϵ_J.

6.5 Conclusions

Artificial intelligence has been used to learn the characteristics of the dissociative CE mechanism allowing both the easy prediction of the voltammetry expected on the basis of known parameters notably the rate and equilibrium constants, formal potential and the diffusion coefficients as well as the inverse process, namely the analysis of noisy experimental data so as to extract unknown parameters. The method avoids in the first place, the need for a full re-simulation for each change of parameters, and in the second case, the need for trial-and-error

approaches to best fit simulation and experiment. The latter feature offers considerable promise for experimental voltammetry.

We further predict that AI method can have a significant impact on, and qualitatively change our approach to mechanistic electrochemistry which in turn underpins many studies in energy transformation and in chemical sensing. We note that the previous work of Kennedy, Zheng and Bond[29] has provided a basis for the qualitative classification of mechanism such as E, EE, or EC by treating the voltammograms as 'pictures' and successfully distinguishing between examples with one voltammetric feature (E or EC) or two (EE) and between single features which either possess both a forwards and a backward (E) or solely exhibit just a forward peak (EC). In this chapter we have assumed the electrochemical mechanism for consideration is known. This knowledge we presume to arise from experimenter's expertise and chemical insight and to be likely based on a qualitative assessment of initial data. On this basis we have provided the means for the verification of the experimenter's hunch (or not) and for the extraction of kinetic and thermodynamic parameters. Going forward a similar approach to the other mechanisms beyond the dissociative CE mechanism might be developed (for example, ECE, DISP, EC' mechanisms and for surface bound species) and ultimately merged with the ideas of Kennedy et al[29] to facilitate automated data analysis of electrode reactions of even unknown chemistry.

Meanwhile it is salutary to note the necessary tasks required of an experimenter to undertake the desired mechanistic analysis using the approach presently advocated. First voltammetric data in the form of current voltage curves must be generated. Second, if these curves are to be analysed in full (using pairs of current and potential values from all parts of the voltammogram) using the above theory as presented, it is important to verify that the electron transfer in the A/B redox couple approximates to being electrochemically reversible.

Third, if so then analysis requires the experimenter to decide which mechanistic parameters are known and which are not. In the above we have assumed that $\boldsymbol{k_f}$ and $\boldsymbol{K_{eq}}$ are known, and is very likely in the case of electrode radius, the total concentration of $\boldsymbol{X}$, the formal potential of the $\boldsymbol{A/B}$ couple and the diffusion coefficients of the species A, B, C and X are also known. Diffusion coefficients will either have been previously reported or can be estimated, for example in some cases using the Wike-Change[33] approximation or similar. The formal potentials may be known but if not, or if the A/B couple is electrochemically irreversible then the experimenter may decide the focus on limiting current data in the steady state limit as a function of total concentration so as to avoid to know details of electrode kinetics. Fourth, the trained AI program is used to generate best fit parameters for $\boldsymbol{k_f}$ and $\boldsymbol{K_{eq}}$ and the other unknowns, if any, such as one or more diffusion coefficients. Fifth we strongly recommend simulation of the full set of voltammograms using the derived best fit parameters to visually critically assess the quality of fit. In the case of acceptable fit the magnitude of likely errors can be assessed similarly.

The authors are presently undertaking several experiments on diverse systems so as to implement and then report on these recommendations in practice. Meanwhile the extent of the tasks required to establish a mechanism point to the need for diligence on the part of the experimenter and the essential need for data converting parameters such as formal potentials and diffusion coefficients.

In the next chapter, we will apply a modified version of Method A, to extract kinetic and thermodynamic parameters from real experiments.

References

1. D. Silver, J. Schrittwieser, K. Simonyan, I. Antonoglou, A. Huang, A. Guez, T. Hubert, L. Baker, M. Lai and A. Bolton, *Nature*, 2017, **550**, 354-359.
2. M. AlQuraishi, *Bioinformatics*, 2019, **35**, 4862-4865.

3. H. Chen, E. Kätelhön, H. Le and R. G. Compton, *Anal. Chem.*, 2021, **93**, 13360-13372.
4. R. G. Compton and C. E. Banks, *Understanding voltammetry*, World Scientific, London, 3rd edn., 2018.
5. H. H. Girault, *Analytical and physical electrochemistry*, EPFL Press, New York, 2004.
6. A. C. Fisher, *Electrode dynamics*, Oxford University Press, Oxford, 1996.
7. I. Svir, A. Oleinick, O. V. Klymenko and C. Amatore, 2018.
8. M. Rudolph, *J. Electroanal. Chem. Interfacial Electrochem.*, 1990, **292**, 1-7.
9. J.-M. Savéant, *Elements of molecular and biomolecular electrochemistry: an electrochemical approach to electron transfer chemistry*, John Wiley & Sons, 2006.
10. R. Miao, L. Chen and R. G. Compton, *Sci. China. Chem.*, 2021, **64**, 322-329.
11. R. Miao, L. Shao and R. G. Compton, *Nano Res.*, 2021, DOI: 10.1007/s12274-021-3353-8.
12. R. Miao and R. G. Compton, *J. Phys. Chem. Lett.*, 2021, **12**, 1601-1605.
13. V. Marinović and A. R. Despić, *Russ. J. Electrochem.*, 2004, **40**, 995-999.
14. T. Fang, L.-L. Zhou, L.-Z. Fu, S.-Z. Zhan and Q.-Y. Lv, *Polyhedron*, 2015, **85**, 355-360.
15. J. A. Rodrigues, C. M. Rodrigues, P. J. Almeida, I. M. Valente, L. M. Gonçalves, R. G. Compton and A. A. Barros, *Anal. Chim. Acta*, 2011, **701**, 152-156.
16. J. Mauzeroll, E. A. Hueske and A. J. Bard, *Anal. Chem.*, 2003, **75**, 3880-3889.
17. J. G. Limon-Petersen, I. Streeter, N. V. Rees and R. G. Compton, *J. Phys. Chem. C*, 2009, **113**, 333-337.
18. J. A. Alden, F. Hutchinson and R. G. Compton, *J. Phys. Chem. B*, 1997, **101**, 949-958.
19. R. G. Compton, E. Laborda, E. Kaetelhoen and K. R. Ward, *Understanding voltammetry: simulation of electrode processes*, World Scientific London, 2nd edn., 2020.
20. J. K. Novev and R. G. Compton, *Curr. Opin. Electrochem.*, 2018, **7**, 118-129.
21. A. Fick, *Ann. Phys.*, 1855, **170**, 59-86.
22. A. Fick, *Lond. Edinb. Dubl. Phil. Mag.*, 1855, **10**, 30-39.
23. J. A. V. Butler, *Trans. Faraday Soc.*, 1924, **19**, 729-733.
24. T. Erdey-Grúz and M. Volmer, *Z. Phys. Chem.*, 1930, **150**, 203-213.
25. A. Einstein, *J Annalen der physik*, 1905, **17**, 549-560.
26. M. Abadi, P. Barham, J. Chen, Z. Chen, A. Davis, J. Dean, M. Devin, S. Ghemawat, G. Irving and M. Isard, 2016.
27. A. Liaw and M. Wiener, *R news*, 2002, **2**, 18-22.
28. T. Chen and C. Guestrin, 2016.
29. G. F. Kennedy, J. Zhang and A. M. Bond, *Anal. Chem.*, 2019, **91**, 12220-12227.
30. A. Géron, *Hands-on machine learning with Scikit-Learn, Keras, and TensorFlow: Concepts, tools, and techniques to build intelligent systems*, O'Reilly Media, 2019.
31. D. P. Kingma and J. Ba, *arXiv preprint arXiv:1412.6980*, 2014.
32. P. Virtanen, R. Gommers, T. E. Oliphant, M. Haberland, T. Reddy, D. Cournapeau, E. Burovski, P. Peterson, W. Weckesser, J. Bright, S. J. van der Walt, M. Brett, J. Wilson, K. J. Millman, N. Mayorov, A. R. J. Nelson, E. Jones, R. Kern, E. Larson, C. J. Carey, İ. Polat, Y. Feng, E. W. Moore, J. VanderPlas, D. Laxalde, J. Perktold, R. Cimrman, I. Henriksen, E. A. Quintero, C. R. Harris, A. M. Archibald, A. H. Ribeiro, F. Pedregosa, P. van Mulbregt, A. Vijaykumar, A. P. Bardelli, A. Rothberg, A. Hilboll, A. Kloeckner, A. Scopatz, A. Lee, A. Rokem, C. N. Woods, C. Fulton, C. Masson, C. Häggström, C. Fitzgerald, D. A. Nicholson, D. R. Hagen, D. V. Pasechnik, E. Olivetti, E. Martin, E. Wieser, F. Silva, F. Lenders, F. Wilhelm, G. Young, G. A. Price, G.-L. Ingold, G. E. Allen, G. R. Lee, H. Audren, I. Probst, J. P. Dietrich, J. Silterra, J. T. Webber, J. Slavič,

J. Nothman, J. Buchner, J. Kulick, J. L. Schönberger, J. V. de Miranda Cardoso, J. Reimer, J. Harrington, J. L. C. Rodríguez, J. Nunez-Iglesias, J. Kuczynski, K. Tritz, M. Thoma, M. Newville, M. Kümmerer, M. Bolingbroke, M. Tartre, M. Pak, N. J. Smith, N. Nowaczyk, N. Shebanov, O. Pavlyk, P. A. Brodtkorb, P. Lee, R. T. McGibbon, R. Feldbauer, S. Lewis, S. Tygier, S. Sievert, S. Vigna, S. Peterson, S. More, T. Pudlik, T. Oshima, T. J. Pingel, T. P. Robitaille, T. Spura, T. R. Jones, T. Cera, T. Leslie, T. Zito, T. Krauss, U. Upadhyay, Y. O. Halchenko, Y. Vázquez-Baeza and C. SciPy, *Nat. Methods*, 2020, **17**, 261-272.

33. C. Wilke and P. Chang, *AIChE J.*, 1955, **1**, 264-270.

Chapter 7 Analysing Experimental Voltammetry with Artificial Intelligence: The Dissociation of Acetic Acid in Aqueous Solution

The last chapter introduced the application of artificial intelligence in voltammetry using training, testing and validation data entirely based on simulation data. This chapter further challenges the methods mentioned before with authentic experimental results obtained by the authors with the predictions of artificial intelligence validated with prior literature data for the inferred paramters[1]. The work has been published in *Analytical Chemistry*[2].

Artificial intelligence (AI) is used to quantitatively analyse the voltammetry of the reduction of acetic acid in aqueous solution generating thermodynamic and kinetic data. Specifically, the variation of the steady state current for the reduction of protons at a platinum microelectrode as a function of the bulk concentration of acetic acid is recorded and analysed giving data in close agreement with independent measurements, provided the AI is trained with accurate and precise knowledge of diffusion coefficients of acetic acid, acetate ions and H^+.

7.1 Introduction

Machine learning has, despite its enormous potential, been used only sporadically in the quantification of analytes in different electroanalytical contexts and less in fundamental electrochemistry. For example, in food chemistry, a support vector machine approach was used to distinguish ale from lager based on cyclic voltammetry, and a neural network was able to estimate alcoholic content[3]. In environmental chemistry, along with cyclic square wave voltammetry, neural networks were applied to quantify the concentration of various pollutants in sea water, including copper, lead, mercury, paraquat (PQ) and Bisphenol-A (BPA)[4]. In biosensor development, by integrating with fast-scan cyclic voltammetry (FSCV) and an

autoencoder, a variant of an artificial neural network, Mao et al. impressively achieved in vivo quantification of the concentration of dopamine, ascorbate and NaCl in rat brains[5]. Multi-component detection of insulin and glucose in serum with the help of neural networks was also reported by Liu et al. recently[6]. Beyond chemical analysis, in fundamental electrochemistry, Bond et al. reported the successful classification of electrode reaction mechanisms (specifically E, EE and EC type processes) using a convolutional neural network[7] and claimed recognition of electrode kinetic between Butler-Volmer and Marcus-Hush types using Bayesian inference[8]. More generally, at least in principle, when electrochemistry is equipped with machine learning for data analysis, the latter allows correlation and analysis of electrochemical data (including voltammograms and chronoamperograms) without the need for deploying mathematically analytical expressions.

Despite the emerging reports on the application to quantification of analytes, the study of electrochemical reactions and mechanisms with machine learning is still largely lacking. Bond and colleagues recently communicated the need for quantification of confidence limits and errors in parameter estimation when making a comparison of experimental data and simulated data. They attributed such absences to possible computational limitations[9]. In response to the desirability for machine learning of parameters in electrochemical reactions, we recently communicated, as reported in the previous chapter, the theoretical study of training neural networks on simulated voltammograms to infer rate/equilibrium constants from the voltammograms of a dissociative CE_{rev} reaction and the reverse process of predicting voltammograms from such constants without recourse to further simulation[10]. The general scheme of the dissociative CE reaction is:

$$\begin{cases} X \underset{k_b}{\overset{k_f}{\rightleftarrows}} A + C, K_{eq} = \dfrac{k_f}{k_b} \\ A + e \rightleftarrows B \end{cases} \qquad \textbf{(7.1)}$$

where k_f and k_b are forward and reverse reaction rate constants respectively and the equilibrium constant, $K_{eq} = \frac{k_f}{k_b}$.

In this chapter we next develop this work in the context of experiment and apply the approach to the extraction of thermodynamic and kinetic parameters for the acetic acid dissociation reaction in aqueous solution enabling comparison with extensive independent reports in the literature so permitting verification and critical evaluation of the AI approach including limitations. In particular authentic experimental data will contain finite background currents and possible contributions from migration and/or convection and/or double layer charging which inevitably distort, to a greater or lesser extent, the voltammetry from that predicted via simulation. Accordingly, it is important to address the question as to whether the AI approach to the analysis of voltammetry can 'live with' the inevitable imperfections of authentic experimental data.

Specifically, to facilitate proving the power of machine learning on parameter extraction from experiments, we quantitatively analyse current – concentration data to extract the thermodynamic and kinetic parameters (K_{eq} and k_f) of acetic acid dissociation using machine learning. The predicted parameters are then checked via simulation and comparison of the results with experiments. Electro-reduction of acetic acid is known to follow a dissociative CE process[11, 12]:

$$\begin{cases} CH_3COOH \underset{k_b}{\overset{k_f}{\rightleftarrows}} H^+ + CH_3COO^- \\ 2H^+ + 2e^- \rightleftarrows H_2 \end{cases} \quad \textbf{(7.2)}$$

Table 7.1 shows the reported K_{eq} and k_f values at 298 K in different aqueous environments where the presence of added electrolyte is known to cause both kinetic and thermodynamic salt effects, albeit relatively small in magnitude (see Table 7.1). K_{eq} values of acetic acid are

readily measured for example most simply from the pH of acetic acid solutions and reported as 1.754×10^{-5} M in pure water[13]. Higher values are seen when electrolyte is present (i.e., 2.82×10^{-5} M in 0.1 M KCl solution[14]). Measurement of k_f has been made by a variety of methods.

Non-electrochemical methods reported include the electrical pulse methods[15]; the high field dispersion and temperature jump method[16]; and the electric field jump (E-jump) relaxation technique[17]. Although acetic acid does not absorb at visible wavelength, a coloured acid-base indicator, Bromocresol green, was coupled in solution to enable spectroscopic detection using a square-wave field effect apparatus[18].

Electrochemical methods reported include: voltammetry using a hydrodynamic modulated rotating disc electrode and analysis using the modified Koutecky-Levich equation[11, 19]; the polarography on acetate-acetic acid solution of low buffering capacity[12]; and a two-cell technique, each with a rotating electrode connected by Wheatstone bridge circuit[20]. A summary of individually measured k_f and K_{eq} values is shown in Table 7.1. The values of k_f range widely from 1.91×10^5 to 3.46×10^6 s^{-1} in different solution compositions.

Table 7.1. Literature Values of the Equilibrium and the Rate Constants of the Acetic Acid Dissociation Reaction.

constant	solution composition	value and reference
K_{eq}, M	CH_3COOH in pure water	1.754×10^{-5}, [13]
	CH_3COOH, CH_3COONa in pure water	1.743×10^{-5} *to* 1.784×10^{-5},[21]
	CH_3COOH / 0.1106 M KCl(aq)	2.805×10^{-5}, [22]
	CH_3COOH/ 0.1 M of KCl, NaCl or LiCl respectively	2.82×10^{-5}, 2.79×10^5, 2.85×10^{-5}, [14]

	CH_3COOH/1 M KCl(aq)	3.06×10^{-5},[23]
k_f , s^{-1} , non-electrochemical methods	0.1×10^{-3} M CH_3COOH in pure water	8×10^5, [15]
	8.3×10^{-5} M CH_3COOH in pure water	8.7×10^5, [16]
	CH_3COOH in pure water	1.91×10^5, [17]
	CH_3COOH coupled with Bromocresol blue in pure water	1.3×10^6,[18]
k_f, s^{-1} electrochemical methods	2.7×10^{-3} M CH_3COOH , 0.03 M CH_3COONa / 1 $M\ KCl$	3.46×10^6, [11]
	2.17×10^{-3} M CH_3COOH / 1.475 M $(CH_3)_4N(Cl)$	1.58×10^6, [12]
	20×10^{-3} M CH_3COOH / 0.1 and 0.3 M KCl	9.1×10^5, [20]
	CH_3COOH /1 M KCl(aq)	3×10^5,[24]
	2.5×10^{-3} M CH_3COOH , 5×10^{-3} M CH_3COONa / 50:50 water-ethanol. Ionic strength adjusted to 1 M with KCl	2.9×10^5, [25]
	CH_3COOH/LiCl(aq) . Ionic strength adjusted to 1 M with LiCl	1.39×10^6, [26, 27]

In the following we report a simple three-step electrochemical approach for estimating these two constants. This chapter follows the work flow of method A reported before and in the previous chapter[10], but the technical implementation is bespoke to account for the exact experimental data.

First, measurements are made of the steady state current for the reduction of protons as a function of the bulk acetic acid concentration, $c^*_{CH_3COOH,total}$ at a Platinum microdisc

electrode. This approach was preferred to cyclic voltammetry because the steady state currents obtained at a microelectrode are independent of electrochemical rate constants and transfer coefficients whereas understanding and simulating a full voltammogram either at a macroelectrode or a micro-electrode for the reduction of H^+ from acetic acid dissociation would require a confident knowledge of the mechanism and the kinetic parameters of the hydrogen evolution reaction on Pt electrode, which remains controversial[28, 29]. Under the conditions employed in the present study, the steady state current depends only on k_f, K_{eq}, and $c^*_{CH_3COOH,total}$ assuming prior knowledge of diffusion coefficients.

Second, simulation of the expected limiting currents with different k_f, K_{eq} and bulk concentration of acetic acids was conducted to obtain the steady state current under different conditions and a neural network was trained and tested with simulated data. The features used for training were the steady state currents at different bulk concentrations of acetic acid and targets were the k_f and K_{eq} values for the acetic acid CE process.

Third, steady state currents obtained from experiments were fed into the trained network to give predictions of k_f and K_{eq} values which were compared with those in Table 7.1 facilitating generic insights into the AI approach. More generally the latter offers the prospect of simulation-free approaches to the quantitative analysis of voltammetric data in which simulations are only used to initially train the AI but thereafter there is no resort to expensive, commercial software, as the exact implementation of which can be user sensitive. The methodology thus promotes the analysis of data in a manner which easily comparable between laboratories. To this end we provide the simulation and machine learning programs for acetic acid reduction reported, along with raw experimental data, at:

https://github.com/nmerovingian/Acetic-Acid-Dissociation-AI

The simulation and machine learning programs for the theoretical study reported before[10] can be found at:

https://github.com/nmerovingian/dissociativeCE-Simulation-MachineLearning

The resources provided will enable readers and hopefully users to fully reproduce the results reported and possibly further explore the application of AI using the training data provided.

7.2 Theory

In this section we first discuss the formal potential of the H^+/H_2 couple and the expected half-wave potential for the reduction of protons in the case that if the proton reduction reaction is electrochemically reversible. Second we outline the simulation of the expected transport limited currents for the proton reduction as a function of K_{eq} and k_f, noting that computational approach is given in reference [10] apart from small changes in boundary conditions as outlined below.

7.2.1 Formal Potential and half wave potential of the $\mathbf{H^+/H_2}$ couple

The formal potential, $E^0_{f,H^+/H_2}$ of the H^+/H_2 couple has been shown to be given by:

$$E^0_{f,H^+/H_2} = E^0_{H^+/H_2} + \frac{RT}{F}\ln\frac{\gamma_{H^+}\sqrt{p^0}}{\sqrt{K_{H_2}10^{k_s c_s}a^0}} \quad \textbf{(7.3)}$$

where $E^0_{H^+/H_2}$ is the standard electrochemical potential, γ_{H^+} is the activity coefficient of H^+ ion in solution. k_s and c_s are the salt parameter and salt concentration respectively which accounts for salt-out effect in an electrolytic solution. p_0 and a_0 are standard pressure and standard activity which are 1 bar and 1 M respectively. K_{H_2} is the Henry's law constant for H_2. R, T and F are gas constant, temperature and Faraday constant respectively. Using parameters from Table 7.2, $E^0_{f,H^+/H_2}$ is calculated as -0.341 V vs. SCE [30].

The half wave potential assuming an electrochemically reversible H^+/H_2 couple for the reduction of protons at a uniformly accessible electrode has been derived previously[30]:

$$E_{1/2} = \frac{\frac{1}{2}\ln\left(\frac{c^*_{H^+}}{c^0}\frac{D_{H_2}}{D_{H^+}}\right)RT}{F} + E^0_{f,H_2/H^+} \qquad \textbf{(7.4)}$$

where $E_{1/2}$ is half wave potential and $c^*_{H^+}$ and c^0 are the bulk concentration of acetic acid and reference concentration (1 M) respectively. The dependence of the half-wave potential on the bulk proton concentration arises from the non-unity stoichiometry of the reaction[30, 31].The formal potential, $E^0_{f,H^+/H_2}$ as derived above is -0.341V vs. SCE. Using the reported pKa value of 4.756 of acetic acid[13] and bulk concentration of acetic acid as 10 mM, $c^*_{H^+}$ is calculated to be 4.10×10^{-4} M and $E_{1/2}$ is estimated as -0.448 V vs. SCE. On the other hand, assuming $c^*_{H^+}$ as the bulk concentration of acetic acid, the calculated $E_{1/2}$ is -0.408 V vs. SCE. Clearly from the CE process with describing the acetic acid reduction with the hypothetical assumption of reversible electrochemistry, the half wave potential would be expected to lie between -0.408 to -0.448 V.

Table 7.2. Parameters Used for Calculation of the Formal Potential of the $\boldsymbol{H^+/H_2}$ Redox Couple and for Simulation.

parameter	explanation	value
$E^0_{H^+/H_2}$ vs. SCE	standard potential of H^+/H_2 vs. saturated calomel electrode	-0.241V, [32]
D_{CH_3COOH}	diffusion coefficient of acetic acid	1.29×10^{-9} m^2 s^{-1} , [13]
$D_{CH_3COO^-}$	diffusion coefficient of acetate	1.089×10^{-9} m^2 s^{-1}, [13]

D_{H^+}	diffusion coefficient of hydrogen ion	$9.311 \times 10^{-9}\ m^2\ s^{-1}$, [13]
D_{H_2}	diffusion coefficient of hydrogen	$5.11 \times 10^{-9}\ m^2\ s^{-1}$, [13]
γ_{H^+}	activity coefficient of Hydrogen ion	0.754, [33]
K_{H_2}	Henry's Law constant of hydrogen	$1292\ bar\ M^{-1}$,[34]
c_{KNO_3}	concentration of KNO_3 electrolyte in experiment	0.1 M
k_{KNO_3}	salt parameter of KNO_3	$0.07\ M^{-1}$,[35]

7.2.2 Simulation equations

The mass transport is assumed to be exclusively diffusive, and the diffusion equations coupled with chemical reactions are solved to show how the steady-state limiting current at a microelectrode depends on the parameters k_f and K_{eq} for different acetic acid concentrations. Note that the electrochemical reaction on a microdisc electrode of radius r can be approximated as a hemispherical electrode with radius $\frac{2r}{\pi}$ to reduce the diffusion problem from two dimensions to one dimension. The relevant steady state diffusion equations can be formulated as:

$$\begin{cases} 0 = D_{CH_3COOH}\dfrac{\partial^2[CH_3COOH]}{\partial r^2} + \dfrac{2}{r}\dfrac{\partial[CH_3COOH]}{\partial r} - k_f[CH_3COOH] + k_b[H^+][CH_3COO^-] \\ 0 = D_{H^+}\dfrac{\partial^2[H^+]}{\partial r^2} + \dfrac{2}{r}\dfrac{\partial[H^+]}{\partial r} + k_f[H^+] - k_b[H^+][CH_3COO^-] \\ 0 = D_{H_2}\dfrac{\partial^2[H_2]}{\partial r^2} + \dfrac{2}{r}\dfrac{\partial[H_2]}{\partial r} \\ 0 = D_{CH_3COO^-}\dfrac{\partial^2[CH_3COO^-]}{\partial r^2} + \dfrac{2}{r}\dfrac{\partial[CH_3COO^-]}{\partial r} + k_f[H^+] - k_b[H^+][CH_3COO^-] \end{cases} \quad \textbf{(7.5)}$$

where D_j is the diffusion coefficient for species j.

If r_e is the radius of the hemispherical electrode, the boundary conditions at the surface of electrode for the steady state reduction of protons:

$$r = r_e \begin{cases} D_{CH_3COOH}\left(\dfrac{\partial[CH_3COOH]}{\partial r}\right)_{r=r_e} = 0 \\ [H^+]_{r=r_e} = 0 \\ D_{CH_3COO^-}\left(\dfrac{\partial[CH_3COO^-]}{\partial r}\right)_{r=r_e} = 0 \end{cases} \quad \textbf{(7.6)}$$

The boundary conditions for the outer boundary of simulation are:

$$r = r_{sim} \begin{cases} c^*_{CH_3COOH} = c_T - \dfrac{-K_{eq} + \sqrt{K_{eq}^2 + 4c_T K_{eq}}}{2} \\ c^*_{H^+} = \dfrac{-K_{eq} + \sqrt{K_{eq}^2 + 4c_T K_{eq}}}{2} \\ c^*_{H_2} = 0 \\ c^*_{CH_3COO^-} = \dfrac{-K_{eq} + \sqrt{K_{eq}^2 + 4c_T K_{eq}}}{2} \end{cases} \quad \textbf{(7.7)}$$

where $c_T = c_{CH_3COOH,total}$ is the concentration of acetic acid added to the solution before chemical equilibrium forming proton and acetate, which are assumed absent in the initial solution. In the absence of electrolysis, $c_{CH_3COOH,total} = c^*_{CH_3COOH} + c^*_{CH_3COO^-}$ and r_{sim} is the outer boundary of the simulation as discussed in reference[10].

7.3 Experimental

7.3.1 Chemicals

Acetic acid (CH_3COOH, 99.8%), potassium nitrate (KNO_3, 99%), potassium chloride (KCl, 99%) and hexaammineruthenium (III) chloride ($Ru(NH_3)_6Cl_3$, 98%) were purchased from Sigma-Aldrich (Dorset, UK) and used as received. All solutions were prepared with deionized water (of resistivity 18.2 MΩ cm at 298 K, Millipore).

7.3.2 Voltammetry and chronoamperometry of acetic acid at a Pt microdisc electrode

All electrochemical measurements were performed with a μAutolab Type III potentiostat analyzer using a standard three electrode arrangement in an optimized and thermostatted electrochemical cell [36] in a Faraday cage . A Pt microdisc electrode (diameter: approximately $10\ \mu m$) was polished with three grades of successively finer aluminum power (1.0, 0.3 and 0.05 μm), washed with deionized water, dried with N_2 flow and served as the working electrode. The counter and reference electrodes were a platinum wire and a saturated calomel electrode (SCE) respectively. The radius of Pt microdisc electrode was calibrated electrochemically as $4.97 \pm 0.05\ \mu m$ by analyzing the steady state voltammetry of 1.0 mM $[Ru(NH_3)_6]^{3+}$ in 0.1 M KCl aqueous solution, using the reported diffusion coefficient for $[Ru(NH_3)_6]^{3+}$of $8.43 \times 10^{-10}\ m^2/s$ at 298 K in 0.1 M KCl solution[37].

Linear sweep voltammetry of 10 mM acetic acid in 0.1 M KNO_3 was performed in the potential range from -0.15 to -1.0 V vs. SCE at a scan rate of $800\ mV/s$ as shown in Figure 7.1. The halfwave potential is measured at $-0.570V\ vs. SCE$, significantly smaller than the halfwave potential of electrochemically reversible H^+/H_2 couple at different concentration (-0.408 to -0.448V), suggesting that the reduction of H^+ on Pt microdisc electrode was at least partly electrochemically irreversible[30].

Acetic acid solutions with four concentrations (10, 20, 40 and 100 mM) were prepared in 0.1 M KNO_3 supporting electrolyte. The solution was degassed for 10 minutes with N_2 before voltammetric or chronoamperometric measurements and temperature stabilized at 298 ± 1 K via a digital temperature controller (SCT1 Digital contact thermometer)[36]. Current time transients for analysis via AI were recorded at an applied potential of -1.0 V vs. SCE for a duration of 10 seconds. The working electrode was polished with 0.05 μm alumina powder and

washed with deionized water between each experiment. Three repeat chronoamperometries were performed for each concentration.

7.4 Simulation and Machine Learning

The simulation program was written in Python. Multiprocessing was used for parallel computing of the working surfaces on an Intel E5 processor. The non-linear diffusion equations were solved using the finite difference method by discretizing the diffusion equations using both expanding space grid and time grid. The resulting multi-diagonal matrix was solved using the Newton-Raphson method for at most 10 iterations[38]. If the mean absolute error in dimensionless concentration was smaller than 10^{-12}, additional iterations were skipped to save time without significant compromise of accuracy. The convergence of the simulation was checked[39-41].

The working surfaces from simulations were used to train a multiheaded Dense Neural Network (DNN) written in TensorFlow[42]. The DNN was trained by using the simulated steady state currents at different concentrations as features to predict the corresponding $\log_{10} k_f$ and $\log_{10} K_{eq}$ as targets. Note that the targets were in logarithm form to reduce the exploding/diminishing gradient problem[43]. The DNN has only 4 hidden layers with relatively small numbers of neurons (<100) to avoid overfitting: a smaller network forced itself to predict rate constants instead of 'memorizing' them.

The implementation of simulation and machine learning programs, along with scripts for visualization and feature engineering can be found at:

https://github.com/nmerovingian/Acetic-Acid-Dissociation-AI

Raw experimental data is also provided in the repository. The more general simulation and machine learning programs for dissociative CE reaction reported before[10] can be found at:

https://github.com/nmerovingian/dissociativeCE-Simulation-MachineLearning.

Note that because of the stochastic nature of neural network, and different hardware and operating systems from the workstation employed by the author, the users' machine learning results may vary slightly from the authors', but generally to less than 0.1 in log10 scale for prediction of rate and equilibrium constants. The simulation results are expected to be consistent in different computing environments.

7.5 Results and Discussion

Figure 7.1 shows the voltammogram for which measurements were made. Current data were measured at a potential of -1.0 V vs. SCE corresponding to the limiting current and the attainment of the steady state current assessed by chronoamperometry as described in the next section. Specifically, the measurement of the limiting current as a function of the bulk concentration of acetic acid is used to avoid the need for any electrode kinetic data or assumption.

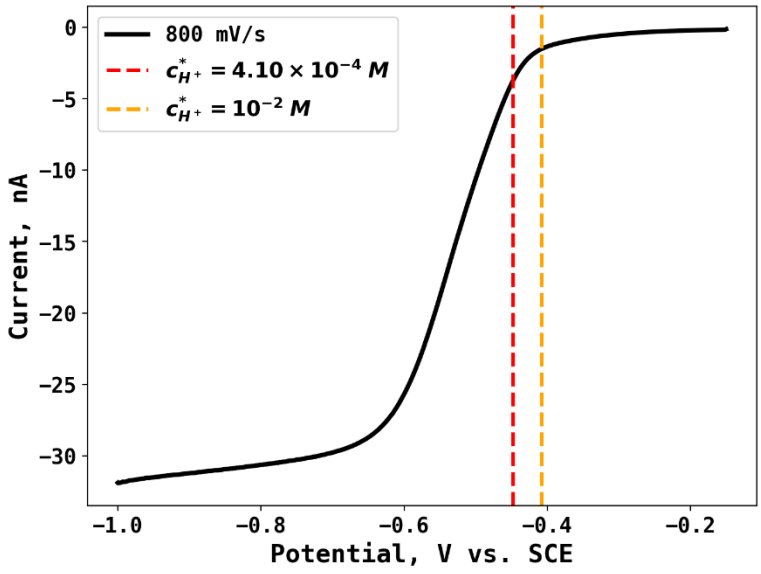

Figure 7.1. The linear sweep voltammetry of 10 mM acetic acid in 0.1 M KNO_3 at a scan rate of 800 mV/s from -0.15 to -1.0 V $vs. SCE$. Dashed lines show the calculated half wave potentials at different bulk concentrations of H^+.

7.5.1 Chronoamperometry of acetic acid

To identify the steady state currents, current-time transients for four different concentrations of acetic acid between 10 and 100 mM in 0.1 M KNO_3 were recorded at a Pt microdisc electrode by stepping the potential from a value where no current flowed to an applied potential of -1.0 V vs. SCE, corresponding to a sufficiently negative potential for a diffusion limited reduction of protons. The corresponding chronoamperograms at four concentrations reach steady state behaviour after 2 seconds. Erring on the side of caution, currents at $t = 10$ s were chosen for quantitative analysis, assumed to be steady state and measured as -30.5 ± 0.4 , -55.2 ± 0.3 , -102 ± 1 and -238 ± 4 nA for 10.0, 20.0, 40.0 and 100 mM of acetic acid with three separate chronoamperograms averaged for each concentration. The steady state currents did not scale proportionally with concentration of acetic acid since the reduction of acetic acid obeys the dissociative CE mechanism. The concentrations of acetic acid and the measured steady state currents were utilized as experimental features for machine learning to predict rate and equilibrium constant as described below.

7.5.2 Simulation of steady-state limiting currents

A wide range of k_f (1 to 10^8 s^{-1}) and K_{eq} (10^{-3} to 10^{-8} M) values were applied to simulate the steady state limiting currents at four different bulk concentrations of acetic acid (10, 20, 40, and 100 mM). The diffusion coefficients of all species reported in the literature are given in Table 7.2. Note that some combinations of K_{eq} and k_f values would generate k_b values exceeding a reasonable magnitude, so simulations were only performed if $k_b \leq 10^{13}$ M^{-1} s^{-1} with the latter values selected to give a considerable margin of error. The steady state currents at different k_f and K_{eq} values are represented on the working surfaces such as the one shown in Figure 7.2 for a bulk concentration of acetic acid of 10 mM. Figure 7.2 shows

that the steady state current increases in magnitude with increasing K_{eq} and k_f. Increasing K_{eq} can increase the magnitude of steady state current since higher K_{eq} increases the bulk concentration of electroactive H^+ at equilibrium. Higher k_f increases the extent of acetic acid dissociation on the voltammetric timescale to replenish H^+ consumed during electrochemical reduction. The working surfaces for bulk concentrations of acetic acid of 20, 40 and 100 mM can be found in the Working Surfaces for the Steady-State Limiting Current in the Appendix.

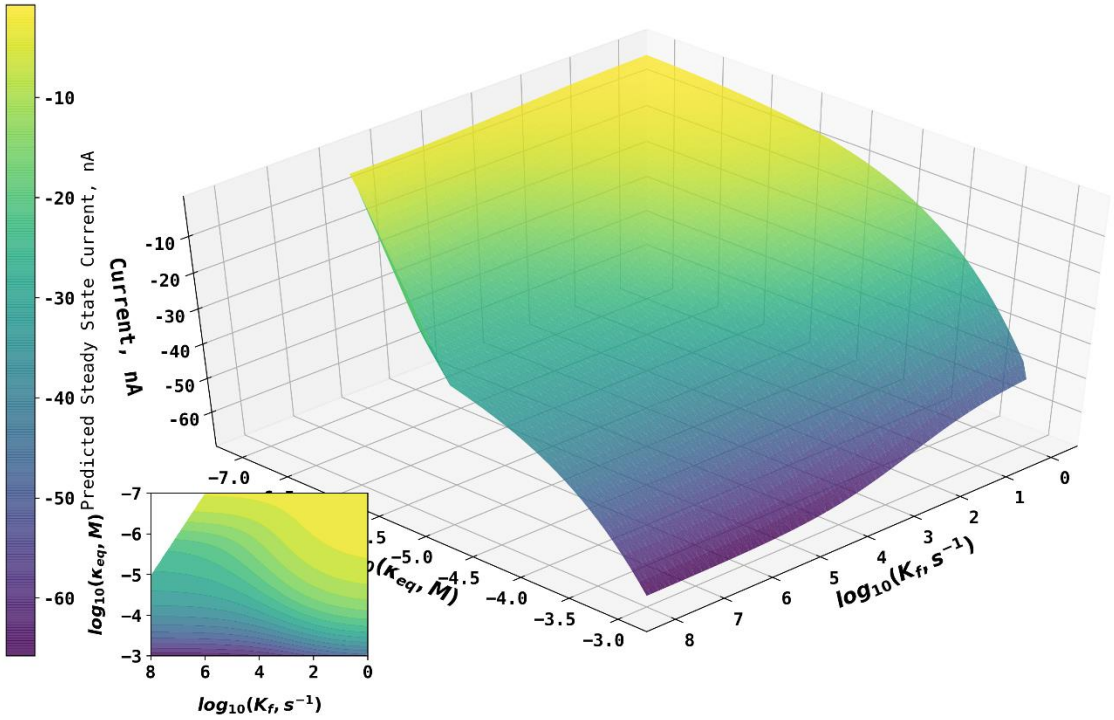

Figure 7.2. The working surface showing the steady state currents at different k_f and K_{eq} values for a bulk concentration of acetic acid of 10 mM. Note: the apparent 'kink' in the left of the surface is because it is not parallel to the $\log_{10} K_{eq}$ axis but rather cross (k_f and K_{eq}) space at an angle. The smooth continuity of the surface is emphasized by the contour plot.

7.5.3 Training and testing the neural network

Using the working surfaces, the neural network was trained to predict $\log_{10} k_f$ and $\log_{10} K_{eq}$ using steady state currents at four different concentrations of acetic acid and trained for 2000 epochs. The loss function was the mean absolute error (MAE) and the optimizer used was Adam (learning rate = 0.001)[44]. To evaluate the performance of the neural network model

after training, it was tested with independent testing datasets and the results are shown in Figure 7.3, as 90.5% of predictions of $\log_{10} k_f$ were within 10% error and 100% of predictions of $\log_{10} K_{eq}$ were within 5% error. The lower accuracy of predictions of $\log_{10} \mathrm{k_f}$ compared to $\log_{10} \mathrm{K_{eq}}$ arises because $\log_{10} \mathrm{k_f}$ had relatively smaller effect on the steady state current but the network was judged sufficient for prediction of constants from experimental results. The performance was benchmarked with a 3rd degree polynomial regression, which results 61.2% of prediction of $\log_{10} k_f$ within 10% error and 86.7% predictions of $\log_{10} K_{eq}$ within 5% error. Details are shown in Benchmark section in the Appendix.

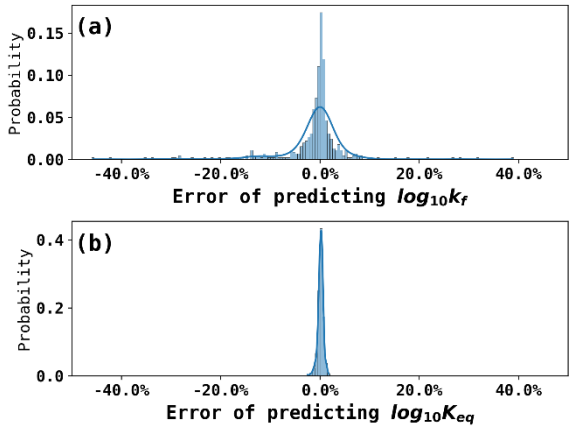

Figure 7.3. Error of predicting rate and equilibrium constants from an independent testing dataset composed of simulated steady state currents. (a) errors of predicting $log_{10} k_f$. 90.5% of predictions of $log_{10} k_f$ were within 10% errors; (b) errors of predicting $log_{10} K_{eq}$. 100% of predictions of $log_{10} K_{eq}$ were within 5% errors.

7.5.4 Predicting rate and equilibrium constants with experimental data

Using the steady state current at the four different concentrations as input of the neural network trained in the last step, the neural network predicted $\mathrm{k_f}$ and $\mathrm{K_{eq}}$ values in logarithmic scale as 6.47 and -4.77 which convert to $2.95 \times 10^6\ \mathrm{s^{-1}}$ and $1.70 \times 10^{-5}\ \mathrm{M}$. The 95% prediction intervals for the of neural network were estimated using the bootstrap method[45]. First, 500 observations were sampled from testing datasets and repeated for 100 times to obtain 100 bootstrapped samples. Second, each bootstrap sample was trained in an independent neural

network to obtain an empirical distribution of bootstrap predictions. At 5% significance level, the upper and lower limit were 97.5 and 2.5% quantile obtained from the bootstrap distribution. The 95% prediction interval were calculated as $2.78 \times 10^6 \; to \; 3.13 \times 10^6 \; s^{-1}$ and 1.67×10^{-5} to 1.71×10^{-5} M for predicted k_f and K_{eq} respectively. These values are fully consistent with the accepted literature values shown in Table 7.1 showing the power of the proposed AI approach in extracting kinetic and thermodynamic data.

7.5.5 Testing the approach with different diffusion coefficients

Not all systems under study will have as well characterized diffusion coefficient as the acetic acid dissociation reaction described above. Sometimes, diffusion coefficients are unknown and frequently uncertain. It is therefore pertinent to ask how well the AI approach responds to variations in the diffusion coefficients used for the proton, acetic acid and acetate ions.

To address this question, we compared the performance of the three-step electrochemical approach with five different sets of diffusion coefficients and the predicted constants using simulated steady state currents as shown in Table 7.3. The values for k_f and K_{eq} obtained for the wrong diffusion coefficients which deviate from the accepted values give noticeably wrong answers.

Table 7.3. The 5 Cases Considered When Varying Diffusion Coefficients of Species and the Predicted $\boldsymbol{k_f}$ and $\boldsymbol{K_{eq}}$ Values.

Case #	description	predicted $k_f, \; s^{-1}$	predicted K_{eq}, M
1	diffusion coefficients shown in Table 7.2	2.95×10^6	1.70×10^{-5}
2	increasing diffusion coefficients in Table 7.2 by 10%	3.02×10^3	5.13×10^{-6}

3	decreasing diffusion coefficients in Table 7.2 by 10%	$> 10^{10}$	3.47×10^{-6}
4	all diffusion coefficients set to 10^{-9} m^2 s^{-1}	9.05×10^{2}	1.56×10^{-3}
5	$D_{H^+} = 9.311 \times 10^{-9}$ m^2 s^{-1} , other species 10^{-9} m^2 s^{-1}	$> 10^{10}$	1.07×10^{-5}

In cases 2 and 3 the diffusion coefficients were arbitrarily set higher or lower than the accepted values by 10%. The effect is that for lowered diffusion coefficients the K_{eq} and k_f values increase to provide more or more rapid dissociation whilst for increased diffusion coefficients, the opposite occurs and the two parameters decrease to reduce the number of protons formed through dissociation on the voltammetric timescale. These trends are exactly what is expected since we are using the limiting current to probe the two parameters of interest and so the inferred values will be very sensitive to the rate of diffusion in addition to k_f and K_{eq}.

It is interesting first that the values of k_f and K_{eq} are changed so markedly, highlighting a limitation of the electrochemical method for their measurement and second that the AI approach stresses the requirement for accurate parameter input in a way which is much more emphatic than using traditional curve fitting approaches.

In the specific example of acetic acid dissociation chosen for study, all three diffusion coefficients are well known and the values used in case 1 are considered to be reliably especially as they are measured via conductivity or Gouy interferometry[46]. In some cases where the diffusion coefficients are unknown, an experimenter might be tempted to estimate or guess the relevant parameters. Thus, in case 4 and 5 we investigate this approach and fix some or all

for the diffusion coefficients as $10^{-9}\, m^2\, s^{-1}$. This set of low values significantly underestimates the D of H^+, and therefore leads to high k_f estimates.

The five cases discussed above showed that incorrect simulation parameters, notably diffusion coefficients lead to incorrect input data for the neural network training and generate unreliable predictions. Thus, in practice, we recommend major caution with simulation parameters for accurate simulations and predictions.

7.6 Conclusions

We have shown how Artificial Intelligence methods can be developed and trained to analyze electrochemical data and extract reliable kinetic and thermodynamic parameters which compare well with those independently measured both by electrochemical and non-electrochemical methods given a mechanism for the electrode reaction is known. The specific approach previously advocated[10] has been shown to be effective when using simulation to train and validate AI programs and then applied to authentic experimental data. However, it is useful to assess the strengths and especially the limitations of the approach. We note that the method meets the challenge presented by Bond and colleagues in giving a well-defined and experimenter – independent method of data analysis. However, it must be recognized that we have applied it to a well-defined system where the mechanism of electrode process under evaluation is known. This is required to perform the simulation necessary to train the AI. Moreover, because the chemistry is clear it is possible to simplify the number of parameters needed for training by adopting the reliable literature data for the diffusion coefficients of the 3 species controlling the magnitude of the current, acetic acid, acetate ions and protons. Even so from the analysis using deliberately wrong diffusion coefficients it is clear that even relatively small errors in the values leads to significant error in the inferred k_f and K_{eq} values.

That said AI allows the sensitivity of the values to be readily checked and the inferences caveated in a way which is not always easily adopted in conventional analysis of voltammograms.

It is evident that the approach of using simulation to train the AI requires a clear understanding of the likely chemistry even if the experimenter is willing to simulate and train AI for different possible mechanisms. Overall this points to a possible need to make complementary measurements, notably spectro-electrochemistry, and/or good chemical intuition to identify realistic chemistry. In the above we deliberately selected to focus our analysis on the limiting current data from our experiments to make our conclusion independent of the mechanism and electrode kinetics of the H^+/H_2 redox couple which would influence cyclic voltammetric data (peak current, peak potentials). The speculative application of a trained network for more complex chemistry is fraught with risk, possibly extreme risk. Thus, in the context of dissociative CE mechanism such as a process undoubtedly underpins the oxidation of hydrazine in aqueous solution where deprotonation of $N_2H_5^+$ prior to oxidation of N_2H_4 is required at some electrodes however the oxidation process is self-inhibiting since it produces nitrogen and protons [47, 48]:

$$N_2H_4 \rightleftarrows N_2 + 4H^+ + 4e^-$$

which act to change the pH of the solution local to the electrode. The application of an AI program trained for a simple dissociative CE process could not capture the essential content of the voltammetry/chronoamperometry and requires chemical expertise from the experimenter. Similarly, the voltammetry of blood reveals signals attributed to the electro-reduction of oxygen released from oxy-hemoglobin close to an electrode[49-51]. Again, the chemistry is not simple: four oxygen molecules are bound to each hemoglobin and have different kinetics and thermodynamics of release. A chemically over-simplified analysis using AI trained for a simple

mechanism would likely gave erroneous or misleading output. Further it is evident that the use of low-quality training data presents implementation risk and that this grows with the complexity of the mechanism because of the number of parameters required. Knowledge of accurate diffusion coefficients is one specific problem and, of course, is intrinsic to all electrochemical data analysis problems. We predict that the role of Human Intelligence ('HI') will remain dominant over the Artificial form for the foreseeable future in electrochemistry at least except for some niche applications! One such immediate niche lies in the analysis of electrode reaction mechanisms where the experimentalist is confident of the generic nature of the reaction, for example as CE, EC, ECE etc. As we have shown the AI approach allows for simulation-free data analysis and hence makes the extraction of parameters independent of the experimenter so better facilitating inter-laboratory comparisons.

In the next chapter, we will shift the focus of the neural network from parameter estimation to the performing of simulations. Using a very recent variant of neural network called "physics-informed neural network", we can "teach" neural networks physical laws like the diffusion equation and the Nernst equation, which in turn facilely solves those equations without discretization mentioned in Chapter 2.

7.7 Appendix

7.7.1 Working surfaces for the steady-state limiting current

The working surfaces of steady-state currents for different bulk concentration of acetic acid with various k_f and K_{eq} values were simulated. The working surface when $c^*_{CH_3COOH,total} = 10\ mM$ is shown in the main text, and the working surfaces when $c^*_{CH_3COOH,total} = 20, 40\ and\ 100\ mM$ are shown below.

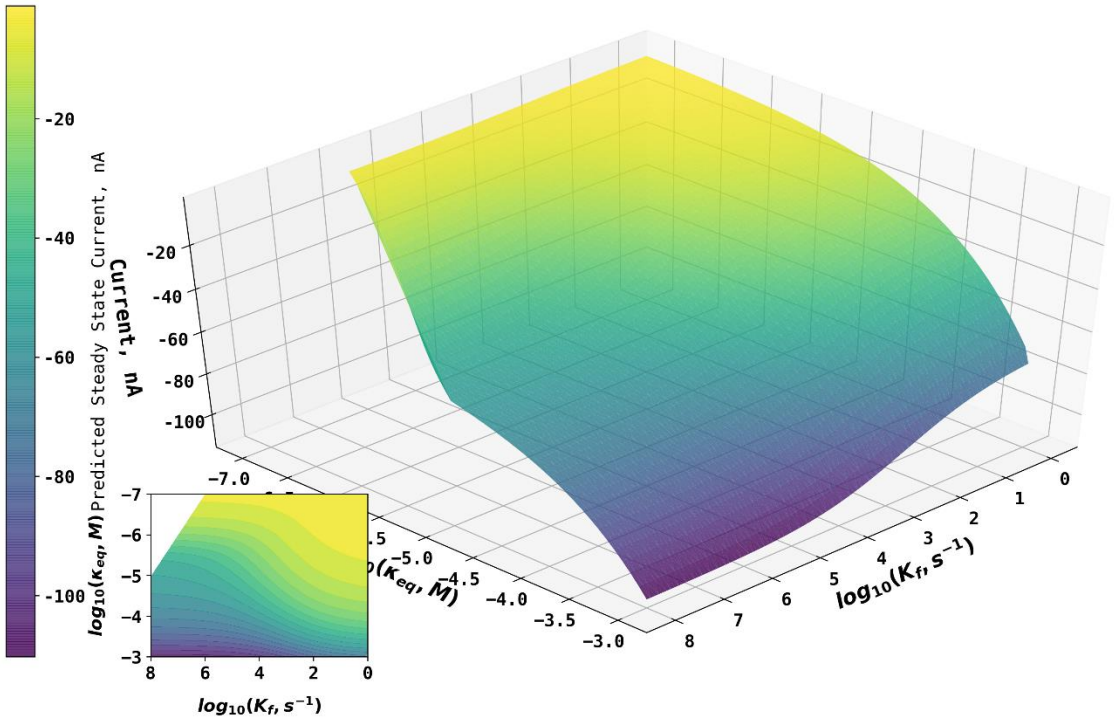

Figure 7.4. The working surface showing the steady state currents at different k_f and K_{eq} values for a bulk concentration of acetic acid of 20 mM.

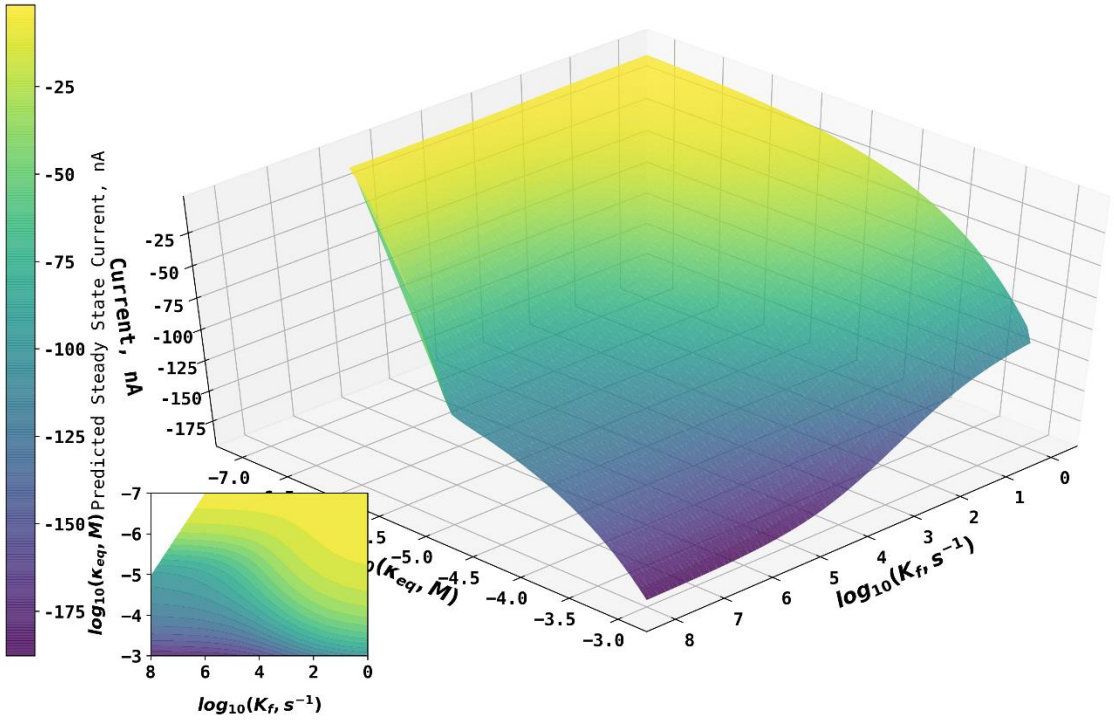

Figure 7.5. The working surface showing the steady state currents at different k_f and K_{eq} values for a bulk concentration of acetic acid of 40 mM.

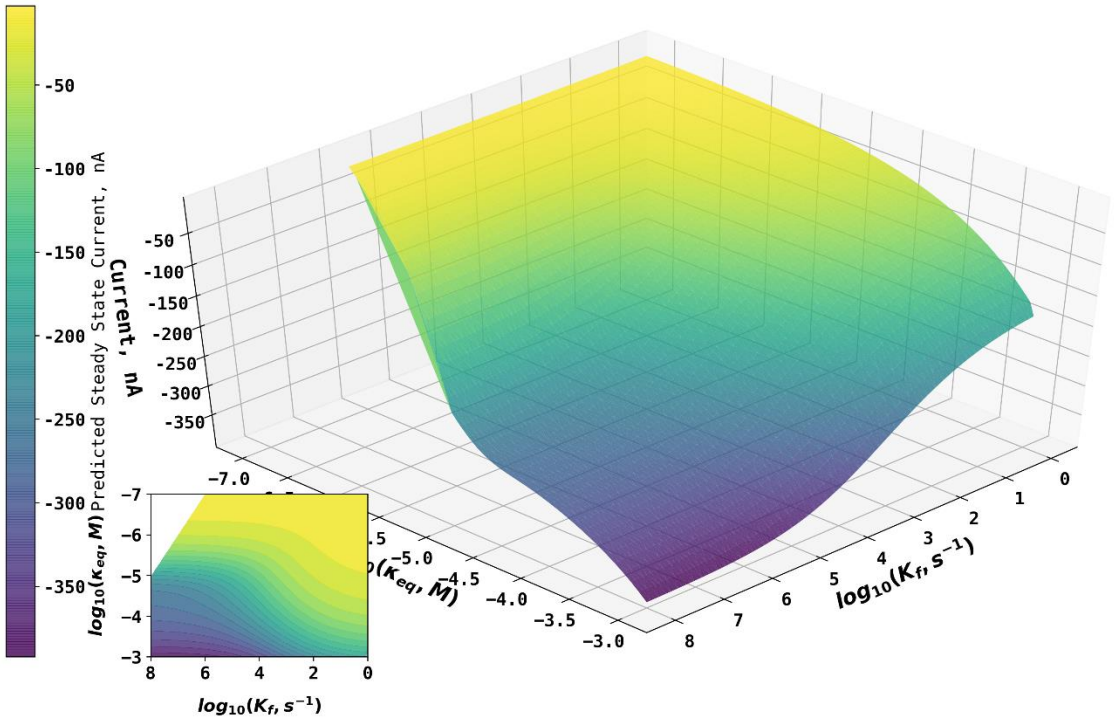

s

Figure 7.6. The working surface showing the steady state currents at different k_f and K_{eq} values for a bulk concentration of acetic acid of 100 mM.

7.7.2 Benchmarking

To benchmark the performance of the neural network, it was benchmarked with 3rd degree polynomial regression. Using the polynomial regression, 61.2% of the predictions of $\log_{10} k_f$ were within 10% error and 86.7% predictions of $\log_{10} K_{eq}$ within 5% error as shown in Figure 7.7.

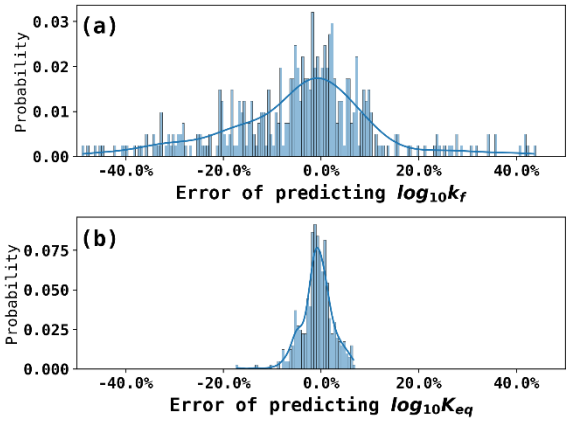

Figure 7.7. Error of predicting rate and equilibrium constants from an independent testing dataset composed of simulated steady state currents using 3rd degree polynomial fitting. (a) errors of predicting $log_{10}\,k_f$. 61.2% of predictions of $log_{10}\,k_f$ were within 10% errors; (b) errors of predicting $log_{10}\,K_{eq}$. 86.7% of predictions of $log_{10}\,K_{eq}$ were within 5% errors.

References

1. H. Chen, E. Kätelhön, H. Le and R. G. Compton, *Anal. Chem.*, 2021, **93**, 13360-13372.
2. H. Chen, D. Li, E. Kätelhön, R. Miao and R. G. Compton, *Anal. Chem.*, 2022.
3. A. Roselló, N. Serrano, J. M. Díaz-Cruz and C. Ariño, *Electroanalysis*, 2021, **33**, 864-872.
4. S. N. Dean, L. C. Shriver-Lake, D. A. Stenger, J. S. Erickson, J. P. Golden and S. A. Trammell, *Sensors*, 2019, **19**, 2392.
5. L. Mao, Y. Xue, W. Ji, Y. Jiang and P. Yu, *Angew. Chem.*, 2021.
6. Y. Zhao, H. Zhang, Y. Li, X. Yu, Y. Cai, X. Sha, S. Wang, Z. Zhan, J. Xu and L. Liu, *Biosens. Bioelectron.*, 2021, **186**, 113291.
7. G. F. Kennedy, J. Zhang and A. M. Bond, *Anal. Chem.*, 2019, **91**, 12220-12227.
8. J. Li, G. F. Kennedy, L. Gundry, A. M. Bond and J. Zhang, *Anal. Chem.*, 2019, **91**, 5303-5309.
9. A. M. Bond, *J. Solid State Electrochem.*, 2020, **24**, 2041-2050.
10. H. Chen, E. Kätelhön, H. Le and R. G. Compton, *Anal. Chem.*, 2021, DOI: 10.1021/acs.analchem.1c03154.
11. Y. Kanzaki, K. Tokuda and S. Bruckenstein, *J. Electrochem. Soc.*, 2014, **161**, H770.
12. R. R. Schroeder and I. Shain, *J. Phys. Chem.*, 1969, **73**, 197-206.
13. W. M. Haynes, *CRC handbook of chemistry and physics*, CRC press, 2014.
14. M. Kilpatrick and R. D. Eanes, *J. Am. Chem. Soc.*, 1953, **75**, 586-587.
15. M. Eigen and J. Schoen, *Ber. Bunsen. Phys. Chem.*, 1955, **59**, 483-494.
16. M. Eigen and E. M. Eyring, *J. Am. Chem. Soc.*, 1962, **84**, 3254-3256.
17. B. R. Staples†, D. J. Turner‡ and G. Atkinson, *Instrum. Sci. Technol.*, 1969, **2**, 127-147.
18. E. M. Eyring, J. J. Auborn and P. Warrick Jr, *J. Phys. Chem.*, 1971, **75**, 2488-2492.
19. V. G. Levich, *Physicochemical hydrodynamics*, 1962.
20. W. J. Albery and R. P. Bell, *Proc. Chem. Soc*, 1963, DOI: 10.1039/PS9630000157, 157-188.
21. E. J. Cohn, F. F. Heyroth and M. F. Menkin, *J. Am. Chem. Soc.*, 1928, **50**, 696-714.
22. M. I. A. Ferra, J. R. Graça and A. M. M. Marques, *J. Chem. Eng. Data*, 2011, **56**, 3673-3678.

23. S. Bruckenstein and D. Nelson, *J. Chem. Eng. Data*, 1961, **6**, 605-606.
24. W. Vielstich and D. Jahn, *Ber. Bunsen. Phys. Chem.*, 1960, **64**, 43-44.
25. P. Delahay and W. Vielstich, *J. Am. Chem. Soc.*, 1955, **77**, 4955-4958.
26. G. Barker and H. W. Nürnberg, *Naturwissenschaften*, 1964, **51**, 191-191.
27. H. Nürnberg and G. Barker, *Naturwissenschaften*, 1964, **51**, 191-192.
28. G. Zwaschka, Y. Tong, M. Wolf and R. Kramer Campen, *ChemElectroChem*, 2019, **6**, 2675-2682.
29. M. C. Tavares, S. A. S. Machado and L. H. Mazo, *Electrochim. Acta*, 2001, **46**, 4359-4369.
30. X. Jiao, C. Batchelor-McAuley, E. Kätelhön, J. Ellison, K. Tschulik and R. G. Compton, *J. Phys. Chem. C*, 2015, **119**, 9402-9410.
31. J. M. Gomez-Gil, E. Laborda and A. Molina, *Anal. Chem.*, 2020, **92**, 3728-3734.
32. A. Bard, *Standard potentials in aqueous solution*, Routledge, 2017.
33. R. A. Robinson and R. H. Stokes, in *Electrolyte solutions*, Courier Corporation, 2002.
34. E. Wilhelm, R. Battino and R. J. Wilcock, *Chem. Rev.*, 1977, **77**, 219-262.
35. F. Long and W. McDevit, *Chem. Rev.*, 1952, **51**, 119-169.
36. X. Li, C. Batchelor-McAuley, J. K. Novev and R. G. Compton, *Phys. Chem. Chem. Phys.*, 2018, **20**, 11794-11804.
37. Y. Wang, J. G. Limon-Petersen and R. G. Compton, *J. Electroanal. Chem.*, 2011, **652**, 13-17.
38. R. G. Compton, E. Laborda, E. Kaetelhoen and K. R. Ward, *Understanding voltammetry: simulation of electrode processes*, World Scientific London, 2nd edn., 2020.
39. E. Kätelhön and R. G. Compton, *Analyst*, 2015, **140**, 2592-2598.
40. E. Kätelhön and R. G. Compton, *Analyst*, 2015, **140**, 3290-3290.
41. E. Kätelhön and R. G. Compton, *Analyst*, 2016, **141**, 1154-1154.
42. M. Abadi, P. Barham, J. Chen, Z. Chen, A. Davis, J. Dean, M. Devin, S. Ghemawat, G. Irving and M. Isard, 2016.
43. G. Philipp, D. Song and J. G. Carbonell, *arXiv preprint arXiv:1712.05577*, 2017.
44. D. P. Kingma and J. Ba, *arXiv preprint arXiv:1412.6980*, 2014.
45. B. Efron, in *Breakthroughs in statistics*, Springer, 1992, pp. 569-593.
46. L. Dunn and R. Stokes, *Aust. J. Chem.*, 1965, **18**, 285-296.
47. R. Miao and R. G. Compton, *J. Phys. Chem. Lett.*, 2021, **12**, 1601-1605.
48. R. Miao, L. Shao and R. G. Compton, *Nano Res.*, 2021, DOI: 10.1007/s12274-021-3353-8.
49. D. Li, C. Batchelor-McAuley and R. G. Compton, *Talanta*, 2021, 123127.
50. Q. H. Gibson and F. J. W. Roughton, *Proc. R. Soc. London*, 1955, **143**, 310-334.
51. F. J. W. Roughton, A. Otis and R. Lyster, *Proc. R. Soc. London*, 1955, **144**, 29-54.

Chapter 8 Physics-Informed Neural Network and its Application in Electrochemistry: Voltammetry

The conventional method of simulating voltammograms was introduced in Chapter 2. In this chapter, we will introduce a new method of simulation using a neural network for a wide range of electrode geometries. This work has been published at the Journal of Physical Chemistry Letters[1].

We propose a discretization-free approach to simulation of cyclic voltammetry using Physics-Informed Neural Networks (PINNs) by constraining a feed-forward neural network with the diffusion equation and electrochemically consistent boundary conditions. Using PINNs, we first predict one-dimensional voltammetry at a disc electrode with semi-infinite or thin layer boundary conditions. The voltammograms agree quantitatively with those obtained independently using the finite difference method and/or previously reported analytical expressions. Further we predict the voltammetry at a microband electrode, solving the two-dimensional diffusion equation, obtaining results in close agreement with the literature. Last, we apply a PINN to voltammetry at the edges of a square electrode, quantifying the non-uniform current distribution near the corner of electrode. In general, we noticed the relative ease of developing PINNs for the solution of, particularly, the higher dimensional problem, and recommend PINNs as a potentially faster and easier alternative to existing approaches for voltammetric problems.

8.1 Introduction

Physics-informed neural networks (PINNs), introduced by Raissi in 2018 to solve the Burger's, Schrodinger, and Alan-Cahn equations among others[2] form a class of neural

networks that can integrate data and abstract mathematical operators, along with the laws of nature, to provide physically consistent solutions. PINNs have been applied widely in modelling, analysis and parameter estimation to lithium-ion batteries[3-6] and fuel cells[7-9]. A PINN can also be informed by chemical kinetics[10, 11] and thermodynamics[12] to solve the partial differential equations (PDEs) that describe diverse physical chemical models. With the growing application of PINN in scientific and engineering contexts, we note that there are no reports applying PINNs to solve electrochemical problems with coupled diffusional mass transport both in general and specially in the context of voltammetry, the most generally applied electrochemical methodology[13, 14]. Simulation of cyclic voltammetry conventionally employs finite difference[15], finite element[16, 17] or random walk algorithms[15], all needing discretization of simulation spaces leading to the difficulty that the requirements of discretization/simulation grow exponentially as simulations expand to higher dimensions[18]. In the following, a discretization-free simulation, empowered by data driven inference of PDEs using PINNs, of 1D and 2D cyclic voltammetry with Nernstian, no-flux or fixed concentration boundary conditions is developed offering a radically new approach to the modelling of voltammetry.

Cyclic voltammetry applies a time dependent potential, E, as a triangular waveform to a working electrode with measurement of the resulting current as a function of the applied potential resulting in a 'voltammogram' in the form of a plot of current vs. potential. The proofs-of-concept in this article focus on simple electrode processes of the form:

$$A + e \rightleftarrows B \qquad \textbf{(8.1)}$$

where A and B are stable, solution phase species. We assume that mass transport in solution to the macro electrode can be described as diffusion in one dimension with Fick's 2nd law of diffusion[19-21]:

$$\frac{\partial c_A}{\partial t} = D_A \frac{\partial^2 c_A}{\partial x^2}$$
$$\frac{\partial c_B}{\partial t} = D_B \frac{\partial^2 c_B}{\partial x^2} \quad \textbf{(8.2)}$$

where D_A and D_B are the diffusion coefficients for A and B respectively. In the present work, the diffusion coefficients of both species are assumed to be equal, so solving only for species A is sufficient for simulation of cyclic voltammetry since it is easily shown that for this condition the sum $c_A + c_B = c_A^*$ where c_A^* is the bulk concentration of A and the bulk concentration of B is assumed to be zero.

We further assume that the boundary condition on the surface of electrode can be described using the Nernst Equation:

$$\mathrm{E} = \mathrm{E}_f^0(A/B) + \frac{RT}{F} \ln \frac{c_A}{c_B} \quad \textbf{(8.3)}$$

where E and E_f^0, are, respectively, the applied potential and the formal potential of A/B couple. R, T and F are the Gas Constant, temperature and the Faraday Constant respectively. For cyclic voltammetry, the triangular waveform of potential E is expressed as:

$$\begin{cases} 0 < t < t_{switch}, E = E_i - \nu t \\ t = t_{switch}, E = E_{switch} \\ t_{switch} < t \leq 2t_{switch}, E = E_{switch} + \nu(t - t_{switch}) \end{cases} \quad \textbf{(8.4)}$$

where E_i is the starting potential of the forward scan, E_{switch} is the potential at which the triangular sweep reverse direction, t_{switch} is the start time of the reverse scan and ν is the potential scan rate (V/s). Positive and negative potential scan rates are usually chosen corresponding to the study of reduction and oxidation processes respectively.

We first apply PINNs to predict two problems in cyclic voltammetry involving one spatial dimension (x). In the first of these, we consider cyclic voltammetry at a macroelectrode, specifically a disc electrode of radius, r_e, with semi-infinite diffusion to allowcomparison with

the well-known response reported in many textbooks[13, 22]. Second, we examine the thin-layer cyclic voltammetry corresponding to one-dimensional diffusion within a fixed and finite volume such as applied within thin layer cells[23, 24] as are commonly encountered in spectro-electrochemistry[25]. We then, second, consider two problems involving two-spatial dimensions, (x, y). The first is cyclic voltammetry at a microband electrode where comparisons with previous finite difference simulations can be made. Second, we investigate a novel problem involving the two-dimensional diffusion to the edges of a square electrode, as shown in Figure 8.1. The continuous time model proposed by Raissi et al. is used[2].

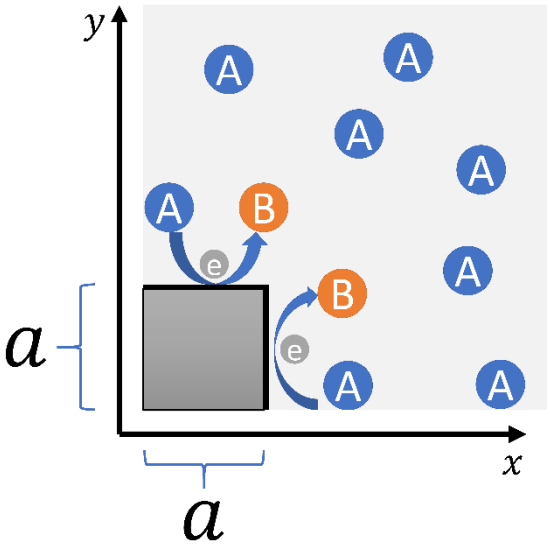

Figure 8.1. The scheme of cyclic voltammetry at the edges of a square electrode with edge length a. Species A and B are free to diffuse in the x, y plane and to interconvert electrochemically at the two edges of the square electrode. The electrochemical reaction of A to B is reversible.

8.2 Theory

The modelling parameters for use in the PINNs are first converted to dimensionless form. Dimensionless parameters (see Table 8.1) are used to remove the dependence on bulk concentration, c^*, electrode size (radius, r_e, for the disc electrode; the width, w, for the microband electrode; and the edge length, a, of the square electrode), and diffusion coefficient,

D, so predictions are general as one prediction of the PINNs is compatible with any set of c^*, electrode size, and D. Using dimensionless parameters can also reduce the vanishing/exploding gradient problem commonly encountered during training of neural networks[26]. The range of scan is noted as $[\theta_i, \theta_{switch}]$, and θ_i and θ_{switch} are the starting potential and reverse potential respectively. The time for the full scan is thus $T_{sim} = \frac{2|\theta_i - \theta_{switch}|}{\sigma}$ where σ is the dimensionless scan rate. The maximum spatial distance in the coordinate X for simulation is guided by Einstein's work on Brownian motion[27]: the root mean square displacement of a particle is $x_{RMS} = \sqrt{2Dt}$ .To ensure that the outer boundary is sufficiently remote as not to be affected by diffusion the outer boundary of the simulation, x_{sim} is located at $6\sqrt{Dt_{sim}}$ in dimensional form and equivalent to $X_{sim} = 6\sqrt{T_{sim}}$ in dimensionless form[28]. At the electrode surface, since the dimensionless concentrations of A and B always sum to 1 at all points in space within the equal diffusion coefficient approximation, the Nernst equation predicts the dimensionless concentration of A as a function of dimensionless potential θ:

$$C_A(X = 0, T) = \frac{1}{1 + e^{-\theta}} \quad \textbf{(8.5)}$$

Table 8.1.Dimensionless parameters for the 1D disc, the 2D microband and the 2D square electrode simulations.

parameter	1-D disc	2-D microband	2-D square edges
concentration	$C_j = c_j/c_A^*$	$C_j = c_j/c_A^*$	$C_j = c_j/c_A^*$
diffusion coefficient	$d_j = D_j/D_A$	$d_j = D_j/D_A$	$d_j = D_j/D_A$
spatial coordinates	$X = x/r_e$	$X = x/w, Y = y/w$	$X = x/a, Y = y/a$
time	$T = D_A t/r_e^2$	$T = D_A t/w^2$	$T = D_A t/a^2$
potential	$\theta = \left(\frac{F}{RT}\right)(E - E_f^0)$	$\theta = \left(\frac{F}{RT}\right)(E - E_f^0)$	$\theta = \left(\frac{F}{RT}\right)(E - E_f^0)$
scan rate	$\sigma = \left(\frac{r_e^2}{D_A}\right)\left(\frac{F}{RT}\right)\nu$	$\sigma = \left(\frac{w^2}{D_A}\right)\left(\frac{F}{RT}\right)\nu$	$\sigma = \left(\frac{a^2}{D_A}\right)\left(\frac{F}{RT}\right)\nu$
current	$J = I/\pi r F c_A^* D_A$	$J = I/F c_A^* D_A b$	$J = I/F c_A^* D_A a$ (each edge)

***c_j, D_j* are respectively the concentration and diffusion coefficients of species *j*. r_e, w, b and a are the radius of the disc electrode, the width and the length of the microband electrode, and the edge length of square electrode respectively.**

The PINN modelling of 1D voltammetry requires prediction of the evolution of the dimensionless concentrationof A, $C(T,X)$, as a function of dimensionless time T and dimensionless distance X from the electrode surface and is described by the dimensionless diffusion equation and boundary conditions in the following form:

$$\begin{aligned} \frac{\partial C}{\partial T} - \frac{\partial^2 C}{\partial X^2} &= 0 \qquad on\ \mathcal{T} \times \Omega_X \qquad (1) \\ C &= \frac{1}{1+e^{-\theta}} \qquad on\ \mathcal{T}, X = 0 \qquad (2) \\ C &= 1 \qquad on\ \mathcal{T}, X = X_{sim} \qquad (3) \\ C &= 1 \qquad on\ T = 0, \Omega_X \qquad (4) \end{aligned} \tag{8.6}$$

where $\mathcal{T} \in [0, T_{sim}]$, $\Omega_X \in [0, X_{sim}]$ represents the temporal and one-dimensional spatial domain respectively. Since the diffusion coefficients of A and B are assumed equal, the dimensionless diffusion coefficients are always 1 and so do not appear in the diffusion equation. Equations 2 and 3 of **(8.6)** are Dirichlet boundary conditions at the surface obeying the Nernst equation and at the outer boundary with a fixed concentration respectively. Equation 4 of **(8.6)** represents the initial state at $T = 0$. Four training datasets are required to enforce the physical laws in the form of the diffusion equation and boundary conditions. For example, to enforce Equation 1 of **(8.6)**, a set of N collocation points $\{T_i, X_i\}_{i=1}^N$ is generated using a random uniform distribution throughout the temporal-spatial domain. Similarly, the data points for the Nernst boundary condition implied by Equation 2 of **(8.6)** is also a set of N collocation points $\{T_i, 0\}_{i=1}^N$ randomly uniformly distributed only in the temporal domain. The data points for Equation 3 and 4 of **(8.6)** are $\{T_i, X_{sim}\}_{i=1}^N$ and $\{0, X_i\}_{i=1}^N$ respectively.

Unlike a conventional neural network trained to predict $C(T,X)$ from (T,X) with an enormous amount of known concentrations in $\mathcal{T} \times \Omega_X$, in a PINN, a dense neural network is used to approximate the unknown solution $C(T,X)$ with only known concentrations at the

boundaries ($X = 0\ or\ X_{sim}$) and for the initial state ($T = 0$). More importantly, Equation 1 of **(8.6)** has to be satisfied for every point inside the whole $\mathcal{T} \times \Omega_X$ domain. To enforce the physics given by Equation 1 of **(8.6)**, and the known concentrations at the boundary and initial state, a loss function $\mathcal{L}$ is composed as a linear combination of four mean square error (MSE) functions:

$$\mathcal{L} = w_1 MSE_f + w_2 MSE_{surf} + w_3 MSE_{outer} + w_4 MSE_{ini} \quad \textbf{(8.7)}$$

where w_j are hyperparameters for training to balance the weights of each MSEs since each MSEs may have different numerical scales. The first MSE_f term represents the error of enforcing the diffusion equation as:

$$MSE_f = \frac{1}{N}\sum_{i=1}^{N}\left(\frac{\partial C_i}{\partial T_i} - \frac{\partial^2 C_i}{\partial X_i^2}\right)^2 \quad \textbf{(8.8)}$$

where C_i is the concentration predicted by the neural network from (T_i, X_i); $\frac{\partial C_i}{\partial T_i}$ and $\frac{\partial^2 C_i}{\partial X_i^2}$ are the gradients calculated by the machine learning framework. The three otherMSEs are the errors of the predicted concentrations at the boundary. For example, MSE_{surf} represents the error of predicting the concentrations at the surface of electrode as:

$$MSE_{surf} = \frac{1}{N}\sum_{i=1}^{N}\left(C_i - \frac{1}{1+e^{-\theta}}\right)^2 \quad \textbf{(8.9)}$$

and MSE_{outer} and MSE_{ini} are the error of predicting the concentration at the outer boundary and at the initial state when $T = 0$. During training, the optimizer of the neural network minimizes the combined loss function $\mathcal{L}$ by tuning the weights and biases of the neural network. Adam[29] was used as the optimizer with a learning rate of 10^{-3}.

8.3 Simulation methods

The PINN program was written in Python using the TensorFlow framework on a workstation with Intel 6800K CPU with 32 GB of RAM and a Nvidia P100 16 GB graphic

card. The program is available at https://github.com/nmerovingian/PINN-CV with theweights of the neural networks for user's convenience. The validation voltammogram for 1D voltammetry was written in Python and the diffusion equation was solved using finite difference method by discretization of both temporal and spatial domains and the resulting multi-diagonal matrix was solved using the Newton-Raphson method[15].

8.4 Results

8.4.1 Cyclic voltammetry at a macroelectrode with semi-infinite boundary condition

After training, the neural network predicts $C(T,X)$ for cyclic voltammetry. For cyclic voltammetry with a dimensionless scan rate of $\sigma = 40$, the concentration is plotted as a function of T and X in Figure 8.2a. Figure 8.2a shows that C decreases with time near the surface of electrode ($X = 0$) when $0.25 < T < 0.75$, which is expected since the overpotential θ is negative between $0.25 < T < 0.75$ so reduction of A to B at the surface of electrode surfaces lowers the surface concentration. When $T > 0.75$, A is regenerated via oxidation of B to A, observing a local high concentration of A near the electrode surface. The dimensionless flux, $J = \frac{C_{T,X=dX} - C_{T,X=0}}{dX}$ and dX is a small spatial step. Figure 8.2b compares the voltammogram predicted by PINN with simulation using the finite difference method[15]. The forward scan peak flux is also compared with Randles-Ševčík equation[30, 31] in dimensionless form as $J_p = -0.446\sqrt{\sigma}$, the excellent agreement with both comparisons showing that the PINN, provided with only the information of the boundary conditions and the diffusion equation, can accurately predict the concentration profile and thus the voltammogram.

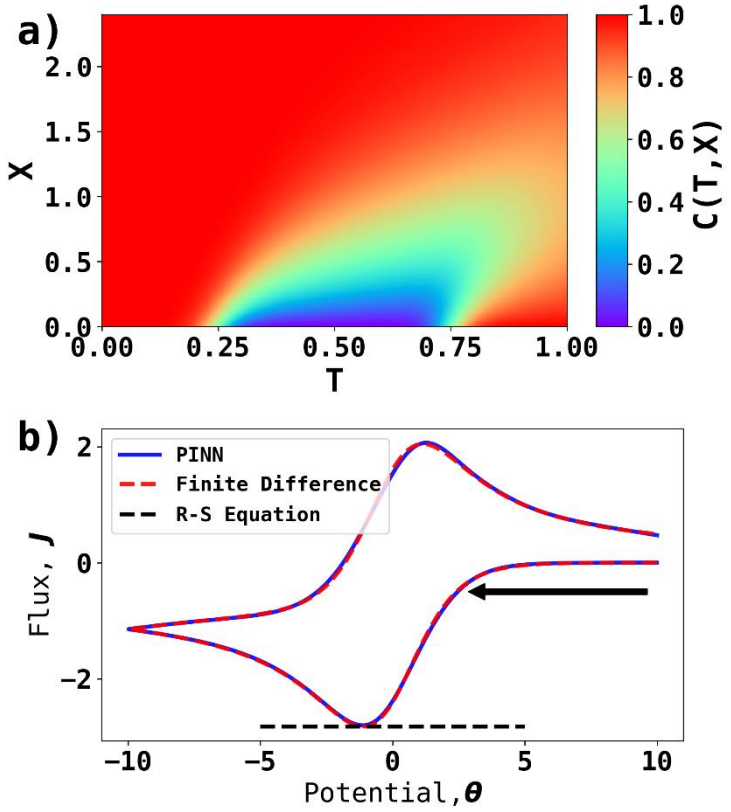

Figure 8.2. Prediction results of PINN for cyclic voltammetry at $\sigma = 40$. (a) The temporal-spatial concentration profile and (b) the voltammogram predicted by PINN (blue line) is compared with voltammogram generated using finite difference method (red dashed line). The peak current is compared with the peak current predicted using the Randles-Ševčík equation (black dashed line). The black arrow indicates the start the initial direction of scan.

8.4.2 Cyclic voltammetry at a macroelectrode with a finite-space boundary condition

A PINN can also be applied to solve cyclic voltammetry with a Neumann boundary condition which we illustrate for thin-layer cyclic voltammetry. Thin-layer cyclic voltammetry is different from normal cyclic voltammetry by having a constrained diffusion layer. In experimental practice the constraint is provided by solid wall opposite the electrode through which material cannot pass[32, 33]. Mathematically this corresponds to a no-flux boundary condition at the outer boundary of simulation. The diffusion equation and boundary conditions can be expressed as:

$$\begin{aligned} \frac{\partial C}{\partial T} - \frac{\partial^2 C}{\partial X^2} = 0 \quad & on\ \mathcal{T} \times \Omega_X \quad (1) \\ C = \frac{1}{1+e^{-\theta}} \quad & on\ \mathcal{T}, X = 0 \quad (2) \\ \frac{\partial C}{\partial X} = 0 \quad & on\ \mathcal{T}, X = \delta \quad (3) \\ C = 1 \quad & on\ T = 0, \Omega_X \quad (4) \end{aligned} \tag{8.10}$$

where the thin layer cell (dimensionless) thickness, δ, also the outer boundary of simulation, defines the scale of the cell thickness to the extent of the diffusion layer via $\delta = \lambda\sqrt{T_{sim}}$where λ is a factor signalling thin-layer behaviour (small λ) and semi-infinite behavior (large λ). The spatial domain Ω_X is defined as $\Omega_X \in \left[0, \lambda\sqrt{T_{sim}}\ \right]$ for PINN prediction. The no-flux boundary condition can be enforced by:

$$MSE_{outer} = \frac{1}{N}\sum_{i=1}^{N}\left(\frac{\partial C_i}{\partial X_i}\right)^2 \tag{8.11}$$

where $X_i = \delta$ representing the outer boundary for the PINN prediction.

Using PINN, the electrochemically reversible cyclic voltammetry when $\sigma = 40$ was simulated corresponding to a thin layer factor $\lambda = 0.035$. The temporal spatial concentration profile predicted by the PINN is shown in Figure 8.3a and the corresponding cyclic voltammogram is shown in Figure 8.3b. Figure 2a shows the thin-layer concentration pattern with A almost fully converted to B when $0.25 < T < 0.75$.

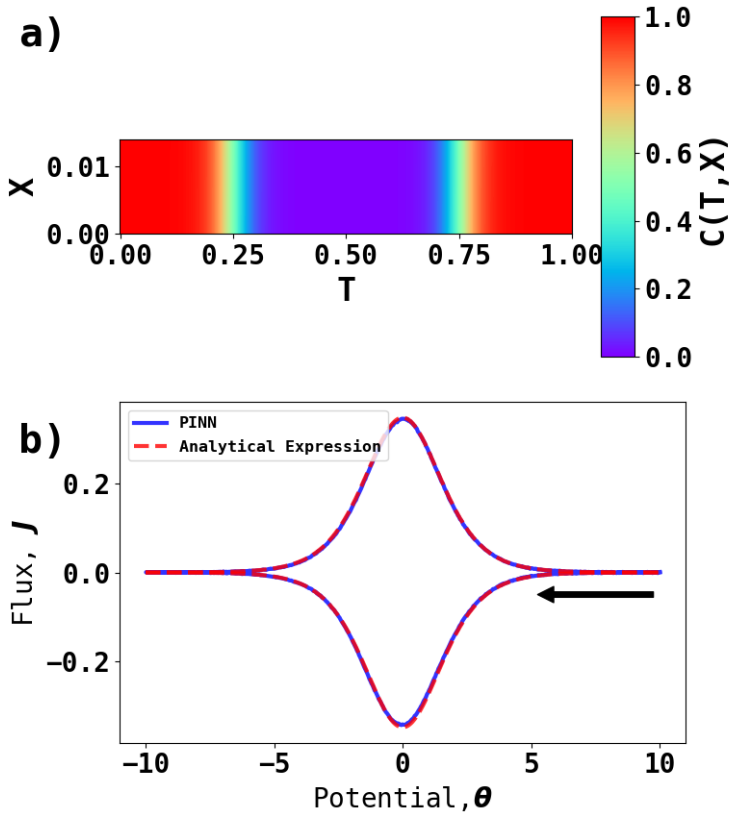

Figure 8.3. Prediction results of PINN for thin layer linear sweep cyclic voltammetry at $\sigma = 40$ and $\lambda = 0.035$. (a) The temporal-spatial concentration profile with thin diffusion layer and (b) the voltammogram predicted by PINN (blue line) is compared with voltammogram predicted by **(8.13)** (red dashed line). The black arrow indicates the start the initial direction of scan.

To validate the results of PINN for thin layer cyclic voltammetry, the peak current and voltammogram is compared with analytical expression derived by Hubbard et al.[33] converted to dimensionless form as:

$$\mathrm{J_{p,thin\ layer}} = -\frac{\sigma X_{sim}}{4} \tag{8.12}$$

$$\mathrm{J_{thin\ layer}} = \mp\sigma X_{sim}\frac{\exp\theta}{(1+\exp\theta)^2} \tag{8.13}$$

where $\mathrm{J_p}$ is the peak flux for forward scan and $\mathrm{J}_{thin\ layer}$ describes the shape of voltammogram as a function of dimensionless potential, θ, and the upper and lower sign refers

to the cathodic and anodic scan respectively. As is evident in Figure 8.3b, the PINN predicted voltammogram closely agrees with the voltammogram predicted by the analytical expression, suggesting that PINN can accurately predict thin-layer voltammetry. To further validate the model, the transition of thin-layer behaviour to semi-infinite behaviour with increasing λ is illustrated by plotting the dependency on λ of the peak flux, J_p, and the peak to peak separation, θ_{pp}. With increasing λ, J_p is expected to transition from the Hubbard equation to the Randles-Ševčík equation and θ_{pp} is expected to increase from $\theta_{pp} = 0$ for thin-layer to $\theta_{pp} = 2.218$ for semi-infinite behaviour[15]. The plot of J_p vs. λ and θ_{pp} vs. λ predicted by PINN is shown in Figure 8.4 and compared with the predictions from simulations using the finite difference method[15]. The excellent agreement shows that the PINN approach to thin-layer cyclic voltammetry worked well. Figure 8.4 shows that both PINN and the finite difference method predicts that when $\lambda > 0.8$, thin-layer cyclic voltammetry converges to semi-infinite cyclic voltammetry.

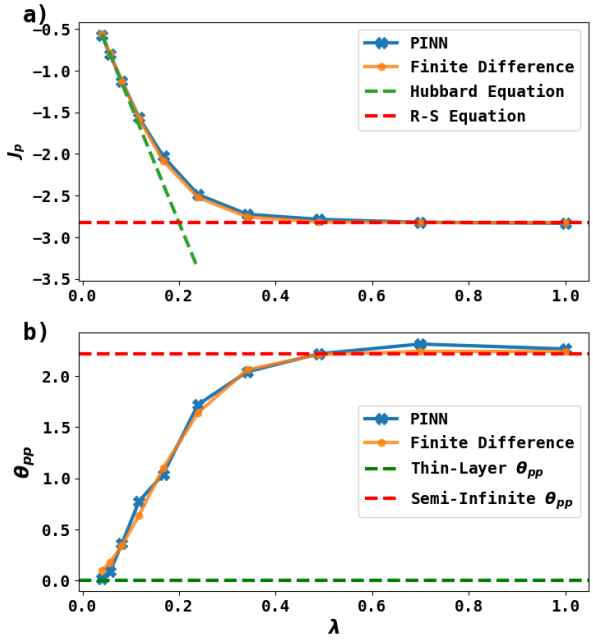

Figure 8.4. (a) The peak flux predicted by PINN (blue line with marker) and finite difference method (yellow line with marker) as a function of λ for $\sigma = 40$. The green and red dashed lines are the currents predicted by the Hubbard equation and the Randles-Ševčík equations

respectively. (b) Peak to peak separation predicted by PINN (blue line with marker) and finite difference method (yellow line with marker) as a function of λ. Green and red dashed lines are expected peak to peak separation for thin-layer and semi-infinite respectively (see text).

8.4.3 Cyclic voltammetry at a microband electrode

To further illustrate and validate the potential applications of PINN in electrochemistry, we explore the PINN prediction for cyclic voltammetry of a microband electrode under semi-infinite diffusion, aiming to predict $\mathrm{C}(T, X, Y)$ on a temporal-2D spatial domain($\mathcal{T} \times \Omega_X \times \Omega_Y, \Omega_Y \in [0, Y_{sim}]$). For two-dimensional diffusion, **(8.8)** becomes:

$$MSE_f = \frac{1}{N}\sum_{i=1}^{N}\left(\frac{\partial C_i}{\partial T_i} - \frac{\partial^2 C_i}{\partial X_i^2} - \frac{\partial^2 C_i}{\partial Y_i^2}\right)^2 \qquad \textbf{(8.14)}$$

to account for diffusion in 2D. To enforce **(8.14)**, a set of N collocation points $\{T_i, X_i, Y_i\}_{i=1}^{N}$ are necessary. A mix of no-flux and fixed concentration boundary conditions are also required to describe the system. To improve optimization and generalization of two-dimensional problems, a learning rate scheduler was utilized to decrease the learning rate by 1% every epoch after 400 epochs[34]. To reduce the collocation points in the entire domain, the outer boundaries were reduced to $X_{sim} = Y_{sim} = 2\sqrt{T_{sim}}$ without significant influence to the results. PINN prediction at $\sigma = 4$ is performed to reveal the convergent diffusion expected at the microband electrode at lower scan rates. Figure 8.5 shows a concentration profile when $T = \frac{1}{2}T_{sim}$ at the reverse potential $\theta_{switch} = -10$. Because of the symmetry of the microband electrode, simulating half of the microband is sufficient. The electrode surface is located at $X = 0, Y = [0,0.5]$ represented by a flat, red rectangle and the convergent diffusion is observed at the upper edge of the microband electrode as illustrated in Figure 8.5a.

To validate the prediction by PINN, we note that the peak current of linear sweep voltammetry at microband electrode predicted via FD simulation by Aoki et al.[35] is:

$$J_{p,microband} = 0.439p + 0.713p^{0.108} + \frac{0.614p}{(1 + 10.9p^2)}, p = \sqrt{\sigma} \quad \textbf{(8.15)}$$

which is reported accurate to within 2.1% error. The voltammogram can be extracted from the gradients at the electrode surface in the concentration profiles in the temporal domain, then filtered with a Savitzky-Golay filter[36] to reduce high-frequency noise. Figure 8.5b compares the PINN predicted voltammogram with the Aoki equation. The peak flux predicted by PINN is 3.3% higher than the Aoki equation, showing the PINN can solve the temporal-spatial problem for 2D simulation of microband electrode within an acceptable level of error. The PINN predictions take approximately four hours with Nvidia P100 16G GPU.

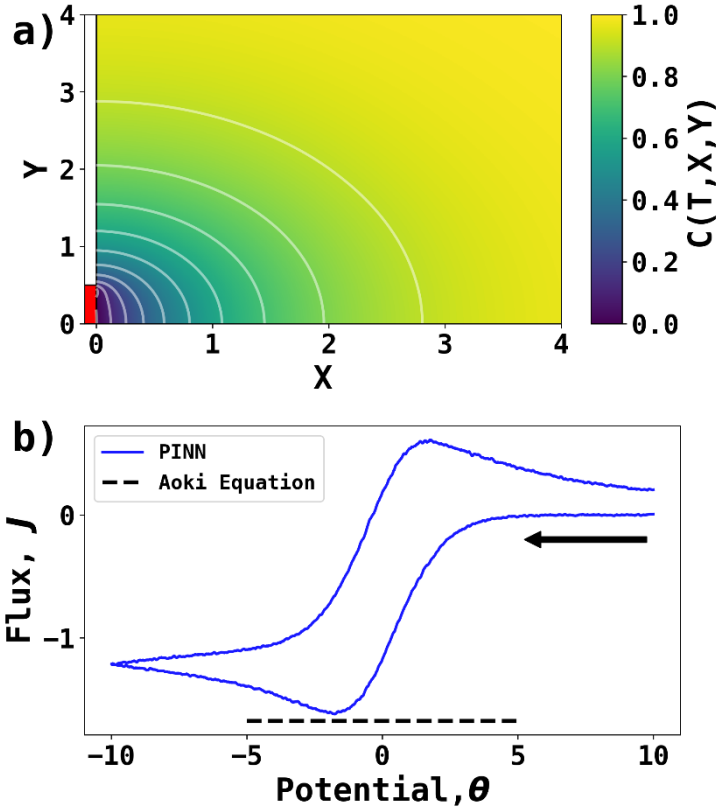

Figure 8.5. PINN prediction of cyclic voltammetry at a microband electrode for $\sigma = 4$. (a) Concentration profile with contours when $T = \frac{1}{2}T_{sim}$ and $\theta = -10$ with contour lines of equal concentration.The red block represents the surface of microband electrode. (b) The peak current of cyclic voltammogram (blue) predicted by PINN is compared with the peak current predicted by the Aoki equation. The black arrow indicates the start the initial direction of scan.

8.4.4 Voltammetry at the edges of a square particle

Last, we employ a PINN to generate new physical insights into the current distributions at non-uniformly accessible electrodes under electrochemically reversible conditions. Specifically, we investigate and model the previously unexplored voltammetric case in which species A and B undergo two-dimensional diffusion in the (x, y) plane with a square electrode located flat in the plane so that electrolysis is confined to the edges of the electrode. In this way the consequences to the electrode current distribution caused by the increased diffusional accessibility at the electrode corner was compared to that seen at locations on the edges distant from the corner. Interesting a clear maximum in the local flux will be seen, but not at the electrode corner as might be expected and the insights have value for nanoparticle electrochemistry[37-39]. Specifically, we explore a PINN solution of cyclic voltammetry at the edges of the square electrode. As above, the two-dimensional diffusion equation is enforced as the mode of mass transport for PINN. Two computational subdomains of diffusion equations are configured to obtain better accuracy and faster training[40]. The square electrode has two electrochemically reaction edges with a Nernstian boundary condition. The PINN prediction of the concentration profile and cyclic voltammetry at the square electrode with two electrochemically active edges were performed at $\sigma = 40$, with the dimensionless edge length set as 1. Figure 8.6a illustrates the concentration profile at $\mathrm{T} = \frac{1}{2}T_{sim}$ and $\theta = -10$. Figure 8.6b shows the flux density at the edges when $\mathrm{T} = \frac{1}{2}T_{sim}$ as a function of X and Y coordinates for top and right edges respectively. The scatter plots showed a small amount of noise possibly due to the stochastic nature of the neural network. The overlapping flux densities on the two edges reflect the symmetry of the square electrode, and thus partly validate the predictions. Interestingly, the magnitude of the flux density is largest for an X/Y coordinate of around 0.8,

instead of exactly at the corner of the particle. Figure 8.6c shows the corresponding voltammograms inferred for the two edges which are almost identical, again confirming the validity of the PINN approach. The occurrence of the maximum current near but not at the corner was unexpected and shows the value of PINN simulations for extracting new semi-quantitative physical insights. In the present case the location at the maximum reflects the increased diffusional accessibility near the corner as expected but also highlights, as inferred with hindsight, that the competition between the two edges plays a significant role.

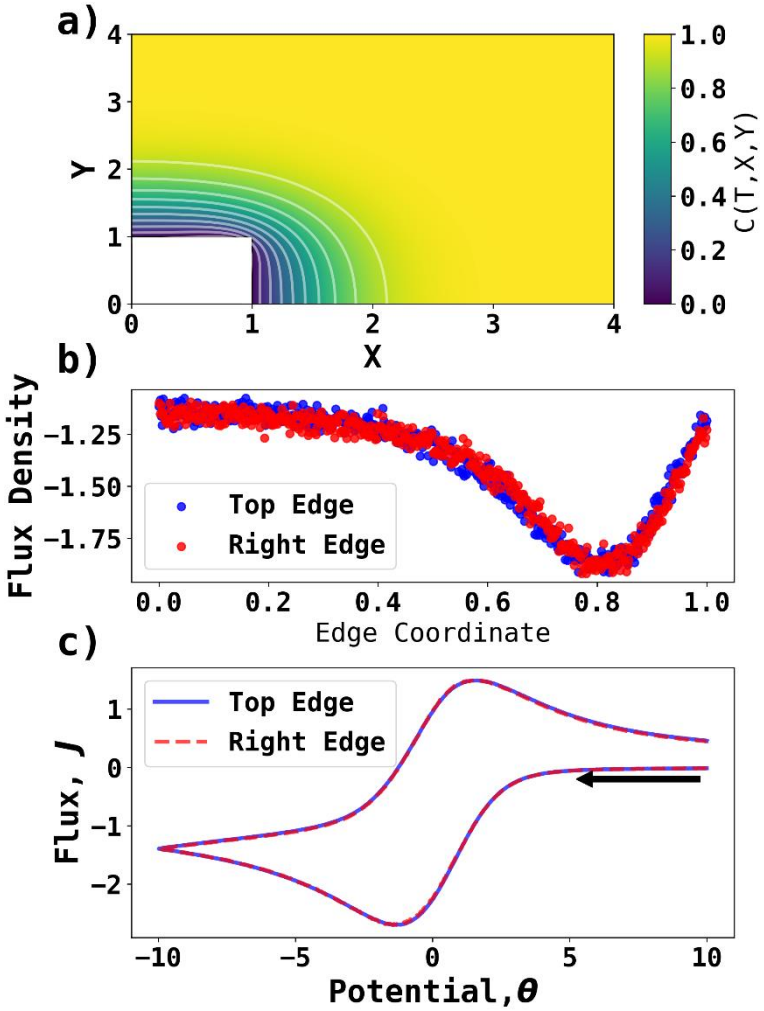

Figure 8.6. PINN prediction of cyclic voltammetry on the edges of a square electrode at $\sigma = 40$. The square electrode has two electrochemically active edges. (a) concentration profile at

$T = \frac{1}{2}T_{sim}$ with contour lines of equal concentration; (b) flux density at the top and right edges when $T = \frac{1}{2}T_{sim}$; (c) Cyclic voltammogram of the two edges. The black arrow indicates the start the initial direction of scan.

8.5 Conclusion

In summary, in the present work we have developed PINN to solve four problems: two one-dimensional cases including voltammetry with semi-infinite or thin-layer boundary condition and two two-dimensional simulations including the microband electrode and the square electrode. The resulting voltammograms are, where available, compared with analytical expressions or voltammograms simulated using finite difference method, proving that PINNs can correctly predict voltammetry, without using any discretization, but with only information of the underlying laws of physics, boundary conditions and the initial state. When training PINNs to predict voltammograms, we found three major advantages of PINNs. First, with a well-established neural network framework like TensorFlow or PyTorch, constructing a neural network is far less daunting than discretizing equations for finite difference or finite element methods. The implication of this is that the investigator can focus on considering the physical models rather than on the mechanics of solution. Instead they simply need to formulate the relevant transport equations and boundary conditions so facilitating a greater range of models to be explored. Second, we found that debugging and modifying PINN programs are relatively easy and comparatively rapid. Users can pause the neural network for a model check point and generate the concentration profile for visual or mathematical inspection. By generating new datasets and slightly modifying the loss function, PINNs can easily adapt to new prediction tasks. Third, PINNs, as a subclass of neural network, can be easily trained on GPU or CPU with minimal modification and are less demanding regarding computer hardware and are usually trained on GPU to take advantage of recent advances in GPU computing powers. In

addition, PINNs can utilize transfer learning from trained neural networks for possibly significant time saving. PINN can be applied to higher dimensions with greater ease, though exponentially more collocation points are necessary to spread the higher dimensional domain. Furthermore, hyperparameters for neural networks, like epochs, learning rate, loss weights, choice of optimizers can also be tuned for better results. The success of PINN in predicting cyclic voltammetry as shown above signals further possible applications to solution of mass (or heat) transfer problems probably coupled with chemical or electrochemical kinetics, providing a powerful (and likely simpler) alternative to the conventional finite difference or finite element methods.

In the next and final chapter, we challenge PINN with more complicated physical laws notably diffusive-convection mass transport with and without coupled homogeneous chemical kinetics as illustrative of hydrodynamic voltammetry. The caveat of training such a neural network will be introduced in the next chapter.

References

1. H. Chen, E. Kätelhön and R. G. Compton, *J. Phys. Chem. Lett.*, 2022, **13**, 536-543.
2. M. Raissi, P. Perdikaris and G. E. Karniadakis, *J. Comput. Phys.*, 2019, **378**, 686-707.
3. M. Aykol, C. B. Gopal, A. Anapolsky, P. K. Herring, B. van Vlijmen, M. D. Berliner, M. Z. Bazant, R. D. Braatz, W. C. Chueh and B. D. Storey, *J. Electrochem. Soc.*, 2021, **168**, 030525.
4. R. G. Nascimento, M. Corbetta, C. S. Kulkarni and F. A. C. Viana, *J. Power Sources*, 2021, **513**, 230526.
5. A. Talukdar, R. S. Patil, A. Kaushik, A. Naha, S. P. Adiga, D. Jung, S. M. Kolake and Y. Sung, *J. Energy Storage*, 2020, **32**, 101962.
6. A. Bills, S. Sripad, W. L. Fredericks, M. Guttenberg, D. Charles, E. Frank and V. Viswanathan, *arXiv preprint arXiv:2008.01527*, 2020.
7. J. Bao, C. Wang, Z. Xu and B. J. Koeppel, *Physics-Informed Machine Learning with Application to Solid Oxide Fuel Cell System Modeling and Optimization*, Pacific Northwest National Lab.(PNNL), Richland, WA (United States), 2019.
8. G. T. Le, L. Mastropasqua, S. B. Adler and J. Brouwer, *ECS Transactions*, 2021, **103**, 1201-1211.

9. D. Wang, J. Bao, Z. Xu, B. Koeppel, O. A. Marina, A. Noring, M. Zamarripa-Perez, A. Iyengar, E. Eggleton, D. T. Schwartz, A. Burgard and D. Miller, *ECS Transactions*, 2021, **103**, 2283-2292.
10. W. Ji, W. Qiu, Z. Shi, S. Pan and S. Deng, *J. Phys. Chem. A*, 2021, **125**, 8098-8106.
11. G. S. Gusmão, A. P. Retnanto, S. C. da Cunha and A. J. Medford, *arXiv preprint arXiv:2011.14473*, 2020.
12. R. G. Patel, I. Manickam, N. A. Trask, M. A. Wood, M. Lee, I. Tomas and E. C. Cyr, *J. Comput. Phys.*, 2022, **449**, 110754.
13. R. G. Compton and C. E. Banks, *Understanding voltammetry*, World Scientific, London, 3rd edn., 2018.
14. P. T. Kissinger and W. R. Heineman, *J. Chem. Educ.*, 1983, **60**, 702.
15. R. G. Compton, E. Laborda, E. Kaetelhoen and K. R. Ward, *Understanding voltammetry: simulation of electrode processes*, World Scientific London, 2nd edn., 2020.
16. K. Harriman, D. J. Gavaghan and E. Süli, *Electrochem. Commun.*, 2003, **5**, 519-529.
17. K. Harriman, D. J. Gavaghan and E. Süli, *J. Electroanal. Chem.*, 2004, **573**, 169-174.
18. C. Batchelor-McAuley and R. G. Compton, *J. Electroanal. Chem.*, 2020, **877**, 114607.
19. A. Fick, *Ann. Phys.*, 1855, **170**, 59-86.
20. A. Fick, *Lond. Edinb. Dubl. Phil. Mag.*, 1855, **10**, 30-39.
21. K. Ngamchuea, S. Eloul, K. Tschulik and R. G. Compton, *J. Solid State Electrochem.*, 2014, **18**, 3251-3257.
22. A. J. Bard and L. R. Faulkner, *Electrochemical Methods: Fundamentals and Applications*, 2nd edn., 2001.
23. E. Laborda, J. González and A. Molina, *Curr. Opin. Electrochem.*, 2020, **19**, 78-87.
24. E. Laborda, A. Molina, F. Martínez-Ortiz and R. G. Compton, *Electrochim. Acta*, 2012, **73**, 3-9.
25. B. A. Coles and R. G. Compton, *J. Electroanal. Chem. Interfacial Electrochem.*, 1983, **144**, 87-98.
26. G. Philipp, D. Song and J. G. Carbonell, *arXiv preprint arXiv:1712.05577*, 2017.
27. A. Einstein, *J Annalen der physik*, 1905, **17**, 549-560.
28. I. B. Svir, A. I. Oleinick and R. G. Compton, *Russ. J. Electrochem.*, 2003, **39**, 160-164.
29. D. P. Kingma and J. Ba, *arXiv preprint arXiv:1412.6980*, 2014.
30. A. Ševčik, *Collect. Czech. Chem. Commun.*, 1948, **13**, 349-377.
31. J. E. B. Randles, *Trans. Faraday Soc.*, 1948, **44**, 327-338.
32. M. P. Soriaga and A. T. Hubbard, *J. Am. Chem. Soc.*, 1982, **104**, 2735-2742.
33. A. T. Hubbard and F. C. Anson, *Anal. Chem.*, 1966, **38**, 58-61.
34. K. You, M. Long, J. Wang and M. I. Jordan, *arXiv preprint arXiv:1908.01878*, 2019.
35. K. Aoki and K. Tokuda, *J. Electroanal. Chem. Interfacial Electrochem.*, 1987, **237**, 163-170.
36. R. W. Schafer, *IEEE Signal processing magazine*, 2011, **28**, 111-117.
37. F. J. Vidal-Iglesias, R. M. Arán-Ais, J. Solla-Gullón, E. Herrero and J. M. Feliu, *ACS Catalysis*, 2012, **2**, 901-910.
38. J. Hernández, J. Solla-Gullón, E. Herrero, A. Aldaz and J. M. Feliu, *J. Phys. Chem. C*, 2007, **111**, 14078-14083.
39. J. Solla-Gullon, E. Garnier, J. M. Feliu, M. Leoni, A. Leonardi and P. Scardi, *J. Appl. Crystallogr.*, 2015, **48**, 1534-1542.
40. A. D. Jagtap, E. Kharazmi and G. E. Karniadakis, *Comput. Methods Appl. Mech. Eng.*, 2020, **365**, 113028.

Chapter 9 Physics-Informed Neural Network and its Application in Electrochemistry: Hydrodynamic voltammetry

In this chapter, Physics-Informed Neural Networks are applied to solve some convective diffusional mass transport problems for hydrodynamic voltammetry. The predictions are validated by comparing with experiments and/or analytical expressions where applicable. This work has been published at Analyst[1].

Electrochemical problems are widely studied in flowing systems since the latter offer improved sensitivity notably for electro-analysis and the possibility of steady-state measurements for fundamental studies even with macro-electrodes. We report the exploratory use of Physics-Informed Neural Networks (PINNs) as a potentially simpler, and easier way to implement alternatives to Finite Difference or Finite Element simulations to predict the effect of flow and electrode geometry on the currents observed in channel electrodes where the flow is constrained to a rectangular duct with the electrode embedded flush with the wall of the cell. Several problems are addressed including the evaluation of the transport limited current at a channel micro-electrode, the transport of material between two adjacent electrodes in a channel flow and the response of an electrode where the electrode reaction follows a preceding chemical reaction. The approach is shown to give quantitative agreement in the limits for which existing solutions are known whilst offering predictions for the case of the previously unexplored CE reaction at a channel microelectrode.

9.1 Introduction

The vast volume of current publications reporting mostly empirical work in the areas of electrocatalysis and electro-analysis testifies to the importance of electrochemistry both in

general and to these specific topics, particularly for energy transformation technology, clean (electro-) synthesis and chemical sensing. At the same time the disappointing speed of substantive progress across these areas, which are essential for the continued and enhanced well-being of mankind,[2] suggests that in place of empiricism a bottom up approach which interplays theory with quantitative experiment[3] is needed to secure the discoveries and changes required. In the case of dynamic electrochemistry, essential theory includes descriptions of electron transfer,[4-8] mass transport[9-11] and interfacial structure.[12] Whilst the experimental implications of theory are established for simple chemistry in well-defined electrode geometries, the extension to many of the systems of current interest including mechanistically complex multi-electron processes such as carbon dioxide reduction, nitrogen activation and water splitting, is challenging largely because models once proposed need, so as to be applied to the quantitative analysis of experimental data, to be mathematically described through solution of sets of coupled partial differential equations with often complicated boundary conditions. This is typically addressed via simulation using finite element (FE) or finite difference (FD) methods[13, 14] which are time-consuming and require significant expertise and experience to accurately implement. The era of machine learning may, however, offer the experimentalist a generic and easy route to solving the equations with minimal programming and allowing the rigorous exploration of a much wider and diverse range of mechanistic hypotheses than hitherto possible via the use of Physics-Informed neural networks.

As outlined in the previous chapter Physics-Informed neural networks (PINNs), were introduced in 2018 by Rassi to provide data driven solution and discovery of partial differential equations (PDEs). They have found extensive use for example in fluid dynamics, including incompressible laminar flow[15], turbulent flow[16] and oceanographic studies[17]. Other examples of the use of PINNs include pricing of financial derivatives,[18] epidemiological models,[18] battery lifetime estimations,[19] and modelling of wind turbine main bearing fatigue.[20] The

abundance of recent publications describing diverse uses have proven the potential of PINN's but to the best of authors' knowledge, the application of convective-diffusion informed PINN in general or specifically to mechanistic or analytical electro-chemistry is lacking, which can be possibly explained by a recent report,[21] asserting the difficulty of training PINN to accommodate convective-diffusion and diffusion-reaction models with relatively fast mass transport and/or chemical kinetics.[21] Nevertheless encouraged by the curriculum learning suggested by Krishnapriyan et al.,[21] in this chapter we solve the convective-diffusion equation for channel electrodes of different geometries, addressing a range of problems of interest to electrochemists and analysts including in the presence of fast coupled chemical kinetics.

A channel (or tubular) electrode[22, 23] comprise an electrode embedded in the wall of a rectangular duct (or circular tube) through which solution flows. Measurements can be made at steady-state where the variation of flow rate give a convenient controllable handle on the voltammetric timescale akin to the use of electrode size in microelectrode voltammetry[24, 25] so allowing the study of electrode reaction mechanisms and kinetics. Further the geometry is compatible with spectro-electrochemical measurements.[26] In additional and most importantly, the channel electrode is the basis of the electroanalytical detectors of high sensitivity, the use of which have grown rapidly with the adoption of microfluidic techniques, flow injection analysis[27, 28] and liquid chromatography[29, 30] into major analytical activities.[31, 32] In fundamental electrochemistry, channel electrodes, partly due to their non-uniformly accessibility, are sensitive in distinguishing different but similar mechanisms, including CE, EC, ECE, DISP, etc.[22] Double channel electrodes consist of an upstream electrode and a downstream electrode in the channel wall, separated by insulating material but linked via flow. The two electrodes can form a generator-collector or generator-generator array or be used as a single combination. Applications of channel electrodes includes characterization of electrolytic processes at the surface of porous silicon electrodes,[33] electrochemical electron paramagnetic resonance

spectroscopy (EPR),[34] droplet detection in microfluidic devices[35] and ion detection at the liquid/liquid interface.[36]

Simulation of channel electrodes, conventionally employs finite difference[37] and/or finite element methods,[31, 38] both requiring bespoke home-written programs[12] based on discretization of simulation space, in the absence of access to expensive commercial software, which also use these approaches, to obtain solutions. These requirements reduce the accessibility and hence extent of application of these methods.[39] Thus, we propose a discretization-free simulation using PINNs, to predict the steady state transport limited currents at the channel electrode particularly as a function of the flow rate and electrode geometry. Three scenarios are investigated, including the single microband channel electrode, the double microband channel electrode and single microband channel electrode coupled with preceding first-order reversible chemical kinetics (CE reaction). The TensorFlow implementation is available at https://github.com/nmerovingian/PINN-Hydrodynamic-Voltammetry for the use of readers.

9.2 Theory

Three specific channel electrode problems are explored using PINNs in this chapter. The first addresses the transport limited current arising from a simple one electron reaction, assumed to be an oxidation, at a channel microband electrode:

$$A \rightarrow B + e \tag{9.1}$$

where A and B are stable solution species flowing in the channel. The second problem is that of the double channel electrode working in generator-detector mode where the electrochemical reaction on the two electrodes are:

$$\begin{cases}\text{Generator: } A \rightarrow B + e \\ \text{Detector: } B + e \rightarrow A\end{cases}, \mathrm{N} = -\frac{I_d}{I_g} \tag{9.2}$$

where I_d and I_g are the currents of the detector and generator electrode respectively and N the collection efficiency of the double channel electrode where the case of both electrodes being of microband geometry is addressed. The third problem is that of preceding chemical reaction (a so-called CE reaction[40]) at a channel electrode where:

$$\begin{cases} R \underset{k_b}{\overset{k_f}{\rightleftarrows}} A, K_{eq} = \frac{k_f}{k_b} \\ A \rightarrow B + e \end{cases} \tag{9.3}$$

where A/B is the electrochemical redox couple and R is electrochemically inert. k_f, k_b and K_{eq} are the forward reaction rate constant, reverse reaction rate constant and equilibrium constant of the preceding chemical reaction, respectively.

In all cases sufficient supporting electrolyte is presumed present so that the transport is exclusively via diffusion and forced convection. In this chapter, the simulation results are compared with previously reported analytical expression and/or experimental results where applicable.

Solution flows through a cell such as shown in Figure 9.1, which contains a rectangular electrode of length x_e, width w. The distance $x_{channel}$ represents the length of the flow cell which is simulated. As discussed below the distances, x_1 and x_2 (measured from the coordinate origin to the upstream edge or to the downstream edge of the electrode) define the position of the electrode within the PINN simulations. The distance x_1 allows for axial diffusion upstream of the electrode whilst a distance $x_{channel} - x_2$ is included in the simulation again to account for axial diffusion effects. The channel has a width of d and height of $2h$.

The flow cell is usually designed that the flow pattern over the electrode is laminar and thus well-defined over the range of flow rates employed. Laminar or turbulent flow is usually characterized via the Reynold numbers where:

$$Re = \frac{2hv_0}{\nu} \tag{9.4}$$

and v_0 is the solution velocity at the center of channel and ν is the kinematic viscosity of the solution. Re is usually experimentally kept below 2000 to avoid turbulent flow, which is more difficult to model. The steady-state flow is assumed to be fully developed at the upstream edge of the simulation which requires a lead-in length $x_{lead-in}$. large enough to allow establishment of steady-state parabolic velocity profile ('Poiseuille flow') caused by the friction between the solution and the cells:

$$x_{lead-in} \gg 0.1hR_e \tag{9.5}$$

The fully developed laminar flow is described as:

$$v_x = v_0\left[1 - \frac{(h-y)^2}{h^2}\right], v_y = 0, v_z = 0 \tag{9.6}$$

where h is the half-height of the cell. The volume flow rate is:

$$v_f = \frac{4}{3}v_0hd \tag{9.7}$$

A similar parabolic profile is established across the diameter of tubular electrodes.[22]

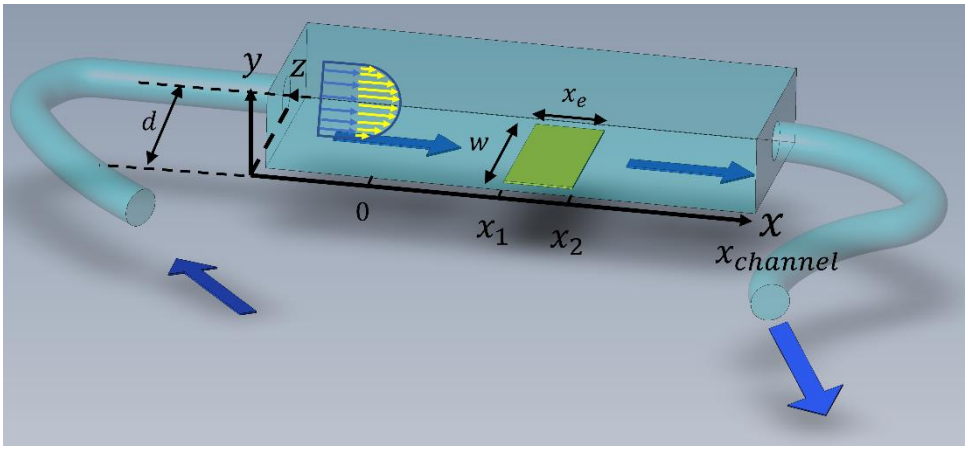

Figure 9.1. A schematic illustration of single microband channel electrode. Parabolic velocity profile is allowed to developed before $x = 0$ and $x = 0$ is the start of simulation. The yellow arrows show the velocity profile of laminar flow. x_1 and x_2 are coordinates along x-axis measured to the upstream and downstream edge of channel and $x_{channel}$ is the length of the flow cell. The height and width of flow cell is $2h$ and d along y and z axes respectively with x=0 at the coordinate origin. The upstream and downstream lengths are denoted as x_a and x_b and the length and width of electrode are x_e and w, respectively. (see text).

9.2.1 Simulation of Steady State limiting Currents at Single Microband Channel Electrodes

The mass transport equation for the channel electrode is:

$$\frac{\partial c_A}{\partial t} = D_A \nabla^2 c_A - \left(v_x \frac{\partial c_A}{\partial x} + v_y \frac{\partial c_A}{\partial y} + v_z \frac{\partial c_A}{\partial z} \right) \quad \textbf{(9.8)}$$

where ∇^2 is the Laplacian operator. Note that the flow rate in y and z directions is zero ($v_y = v_z = 0$) and at steady state $\frac{\partial c_A}{\partial t} = 0$. Since the electrode width is usually much larger than the length, transverse diffusion in the z-direction can be neglected so reducing the simulation to a two-dimensional problem. Thus, the convective-diffusion mass transport at steady state simplifies to

$$0 = D_A \frac{\partial^2 c_A}{\partial x^2} + D_A \frac{\partial^2 c_A}{\partial y^2} - v_x \frac{\partial c_A}{\partial x} \quad \textbf{(9.9)}$$

where D_A is the diffusion coefficient of species A.

To facilitate an approximate analytical solution to the problem Levich[11] further simplified by first neglecting axial diffusion which is a good approximation for macroelectrodes but not for microelectrodes[41] and second by introducing the Lévêque approximation[42] which linearizes the flow profile close to the electrode leading to:

$$0 = D_A \frac{\partial^2 c_A}{\partial y^2} - v_x \frac{\partial c_A}{\partial x}, v_x = v_0 \left[1 - \frac{(h-y)}{h}\right] \quad \textbf{(9.10)}$$

These simplifications allow derivation of the following approximate analytical expression for the transport limited current:

$$I_{lim} = 0.925 n F c_A w (x_e D_A)^{\frac{2}{3}} \left(\frac{v_f}{hd}\right)^{\frac{1}{3}} \quad \textbf{(9.11)}$$

For the PINN simulation (see below for details), **(9.9)** is solved subject to the following boundary conditions:

$$\begin{aligned} \frac{\partial c_A}{\partial y} = 0, x = [0, x_1], y = 0 \quad & (1) \\ c_A = 0, x = [x_1, x_2], y = 0 \quad & (2) \\ \frac{\partial c_A}{\partial y} = 0, x = [x_2, x_{channel}] \quad & (3) \\ c_A = c_A^*, x = 0, y = [0,2h] \quad & (4) \\ \frac{\partial c_A}{\partial y} = 0, x = [0, x_{channel}], y = 2h \quad & (5) \end{aligned} \quad \textbf{(9.12)}$$

where c_A^* is the bulk concentration of A at the inlet of channel where B is not present Equation 1,3,5 of **(9.12)** represents the no-flux boundary conditions on the surface of insulating materials. (12.2) enforces the zero concentration of A on the surface of electrode due to the application of a high overpotential for the oxidation of A.

9.2.2 Simulation of a Double Microband Channel Electrode

Figure 9.2shows a schematic diagram of a double channel electrode where five distances are used to define the simulation space and the electrode geometry: $x = 0$ is the start of the simulation, $x_1$and x_2 are the upstream and downstream coordinates of the generator electrode; x_3 and x_4 are the coordinates of the extremities of the detector electrode. $x_g = x_2 - x_1$ and $x_d = x_4 - x_3$ are the length of the generator and detector electrodes respectively. Note that the gap between the two electrodes, $x_b = x_3 - x_2$, is a key parameter in controlling the collection efficiency.[43, 44]

If species A and B in Figure 9.2 are assumed to have identical diffusion coefficients at all points of space, then it can be shown that $c_A + c_b = c_A^*$. In this way the problem is reduced to just one species. Accordingly, the problem is formulated considering only the mass transport of A. The boundary conditions for double microband channel electrode specifies different concentration at the surface of the generator and detector electrodes.

$$\begin{aligned}
\frac{\partial c_A}{\partial y} = 0, x = [0, x_1], y = 0 \quad (1)\\
c_A = 0, x = [x_1, x_2], y = 0 \quad (2)\\
\frac{\partial c_A}{\partial y} = 0, x = [x_2, x_3] \quad (3)\\
c_A = c_A^*, x = [x_3, x_4] \quad (4)\\
\frac{\partial c_A}{\partial y} = 0, x = [x_4, x_{channel}\,] \quad (5)\\
c_A = c_A^*, x = 0, y = [0,2h] \quad (6)\\
\frac{\partial c_A}{\partial y} = 0, x = [0, x_{channel}], y = 2h \quad (7)
\end{aligned} \qquad \textbf{(9.13)}$$

Equation 1,3,5,7 of **(9.13)** correspond to no flux boundary conditions at the insulating wall of the channel electrode. The electrochemical reactions on the generator and detector electrodes are represented by equation 2 and 4 of **(9.13)** respectively. Mass transport from upstream of channel electrode is represented by equation 7 of **(9.13)**.

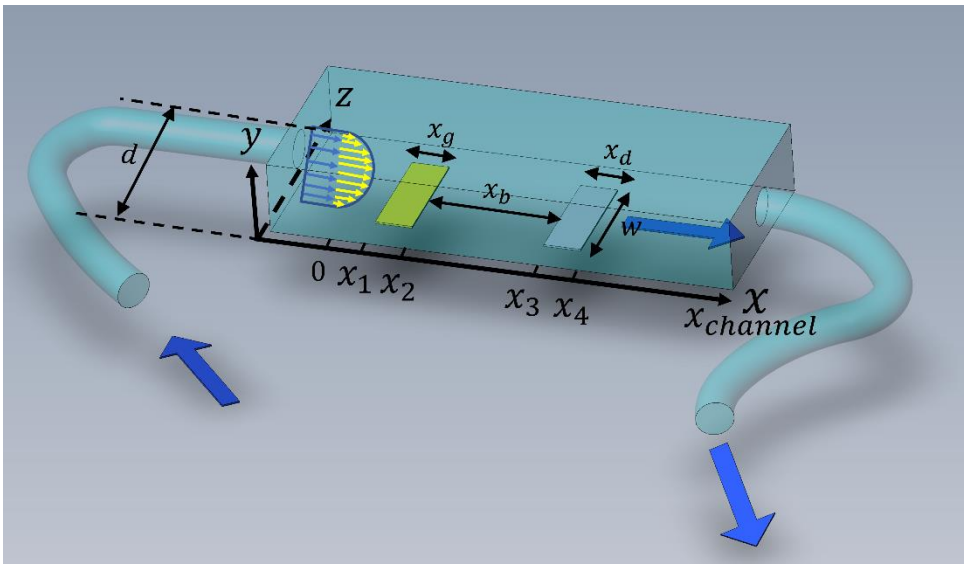

Figure 9.2. A schematic illustration of double microband channel electrode. Parabolic velocity profile is allowed to developed before $x = 0$ and $x = 0$ is the start of simulation. The yellow arrows show the velocity profile of laminar flow. x_1 and x_2 are the upstream and downstream coordinates for generator electrode (golden) and x_3 and x_4 are upstream and downstream coordinates of detector electrode (metallic color). The height and width of flow cell is $2h$ and d along y and z axes respectively with x=0 at the coordinate origin. The length of upstream, gap and downstream distances are denoted as x_a, x_b and x_c respectively and the length of generator and detector electrode is x_g and x_d ,respectively (see text).

9.2.3 Simulation of Single Channel Electrode with CE reaction

The mass transport equation for a channel electrode with coupled preceding chemical reaction at steady state is:

$$\begin{cases} 0 = D_R \dfrac{\partial^2 c_R}{\partial y^2} + D_R \dfrac{\partial^2 c_R}{\partial x^2} - v_x \dfrac{\partial c_R}{\partial x} - k_f c_R + k_b c_A \\ 0 = D_A \dfrac{\partial^2 c_A}{\partial y^2} + D_A \dfrac{\partial^2 c_A}{\partial x^2} - v_x \dfrac{\partial c_A}{\partial x} + k_f c_R - k_b c_A \end{cases} \quad \textbf{(9.14)}$$

where D_R is the diffusion coefficient for reactant R. Pre-equilibrium is assumed at x=0 and in bulk solution for the preceding chemical reaction where $K_{eq} = \frac{c_A^*}{c_R^*}$ and $c^* = c_A^* + c_R^*$. The following boundary conditions describe the problem for calculating the transport limited current due to the reduction of A:

$$\begin{aligned}
\frac{\partial c_A}{\partial y} = 0, x = [0, x_1], y = 0 \quad (1)\\
c_A = 0, x = [x_1, x_2], y = 0 \quad (2)\\
\frac{\partial c_A}{\partial y} = 0, x = [x_2, x_{channel}] \quad (3)\\
c_A = c_A^*, x = 0, y = [0,2h] \quad (4)\\
\frac{\partial c_A}{\partial y} = 0, x = [0, x_{channel}], y = 2h \quad (5)
\end{aligned} \tag{9.15}$$

The boundary conditions for the reactant, R, which is electrochemically inactive, are:

$$\begin{aligned}
\frac{\partial c_R}{\partial y} = 0, x = [0, x_{channel}], y = 0 \quad (1)\\
c_R = c_R^*, x = 0, y = [0,2h] \quad (2)\\
\frac{\partial c_R}{\partial y} = 0, x = [0, x_{channel}], y = 2h \quad (3)
\end{aligned} \tag{9.16}$$

9.2.4 Dimensionless Parameters

To solve the PDEs using PINN, dimensionless parameters (see Table 9.1) are pivotal to circumvent the expanding/diminishing gradient problem[45] while increasing the generalizability of the models.[13] By removing dependence on the electrode length, x_e, diffusion coefficient, D, and bulk concentration, c^*, the dimensionless results can be converted back to dimensional ones with any set of parameters. By definition, the dimensionless diffusion coefficient of A is always unity and so does not appear explicitly in the dimensionless mass transport equations. Without preceding chemical reaction, the dimensionless bulk concentration of species A is $C_A^* = 1$; With preceding chemical reaction and chemical equilibrium in the upstream solution, $C_R^* = \frac{1}{1+K_{eq}}, C_A^* = \frac{K_{eq}}{1+K_{eq}}$. Using the length of electrode, x_e, for a single channel electrode (and the length of generator electrode, x_g, for double channel

electrode) as a characteristic dimension and the Peclet number, Pe, reflects the relative influence of mass transport by convection and diffusion:

$$Pe = \frac{v_m x_e}{D_A} \tag{9.17}$$

where v_m is the mean flow velocity given by $v_m = \frac{2}{3} v_0$. The dimensionless form of mass transport equation, for single and double microband channel electrode is,

$$0 = \frac{\partial^2 C_A}{\partial Y^2} + \frac{\partial^2 C_A}{\partial X^2} - V_x \frac{\partial C_A}{\partial X} \tag{9.18}$$

where (Table 9.1)the dimensionless flow rate, V_x, is:

$$V_x = \frac{3}{2} P_e \left[1 - \left(\frac{(H - Y)^2}{H^2}\right)\right] \tag{9.19}$$

For channel electrode coupled with CE mechanics, the mass transport equation can be written as:

$$\begin{cases} 0 = d_R \frac{\partial^2 C_R}{\partial Y^2} + d_R \frac{\partial^2 C_R}{\partial X^2} - V_x \frac{\partial C_R}{\partial X} - K_f C_R + K_b C_A \\ 0 = \frac{\partial^2 C_A}{\partial Y^2} + \frac{\partial^2 C_A}{\partial X^2} - V_x \frac{\partial C_A}{\partial X} + K_f C_R - K_b C_A \end{cases} \tag{9.20}$$

Table 9.1. Table of conversions to dimensionless parameters. x_e is the length of electrode for single microband channel electrode and x_g is the length of generator electrode for double channel electrode. D_j stands for diffusion coefficient of any species j.

	Single microband channel electrode	Single microband channel electrode with CE reaction	Double microband channel electrode
Spatial coordinate	$X = \frac{x}{x_e}, Y = \frac{y}{x_e}, H = \frac{h}{x_e}$	$X = \frac{x}{x_e}, Y = \frac{y}{x_e}, H = \frac{h}{x_e}$	$X = \frac{x}{x_g}, Y = \frac{y}{x_g}, H = \frac{h}{x_g}$
Concentration	$\mathrm{C_A} = \frac{c_A}{c_A^*}$	$C_A = \frac{c_A}{c^*}, C_R = \frac{c_R}{c^*}$	$C_A = \frac{c_A}{c_A^*}$
Diffusion coefficient	$d_j = \frac{D_j}{D_A}$		
Peclet number	$Pe = \frac{v_m x_e}{D_A}$	$Pe = \frac{v_m x_e}{D_A}$	$Pe = \frac{v_m x_g}{D_A}$
Velocity flow rate	$V_x = \frac{3}{2} Pe \left[1 - \left(\frac{(H-Y)^2}{H^2}\right)\right]$		
First order chemical reaction	N/A	$K = \frac{k x_e^2}{D_A}$	N/A
Current	$I = Fwc_A^* D_A J$	$I = Fwc^* D_A J$	$I_g = Fwc_A^* D_A J_g$ $I_d = Fwc_A^* D_A J_d$

9.3 PINN Simulation

PINN simulation of the steady state mass transport with a single microband channel electrode requires prediction of concentration profile $\mathrm{C_A(X,Y)}$ where X and Y are dimensionless coordinates. $\mathrm{C}_A(X,Y)$ can be described as a combination of the convective-diffusion equation and boundary conditions:

$$
\begin{aligned}
\frac{\partial^2 C_A}{\partial Y^2} + \frac{\partial^2 C_A}{\partial X^2} - V_x \frac{\partial C_A}{\partial X} = 0, \Omega_X \times \Omega_Y \quad (1)\\
\frac{dC_A}{dY} = 0, X = [0, X_1], Y = 0 \quad (2)\\
C_A = 0, X = [X_1, X_2] \quad (3)\\
\frac{dC_A}{dY} = 0, X = [X_2, X_{channel}], Y = 0 \quad (4)\\
C_A = 1, X = 0, \Omega_Y \quad (5)\\
\frac{dC_A}{dY} = 0, \Omega_X, Y = Y_{channel} \quad (6)
\end{aligned}
\qquad \textbf{(9.21)}
$$

where $\Omega_X \in [0, X_{channel}], \Omega_Y \in [0, Y_{channel}]$, and represent the two-dimensional spatial domain for simulation. $X_{channel}$ is the dimensionless simulation length in the X direction. While X_e is always equal to one by definition, X_1 is set between 0.1 and 0.5 to allow diffusion upstream. $X_{channel}$ is thus between 1.2 and 2.0 to allow diffusion downstream. The faster the convection (high Pe), the less significant the contribution of axial diffusion and the smaller the $X_{channel}$. $Y_{channel}$ is chosen around 10 to 20 so that the boundary on the opposite side of electrode is less affected by the interfacial reaction(s). Equation 1 of **(9.21)** represents the PDE to be solved using PINN; Equation 2 and 4 of **(9.21)** are the no-flux boundary conditions on the insulating surface. Equation 6 of **(9.21)** describes the no-flux boundary condition at the outer boundary of simulation and is unperturbed by electrochemical reaction on the microband channel electrode. The electrochemical reaction on electrode surface is enforced by equation 3 of **(9.21)** as the surface concentration of *A* is zero. Finally, equation 5 of **(9.21)** enforces the boundary condition at the upstream of channel electrode, which should always be the bulk concentration of species A.

When neural networks are constrained by physical laws like the convective-diffusion equation above in **(9.21)**, they are said to be physical-informed. Unlike conventional supervised learning with neural network, which predicts $C(X, Y)$ by feeding known concentrations

corresponding to known spatial coordinates, PINN has only the knowledge of the physical equation and the boundary conditions. PINNs are trained by enforcing the physical laws with sets of collocation points, each set represents a physical constraint for PINN to satisfy. For example, to satisfy equation 1 of **(9.21)**, $\mathcal{N}$ collocation points $\{X_i, Y_i\}_{i=1}^{\mathcal{N}}$ are generated with a uniform random distribution on the $\Omega_X \times \Omega_Y$ spatial domain to predict concentration, $\{C(X_i, Y_i)\}_{i=1}^{\mathcal{N}}$, while satisfying the physical constraint by minimizing the mean square error (MSE) of physical constraints:

$$MSE_1 = \frac{1}{\mathcal{N}} \sum_{i=1}^{\mathcal{N}} \left(\frac{\partial^2 C_A}{\partial Y^2} + \frac{\partial^2 C_A}{\partial X^2} - V_x \frac{\partial C_A}{\partial X} \right)^2 \quad \textbf{(9.22)}$$

Calculation and optimization of PINN benefits from automatic differentiation (AD) commonly available in neural network frameworks, hence avoiding discretization and mesh setup. To satisfy the six equations of channel electrode, the overall loss of PINN is a linear combination of six MSE functions:

$$\mathcal{L} = \sum_{i=1}^{6} w_i MSE_i \quad \textbf{(9.23)}$$

where w_i is the weight of each MSE functions to accommodate errors which may have different magnitudes. During training, the overall loss is minimized by the Adam optimizer[46] (learning rate = 10^{-3}) and a hyperbolic tangent (tanh) is used as the activation function for its superior ability to approximate analytic functions.[47] The performance of the PINN depends on the number of collocation points,[48] and in this article $\mathcal{N}$ is set to 10^6 or 2×10^6 to satisfy both convergence and computer memory requirements. When the Peclet number, $Pe > 10$, curriculum learning (training stepwise from low Pe to high Pe) is used to assist convergence.[21]

After training, a concentration profile at $\Omega_X \times \Omega_Y$ is obtained. The flux on the surface of electrode is calculated as:

$$J = \int_{X_1}^{X_2} \left(\frac{\partial C_A}{\partial Y}\right)_{Y=0} dX \tag{9.24}$$

where $\left(\frac{\partial C_A}{\partial Y}\right)_{Y=0}$ can be approximated as $\left(\frac{C_{A,Y=\delta Y} - C_{A,Y=0}}{\delta Y}\right)$.

Note that to predict the concentration of the two species in the CE reaction, two neural networks, each predicting one species, are integrated in the PINN.

9.3.1 Simulation Method

The simulation programs were written in Python and the neural networks were implemented using TensorFlow. The simulations were run using a Nvidia V100 GPU and 12 allocated CPU cores using the Advanced Research Computing (ARC) facility at the University of Oxford. The implementation is available at https://github.com/nmerovingian/PINN-Hydrodynamic-Voltammetry .

9.4 Results and Discussion

In the following, first, PINN is applied to a single channel electrode and the predictions are compared with experimental results as a function of volume flow rate, v_f. Second, a PINN prediction of the collection efficiency of a double channel electrode is made as a function of the electrode lengths and gap. The results are compared with limiting analytical expressions derived under the Lévêque approximation in the presence of axial diffusion. Third, PINN predictions of the steady state flux for a CE reaction at a single microband channel electrode are investigated.

9.4.1 Single Microband Channel Electrode

First, PINN simulation was conducted by setting $Pe = 2.9$. Figure 9.3 presentsthe PINN prediction of steady state concentration profile and flux densities at the channel electrode. The concentration profiles show a progressive build-up of electrogenerated depletion in the

direction of flow whilst this extends to a limited extent upstream of the electrode as a result of axial back-diffusion. Downstream of the electrode, the depletion spreads out into the bulk of the solution and gradually the local concentrations tend towards the upstream bulk value as convection replenishes the depletion. The flux density at the channel electrode, as shown in Figure 3b, is not uniform. Note that in the limit of the Lévêque approximation and the neglect of axial diffusion, the flux scales as the inverse cube root of the distance from the upstream edge of the electrode which is approximately the case for the PINN results with the deviations attributed to the two approximations.

To facilitate comparison with literature experimental results, the dimensionless PINN simulations were converted to dimensional values with the following parameters, $2h = 0.05\ cm,\ w = 0.364\ cm,\ d = 0.6\ cm,\ D = 2.3 \times 10^{-5}\ cm^2\ s^{-1},$ and $c_A^* = 1.14\ mM$.[37] Two electrode lengths, 4 μm and 11 μm were considered and thediffusion coefficients of all species were assumed to be $2.3 \times 10^{-5}\ cm^2\ s^{-1}$. These diffusion coefficients correspond to ferrocene/ferrocenium redox couple in acetonitrile solution.[37, 49]

To test the 'convergence' of the PINN, Figure 9.4 illustrates the steady state flux predicted as a function of number of collocation points, $\mathcal{N}$, for the case $x_e = 11\ \mu m$ and $v_f = 0.004\ cm^3\ s^{-1}$. It is seen that when $\mathcal{N} \geq 10^6$, the steady state current converges to ca 1.4 μA. For the simulations reported below, in Figure 9.3 and Figure 9.5, the value of $\mathcal{N} = 10^6$ was applied.

PINN simulation of channel electrode was validated by comparing predictions for the ferrocene oxidation at the channel electrode with the experimental data[37] which reports the effect of the volume flow rate on the limiting current for the two channel electrodes of different lengths given above: from 0.005 to 0.03 $cm^3\ s^{-1}$ for 4 μm electrode ($Pe = 2.90$ to 17.37) and 0.001 to 0.01 $cm^3\ s^{-1}$ ($Pe = 1.59$ to 15.94) for 11 μm electrode. Figure 9.5 presents the

PINN predicted steady state current and experimental current as a function of volume flow rate, v_f. Good agreement with experimental results is observed as the maximum difference from experimental currents is less than $0.05\ \mu A$, suggesting that PINN can quantitatively predict the steady state current for microband channel electrodes under conditions where both diffusions, axial and normal, as well as the convection contribution to the mass transport.

PINN simulations were attempted for simplified models in which the axial diffusion was turned off and/or the Lévêque approximation made in place of **(9.10)**. In Figure 9.3b, the red-dashed line illustrates the flux density with Lévêque approximation and neglecting axial diffusion. Compared with the solid blue line representing PINN prediction without approximations, the red-dashed line shows a lower flux density and a sharper peak in the flux at the upstream edge of electrode, showing the greater relative contribution of convection when axial diffusion is assumed to be absent. It is interesting to note that the PINN solution was more easily successful with the physically realistic model whereas it was quantitatively challenged by the two approximations previous used to enable analytical mathematical approaches.

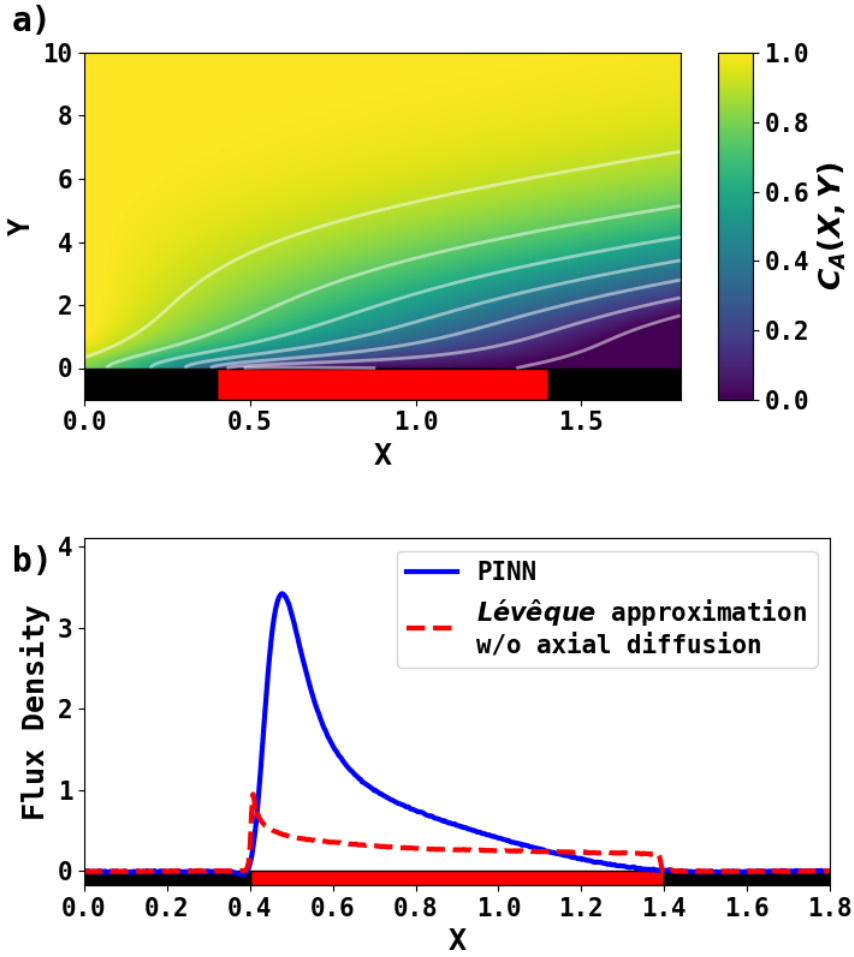

Figure 9.3. PINN prediction of transport-limited current at microband electrode when $Pe = 2.9$. (a) Concentration profile at steady state. (b) Flux density at steady state for the channel electrode using PINN without simplification (blue line); Flux density predicted by PINN using Lévêque approximation and neglecting axial diffusion (red dashed-line). Red square represents the electrode and black squares are the insulating material.

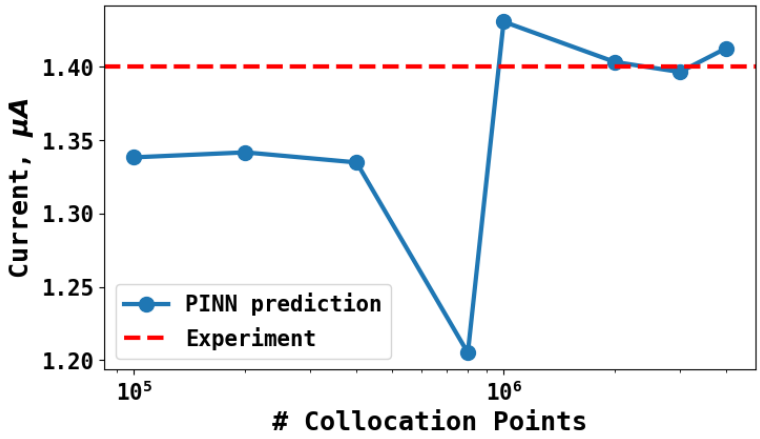

Figure 9.4. PINN prediction of steady state current (blue line with marker) at 11 μm electrode and $v_f = 0.004\ cm^3\ s^{-1}$ as a function of number of collocation points, $\mathcal{N}$ and compared with experimental results (red-dash line).

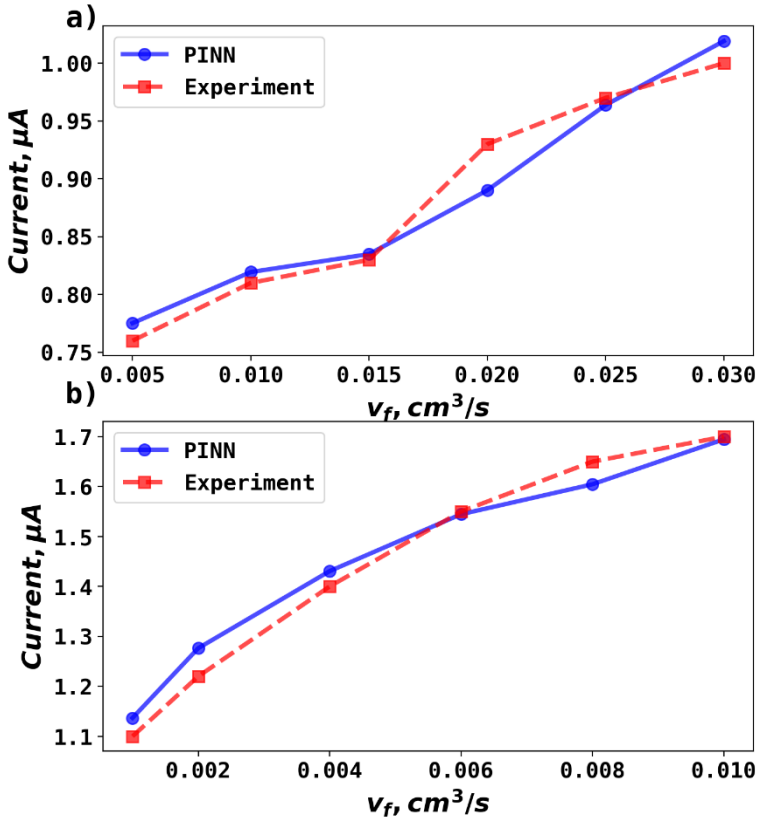

Figure 9.5. Compare PINN prediction with experiment for oxidation of ferrocene at different electrode length. (a) Electrode length, $x_e = 4\ \mu m$. (b) Electrode length, $x_e = 11\ \mu m$.

9.4.2 Double Microband Channel Electrode

We consider the case of a double microband channel electrode which employs a generator-detector setup,[50] in which a downstream detector electrode reduces the electro-generated product, B, from the electro-oxidation of A at an upstream generator electrode. The ratio of the detector electrode current relative to the generator electrode current is termed the collection efficiency, N, which for a stable species undergoing transport is controlled by the geometry of the double channel electrode and the flow rate.

To explore these parameters, we made PINN prediction while keeping the length of both the generator and the detector electrode identical, with the dimensionless gap X_b between the electrodes, varied from $\frac{1}{11}$ to 1 and Pe fixed at 100. The upstream simulation space is enforced by setting $\mathrm{X}_1 = \frac{2}{11}$ and the downstream space by fixing $\mathrm{X}_{channel} - X_4 = \frac{2}{11}$. The simulation distance in Y direction is $\mathrm{Y}_{channel} = 2.5X_{channel}$. The number of collocation points, for the simulations shown in Figure 9.6 and Figure 9.7 was $\mathcal{N} = 10^6$.

The concentration profiles and flux densities predicted by the PINN are shown in Figure 9.6. The concentration profiles show a plume of electrogenerated material flowing downstream and being partially but not completely consumed at the detector electrode. The electrogenerated material extends upstream of the generator electrode where it is carried by axial diffusion against the flow.

The plots of the flux density on the generator electrode show two maxima. The upstream peak resembles that observed above for a single channel electrode and again reflects the high flux delivered convectively and diffusively in this region. The second (downstream peak) is attributed to axial back diffusion against the flow leading to upstream transport of some A following regeneration from B at the detector electrode). With increasing gap distance,

the flux density in the second peak in the generator flux decrease relatively to the first peak because the 'positive feedback' from the detector electrode decreases. In addition, note that a longer gap length facilitates the diffusion of electrochemically generated B away from surface of electrode, leading to reduced flux density at the detector electrode.

To validate the PINN prediction, the predicted collection efficiency was compared with analytical expressions. Matsuda and Braun[44, 51, 52] have developed an approximate analytical expression for the collection efficiency of a double channel electrode as:

$$N = 1 + X_d^{2/3}\left[1 - F(X_b)\right] - (1 + X_b + X_d)^{2/3} \times \left[1 + F\left\{\left(\frac{X_b}{X_d}\right)(1 + X_b + X_d)\right\}\right] - F\left(\frac{X_b}{X_d}\right) \quad \textbf{(9.25)}$$

where X_b and X_d are the dimensionless gap and detector electrode length respectively. The function F is tabulated by Albery and Bruckenstein[43] as:

$$F(x) = \frac{\sqrt{3}}{4\pi}\ln\frac{\left(1 + x^{1/3}\right)^3}{(1 + x)} + \frac{3}{2\pi}\tan^{-1}\left(\frac{2x^{1/3} - 1}{\sqrt{3}}\right) + \frac{1}{4} \quad \textbf{(9.26)}$$

The collection efficiency predicted by PINN is compared with the predictions of the Matsuda/Braun expression in Figure 9.7and a good agreement is observed between the two, suggesting that PINN can quantitatively simulate the mass transport of a double microband electrode and generate a good estimate of the collection efficiency.

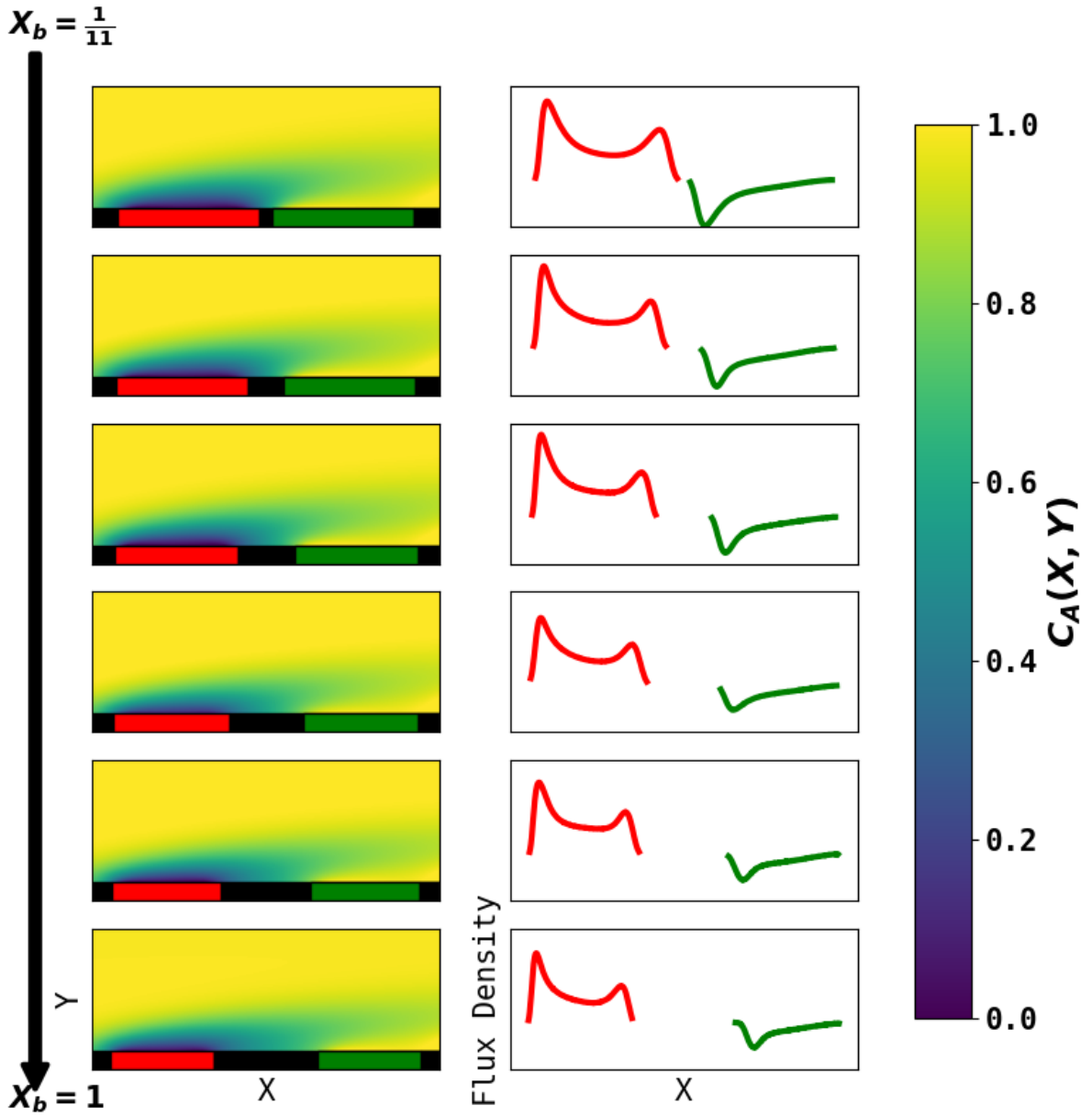

Figure 9.6. PINN prediction of double channel electrode at steady state by varying X_b from $\frac{1}{11}$ to 1 with a step size of $\frac{2}{11}$ while the length of generator and detector electrode are equal. (left) Concentration profile at steady state. Generator electrode, detector electrode and insulating material are represented with red, green and black boxes. (right) Flux density at each electrode. Red line and green line are for generator and detector electrode respectively.

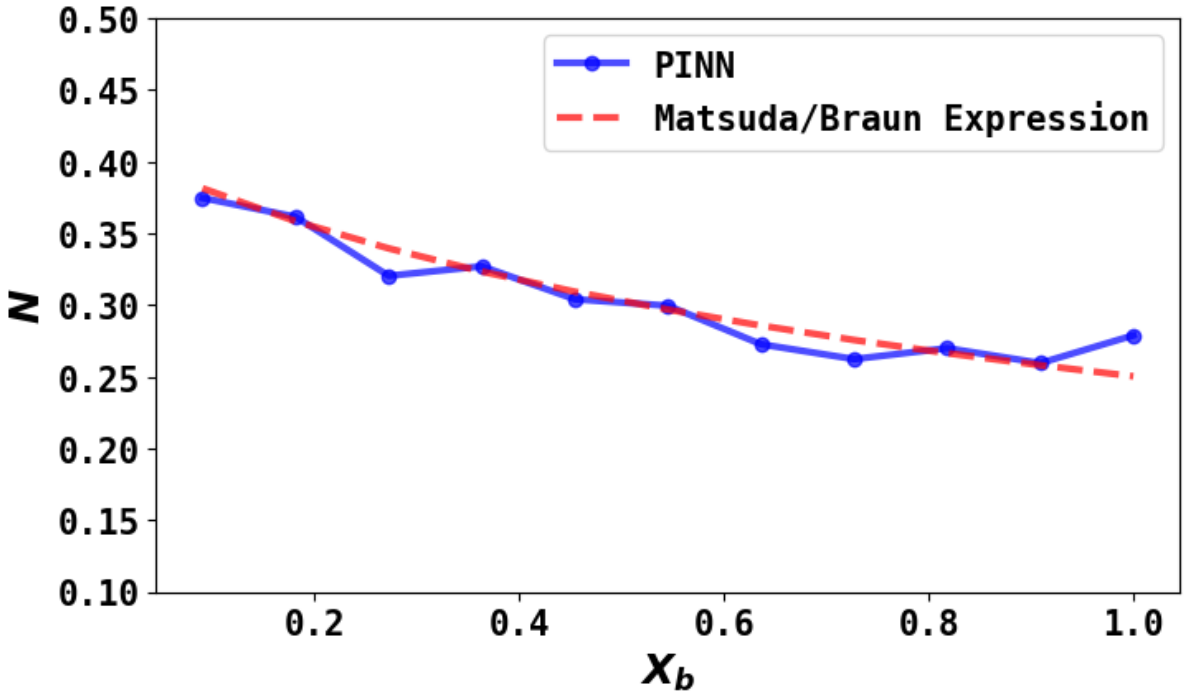

Figure 9.7. Compare PINN prediction of collection efficiency (N) with Matsuda/Braun equation as a function of dimensionless gap distance X_b.

9.4.3 Channel Electrode with CE reaction

As a third paradigm case, PINN simulations of a microband channel electrode assuming $x_e = 11\ \mu m.$ with CE reaction are performed with increasing dimensionless forward reaction rate constants, from $K_f = 0$ to $K_f = 100$ while fixing $K_{eq} = 0.5$. Hence, the dimensionless concentrations of R and A in bulk equilibrated solution, prior to entering the flow cell and upstream of the electrode are $C_R^* = \frac{2}{3}$ and $C_A^* = \frac{1}{3}$ respectively and $C^* = C_R^* + C_A^* = 1$. Two flow rates are considered: $Pe = 1.59$ and 6.38, and the corresponding volume flow rates are $v_f = 0.001\ cm^3\ s^{-1}$ and $0.004\ cm^3\ s^{-1}$. The number of collocation points are set to $\mathcal{N} = 2 \times 10^6$. Figure 9.8shows the concentration profiles of A and R and the flux density of a PINN simulation when $K_f = 1$ and $Pe = 1.59$. Figure 9.8a illustrates the depletion of R near the surface of electrode, to generate A, as the subsequent removal of A pushes the chemical

equilibrium towards product; Figure 9.8b presents the concentration profile of A, showing depletion of A along the flow direction and mass transport upstream due to axial back-diffusion. The pattern of concentration profile is like Figure 9.3a, but the concentration gradients differ and result in different flux densities. From Figure 9.8c, the flux density when $K_f = 1$ is higher than $K_f = 0$, reflecting the extra current contribution from the preceding chemical reaction generating extra A for consumption at the electrode.

Matsuda et al.[53] developed an approximate analytical expression relating the diffusion-controlled current with the kinetic current by neglecting axial diffusion:

$$\frac{I}{I_d} = \frac{1.290\Lambda}{\tanh\left(1.290\Lambda\frac{k_b}{k_f}\right) + 1.290\Lambda} \tag{9.27}$$

where I_d is the diffusion-limited current assuming that the bulk dimensionless concentration $C_A^* = 1$ and Λ is a dimensionless parameter reflecting kinetic, thermodynamic and mass transport parameters derived assuming the diffusion coefficients of all species are equal to that of A:

$$\Lambda = \left(\frac{hx_e}{3v_m}\right)^{\frac{1}{3}} \left\{k_f\left(1 + \frac{k_b}{k_f}\right)\right\}^{\frac{1}{2}} \frac{k_f}{k_b} D_A^{-\frac{1}{6}} \tag{9.28}$$

Figure 9.9 shows the PINN prediction of transport limited currents as a function of K_f at $K_{eq} = 0.5$ and two different Pe: (a) 6.38, (b) 1.59. The PINN predictions (blue line with marker) were benchmarked with the Matsuda equation (orange line with marker) and Figure 9.9 suggests that the two lines approachthe diffusion limited current (red dash-dot line) with increasing K_f. As expected increasingly fast homogeneous kinetics leads to increased currents as more A is made available for reaction on the voltammetric timescale. However, the PINN prediction suggests that in comparison with the Matsuda equation, faster homogeneous kinetics are generally required to access the same currents in the kinetically controlled regime consistent with the fact

that the electrode modelled is of microelectrode dimensions and so experiences a shorter voltammetric timescale than the Matsuda equation designed for macroelectrodes. On the other hand, the increased rate of mass transport leads to the establishment of the full diffusion-controlled limit for lower values of K_f. The mathematical derivations of **(9.27)** and **(9.28)** are at the limits of analytical theory and require the adoption of severe approximations. It is evident that PINNs have the potential to make predictions via physically more realistic models.

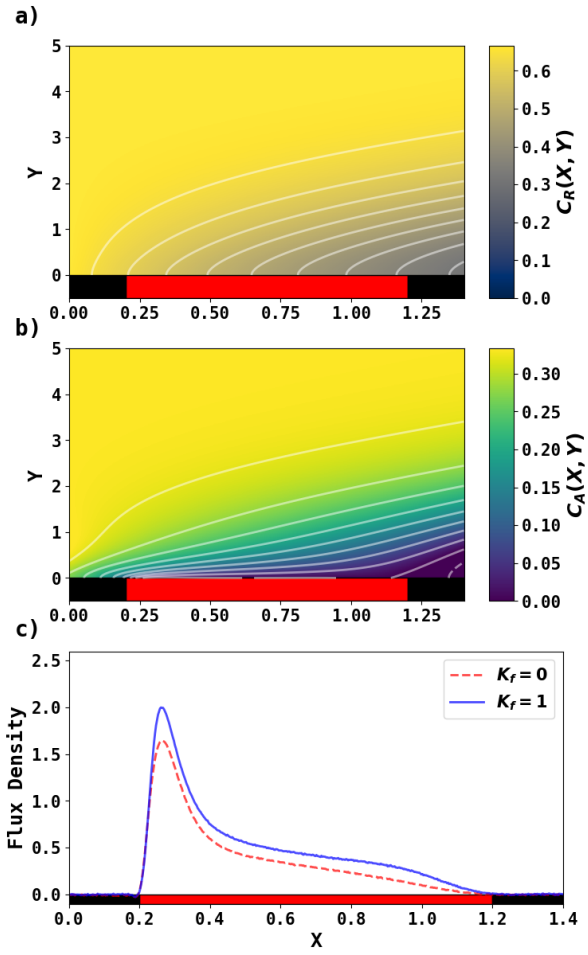

Figure 9.8. PINN prediction of channel electrode coupled with CE reaction, when $K_f = 1, K_{eq} = 0.5$ and $Pe = 1.59$. (a,b) Concentration profile of R and A respectively. (c) Flux density of electrochemical reaction of A when $K_f = 0$ and $K_f = 1$.

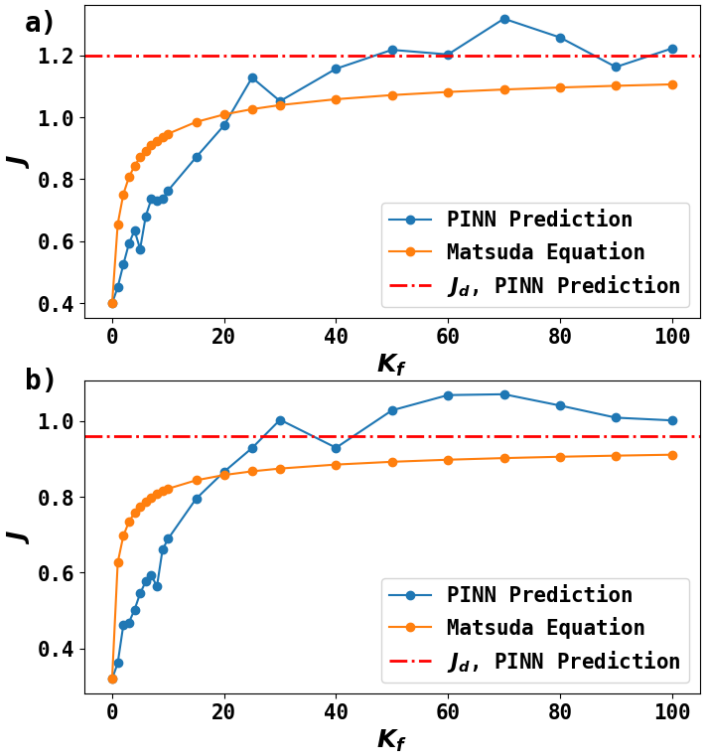

Figure 9.9. PINN prediction of kinetic flux (orange line with marker) as a function of dimensionless forward reaction rate constant at fixed Keq and comparison with flux predicting by Matsuda equation (blue line with marker). Red dash-dot line represents the mass transport limiting current when $C_A^* = 1$. (a) $K_{eq} = 0.5, Pe = 6.38$, (b) $K_{eq} = 0.5, Pe = 1.59$.

9.5 Conclusions

In summary, we have implemented PINNs to solve three problems in hydrodynamic voltammetry: transport limited currents at single microband channel electrodes, the collection efficiency of a double microband channel electrode and the kinetically controlled currents expected at a channel electrode for a CE reaction. The resulting steady-state currents were compared with experiments or analytical expression where available, proving that PINNs is a rapid and simple to implement alternative to FD and FE simulations for solving electroanalytical convective-diffusion problems including those with coupled homogeneous chemical kinetics. In the latter case we facilitated PINN solution for the prediction of the concentration of two species via the cooperation of two embedded neural networks in the PINN. We have also demonstrated that PINNs can be applied to convection-diffusion problems with

fast mass transport (high *Pe* number), using curriculum learning to accelerate convergence. Together with our previous chapter on diffusion only voltammetry,[54] the work on hydrodynamic voltammetry establishes the basis of PINN simulation for the application of PINNs in electrochemistry and electro-analytical chemistry, being an easier and/or cheaper alternative to finite element or finite difference method.

References

1. H. Chen, E. Kätelhön and R. G. Compton, *Analyst*, 2022, **147**, 1881-1891.
2. Q. Chang, China lifts 770 million rural people out of poverty: white paper, http://en.people.cn/n3/2021/0414/c90000-9838854.html, (accessed Feburary 18, 2020).
3. scientific method, https://www.britannica.com/science/scientific-method, (accessed Feburary 17, 2022).
4. J. A. V. Butler, *Trans. Faraday Soc.*, 1924, **19**, 729-733.
5. T. Erdey-Grúz and M. Volmer, *Z. Phys. Chem.*, 1930, **150**, 203-213.
6. R. A. Marcus, *J. Chem. Phys.*, 1956, **24**, 966-978.
7. R. A. Marcus, *J. Chem. Phys.*, 1957, **26**, 867-871.
8. N. S. Hush, *J. Chem. Phys.*, 1958, **28**, 962-972.
9. A. Fick, *Ann. Phys.*, 1855, **170**, 59-86.
10. A. Fick, *Lond. Edinb. Dubl. Phil. Mag.*, 1855, **10**, 30-39.
11. V. G. Levich, *Physicochemical hydrodynamics*, 1962.
12. A. Frumkin, *Zeitschrift für Physik*, 1926, **35**, 792-802.
13. R. G. Compton, E. Laborda, E. Kaetelhoen and K. R. Ward, *Understanding voltammetry: simulation of electrode processes*, World Scientific London, 2nd edn., 2020.
14. D. Britz and J. Strutwolf, *Digital simulation in electrochemistry*, Springer, 2005.
15. C. Rao, H. Sun and Y. Liu, *Theor. Appl. Mech. Lett.*, 2020, **10**, 207-212.
16. X.-D. Bai and W. Zhang, *Computers & Fluids*, 2022, **235**, 105266.
17. Y. Huang, Y. Tang, H. Zhuang, J. VanZwieten and L. Cherubin, *Frontiers in Artificial Intelligence*, 2021, **4**.
18. Y. Bai, T. Chaolu and S. Bilige, *Nonlinear Dynamics*, 2022, DOI: 10.1007/s11071-021-07146-z.
19. M. Aykol, C. B. Gopal, A. Anapolsky, P. K. Herring, B. van Vlijmen, M. D. Berliner, M. Z. Bazant, R. D. Braatz, W. C. Chueh and B. D. Storey, *J. Electrochem. Soc.*, 2021, **168**, 030525.
20. Y. A. Yucesan and F. A. Viana, *International Journal of Prognostics and Health Management*, 2020, **11**.
21. A. Krishnapriyan, A. Gholami, S. Zhe, R. Kirby and M. W. Mahoney, *Advances in Neural Information Processing Systems*, 2021, **34**.
22. R. G. Compton and P. R. Unwin, *J. Electroanal. Chem. Interfacial Electrochem.*, 1986, **205**, 1-20.
23. J. A. Cooper and R. G. Compton, *Electroanalysis*, 1998, **10**, 141-155.
24. J. A. Alden, M. A. Feldman, E. Hill, F. Prieto, M. Oyama, B. A. Coles, R. G. Compton, P. J. Dobson and P. A. Leigh, *Anal. Chem.*, 1998, **70**, 1707-1720.

25. J. Alden and R. Compton, *Anal. Chem.*, 2000, **72**, 198A-203A.
26. B. A. Coles and R. G. Compton, *J. Electroanal. Chem. Interfacial Electrochem.*, 1983, **144**, 87-98.
27. J. RfiiiCka and E. H. Hansen, *Flow Injection Analysis*, John Wiley & Sons, 1988.
28. J. Ruzicka, *Anal. Chem.*, 1983, **55**, 1040A-1053A.
29. D. A. Roston, R. E. Shoup and P. T. Kissinger, *Anal. Chem.*, 1982, **54**, 1417A-1434A.
30. D. A. Roston and P. T. Kissinger, *Anal. Chem.*, 1982, **54**, 429-434.
31. C. Renault, M. J. Anderson and R. M. Crooks, *J. Am. Chem. Soc.*, 2014, **136**, 4616-4623.
32. H. Wang, E. Rus and H. D. Abruña, *Anal. Chem.*, 2010, **82**, 4319-4324.
33. J. Booth, R. G. Compton, J. A. Cooper, R. A. Dryfe, A. C. Fisher, C. L. Davies and M. K. Walters, *J. Phys. Chem.*, 1995, **99**, 10942-10947.
34. A. J. Wain, R. G. Compton, R. Le Roux, S. Matthews, K. Yunus and A. C. Fisher, *J. Phys. Chem. B*, 2006, **110**, 26040-26044.
35. S. Liu, Y. Gu, R. B. Le Roux, S. M. Matthews, D. Bratton, K. Yunus, A. C. Fisher and W. T. Huck, *Lab on a Chip*, 2008, **8**, 1937-1942.
36. S. S. Hill, R. A. W. Dryfe, E. P. L. Roberts, A. C. Fisher and K. Yunus, *Anal. Chem.*, 2003, **75**, 486-493.
37. R. G. Compton, A. C. Fisher, R. G. Wellington, P. J. Dobson and P. A. Leigh, *J. Phys. Chem.*, 1993, **97**, 10410-10415.
38. C. Amatore, N. Da Mota, C. Lemmer, C. Pebay, C. Sella and L. Thouin, *Anal. Chem.*, 2008, **80**, 9483-9490.
39. T. Holm, J. A. Diaz Real and W. Mérida, *J. Electroanal. Chem.*, 2019, **842**, 115-126.
40. A. Testa and W. Reinmuth, *Anal. Chem.*, 1961, **33**, 1320-1324.
41. R. G. Compton and C. E. Banks, *Understanding voltammetry*, World Scientific, London, 3rd edn., 2018.
42. A. Lévêque, *Les lois de la transmission de chaleur par convection*, Dunod, 1928.
43. W. J. Albery and S. Bruckenstein, *Trans. Faraday Soc.*, 1966, **62**, 1920-1931.
44. H. Matsuda, *J. Electroanal. Chem. Interfacial Electrochem.*, 1968, **16**, 153-164.
45. F. M. Rohrhofer, S. Posch and B. C. Geiger, *arXiv preprint arXiv:2105.00862*, 2021.
46. D. P. Kingma and J. Ba, *arXiv preprint arXiv:1412.6980*, 2014.
47. T. De Ryck, S. Lanthaler and S. Mishra, *Neural Networks*, 2021, **143**, 732-750.
48. R. Leiteritz and D. Pflüger, *arXiv preprint arXiv:2112.05620*, 2021.
49. Y. Wang, E. I. Rogers and R. G. Compton, *J. Electroanal. Chem.*, 2010, **648**, 15-19.
50. E. O. Barnes, G. E. Lewis, S. E. Dale, F. Marken and R. G. Compton, *Analyst*, 2012, **137**, 1068-1081.
51. H. Gerischer, I. Mattes and R. Braun, *J. Electroanal. Chem.*, 1965, **10**, 553-567.
52. R. Braun, *J. Electroanal. Chem. Interfacial Electrochem.*, 1968, **19**, 23-35.
53. K. Tokuda, K. Aoki and H. Matsuda, *J. Electroanal. Chem. Interfacial Electrochem.*, 1977, **80**, 211-222.
54. H. Chen, E. Kätelhön and R. G. Compton, *J. Phys. Chem. Lett.*, 2022, **13**, 536-543.

Chapter 10 Summary

Computational electrochemistry is unsurprisingly a broad topic and the thesis aims at expanding the understandings and applications of computational electrochemistry. The thesis covers finite difference method to simulate electrochemical reactions, the synergy of finite difference simulation to train machine learning models for electrochemistry and the application of Physics-Informed Neural Network (PINN) as a novel tool to solve partial differential equations (PDEs) for voltammetry.

The thesis starts with introduction of the electroanalytical experiments like voltammetry and cyclic voltammetry in and its theories 0 followed by a gentle introduction of finite difference method in Chapter 2 to solve for partial differential equations of the underlying experiment and caveats of simulation including dimensionless parameters, expanding space and time grid and random walk method for simulations at low concentrations.

In the next three chapters, we explored the effect of chemical reaction on Tafel analysis and found that preceding chemical reaction reduces the apparent transfer coefficient while following chemical reaction increases the apparent transfer coefficient, cautions the effect of chemical reaction on identifications of numbers of electrons involved.

In Chapter 6, we developed data-driven artificial neural networks, trained with simulations, to predict voltammograms and to extract kinetic and thermodynamic parameters from voltammograms. The framework is tested and validated in Chapter 7 with experiment of dissociative CE reaction of acetic acid. Using only the steady state current at different bulk concentrations of acetic acid, the equilibrium and forward reaction rate constant on acetic acid dissociation is obtained and agreed with literature.

Lastly, we introduced a new tool, PINN, to simulate a voltammogram. PINN simulation does not require discretization of PDE (hence no background in discrete calculus required), but by constraining the neural network with PDE, boundary and initial conditions to solve PDE and to offer a solution. First, PINN prediction of cyclic voltammetry at a macroelectrode with both semi-infinite and thin-layer boundary conditions performed and validated. 2D models including microband electrode and a cube particle electrode are also performed and validated. In Chapter 9, PINN is challenged with convective-diffusion in channel electrode to predict the steady state currents. Three cases, including steady state current at a microband electrode, collection efficiency of double channel electrode and channel electrode with coupled chemical reaction. The results are validated with experiments or analytical expressions, showing that PINN can accurately solve for the more complicated convective-diffusion problem.

In summary, this thesis explores a wide spectrum of computational electrochemistry: from traditional finite difference simulation, to AI prediction and PINN simulation. The thesis may offer new insights and tools to electrochemists seeking to simulate experiment with less computational time (AI prediction method), or less implementation time (PINN method). The code repositories for each project are available online to better serve the electrochemistry society.